

IDŐJÁRÁS

QUARTERLY JOURNAL OF THE HUNGARIAN METEOROLOGICAL SERVICE

CONTENTS

<i>Zoltán Sipos, André Simon, Kálmán Csirmaz, Tünde Lemler, Robert-Daniel Manta, and Zsófia Kocsis: A case study of a derecho storm in dry, high-shear environment</i>	1
<i>Vasilică Istrate, Radu Vlad Dobri, Florentina Bărcăcianu, Răzvan Alin Ciobanu, and Liviu Apostol: Sounding-derived parameters associated with severe hail events in Romania</i>	39
<i>András Horkai: A statistical analysis of the relationship between domestic hot water consumption and mean outdoor temperature in Budapest</i>	53
<i>Sadegh Karimi, Hamid Nazaripour, and Mohsen Hamidianpour: Spatial and temporal variability in precipitation extreme indices in arid and semi-arid regions of Iran for the last half-century</i>	83
<i>Mihály Kocsis, Attila Dunai, János Mészáros, Zoltán Magyar and András Makó: Soil-specific drought sensitivity of Hungarian terroirs based on yield reactions of arable crops</i>	105
<i>Hristo Chervenkov and Kiril Slavov: Geo-statistical comparison of UERRA MESCAN-SURFEX daily temperatures against independent data sets</i>	123
<i>Angela Anda, László Menyhárt, and Brigitta Simon: Evapotranspiration and yield components of soybean</i>	137
<i>Mahdi Sedaghat, Hasan Hajimohammadi, and Vahid Shafaie: Synoptic aspects associated with pervasive dust storms in the southwestern regions of Iran</i>	151

IDŐJÁRÁS

Quarterly Journal of the Hungarian Meteorological Service

Editor-in-Chief
LÁSZLÓ BOZÓ

Executive Editor
MÁRTA T. PUSKÁS

EDITORIAL BOARD

ANTAL, E. (Budapest, Hungary)	MIKA, J. (Eger, Hungary)
BARTHOLY, J. (Budapest, Hungary)	MERSICH, I. (Budapest, Hungary)
BATCHVAROVA, E. (Sofia, Bulgaria)	MÖLLER, D. (Berlin, Germany)
BRIMBLECOMBE, P. (Hong Kong, SAR)	PINTO, J. (Res. Triangle Park, NC, U.S.A.)
CZELNAI, R. (Dörgicse, Hungary)	PRÁGER, T. (Budapest, Hungary)
DUNKEL, Z. (Budapest, Hungary)	PROBÁLD, F. (Budapest, Hungary)
FERENCZI, Z. (Budapest, Hungary)	RADNÓTI, G. (Reading, U.K.)
GERESDI, I. (Pécs, Hungary)	S. BURÁNSZKI, M. (Budapest, Hungary)
HASZPRA, L. (Budapest, Hungary)	SZALAI, S. (Budapest, Hungary)
HORVÁTH, Á. (Siófok, Hungary)	SZEIDL, L. (Budapest, Hungary)
HORVÁTH, L. (Budapest, Hungary)	SZUNYOGH, I. (College Station, TX, U.S.A.)
HUNKÁR, M. (Keszthely, Hungary)	TAR, K. (Debrecen, Hungary)
LASZLO, I. (Camp Springs, MD, U.S.A.)	TÁNCZER, T. (Budapest, Hungary)
MAJOR, G. (Budapest, Hungary)	TOTH, Z. (Camp Springs, MD, U.S.A.)
MÉSZÁROS, E. (Veszprém, Hungary)	VALI, G. (Laramie, WY, U.S.A.)
MÉSZÁROS, R. (Budapest, Hungary)	WEIDINGER, T. (Budapest, Hungary)

Editorial Office: Kitaibel P.u. 1, H-1024 Budapest, Hungary

P.O. Box 38, H-1525 Budapest, Hungary

E-mail: journal.idojaras@met.hu

Fax: (36-1) 346-4669

**Indexed and abstracted in Science Citation Index Expanded™ and
Journal Citation Reports/Science Edition**

Covered in the abstract and citation database SCOPUS®

Included in EBSCO's databases

Subscription by mail:

IDŐJÁRÁS, P.O. Box 38, H-1525 Budapest, Hungary

E-mail: journal.idojaras@met.hu

IDŐJÁRÁS

Quarterly Journal of the Hungarian Meteorological Service
Vol. 125, No. 1, January – March, 2021, pp. 1–37

A case study of a derecho storm in dry, high-shear environment

**Zoltán Sipos¹, André Simon^{2,*}, Kálmán Csirmaz², Tünde Lemler²,
Robert-Daniel Manta¹, and Zsófia Kocsis²**

¹ *National Meteorological Administration*
Sos. București-Ploiești nr. 97, Sector 1,
013686 București, Romania

² *Hungarian Meteorological Service*
Kitaibel Pál u. 1, 1024 Budapest, Hungary

**Corresponding author E-mail: simon.a@met.hu*

(Manuscript received in final form January 29, 2020)

Abstract— The present study examines the origin and environmental conditions of the severe convective windstorm on September 17, 2017, which affected several countries in the central and southeastern Europe, above all Serbia and Romania. The large area of the damage swath (at least 500 km long) and high wind gusts (up to 40 m/s) would classify this event as a derecho or at least as a storm very similar to derechos (with respect to newer definition proposals). Small-scale bow echoes were found in areas with highest reported wind gusts, and some thunderstorms within the storm-producing convective system were probably supercells. The existence of high wind shear and storm rotation could be also related to the significant rightward deflection of the system with respect to the mean wind and propagation of other thunderstorms and systems observed on that day. In contrary to many other known derecho events, this storm propagated toward a very dry airmass exhibiting only low or moderate convective available potential energy (CAPE) values. This is shown by soundings, ECMWF model outputs, and vertical profiles from the IASI L2 satellite sounder. Several convective parameters (e.g. CAPE, downdraft CAPE, derecho composite parameter, 0-3-km relative humidity, 0-6-km shear) were evaluated and compared with proximity soundings of other described European derechos or with the available climatology. The possibility of a balance between the cold pool-generated horizontal vorticity and the environmental shear is also discussed. It is concluded that identification of low-level humidity sources (with aid of storm-relative wind vectors or streamlines) can be important in forecasting of thunderstorm systems moving toward an airmass, which is seemingly too dry for development and maintenance of deep convection. It is also shown that due to low CAPE values, some composite parameters would not indicate favourable conditions for a long-lived convective system. The lack of radiosonde observations can be partially supplemented by data from the IASI L2 sounder, which profiles can be largely different from model forecasts, showing much drier air in the mid-

and upper troposphere in this case. It is concluded that due to the absence of strong synoptic forcing and larger pressure gradient at surface, convective processes played major role in the windstorm development. The presence of high temperature lapse rates at low- and mid-levels, high wind shear and unusually dry pre-storm airmass could be considered as the most important signatures related to the storm severity.

Key-words: derecho, high-shear, dry air, low-to-moderate CAPE, storm-relative wind, IASIL2 profiles, bow echo, WER echo

1. Introduction

On September 17, 2017, a mesoscale convective system (MCS) caused severe windstorm over Serbia and Romania. The highest measured gust reached 40 m/s, wind gusts exceeding 26 m/s (and damages by wind) occurred in an approximately 500 km long and at least 100 km wide swath over the northern part of Serbia and western part of Romania (*Fig. 1*). This would classify the event as a derecho (*Johns and Hirt, 1987, hereafter JH87*) or at least as a derecho-like storm according the newer definition proposal (*Corfidi et al., 2016*). In JH87 the condition for the length of the major axis of the derecho was 400 km, whereas in *Corfidi et al., 2016* it was increased to 650 km. The JH87 paper described two kinds of derecho storms - progressive and serial. In the presented case we could see one compact pattern of high wind gusts and accompanied damages, which was extending nearly in the direction of the mean flow, which is typical for progressive derecho types. Although severe thunderstorms are common in Serbia and Romania (*Lemon et al., 2003, Antonescu and Burcea, 2010, Pavlović-Berdon et al., 2013, Antonescu and Bell, 2015, Rabrenović, 2015*), storms causing such widespread windstorms are relatively rare in this area and are less documented in scientific papers. We are aware of only few publications dealing with large convective systems in southeastern Europe, though some storms were recently studied also with aid of numerical models (*Lompar et al., 2017*) and there were also attempts for climatology of convective gusts (*Rabrenović and Gatzen, 2017*). One of the well documented events in the neighboring region was the derecho storm of July 20, 2011 (*Gospodinov et al., 2015*), which hit Bulgaria and the southern part of Romania. Other known and published derecho events refer rather to the area of Central Europe, Spain, or Finland (*Gatzen, 2004; Gatzen and Púčik, 2011; Púčik et al., 2011; Simon et al., 2011; Celiński-Mysław and Matuszko, 2014; López, 2007; Punkka et al., 2006*). Because of relatively small number of known cases, little is known about the climatology of derechos and similar windstorms in Europe, except of some regions as Germany (*Gatzen et al., 2015*). More information about the environment and macrosynoptic conditions for long-lived convective windstorms is available from the USA (*Evans and Doswell, 2001, hereafter ED01, Coniglio et al., 2004*). ED01 provided analysis of 67 derechos upon 113 proximity soundings. They identified cases with “weak” and “strong”

synoptic forcing. The latter ones were associated with advancing mid-level trough accompanied by well-expressed surface cyclone. They found that derechos can develop and exist in many different instability and wind shear conditions. Although, early numerical simulations (*Rotunno et al.*, 1988, hereafter RKW88, *Weismann*, 1992) of long-lived mesoscale convective systems indicated that such storms could be maintained rather when high wind shear is present at low- and middle tropospheric levels, derecho cases occur also in moderate wind shear environments. Still, wind shear and transport of momentum from higher levels in the cold pool area can be important for the propagation of the system and for the speed of wind gusts (*Mahoney et al.*, 2009). Derecho storms were also reported in situations with very low or no convective available potential energy (CAPE) in neighboring soundings, although this is typical rather for strong synoptic forcing (ED01, *Gatzen et al.*, 2011). High relative humidity (above 70%) is typically found in derecho environments at low levels, while replaced by drier air at mid-levels (*Coniglio et al.*, 2004). Studies of MCS storms (*Cohen et al.*, 2007) also showed steeper lapse rates (6–8 K/km) at mid-levels compared to weak MCS events. In the synoptic-scale flow, 250 hPa flow divergence is often found in the proximity of these storms, and in most of the cases a well-defined 500 hPa upstream trough is found, though, ridge or zonal flows were also observed (*Coniglio et al.*, 2004). Severe, long-lasting convective storms are related to quasi-linear convective systems, often exhibiting bow echoes (*Fujita*, 1978) or mesovortices (*Weisman and Trapp*, 2003), which can be detected on the radar imagery. The presence of these features is also expected in the newer derecho definition (*Corfidi et al.*, 2016). Supercell storms (*Browning*, 1962) occasionally also cause long swathes of severe weather along their path, however, the size of the storm-impact territory and width of the swath is inferior compared to derecho storms. Supercells can be embedded in long-lived mesoscale systems (*Corfidi*, 2003, *Bunkers et al.*, 2006) or can be attached to developing convective systems (*Taszarek et al.*, 2019). On radar images, the presence of supercell mesocyclone is usually identified upon radial-doppler wind measurements as a mesoscale vortex signature (MVS). An indirect evidence of the supercell-related flow is the presence of persistent weak echo regions (WER) or bounded weak echo regions (BWER) in the field of radar reflectivity (*Moller et al.*, 1994). It can be expected that embedded supercells cause a local intensification of the windstorm or even deflection of the propagation of the whole system (*Corfidi*, 2003). Though, the rate of this influence is ambiguous, since it is often observed that the presence of low-level jet causes deviation of the MCS propagation with respect to the mean flow, which is typically rightward (*Corfidi et al.*, 1996, *Corfidi*, 2003). Climatological studies suggested that mostly the deviation between the MCS motion and deep-layer shear vector remains within 30 degrees, even in case of derechos (*Cohen et al.*, 2007).

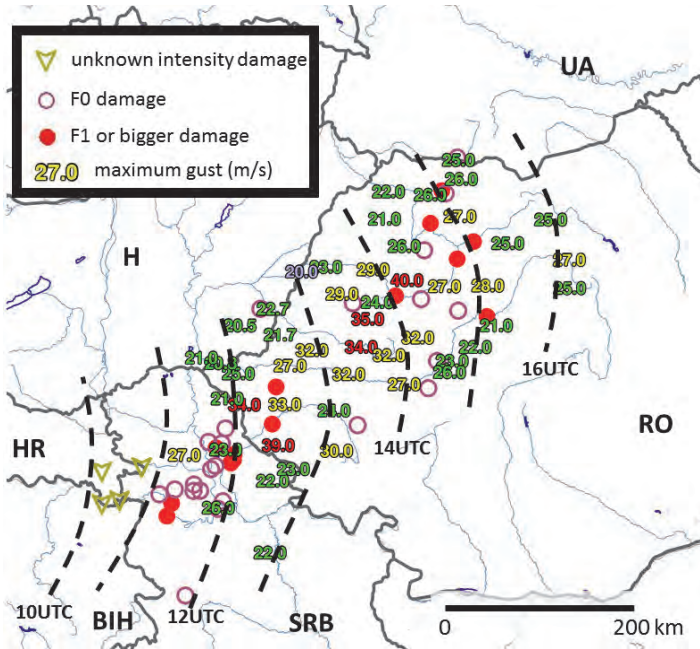


Fig. 1. Maximum wind gusts measured during the September 17, 2017 windstorm by surface weather stations (number, m/s) and damage reports (F0 - empty circles, F1 - full circles, unknown - wind squall symbols). Depicted are only gusts exceeding 20 m/s. Positions of the leading edge of the convective system are shown by dashed lines. Letters BIH, H, HR, RO, SRB, UA denote Bosnia and Herzegovina, Hungary, Croatia, Romania, Serbia, Ukraine.

The above-mentioned typical features of long-lived convective windstorms were considered also during the study of the evolution of the September 17, 2017 storm and of its environment. We focused primarily on the pre-storm environment as derived from available soundings, numerical model analyses, and forecasts. Section 2 describes available sources of data, tools, and parameters chosen for the study. Section 3 gives an overview of the synoptic-scale situation and main characteristics of the storm environment acquired from soundings. Section 4 provides an insight to the structure and evolution of the convective system using radar and satellite imagery. Section 5 summarizes the known impact of the storm, above all in Romania. Section 6 shows the most important characteristics of the pre-storm environment, as derived from numerical weather prediction (NWP) data and compares them with environments of other known derecho events or with available climatology. The possibility of an equilibrium between the cold pool-generated vorticity and pre-storm wind shear is also discussed. Most important findings are summarized in Section 7.

2. Methodology

The present study was done using information from several types of observations (aerological, radar, satellite, and surface measurements) and outputs (analyses and forecasts) of the ECMWF numerical model. At the Hungarian Meteorological Service (OMSZ), an operational, mosaic radar imagery of Hungarian, Croatian, and Slovak radars was used throughout the study (depicted in *Fig. 2*). This imagery enabled us to follow the development of the convective system along large part of its track. However, for cells evolving over Romania (which were situated rather at the edge of the above-mentioned mosaic imagery), we also examined available products of Romanian radars (*Table 1*). Differences between the respective radar imageries were mostly quantitative (e.g., higher column maximum radar reflectivity measured by Romanian radars in case of some intense thunderstorms). These could be caused by different technical specifications and scanning strategies of the radars, screening effects, etc.



Fig. 2. Positions of radars (full circles) and area of coverage of the mosaic radar imagery of Hungarian, Croatian, and Slovak radars used in the study (shaded). The range of the Romanian radars in the eastern and central parts of the country is indicated by dashed circles. Empty circles show the positions of soundings on September 17, 2017, at 00:00 and 12:00 UTC. Letters ZAD, ZAG, SZE, BEO, NIS denote Zadar, Zagreb, Szeged, Beograd, Nis. Letter JIM and rectangle shows the position of IASI L2 profile over Jimbolia (Romania). The smaller full dots show the positions of pseudo-soundings from the ECMWF used for the calculation of convective parameters and characterization of the pre-storm environment valid for September 17, 2017 at 12:00 UTC.

Table 1. Overview of the radars and radar parameters used in the September 17, 2017 study.

Station	Pogányvár	Budapest	Szentes	Nyíregyháza- Napkor	Bilogora	Osijek	Timisoara	Oradea	Tarnaveni/ Bobohalma
Type	DWSR- 2501C	DWSR- 2500C	DWSR -5001C	DWSR- 2501C	WSR- 88D	DWSR 74 S	WSR 98D	WSR 98D	WSR 98D
Band	C-band	C-band	C-band	C-band	S-band	S-band	S-band	S-band	S-band
range (km)	240	240	240	240	240	240	230	230	230
beam width	0.9°	0.94°	0.95°	0.96°	2.1°	2.1°	0.99°	0.99°	0.99°

We used data of synoptic stations with hourly frequency (those, which were subject to international data exchange). We combined the radar and surface data also with the METEOSAT8 satellite outputs (mainly the 10.8 μm infrared channel imagery). For the determination of the environment of various derecho cases (listed in Table 7), we used proximity soundings, which were launched in the area of the track of the storms, or in the nearby area, prior to the event. We preferably used soundings cited in the corresponding papers and studies (referenced in Table 7). For the September 17, 2017 windstorm we also used temperature and humidity profiles from IASI L2 satellite sounder data valid for 09:00 UTC. We preferably chose the same places for IASI diagnostics, where also surface observations and ECMWF model pseudosoundings were available. The surface IASI temperature and dew point values were replaced with observations of surface weather stations, knowing that the IASI errors are typically high at the surface (Roman *et al.*, 2016).

The convective parameters were calculated by a program developed at OMSZ (Csirmaz, 2013) using standard approaches published in scientific literature (Rasmussen and Blanchard, 1998; Gilmore and Wicker, 1998; Bunkers *et al.*, 2000, etc.). The overview of these parameters is given in Table 2. We also calculated the derecho composite parameter or DCP (refer to website of the Storm Prediction Center, 2019 or to Lagerquist *et al.*, 2017). This index yields:

$$DCP = \left(\frac{DCAPE}{980} \right) \left(\frac{MUCAPE}{2000} \right) \left(\frac{0-6\text{km shear}}{10.288} \right) \left(\frac{0-6\text{km mean wind}}{8.23} \right), \quad (1)$$

where the magnitudes of the 0–6-km above ground level (AGL) shear and mean wind are in m/s and the constants in the denominator were modified correspondingly (knots were used in the original definition). The use of such composite parameters or indices is often criticized, because the way they are constructed is empirical, often without physical background (Doswell and Schultz, 2006; Bunkers, 2009). DCP was used here only as an indicator, whether the studied situation would fit the usual environment, in which derechos form. It is considered that favorable environments are characterized by $DCP > 2$ (Lagerquist *et al.*, 2017).

Table 2. Overview of convective parameters and indices used in the presented study and operationally calculated at OMSZ.

Parameter	Explanation	Unit	Remark
SBCAPE (Emanuel, 1994) (Doswell and Rasmussen, 1994)	Surface-based convective available potential energy	J/kg (m^2s^{-2})	Calculated with surface parcel, using virtual temperature
SBCIN (Colby, 1984)	Surface-based convective inhibition	J/kg	Corresponding to SBCAPE calculation
MLCAPE (e.g. Craven <i>et al.</i> , 2002, Davies;2004)	Mixed-layer CAPE	J/kg	Calculated with initial parcel with averaged potential temperature and mixing ratio in the lowest 100 hPa
MUCAPE (e.g. Thompson <i>et al.</i> , 2003)	Most unstable CAPE	J/kg	Calculated with most unstable initial parcel between the surface and 500 hPa
MLCIN (Colby, 1984; Davies, 2004)	Mixed-layer convective inhibition	J/kg	Corresponding to MLCAPE calculation
MUCIN (Colby, 1984)	Most unstable parcel convective inhibition	J/kg	Corresponding to MUCAPE calculation
DCAPE (Gilmore and Wicker, 1998)	Downdraft convective available potential energy	J/kg	Calculated with virtual temperature and initial parcel with lowest equivalent potential temperature below 500 hPa
BLI (Galway, 1956; Fujita, 1970)	Best Lifted Index	K	Calculated with virtual temperature and returning the most unstable value for parcels initiated below 1500m
Bunkers Storm Motion Vector (Bunkers <i>et al.</i> , 2000)	Storm motion vector for supercells propagating left- or right to the mean wind vector	m/s	Constructed with 0-6 km and 0-500m mean wind vectors
0-3-km SREH (Davies-Jones <i>et al.</i> , 1990)	Storm-relative environmental helicity	J/kg	The Bunkers storm motion vector or the actual storm motion vector was used to calculate storm-relative wind
0-3-km RH	Averaged relative humidity for 0-3-km AGL layer	%	
MLMR (Petersen <i>et al.</i> , 1996; University of Wyoming, 2019)	Mean mixed-layer mixing ratio	g/kg	From the Wyoming website, calculated as average mixing ratio in the lowest 500 m
DCP (Storm Prediction Center, 2019, Lagerquist <i>et al.</i> , 2017)	Derecho composite parameter	dimension less	The wind shear and wind speed parameters recalculated from kt to m/s

For the study of the synoptic situation and convective environment we used the September 17, 2017, 00:00 and 12:00 UTC analyses and forecasts of the global, hydrostatic ECMWF model (Persson, 2011). The model has nearly 0.1 degree (9 km) horizontal resolution in the area of the study and uses 137 vertical levels. The model uses parameterization of convection and convective gusts (Bechtold and Bidlot, 2009). Besides charts of meteorological parameters, we also used pseudotemps (pseudo-soundings) for 25 stations in the pre-storm environment on September 17, 2017, at 12:00 UTC (depicted in Fig. 2). The pseudotemp data were used to estimate the magnitude of SBCAPE and its sensitivity on the initial parcel properties (temperature, dew point, pressure).

Finally, for the visualization and calculation of certain features (e.g., streamlines) we used the system HAWK (Hungarian Advanced Work Station) developed at OMSZ (Rajnai and Vörös, 2010).

3. Synoptic situation and pre-storm soundings

On September 17, 2017, at 12:00 UTC, there was a large but shallow area of low pressure over the central and southeastern parts of Europe, with a cold front over the Adriatic Sea, Croatia, Bosnia-Herzegovina, and Hungary, which was moving toward east (Fig. 3). A strong southerly flow of warm air and high temperature gradient could be found at 850 hPa (Fig. 4) over Serbia and eastern part of Romania (the temperature changed by 11 °C on 400 km distance in northwest-southeast direction). At the same time, there was a very strong, diffluent southwesterly flow at 500 hPa (Fig. 5) and at levels above. This flow was around a large cyclone centered over the Benelux states and northern Germany, which slowly extended toward east.

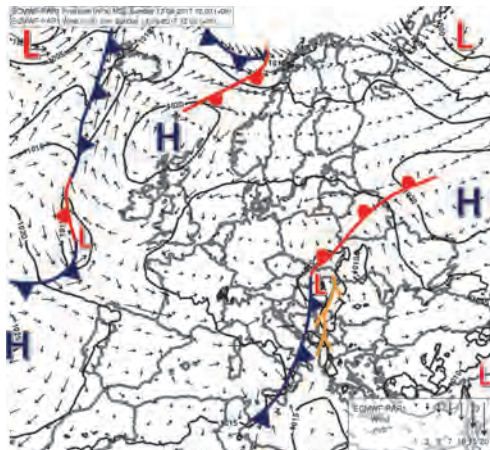


Fig. 3. Surface fronts and ECMWF analysis of mean sea-level pressure (solid lines, hPa) and 10 m wind (arrows, m/s) valid for September 17, 2017, 12:00 UTC. Tree-shaped symbols indicate convergence lines. Labels L and H are used for lows and highs. Wind vectors of 1, 3, 5, 7, 10, 15, 20 m/s are depicted.

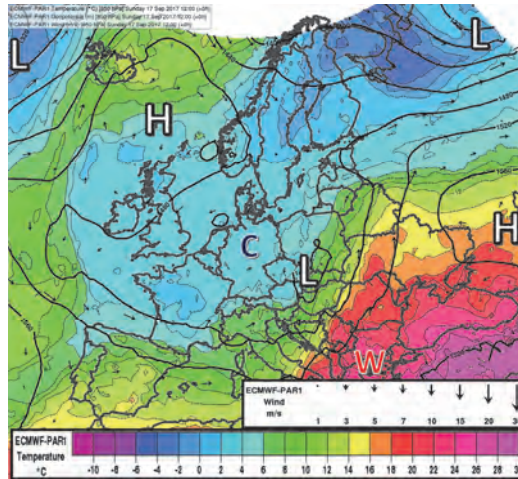


Fig. 4. ECMWF analysis of 850 hPa geopotential (thick solid lines, by 40 gpm), temperature (shades and thin dashed lines, by 2 °C) and wind (arrows, m/s) valid for September 17, 2017, 12:00 UTC. Labels L and H are used for lows and highs, W and C for local temperature maxima and minima. The range of the temperature scale is from -12 °C to 30 °C by 2 °C. Wind vectors of 1, 3, 5, 7, 10, 15, 20, 30 m/s are depicted.

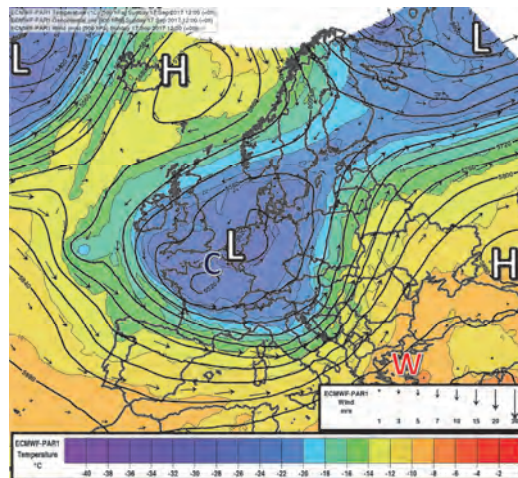


Fig. 5. As in Fig. 4., but for the 500 hPa level. The range of the temperature scale is from -42 °C to 0 °C by 2 °C. Wind vectors of 1, 3, 5, 7, 10, 15, 20, 30 m/s are depicted.

The regional analysis of mean sea level pressure and synoptic observations at 12:00 UTC (Fig. 6) indicated that the storm-producing deep convection occurred at a pre-frontal convergence line extending across a meso-scale area of low pressure over the Serbian-Romanian border. Similarly to the 850 hPa chart, the surface observations also showed high temperature contrasts. In the region,

where the storm occurred, the daily maxima reached 30–34 °C, which is unusual for the given period of year in this region. For example, at the Beograd Surčin station in Serbia, the 1952–1992 average maximum temperature in September was 24 °C (*World Climate*, 2019). Northeast of the storm area, the 2m temperature reached mostly 18–25 °C.

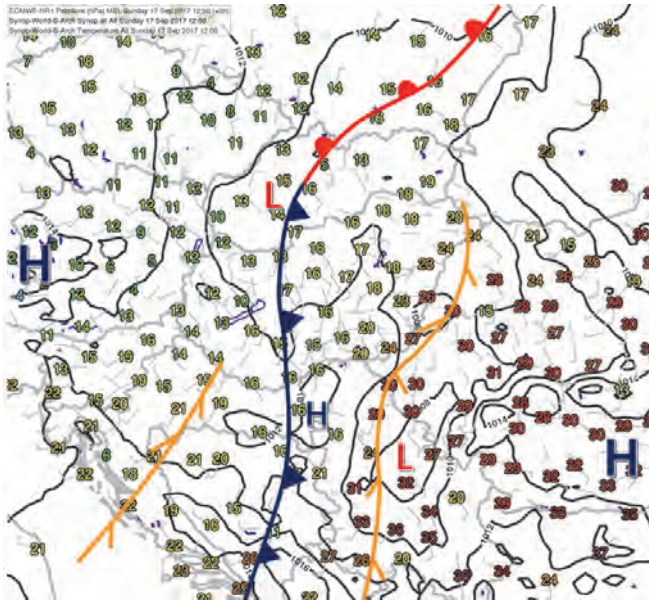


Fig. 6. Analysis of mean sea level pressure (lines, by 2 hPa), 10 m wind (barbs, m/s), and 2m temperature (numbers, °C) observed at respective synoptic stations and of surface fronts/convergence lines valid for September 17, 2017, 12:00 UTC. In the wind visualization (used also in other figures of this paper), half barbs represent 2.5 m/s, full barbs 5 m/s, and flags 25 m/s wind speed values.

Derechos are sometimes distinguished according the synoptic situation as strong forcing (SF), weak forcing (WF), or hybrid events. The original definition (ED01) is rather vague, allowing quite wide interpretation. We believe that the case described here belonged to weak forcing events, because the system was not related to strong surface synoptic-scale cyclone and there was no rapid development or propagation of large-scale troughs and cyclones, in the upper-air fields. The strongly convective character of the event is also underlined by the fact that after the passage of the storm, the 10m wind turned back to the original, southerly direction at many stations and weakened. This is rather typical for the summer convective storms, with prevailingly weak forcing.

Just prior to the arrival of the storm, there was a sounding at Beograd Košutnjak (13275) referred to 12:00 UTC (*Fig. 7a*). It showed that the air was dry at low levels, with high (up to 20 °C) dewpoint depression and relatively high lifted condensation level (LCL), which was situated at around 700 hPa. The temperature lapse rate was high at low levels (8.95 K/km between 925 and 600 hPa) but topped with an inversion at 600 hPa height. Therefore, there was only very little CAPE (SBCAPE was 14 J/kg) concentrated just below the inversion. The lowest 0-6-km wind shear was 39.5 m/s. Very high deep layer shear was found also in other soundings in the storm area (*Table 3*). However, the Beograd sounding was the only one, which was situated directly in the storm track and could be related to the pre-storm environment.

Table 3. Comparison of parameters derived from soundings in the area of the studied storm on September 17, 2017.

Sounding	Position/stage of the storm development	MUCAPE (MUCIN) (J/kg)	MLCAPE (MLCIN) (J/kg)	0-6-km shear (m/s)	DCAPE (J/kg)	MLMR (g/kg)	0-3-km RH (%)	DCP
Beograd (13275) 12 UTC	forward flank of the system, mature	22.5 (69.5)	6.2 (131)	39.5	632.3	5.8	42.4	0.074
Nis* (13388) 12 UTC	southeast of the system, mature	958.1 (50.8)	129.6 (187)	22.9	704.5	NA	42.8	1.28
Szeged (12982) 12 UTC	northern flank of the system, mature	65.7 (0)	2.2 (0)	42.5	55.6	9.4	75.1	0.014
Zagreb (14240) 12UTC	behind the system, mature	842.8 (0)	423.8 (0)	35	360	10.2	89.7	1.24
Zadar (14430) 00 UTC	early development	1069.9 (0.8)	895.2 (13.2)	31.9	599.7	13.3	87.2	2.5

* The 985 hPa (27m AGL) level was omitted in the calculation due to not realistic jump in dewpoint. The MLMR parameter was not available from this sounding.

The hodograph of the storm-relative wind demonstrated a clockwise turn (veering) of the wind from northeasterly-easterly direction at surface to southerly at the 600 hPa level. This suggests the possibility of a strong helical flow at low- and mid-levels in the environment of the thunderstorms (the 0–3-km SREH was 426 J/kg). At the time of the sounding, the direction of the convective system propagation was approximately 30 degrees right of that of the 0–6 or 0–12-km mean wind. Although the rightward deviation of the motion with respect to mean flow is usual for isolated supercell storms, it is sometimes observed in case of mesoscale convective systems too. It is interpreted as a result of superposition of the mean cloud-layer wind and motion of newly generated convective cells,

directed in the low level jet (Corfidi *et al.*, 1996, Corfidi, 2003). In the presented case, the direction of motion vector for right-moving supercells calculated with the method of Bunkers (Bunkers *et al.*, 2000) was the closest to the observed MCS propagation vector. We also calculated the motion vector proposed for upwind-propagating MCSs (its direction was nearly half-way between the observed motion vector and the direction of the mean winds). Although the studied system could be rather classified as downwind-propagating, the corresponding vector constructed according Corfidi's proposal (Corfidi, 2003) would have a magnitude of about 63 m/s (not shown), which is too high for our case. It is possible that the rightward deviation of the whole system was also influenced by the winds in the cold pool (which were northwesterly at the surface, according to the synoptic measurements). Unfortunately, there was no sounding (or other wind observation), which would be representative for the cold pool area and situated directly along the storm track, so this assumption cannot be verified from observations.

Besides soundings, it was also possible to investigate the pre-storm airmass temperature and humidity properties with IASI satellite profiles valid for 09:00 UTC. For example, a profile inferred at the Serbian-Romanian border at Jimbolia (Fig. 7b) showed relatively dry air for the entire troposphere. The relative humidity was everywhere below 55%, the driest tropospheric levels were around 600 (30%) and 500 hPa (22%) levels. The air was conditionally unstable, although the CAPE was only about 360 J/kg.

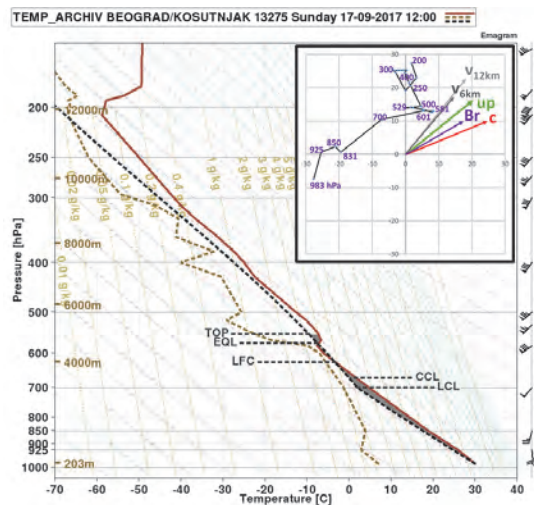


Fig. 7a. Beograd sounding and hodograph of storm-relative wind (shown in rectangle) valid for September 17, 2017, 12:00 UTC. Winds are in m/s (the meaning of the barbs is the same as in Fig. 6). The stable (unstable) area of the sounding is shaded by dark (light) grey color. The storm motion is shown by vector *c* in the hodograph (the magnitude of the vector is 26.5 m/s). Other vectors *v* 6km and *v* 12km are density averaged winds for 0-6-km and 0-12-km depth, respectively. *u_p* indicates MCS motion vector for upwind propagating systems (Corfidi *et al.*, 1996), *Br* is for Bunkers motion vector for right moving supercells (Bunkers *et al.*, 2000). Pressure levels in hPa are labeled. The start of the hodograph is at the anemometric height (983 hPa).

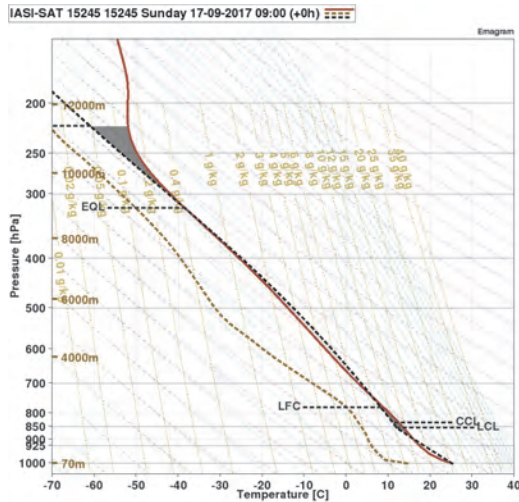


Fig. 7b. IASI L2 vertical profile of temperature and dew point valid for the area of Jimbolia station (emphasized in Fig. 2) and for September 17, 2017, 09:00 UTC. The light grey area is for positive CAPE (362 J/kg), CIN area is dark grey (16 J/kg). DCAPE was estimated as 386 J/kg.

4. Development of the storm from radar and satellite observations

Intense development of deep convection could be observed over Croatia and Bosnia-Herzegovina already in the morning hours of September 17, 2017 (Fig. 8a). A weak precipitation system also passed over the common border of Serbia and Romania, but dissipated fast. There is no information about severe events related to these early convective precipitation bands. However, related precipitation and evaporation could possibly increase the near-surface humidity and support the development of convection in later hours. The origin of the studied convective system could be traced back to convective clouds, which started to develop at around 06:25 UTC over the Adriatic Sea. The environment here was favorable for thunderstorms as indicated by the 00 UTC sounding at Zadar with moderate SBCAPE, reaching 687 J/kg and 41 mm of total precipitable water. According to the mosaic radar imagery, three segments of the convective system (denoted A, B, C) could be tracked, although the convective cells at the leading edge of these segments were not stationary and underwent frequent transition. High radar reflectivity (> 55 dBz) in some of these cells was detected already at around 09:00 UTC (Fig. 8b). Thereafter, the direction of the system propagation started to deviate to the right with respect to motion of the previous cells and precipitation systems. At the start of the windstorm at

11:00 UTC the convective system was quite compact (*Fig. 9a*), resembling quasi-linear MCSs with trailing stratiform precipitation (TS). However, at around 12:30 UTC (*Fig. 9b*) its structure changed significantly, the maximum radar reflectivity in each of the segments decreased and some cells dissipated completely. It is possible that in some cases the maximum radar reflectivity was underestimated because of the distance from available radars or because of screening effects, but the weakening of convection and dissipation of cloudiness was recognizable on the satellite imagery as well (not shown). This could have been the result of the intrusion of dry environmental air, which presence was indicated on Belgrade sounding. In *Fig. 9b* one can also recognize further development of deep convection near the border of Bosnia-Herzegovina, Serbia, and Croatia but the comparison with surface wind observations clearly showed that the windstorm was related to the leading edge of the convective system, denoted by the A,B,C segments.

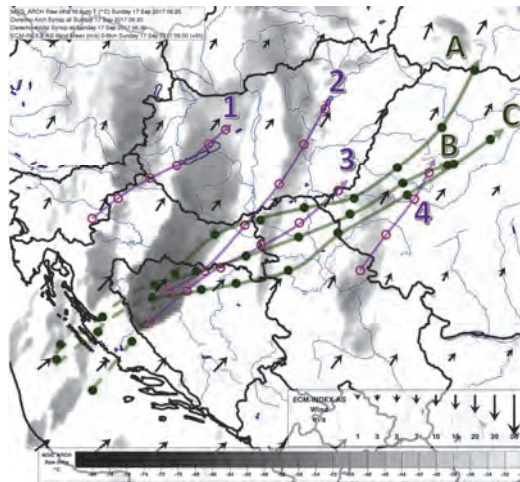


Fig. 8a. Tracks of certain significant storms and segments of the September 17, 2017 convective system (long thick annotated curves with arrowheads). Circles show the positions of the storms (usually the maximum radar reflectivity) with hourly intervals, starting from 06:30 UTC. Labels 1-4 denote those systems, which were not associated with the windstorm, A-C were the segments of the derecho-producing storm. Note that the 06:25-08:25 UTC positions of the A-C segments were only roughly estimated upon satellite imagery, the storms were out of the ranges of available radars at that time. The shades show the cloud-top temperature of the MSG IR 10.8 μm channel (°C) valid for 06:25 UTC. Arrows depict the 0-6 km mean wind (m/s) from the 6h forecast of the ECMWF run based on September 17, 2017, at 00:00 UTC. The range of the temperature scale is from -82 °C to -30 °C by 2 °C. Mean wind vectors of 1, 3, 5, 7, 10, 15, 20, 30, 50 m/s are depicted.

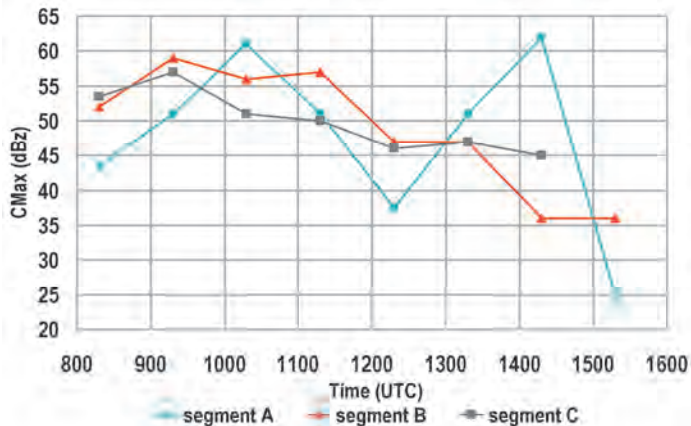


Fig. 8b. Course of the column maximum radar reflectivity (dBz) in the A-C segments of the September 17, 2017 windstorm producing convective system between 08:15 and 15:15 UTC inferred from the mosaic radar imagery of Hungarian, Croatian, and Slovak radars.

Some of the cells of the convective system were remarkably more intense and persistent compared to their neighbors. This was the case of the thunderstorm in the segment C over Serbia between 11:10 and 12:15 UTC exhibiting a forward-flank WER echo around 11:30 UTC (not shown). Another storm could be identified between 13:45 and 14:40 UTC as part of the A segment in western Romania (Fig. 9c). The maximum radar reflectivity reached 67 dBz in this cell according to the Tarnaveni radar and a WER echo could be found at 14:00 and 14:15 UTC (Figs. 10a, 10b and 10c). A notable feature was a small-scale (30 km in direction perpendicular to its propagation) bow echo, which also started to develop after 13:45 UTC and a weak echo in radar reflectivity behind it, observed from both Hungarian and Romanian radars. This bow echo passed over the city of Huedin, where 40 m/s peak gust was observed. It is probable that the above mentioned intense storms were supercells, which developed at the leading edge of the convective system, although there are no such Doppler radar velocity data, which would undoubtedly confirm the presence of mesocyclone in these storms.

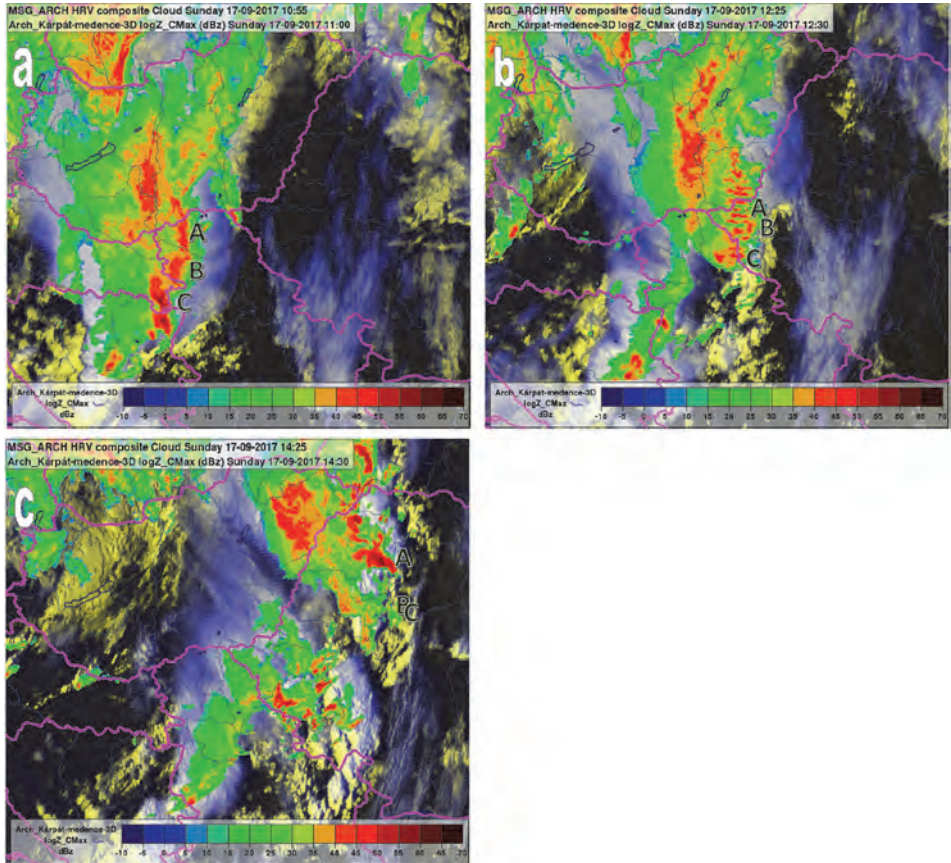


Fig. 9a. MSG 'HRV cloud' composite image valid for September 17, 2017, 10:55 UTC and column maximum radar reflectivity (dBz) of the mosaic radar imagery valid for 11:00 UTC (color shades). Labels A, B, C denote the segments of the derecho-producing convective system. The range of the reflectivity scale is from -10 to 70 dBz by 5 dBz.

Fig. 9b. As in *Fig. 9a* but for 12:25 (12:30) UTC.

Fig. 9c. As in *Fig. 9a* but for 14:25 (14:30) UTC.

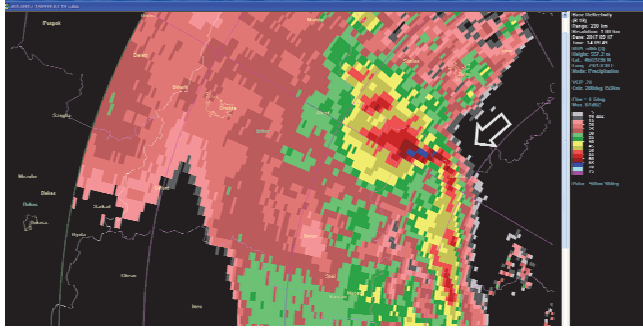


Fig. 10a. Detail from the Tarnaveni radar imagery (west Romania) showing the PPI 1.5° measurement of radar reflectivity on September 17, 2017, at 14:10 UTC in the region of Huedin city. The shades of radar reflectivity start at 5 dBz (light grey), the colors change for 15 dBz (pink), 30 dBz (green), 40 dBz (yellow), 50 dBz (light red), and 65 dBz (blue). The maximum measured value was 67 dBz. The arrow points toward the small-scale bow echo pattern on the right flank of an intense (probably supercell) storm.

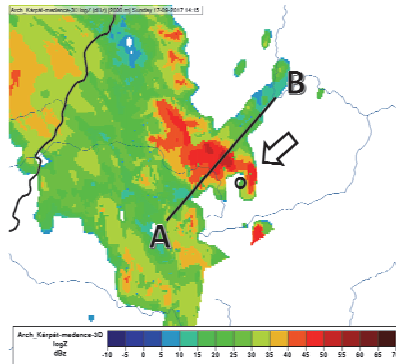


Fig. 10b. 2 km CAPPI reflectivity of the mosaic radar imagery (shades, dBz) valid for September 17, 2017, 14:15 UTC with the depicted sense of the AB cross-section in Fig. 10c. The arrow points toward the bow echo pattern. The circle shows the position of Huedin (where 40 m/s gust was observed). The range of the reflectivity scale is from -10 to 70 dBz by 5 dBz.

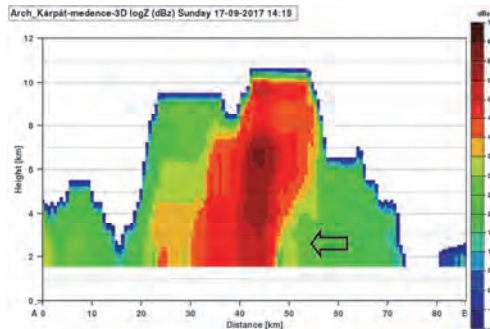


Fig. 10c. Vertical cross-section through the mosaic radar reflectivity field valid for September 17, 2017, 14:15 UTC (the sense of the section is depicted in Fig. 10b). The arrow points toward the WER echo pattern on the forward flank of the storm.

5. Impact of the storm

First damage reports, which could be associated with the studied windstorm were from the border region of Serbia, Croatia, and Bosnia-Herzegovina (website of the European Severe Weather Database, hereafter ESWD 2019). However, there were no details further specifying the character of this damage. More information is from northern Serbia, mainly from the region between Beograd and Novi Sad (affected by the C segment of the system). Reports about injured people (at least 2 cases) were from the region north of Beograd (ESWD, 2019). There were also several videos available on the internet (youtube.com, 2017) showing for example a detached roof of a house transported by wind in Hrtkovci (Nevreme u Hrtkovcima 1) and falling of a tree on the road at Tomaševac (Nevreme (Tornado)-Srbija on September 17, 2017 (Okolina Zrenjanina-Tomasevac)). Damage by wind was reported at least from 21 cities and villages. The most detailed information about the storm impact was from Romania (Disaster Management of Romania: Inspectoratul General pentru Situatii de Urgenta, IGSU, personal communication). Between September 17, 2017, 12:00 UTC and September 18, 2017, 03:00 UTC, windstorm damages and consequences were reported in 212 localities from 15 counties (Alba, Arad, Bihor, Bistrița-Năsăud, Brașov, Cluj, Hunedoara, Harghita, Iași, Maramureș, Mureș, Suceava, Sălaj, Timiș). During the storm, 8 people deceased (Arad 1, Bistrica-Năsăud 2, Timiș 5 cases) and 137 were injured (Alba 6, Arad 15, Bihor 35, Hunedoara 1, Maramureș 10, Sălaj 1, Timiș 49). At least 116 dwellings were affected in Timiș and Sălaj counties, over 290 trees were taken down on roads, cars and buildings with a totally of 35 vehicles damaged, 137 roofs were partially or totally affected by the strong wind gusts. Ministry of Internal Affairs forces intervened to rescue 204 people (in the counties of Alba, Arad, Bihor, Bistrița-Năsăud, Cluj, Hunedoara, Maramureș, Sălaj, Timiș, and Maramureș). The spatial distribution of the material damage, number of injured people, and casualties are shown in *Fig. 11a*. The forestry reported 460000 m³ of fallen trees, from this 246000 m³ occurred on compact area (Regia Nationala a Padurilor, Romsilva, personal communication). The national road management service reported that road traffic was disrupted on 12 national roads (DN1, DN6, DN7, DN13B, DNI7C, DN18, DN18B, DN58, DN 68, DN 69, DN 79, DN79A) and 6 county roads (DJ795, DJ107P, DJ688, DJ764B, DJ79B, DJ 708) due to falling trees (*Fig. 11b*). Furthermore, 42 railway sections were affected due to falling trees in the regional area of Timișoara, Cluj, Brașov, and Iași and 42 school units were closed on September 18, 2017 (Arad 1, Bihor 18, Cluj 1, Timiș 22) as a result of severe weather consequences. The damage distribution indicates a widespread impact of the storm, which was related not only to the most intense convective cells (e.g., in segment A), although their contribution to the total damage was probably the largest.

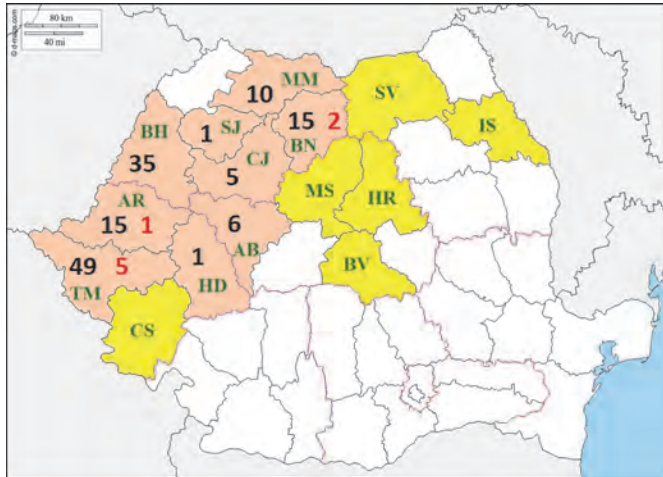


Fig. 11a. Impact of the September 17, 2017 windstorm in Romania. Yellow shade shows counties, where only material damage was reported, in orange-shaded counties there were also injured people (black numbers) or casualties (red numbers). The abbreviations of the counties are as follows: CS-Caraș, TM-Timiș, AR-Arad, BH-Bihor, HD-Hunedoara, AB-Alba, CJ-Cluj, SJ-Sălaj, MM-Maramureș, BN-Bistrica-Năsăud, MS-Mureș, HR-Harghita, BV-Brașov, SV-Suceava, IS-Iași. The source of the background chart: D-maps.com, https://d-maps.com/carte.php?num_car=5808&lang=en

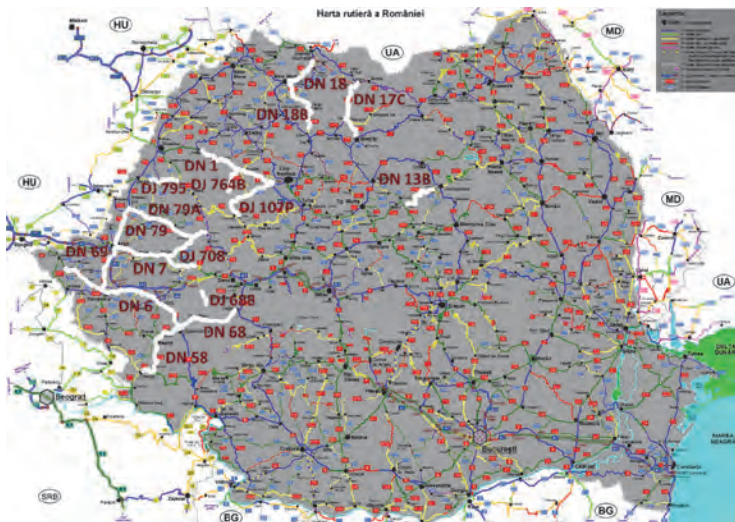


Fig. 11b. Closed roads (thick white lines) in Romania due to the September 17, 2017 windstorm consequences. Road numbers are also shown. Source: forum.construim-romania.ro

According to ESWD, the studied windstorm probably affected also some areas in Ukraine, in the border region with Romania. A weak (F0 intensity) tornado was reported from Velikyj Bychkiv at around 16:00 UTC (ESWD, 2019). The windstorm caused also several damages in Hungary, in the border area with Romania, mainly in the Békés county (data of the National Disaster Management Directorate General in Hungary). There were at least 44 interventions of the disaster management, which were concentrated near the city of Békéscsaba (due to uprooted trees, broken branches, and consequent damages on cars, electric power lines, and roofs of houses).

6. Convective parameters and characteristics of the pre-storm environment

Because there were only few representative soundings in the area of the storm, the distribution of humidity and instability parameters was studied with use of ECMWF analyses and forecasts as well. These enabled to follow the environmental conditions of the storm along its lifetime. We also tried to depict the storm-relative flow in order to identify the areas, which could have been the sources of moisture/dryness and instability. On the 950 hPa specific humidity charts it was possible to see that the studied convective system travelled from relatively moist (10 g/kg) area over Croatia toward much drier (6 g/kg) environment over Serbia on September 17, 2017, at 09:00 UTC (*Fig. 12a*). Very similar was the distribution of the ECMWF-calculated MUCAPE (*Fig. 12d*), which coincided with the moist areas near the surface. At 12:00 UTC one can register that the band of moister air moved towards east. Still, there was drier (6–9 g/kg) air on the eastern and southern side of the convective system, mainly over southern Serbia and its border to Romania. However, at the 950 hPa level the storm-relative flow was northeasterly, hence, the northern part of the system encountered somewhat moister (around 9 g/kg) air from southeastern Hungary and its adjacent border territory with Romania (*Fig. 12b*). Similarly to specific humidity, also the area with non-zero MUCAPE progressed towards east (*Fig. 12e*). The model-inferred MUCAPE values were rather low (mostly around 100 J/kg).

At 14:00 UTC the drier air was present over the central part of Romania (*Fig. 12c*), while the area, where the system propagated and tended was rather moist. At that time it is already possible to see higher values of MUCAPE on the downstream side of the system (*Fig. 12f*) and also in the area of the newly developed convective cloud system over the northern part of Serbia.

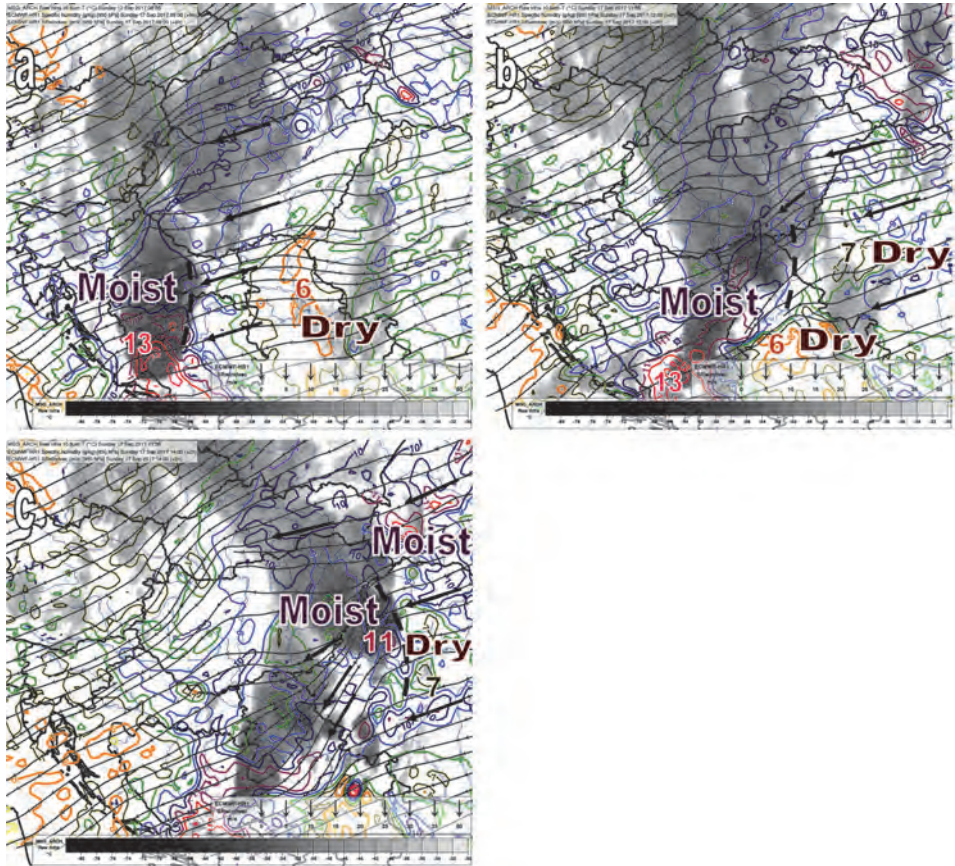


Fig. 12a. ECMWF 9h forecast of 950 hPa specific humidity (colored lines range by 1 g/kg, the 6 g/kg is emphasized by thicker orange line) and of storm-relative wind (streamlines) valid for September 17, 2017, 09:00 UTC. The MSG IR 10.8 μm channel image (shades, $^{\circ}\text{C}$) from 08:55 UTC is in the background. The moist and dry low-level air regions are highlighted, the thick dashed line shows the position of the leading edge of the convective system (convergence line). Some humidity lines are labeled with big letters for easier identification of the moist and dry areas. The thick arrows denote the direction of the streamlines in the neighborhood of the system.

Fig. 12b. As in *Fig. 12a.* but for September 17, 2017, 12:00 UTC and September 17, 2017, 12:00 UTC ECMWF analyses.

Fig. 12c. As in *Fig. 12a.* but for September 17, 2017, 14:00 UTC and for the +2h forecast of the September 17, 2017, 12:00 UTC run of the ECMWF model.

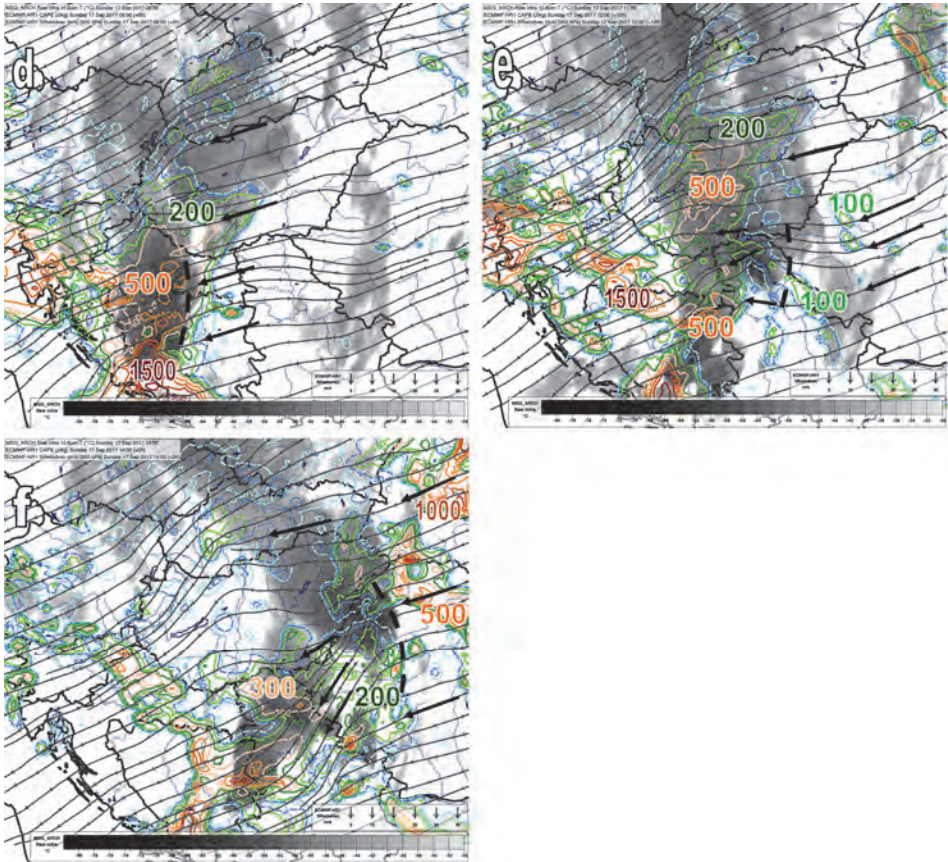


Fig. 12d. As in *Fig. 12a.* but for MUCAPE contours (25, 50, 100, 200, 300, 500, 750, 1000, 1500, 2000 J/kg). Some lines are labeled with big letters for easier identification of forecast MUCAPE in the system and its environment.

Fig. 12e. As in *Fig. 12d.* but for September 17, 2017, 12:00 UTC and for the +12h forecast of the September 17, 2017, 00:00 UTC run of the ECMWF model.

Fig. 12f. As in *Fig. 12d.* but for September 17, 2017, 14:00 UTC and for the +2h forecast of the September 17, 2017, 12:00 UTC run of the ECMWF model.

If we look at the relative humidity conditions at the 950 hPa level at 12:00 UTC (*Fig. 13a*), we can see that the air at the southern and eastern flank of the system was much less saturated (20–40%) than the storm-relative inflow area (about 60%). However, with increasing height, the situation changed and at 700 hPa the storm-relative flow was easterly-southeasterly (*Fig. 13b*), pointing toward the storm from the area with low relative humidity. Both specific and relative humidity distributions indicate that the northern part of the system encountered moister air at low levels and persisted, whereas the thunderstorms on its southern flank quickly dissipated due to inflow of dry, unsaturated environmental air.

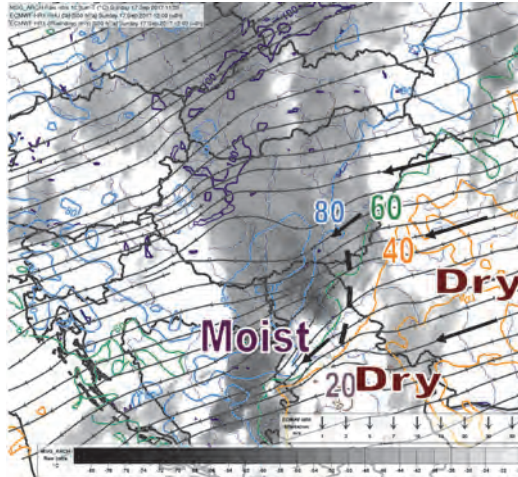


Fig. 13a. As in Fig. 12b. but for the contours of the 950 hPa relative humidity (by 20%). Some humidity lines are labeled with big letters for easier identification of the relatively moist (more saturated) and dry areas. Thick arrows denote the direction of the streamlines in the neighborhood of the system.

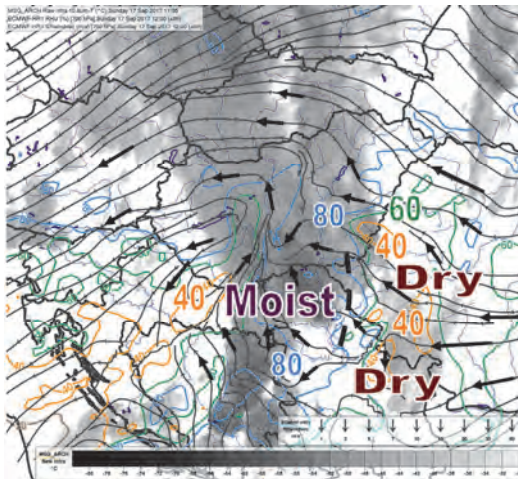


Fig. 13b. As in Fig. 13a but for the 700 hPa relative humidity and 700 hPa streamlines of the storm-relative wind.

It was already mentioned that the thunderstorms developed along a surface line of convergence, which was moving together with the system. The low level wind convergence was visible also in the model analyses at the 925 hPa level and relatively wide area of ascending motions was diagnosed at 800 hPa (Fig. 14a). On the southwest-northeast vertical cross-section (Fig. 14b) it is shown that these motions extended over a large portion of the troposphere. The occurrence of ascending vertical motions coincided with an upper-air potential vorticity (PV)

anomaly, which could be also detected on the section. We hypothesize that these motions could provide some additional lift for generating convection in the mid-troposphere. Although, it is probable that during the mature stage of the storm, the main sources of lift were the convective system itself and its outflow.

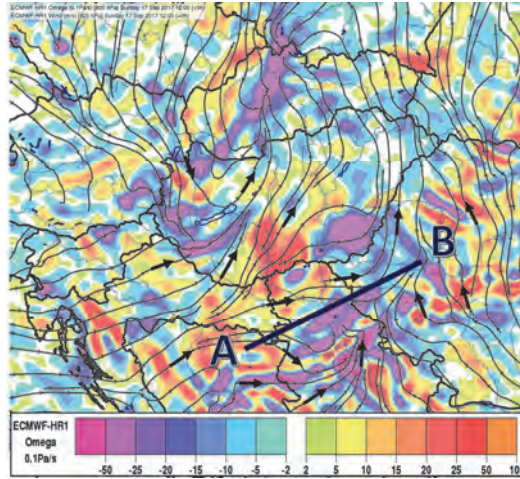


Fig. 14a. ECMWF September 17, 2017, 12:00 UTC analysis of 800 hPa vertical motions (Omega, shades, 0.1 Pa/s) and 925 hPa wind (streamlines, m/s). The AB line shows the sense of the cross-section in Fig. 14b. The range of the vertical motions scale is from $-55 \cdot 10^{-1}$ to $-2 \cdot 10^{-1}$ Pa/s (lilac and bluish shades) and from $2 \cdot 10^{-1}$ to $100 \cdot 10^{-1}$ Pa/s (green, yellow and red shades). The thick arrows denote the direction of the streamlines in the neighbourhood of the system.

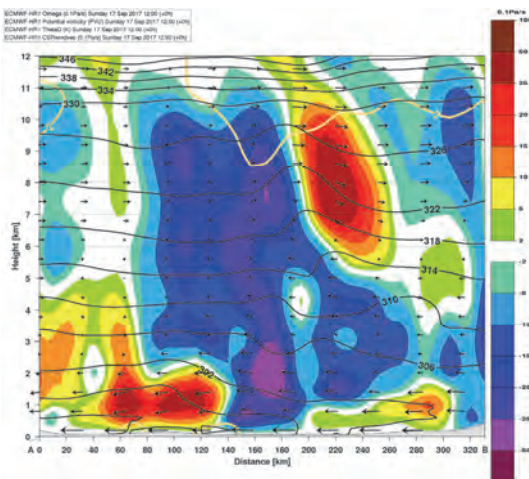


Fig. 14b. Vertical cross-section of the September 17, 2017, 12:00 UTC ECMWF analysis of vertical motions (Omega, shades, 0.1 Pa/s), potential temperature (lines by 4 K), potential vorticity (only 2 PVU is contoured by thicker light brown line), and storm-relative wind (arrows, m/s) projected to the cross-section plane. The sense of the section was shown in Fig. 14a.

The above presented model outputs give some explanation on the persistence of deep convection from humidity point of view and concerning lift. However, there is uncertainty in the significance of the environmental (conditional) instability and magnitude of CAPE. Although the model outputs indicate that there was at least low CAPE behind the leading edge of the storm, the pre-storm instability is important for the generation of new cells. The magnitude of CAPE (and of several versions of this parameter) largely depends on the surface or near-surface humidity conditions (dew-point), which is often uncertain. That is why we also examined temperature lapse rates between the 600–925 and 400–700 hPa levels. At 12:00 UTC, the 600–925 hPa lapse rate was especially high in the dry, unsaturated air, somewhere it was almost dry-adiabatic (*Fig. 15a*). At mid-levels, the unstable area extended more towards north, lapse-rates around 7 K/km could be usually found along the track of the storm (*Fig 15 b*).

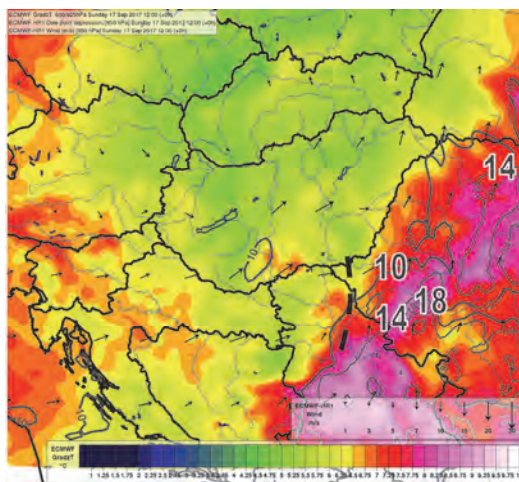


Fig. 15a. ECMWF September 17, 2017, 12:00 UTC analysis of the 600-925 hPa lapse rate (shades, K/km), 850 hPa dew point depression (lines above 10 K which is emphasized by thicker contour), and 850 hPa wind (arrows, m/s). The range of the lapse rate scale is from 0.75 K/km to 10 K/km by 0.25 K/km. Yellow shades belong to lapse rate bigger than 6 K/km, orange shades start from 7 K/km, 8 K/km rate is in magenta color, etc. Wind vectors of 1, 3, 5, 7, 10, 15, 20, 30 m/s are depicted. Big labels show contours of dew point depression of 10, 14, 18 K. The thick dashed line shows the position of the leading edge of the convective system.

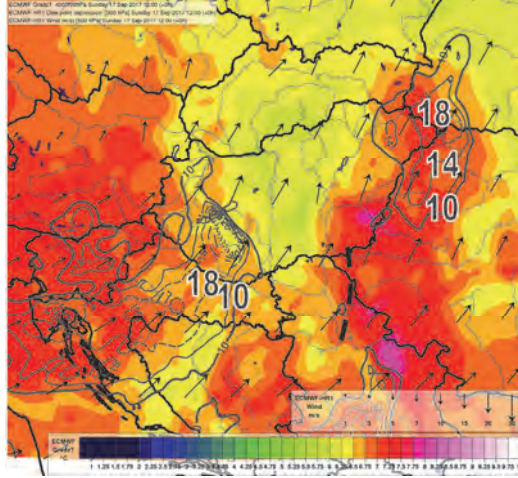


Fig. 15b. As in Fig. 15a. but for the 400-700 hPa lapse rate, 500 hPa dew point depression, and 500 hPa wind.

It must be also taken into account that the model-derived and observed near-surface temperature and humidity conditions can be different, and this can largely influence CAPE calculations. To check this, we evaluated the model outputs (both analysis and forecast) of surface-based CAPE (SBCAPE) at the points with synoptic observations in the pre-storm environment. We recalculated the SBCAPE with a surface parcel starting from the observed temperature, dew-point, and pressure values (Table 4). This evaluation showed that the model 2m temperature and dew-point were underestimated in average, though their BIAS was not very high. This had an impact on the SBCAPE values, which became higher in average, after the correction. The increase in CAPE (in a few pseudotemps it was even exceeding 1000 J/kg) was visible for example at stations close to the convective system, because of higher dew points (up to 16 °C). The maximum-unstable CAPE (MUCAPE) values were mostly close to SBCAPE or identical (therefore not shown). The comparison with IASI profiles showed that the ECMWF forecasts based on the 00:00 UTC run were moister in the mid- and upper tropospheric levels compared to the satellite measurements at several pre-storm locations (compare Fig. 7b and Fig. 16). It is possible that in the reality, the area of dry mid- and upper-tropospheric airmass was larger than the predicted, covering bigger areas of northern Serbia and western Romania.

Table 4. Mean temperature and dew point BIAS of the ECMWF analysis and forecast valid to September 17, 2017, 12:00 UTC and with respect to 25 synoptic observations in the pre-storm area. Surface-based CAPE was calculated and averaged for both reference outputs (pseudotemps) and with a corrected surface parcel starting with temperature, dew-point, and pressure values observed at the respective stations. SBCIN values are shown in parenthesis.

	2m temperature BIAS (°C)	2m dew point BIAS (°C)	SBCAPE (SBCIN) (J/kg)	corrected SBCAPE (SBCIN) (J/kg)
ECMWF analysis	-0.98	-0.11	370.56 (94.67)	646.24 (57.51)
ECMWF 12h forecast	-0.34	-0.27	402.76 (54.33)	660.16 (41.63)

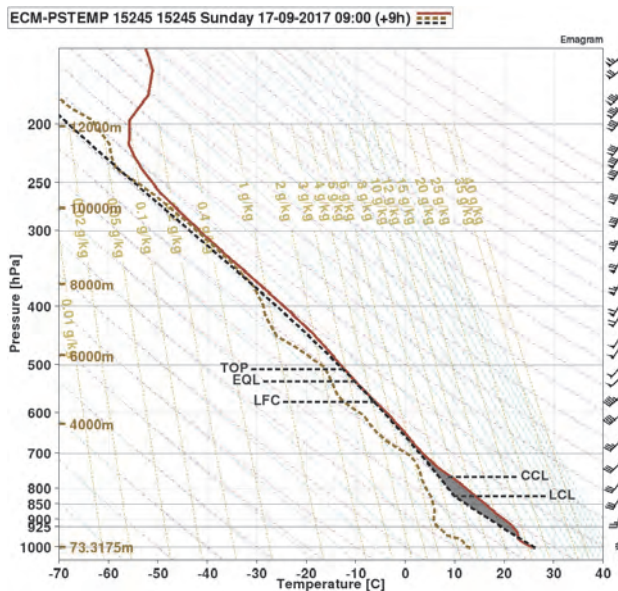


Fig. 16. As in Fig. 7b but inferred from the 9h forecast of the September 17, 2017, 00:00 UTC run of the ECMWF model valid for Jimbolia (Romania).

The intensity of the convective downdrafts and outflows is often studied with the DCAPE parameter, despite of uncertainties in its calculation (Gilmore and Wicker, 1998). Dry environment with high lapse rate also implies high DCAPE values. Already at 09:00 UTC it was possible to diagnose 350–400 J/kg DCAPE over Croatia and Bosnia-Herzegovina (not shown). At 12:00 UTC (Fig. 17), the magnitude of DCAPE was even bigger according to the ECMWF analyses (exceeding 500 J/kg) in the pre-storm region. The presence of dry air at

low levels also resulted in low MLCAPE (mostly below 100 J/kg, see *Table 5*). It is noteworthy that the analyzed ECMWF 0-6-km wind shear was significantly (by 5–10 m/s) lower compared to the measurements of the Beograd or Szeged 12:00 UTC soundings (refer to *Table 3*). The 12:00 UTC ECMWF analysis chart (not shown) indicated that the deep-layer shear was higher on the northern flank of the storm track (along the Hungarian-Romanian border), which could also contribute to better persistence of thunderstorms in this area.

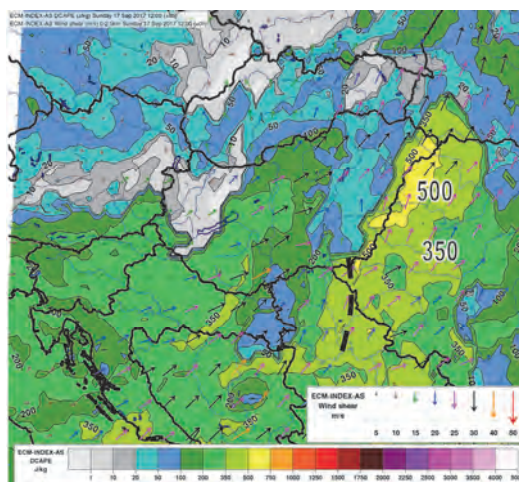


Fig. 17. ECMWF September 17, 2017, 12:00 UTC analysis of DCAPE (shades, J/kg) and 0-2.5 km wind shear (arrows, m/s). Big labels show contours of DCAPE of 350 and 500 J/kg. The range of the DCAPE scale is from 0 to 5000 K/km specified by values of 1, 10, 20, 50, 100, 200, 350, 500, 750, 1000, 1250, 1500, 1750, 2000, 2250, 2500, 3000, 3500, 4000, 5000 J/kg. The meaning of the thick dashed line is the same as in *Figs. 12, 13, and 15*.

Table 5. Minimum, maximum, and average values of some convective and environmental parameters derived from 25 pseudotemps in the pre-storm area and valid for the September 17, 2017, 12:00 UTC ECMWF model analysis.

parameter	MLCAPE (J/kg)	MUCAPE (J/kg)	BLI	0-6-km shear (m/s)	0-6-km mean wind (m/s)	DCAPE (J/kg)	0-3-km RH (%)	DCP
minimum	0	10	-5.1	23.5	15.6	286	28.8	0.02
maximum	356	939	0.3	36.1	22.7	505	64.1	0.98
average	69.6	387.8	-2.06	30.1	19.7	398.2	46.6	0.53

For some years, there was a debate among scientists about the importance of the equilibrium between the environmental low-level wind shear and horizontal vorticity provided by the cold-pool negative buoyancy (e.g., *Bryan et al.*, 2006; *Coniglio et al.*, 2012). The RKW theory (*Rotunno et al.*, 1988) says that such equilibrium favors development of upright updrafts:

$$\Delta u^2 = c^2, \quad (2)$$

$$c^2 = 2 \int_0^H (-B) dz, \quad (3)$$

where Δu is the environmental wind shear, c is the velocity of the net buoyant generation of vorticity, B is the buoyancy, and H is the depth of the cold pool. The theory was later extended by the inclusion of the rear-inflow-jet effects and cold-pool shear (*Weisman*, 1992). However, the existence of this equilibrium is not an ultimate condition for the persistence of a convective system. First, we integrated the negative buoyancy through a 2 km deep layer from the Beograd 12:00 UTC sounding. For the cold pool representation, we used the wet adiabat, which ended at surface at 20.4 °C temperature - measured at the Beograd Vračar station (13274) at 13:00 UTC in the cold pool. The integrated negative buoyancy was -357.74 J/kg, and the corresponding velocity c was 26.75 m/s (its square would be 715.48 m²s⁻²). On the other hand, the 0–2 km pre-frontal windshear component (in the direction of storm propagation) was 16.23 m/s (its square was 263.55 m²s⁻²). This would suggest that even if the pre-storm deep-layer wind shear was large, the system was cold-pool dominated. However, we do not have any exact information about the influence of the rear-inflow-jet. We know that at 12:00 UTC, another meteorological station at Beograd Surčin (its WMO Id is 13272 and it is situated 12 km northwest of the sounding station) reported 13 m/s northwesterly (320°) wind at 10 m, already in the cold pool area. If we expect that the storm-relative wind component at the top of the cold pool was zero, this record would result in a 22.53 m/s cold-pool shear component (its square yields 507.7 m²s⁻²), which would substantially compensate the effect of the buoyant generation of vorticity in the cold pool. However, for more exact calculations we would need more observations or a non-hydrostatic numerical simulation.

In *Table 6* one can find more results of c versus Δu comparison calculated for different heights of the cold pool. It shows that with increasing height of the cold pool also the vorticity balance defined by Eq.(2) becomes more satisfied, because the magnitude of the pre-storm shear increased significantly with height. Another issue is also the impact of the wind shear above the cold pool height (*Coniglio et al.*, 2006), which can also balance the cold-pool vorticity generation. In the studied case, the 2–6 km pre-frontal wind shear component from Beograd sounding was 21.7 m/s (its square was 472.23 m²s⁻²), which would mean a significant contribution to the 0-2 km shear effect.

Table 6. Comparison of the velocity of the net buoyant generation of vorticity and environmental wind shear derived from the Beograd Košutnjak (13275) September 17, 2017, 12:00 UTC sounding for several cold-pool heights.

cold-pool height (m AGL)	velocity of the net buoyant generation of vorticity		environmental wind shear	
	c (m/s)	c^2 (m^2s^{-2})	Δu (m/s)	Δu^2 (m^2s^{-2})
1500	25.38	644.37	11	121.1
2000	26.75	715.48	16.23	263.55
2500	26.87	721.78	21.46	460.7

Finally, it is interesting to compare the September 17, 2017 pre-storm characteristics with environments of other derechos or with the published statistics (ED01) based on proximity soundings (Table 7). We can see that both sounding and model-derived MUCAPE values were significantly lower compared to other derechos, except of the cold-season one (Gatzen *et al.*, 2011). On the other hand, concerning deep layer shear, the presented storm belonged to the high-shear events. Despite of the relatively dry environment, the DCAPE was still below the magnitude usually observed in derecho environments. On the other hand we could see that 40–50% average low level relative humidity occurred also by other derecho events. We also looked at the mean mixed-layer mixing ratio (not shown), where the 12:00 UTC Beograd sounding record (5.76 g/kg) was the lowest. For other presented cases it was between 6 and 19 (average was 11 g/kg). The pre-storm DCP (both measured and model-calculated) would also not indicate a usual environment of a long-lived storm, although we can see that for several other events it was also only about 1 or somewhat higher. The reason is above all the low CAPE and also moderate DCAPE with respect to other derecho environments. The presented cases in Table 7 of course show only a fraction of all possible situations, even in Europe. One should also take into account that the environment conditions change during the storm’s lifetime, hence it is sometimes difficult to represent the entire storm evolution with a single sounding. A good example is the case of the May 8, 2009 derecho (Coniglio *et al.*, 2011), which developed in a low-CAPE, high-shear environment and propagated toward a very buoyant and moist airmass.

Table 7. Comparison of some characteristics of the September 17, 2017 storm and its environment with some other known/published derecho events and the *Evans* and *Doswell* (2001) (ED01) statistics (showing the 25 and 75 percentiles). RH is relative humidity, NR is not relevant, WF is weak forcing, SF is strong forcing. The data were inferred from soundings in the proximity of the derecho events, data in parenthesis are from numerical analyses, cited in the publications.

Storm date/statistics	Region (Sounding ID)	Forcing	MUCAPE or SBCAPE* (J/kg)	0-6-km shear (m/s)	System speed (m/s)	DCAPE (J/kg)	0-3-km RH (%)	DCP
Sep 17, 2017 (this paper)	Serbia/Romania (13275)	WF	22.5 (387.8)	39.5 (30.1)	26.5	632.3 (398.2)	42.4 (46.6)	0.074 (0.53)
ED01 25%	NR	NR	1686	11.8	15	817.3	NR	NR
ED01 75%	NR	NR	3947.5	20.0	20	1235.8	NR	NR
July 5, 2002 (<i>Punkka et al.</i> , 2006)	Finland, Russia, Estonia (26063)	hybrid?	1476.3 (1500)	14.9	20-25	577.1	54.8	1.05
July 10, 2002 (<i>Gatzen</i> , 2004)	Germany (10393)	hybrid?	1319.5	15.7	~ 20	744.2	58	0.98
March 1, 2008 (<i>Gatzen et al.</i> , 2011)	Central Europe (11520)	SF	1.85	40.4 (50)	27.8	33.9	94.4	4 10^{-4}
June 25, 2008 (<i>Simon et al.</i> , 2011)	Central Europe (11035)	WF	2085.1 (2500)	24	17.5	767	54.1	2.5
May 8, 2009 (<i>Coniglio et al.</i> , 2011)	Central USA: Colorado, Kansas, Missouri (72440 SGF)	WF	3154 (300-500 **)	27.3 (27.5-35 **)	~ 23.5	442.8 (600 **)	77.7	3.92
July 20, 2011 (<i>Gospodinov et al.</i> , 2015)	Bulgaria (15614)	hybrid	777.3 (1424)	23.3	~ 18	793.8	42.5	1.27
June 30, 2014 (<i>Friedlein et al.</i> , 2015)	Midwest USA: e.g., Nebraska, Illinois, Iowa, Michigan (74560 ILX)	SF	4018.5 (4000-6000)	20.4 (20-30)	27	378.6	51.8	3.22

* All sounding records are MUCAPes, certain referenced values are SBCAPes (e.g., *Gospodinov et al.*, 2015)

** refers to early development of the storm

7. Conclusions

The case of the September 17, 2017 windstorm showed several characteristics, which were typical for a derecho event. High wind gusts and extensive damage occurred on the leading edge of a mesoscale convective system with trailing stratiform precipitation (TS-type, *Parker and Johnson, 2000*). The propagation speed of the system was high even in comparison with some climatological studies, where the median for derecho-producing MCSs was about 21 m/s (*Cohen et al., 2007*). This was related to very strong winds and wind shear observed in the storm's environment. Despite of the strong mid- and upper tropospheric flow, the synoptic setting of the event was different from cold-season derechos, which are often related to a deep synoptic-scale cyclone and its cold front. The intensity of the studied storm was determined mainly by deep convection and to a less extent by large-scale pressure distribution. This can be demonstrated by the fact that the maximum wind gust forecast of the hydrostatic ECMWF model (including parameterization of convection) was 22 m/s for the plain territory of Romania and 24 m/s for the mountain regions, although the maximum observed gusts reached 40 m/s. The ECMWF model indicated a presence of weak mesosynoptic-scale upward vertical motions in mid- and upper tropospheric levels, which could be important for the development of convection and maintenance of the system. However, these vertical motions were not of frontal origin.

The convective system did not exhibit a large-scale, long-lived bow echo, which is often observed during derecho events and provides an important hint on presence of severe wind. On radar imagery, we could see only smaller-scale bow echoes over Romania or in the border region of Romania and Serbia. The system also showed a tendency to split into several segments and cells, maximum radar reflectivity of which was sometimes rather low, mainly on the southern and southeastern flank of the system (probably due to the inflow of drier environmental air). Splitting of system to individual cells or even chain of supercells is often expected in case of very high wind shear (*Bluestein and Jain, 1985; Bluestein and Weisman, 2000*). In our case, the compactness of the area of high wind gusts and associated damages indicate that these cells developed on the leading edge of one large, propagating cold pool. Due to high wind shear and possible presence of a rear-inflow jet, it is likely that the system was not cold pool-dominated and an equilibrium could develop between the cold pool-generated horizontal vorticity and environmental shear. Also, because of low CAPE values in the pre-storm area, we did not observe that new cells would develop much ahead of the leading edge of the system, which is one mode of propagation of MCSs, due to gravity wave or bore generation (*Lane and Moncrieff, 2015*).

Concerning the pre-storm environment, low CAPE values, associated with low relative and specific humidity would be rather typical for a cold season

derecho with strong forcing than for the described event. This feature poses a challenge for predictability of similar storms, since thunderstorms are usually not expected when the 0-3-km average relative humidity drops below 50% (severe weather forecasters at OMSZ, personal communication). The pre-storm specific humidity was also quite low. For average non-severe thunderstorms in Europe, sounding-based climatology indicates low level mixing ratio exceeding 8 g/kg in 75% of the cases. It is noteworthy that convective events accompanied by extremely severe wind gusts or weak tornadoes have lower 25th percentile of occurrence (somewhat above 7 g/kg), and less than 10% of such cases can occur in very dry conditions, when the mixing ratio can be below 6 g/kg (*Taszarek et al.*, 2017). It is possible that the presence of unsaturated dry air close to the surface (and not only at mid-levels) could have influenced the intensity of the gusts via stronger evaporation of precipitation and intensification of downdrafts. As the convective system propagated, it carried also a more humid air from the west, which could be involved in the development of new convective cells. It is also important that at low levels, the storm-relative inflow was from moister regions on the northern-northeastern flank of the system. This could motivate to use products with depiction of storm-relative flow in the operational service. One should carefully identify possible sources of low-level humidity and admit that the environmental (pre-storm) relative and specific humidity in such cases can be lower than thresholds used for isolated thunderstorms.

Low CAPE values in the pre-storm region had also a consequence of low magnitude of “composite” parameters as DCP, which is, therefore, not useful as a derecho indicator in similar cases. Involvement of observed surface dew point and temperature in CAPE calculation showed that there could have been an increase of low-level humidity and buoyancy just ahead of the system, though this was present only at certain locations.

The investigated case is interesting from derecho climatology point of view, because it showed features typical for both warm- and cold season derechos, and some of its parameters (environmental wind shear, pre-storm moisture content) were rather unusual concerning available derecho statistics. It also occurred relatively late with respect to peak thunderstorm activity over the continent (including occurrence of intense MCSs), which is usually expected from May to August (*Antonescu and Burcea*, 2010). On the other hand, there was a strong southerly warm air advection and temperature conditions, which are atypical in mid-September, in this part of Europe.

Huge impact of the storm should motivate further study of similar long-lived convective events, which are relatively rare and challenging from the forecasting point of view. A new perspective on the dynamics of the storm and its relation to the environment could be brought by forecasts of a high-resolution non-hydrostatic model. At the time of the event, such forecasts were not provided operationally for the entire area of the windstorm, because it would require a large domain and computational power. Outputs of such simulations

could answer some important questions - for example, why the first convective systems occurring in the morning of September 17, 2017 did not cause substantial wind gusts, what was the reason for strong rightward deflection of the system during some periods of its existence, or how big was the influence of the rear-inflow-jet on the dynamics of the system. More detailed study and early detection of similar storms would also require higher density of observations and above all more information about the vertical wind profile from both pre-storm and cold pool area.

Acknowledgements: The authors are grateful to many colleagues, who helped with processing of the input data and visualisation, above all to *Rita Rétfalvi Hodossyné* and *Ildikó Szeenyán* (OMSZ). We would like to express our thank to *Márk Rajnai* (OMSZ) and *Roland Steib* (OMSZ) for many useful information and helpful discussions.

References

- Antonescu, B. and Bell, A., 2015: Tornadoes in Romania. *Mon. Weather Rev.* 143, 689–701.
<https://doi.org/10.1175/MWR-D-14-00181.1>
- Antonescu, B. and Burcea, S., 2010: A cloud-to-ground lightning climatology for Romania. *Mon. Weather Rev.* 138, 579–591.
- Bechtold, P. and Bidlot, J., 2009: Parameterization of convective gusts. *ECMWF Newsletter* 119, 15–18.
- Bluestein, H.B. and Jain, M.H., 1985: Formation of mesoscale lines of precipitation: Severe squall lines in Oklahoma during the spring. *J. Atmos. Sci.* 42, 1711–1732.
- Bluestein, H.B. and Weisman, M.L. 2000: The interaction of numerically simulated supercells initiated along lines. *Mon. Weather Rev.* 128, 3128–3149.
[https://doi.org/10.1175/1520-0493\(2000\)128<3128:TIONSS>2.0.CO;2](https://doi.org/10.1175/1520-0493(2000)128<3128:TIONSS>2.0.CO;2)
- Browning, K. A., 1962: Cellular structure of convective storms. *Meteor. Mag.* 91, 341–350.
- Bryan, G.H., Knievel, J.C., and Parker, M.D., 2006: A multimodel assessment of RKW theory's relevance to squall-line characteristics. *Mon. Weather Rev.* 134, 2772–2792.
- Bunkers, M.J., 2009: Comments on “Observational analysis of the predictability of mesoscale convective systems.” *Wea. Forecasting* 24, 351–355.
<https://doi.org/10.1175/2008WAF2222129.1>
- Bunkers, M.J., Klimowski, B.A., Zeitler, J.W., Thompson, R.L., and Weisman, M.L., 2000: Predicting supercell motion using a new hodograph technique. *Wea. Forecasting* 15, 61–79.
[https://doi.org/10.1175/1520-0434\(2000\)015<0061:PSMUAN>2.0.CO;2](https://doi.org/10.1175/1520-0434(2000)015<0061:PSMUAN>2.0.CO;2)
- Bunkers, M.J., Hjelmfelt, M.R., and Smith, Jr., P.L., 2006: An observational examination of long-lived supercells. Part I: Characteristics, evolution, and demise. *Wea. Forecasting* 21, 673–688.
<https://doi.org/10.1175/WAF949.1>
- Celiński-Mysław D. and Matuszko D., 2014: An analysis of the selected cases of derecho in Poland. *Atmos. Res.* 149, 263–281. <https://doi.org/10.1016/j.atmosres.2014.06.016>
- Cohen, A.E., Coniglio, M.C., Corfidi, S.F., and Corfidi, S.J., 2007: Discrimination of mesoscale convective system environments using sounding observations. *Wea. Forecasting* 22, 1045–1062.
<https://doi.org/10.1175/WAF1040.1>
- Colby, F. P., 1984: Convective Inhibition as a Predictor of Convection during AVE-SESAME II. *Mon. Weather Rev.* 112, 2239–2252.
[https://doi.org/10.1175/1520-0493\(1984\)112<2239:CIAAPO>2.0.CO;2](https://doi.org/10.1175/1520-0493(1984)112<2239:CIAAPO>2.0.CO;2)
- Coniglio M.C., Stensrud D.J., and Richman M.B., 2004: An observational study of derecho-producing convective systems. *Wea. Forecasting* 19, 320–337.
[https://doi.org/10.1175/1520-0434\(2004\)019<0320:AOSODC>2.0.CO;2](https://doi.org/10.1175/1520-0434(2004)019<0320:AOSODC>2.0.CO;2)

- Coniglio, M.C., S. F. Corfidi, and Kain, J. S., 2011: Environment and early evolution of the 8 May 2009 derecho-producing convective system. *Mon. Weather Rev.* 139, 1083–1102. <https://doi.org/10.1175/2010MWR3413.1>
- Coniglio, M. C., Corfidi, S.F., and Kain, J.S., 2012: Views on applying RKW theory: An illustration using the 8 May 2009 derecho-producing convective system. *Mon. Weather Rev.* 140, 1023–1043. <https://doi.org/10.1175/MWR-D-11-00026.1>
- Coniglio, M.C., Stensrud, D.J., and Wicker, L.J., 2006: Effects of upper-level shear on the structure and maintenance of strong quasi-linear mesoscale convective systems. *J. Atmos. Sci.* 63, 1231–1252. <https://doi.org/10.1175/JAS3681.1>
- Corfidi, S.F., 2003: Cold pools and MCS propagation: Forecasting the motion of downwind-developing MCSs. *Wea. Forecasting* 18, 265–285. [https://doi.org/10.1175/1520-0434\(2003\)018<0997:CPAMPF>2.0.CO;2](https://doi.org/10.1175/1520-0434(2003)018<0997:CPAMPF>2.0.CO;2)
- Corfidi, S.F., Cohen, A.E., Coniglio, M.C., and Mead, C.M., 2016: A proposed revision to the definition of "Derecho". *Bull. Amer. Meteor. Soc.* 96, 935–949. <https://doi.org/10.1175/BAMS-D-14-00254.1>
- Corfidi, S.F., Merritt, J.H., and Fritsch, J.M., 1996: Predicting the movement of mesoscale convective complexes. *Wea. Forecasting* 11, 41–46. [https://doi.org/10.1175/1520-0434\(1996\)011<0041:PTMOMC>2.0.CO;2](https://doi.org/10.1175/1520-0434(1996)011<0041:PTMOMC>2.0.CO;2)
- Craven, J.P., Jewell, R.P., and Brooks, H.E., 2002: Comparison between Observed Convective Cloud-Base Heights and Lifting Condensation Level for Two Different Lifted Parcels, *Wea. Forecasting* 17, 885–890. [https://doi.org/10.1175/1520-0434\(2002\)017<0885:CBOCCB>2.0.CO;2](https://doi.org/10.1175/1520-0434(2002)017<0885:CBOCCB>2.0.CO;2)
- Csirmaz, K., 2013: A konvektív előrejelzéshez használt diagnosztikus paraméterek és indexek számolásának dokumentációja, Technical documentation, OMSZ, 27 p. (in Hungarian)
- Davies, J.M., 2004: Estimations of CIN and LFC Associated with Tornadoic and Nontornadoic Supercells, *Wea. Forecasting* 19, 714–726. [https://doi.org/10.1175/1520-0434\(2004\)019<0714:EOCALA>2.0.CO;2](https://doi.org/10.1175/1520-0434(2004)019<0714:EOCALA>2.0.CO;2)
- Davies-Jones, R., Burgess, D., and Foster, M., 1990: Test of helicity as a tornado forecast parameter. Preprints, 16th Conf. on Severe Local Storms, Kananaskis Park, AB, Canada: Amer. Meteor. Soc., 588–592.
- Doswell C.A., III and Rasmussen, E.N., 1994: The Effect of Neglecting the Virtual Temperature Correction on CAPE Calculations. *Wea. Forecasting* 9, 625–629. [https://doi.org/10.1175/1520-0434\(1994\)009<0625:TEONTV>2.0.CO;2](https://doi.org/10.1175/1520-0434(1994)009<0625:TEONTV>2.0.CO;2)
- Doswell, C.A., III and Schultz, D.M., 2006: On the use of indices and parameters in forecasting severe storms. *Electron. J. Severe Storms Meteor.* 1, 1–22.
- Emanuel, K.A., 1994: Atmospheric Convection. Oxford University Press. 580 pp.
- EUMETSAT, 2014: IASI L2 PPFv6: Validation Report. Internal report, EUMETSAT, EUM/TSS/REP/14/776, 290 pp. http://www.eumetsat.int/website/wcm/idc/idcplg?IdcService=GET_FILE&dDocName=PDF_DMT_776443&RevisionSelectionMethod=LatestReleased&Rendition=Web
- European Severe Weather Database, 2019: Website of the European Severe Weather Database. Accessed 16 April 2019, <http://www.eswd.eu/>
- Evans J.S., and Doswell III C.A., 2001: Examination of derecho environments proximity soundings. *Wea. Forecasting* 16, 329–342. [https://doi.org/10.1175/1520-0434\(2001\)016<0329:EODEUP>2.0.CO;2](https://doi.org/10.1175/1520-0434(2001)016<0329:EODEUP>2.0.CO;2)
- Friedlein, M.T., Castro, R., Lenning, E., Lyza, W.A., Knupp, K.R., 2015: Evolution of the 30 June 2014 Double Derecho Event in Northern Illinois and Northwest Indiana. Proceedings, 27th Conference on Weather Analysis and Forecasting/23rd Conference on Numerical Weather Prediction, Chicago, Illinois., 9 pp.
- Fujita, T.T., D.L. Bradbury, and C.F. Thullenar, 1970: Palm Sunday tornadoes of April 11, 1965. *Mon. Wea. Rev.*, 98, 29–69. [https://doi.org/10.1175/1520-0493\(1970\)098<0029:PSTOA>2.3.CO;2](https://doi.org/10.1175/1520-0493(1970)098<0029:PSTOA>2.3.CO;2)
- Fujita, T.T., 1978: Manual of downburst identification for project NIMROD. *Satellite and Mesometeorology Res. Pap. No. 156*, University of Chicago, Dept. of Geophysical Sciences, pp. 104.

- Galway, J.G., 1956. The lifted index as a predictor of latent instability. *Bull. Am. Meteorol. Soc.* 37, 528–529. <https://doi.org/10.1175/1520-0477-37.10.528>
- Gatzen, C., 2004: A derecho in Europe: Berlin, 10 July 2002. *Wea. Forecasting* 19, 639–645. [https://doi.org/10.1175/1520-0434\(2004\)019<0639:ADIEBJ>2.0.CO;2](https://doi.org/10.1175/1520-0434(2004)019<0639:ADIEBJ>2.0.CO;2)
- Gatzen, C., Fink, A., Joaquim, P., Schultz, D., 2015. Analysis of a 18-year climatology of German derechos. Presentation, 8th European Conference on Severe Storms, 14–18 September 2015, Wiener Neustadt, Austria.
- Gatzen, C., Púčik, T., and Rýva, D., 2011: Two cold-season derechos in Europe. *Atmos. Res.* 100, 740–748. <https://doi.org/10.1016/j.atmosres.2010.11.015>
- Gilmore, M.S. and Wicker, L.J., 1998. The influence of midtropospheric dryness on supercell morphology and evolution. *Mon. Weather Rev.* 126, 943–958. [https://doi.org/10.1175/1520-0493\(1998\)126<0943:TOMDO>2.0.CO;2](https://doi.org/10.1175/1520-0493(1998)126<0943:TOMDO>2.0.CO;2)
- Gospodinov, I., Dimitrova, Ts., Bocheva, L., Simeonov, P., Dimitrov, R., 2015: Derecho-like event in Bulgaria on 20 July 2011. *Atmos. Res.* 158–159, 254–273. <https://doi.org/10.1016/j.atmosres.2014.05.009>
- Johns, R. H. and Hirt, W. D., 1987: Derechos: widespread convectively induced windstorms. *Wea. Forecasting* 2, 32–49. [https://doi.org/10.1175/1520-0434\(1987\)002<0032:DWCIW>2.0.CO;2](https://doi.org/10.1175/1520-0434(1987)002<0032:DWCIW>2.0.CO;2)
- Lagerquist, R., McGovern A., and Smith, T., 2017: Machine learning for real-time prediction of damaging straight-line convective wind. *Wea. Forecasting* 32, 2175–2193. <https://doi.org/10.1175/WAF-D-17-0038.1>
- Lane, T. P., and Moncrieff, M. W., 2015: Long-lived mesoscale systems in a low-convective inhibition environment. Part I: Upshear propagation. *J. Atmos. Sci.* 72, 4297–4318. <https://doi.org/10.1175/JAS-D-15-0073.1>
- Lemon, L. R., Stan-Sion, A., Soci, C., and Cordoneanu, E., 2003: A strong, long-track, Romanian tornado. *Atmos. Res.* 67–68, 391–416. [https://doi.org/10.1016/S0169-8095\(03\)00063-2](https://doi.org/10.1016/S0169-8095(03)00063-2)
- Lompar, M., Curic, M., and Romanic, D., 2017: Simulation of a severe convective storm using a numerical model with explicitly incorporated aerosols. *Atmos. Res.* 194, 164–177. <https://doi.org/10.1016/j.atmosres.2017.04.037>
- Lopez J. M., 2007: A mediterranean derecho: Katalonia (Spain), 17th August 2003, *Atmos.Res.* 83, 272–283. <https://doi.org/10.1016/j.atmosres.2005.08.008>
- Mahoney, K.M., Lackmann, G.M., and Parker, M.D., 2009: The role of momentum transport in the motion of a quasi-idealized mesoscale convective system. *Mon. Weather Rev.* 137, 3316–3338. <https://doi.org/10.1175/2009MWR2895.1>
- Moller, A.R., Doswell III, C.A., Foster, M.P., and Woodall, G.R. 1994: The operational recognition of supercell thunderstorm environments and storm structures. *Wea. Forecasting* 9, 327–347. [https://doi.org/10.1175/1520-0434\(1994\)009<0327:TOROST>2.0.CO;2](https://doi.org/10.1175/1520-0434(1994)009<0327:TOROST>2.0.CO;2)
- Parker, M.D., and Johnson, R.H., 2000: Organizational modes of midlatitude mesoscale convective systems. *Mon. Weather Rev.* 128, 3413–3436. [https://doi.org/10.1175/1520-0493\(2001\)129<3413:OMOMMC>2.0.CO;2](https://doi.org/10.1175/1520-0493(2001)129<3413:OMOMMC>2.0.CO;2)
- Pavlović-Berdon, N., Zarić, M., and Stanković, A., 2013: The occurrence of a tornado in Serbia on 31 march 2013. *Journal of the Geographical Institute Jovan Cvijic, SASA.* 63, 321–334. <https://doi.org/10.2298/IJGI1303321P>
- Persson, A., 2011: User guide to ECMWF forecast products. *Meteorol. Bull.* M3.2, ECMWF.
- Petersen, W. A., Rutledge, S. A., and Orville, R. E., 1996: Cloud-to-Ground Lightning Observations from TOGA COARE: Selected Results and Lightning Location Algorithms, *Mon. Weather Rev.* 124, 602–620. [https://doi.org/10.1175/1520-0493\(1996\)124<0602:CTGLOF>2.0.CO;2](https://doi.org/10.1175/1520-0493(1996)124<0602:CTGLOF>2.0.CO;2)
- Púčik, T., Francová, M., Rýva, D. Kolář, M., and Ronge, L., 2011: Forecasting challenges during the severe weather outbreak in Central Europe on 25 June 2008. *Atmos. Res.* 100, 680–704. <https://doi.org/10.1016/j.atmosres.2010.11.014>
- Punkka A.-J., Teittinen J., and Johns R.H., 2006: Synoptic and mesoscale analysis of a high-latitude derecho-severe thunderstorm outbreak in Finland on 5 July 2002, *Wea. Forecasting* 21, 752–763. <https://doi.org/10.1175/WAF953.1>

- Rabrenović, M., 2015: Analysis of an outbreak of extremely severe weather followed by tornado in Serbia. Presentation, 8th European Conference on Severe Storms, 14-18 September 2015, Wiener Neustadt, Austria.
- Rabrenović, M. and Gatzen, C., 2017: Analysis of severe convective wind gusts in Serbia. Presentation, 9th European Conference on Severe Storms, ECSS2017-189, 18-22 September 2017, Pula, Croatia.
- Rajnai, M., and Vörös, M., 2010: Recent Developments in HAWK-3. Presentation, 21st Workshop of the European Working Group on Operational meteorological Workstations, EGOWS, ECMWF, Reading, UK, 1st June 2010.
- Rasmussen, E. and Blanchard, D., 1998. A baseline climatology of sounding-derived supercell and tornado forecast parameters. *Wea. Forecasting* 13, 1148–1164.
[https://doi.org/10.1175/1520-0434\(1998\)013<1148:ABCOSD>2.0.CO;2](https://doi.org/10.1175/1520-0434(1998)013<1148:ABCOSD>2.0.CO;2)
- Roman, J. A., Knuteson, R., August, T., Hultberg, T., Ackerman, S.A., and Revercomb, H., 2016: A global assessment of NASA AIRS v6 and EUMETSAT IASI v6 precipitable water vapor using ground-based GPS SuomiNet stations. *J. Geophys. Res. Atmos.* 121, 8925–8948.
<https://doi.org/10.1002/2016JD024806>
- Rotunno, R.J., Klemp, J. B., and Weisman, M. L., 1988: A theory for strong, long-lived squall lines. *J. Atmos. Sci.* 45, 463–485.
[https://doi.org/10.1175/1520-0469\(1988\)045<0463:ATFSL>2.0.CO;2](https://doi.org/10.1175/1520-0469(1988)045<0463:ATFSL>2.0.CO;2)
- Simon A., Kaňák J., Sokol A., Putsay M., Uhrinová L., Csirmaz K., Okon L., and Habrovský R., 2011: Case study of a severe windstorm over Slovakia and Hungary on 25 June 2008, *Atmos. Res.* 100, 705–739. <https://doi.org/10.1016/j.atmosres.2010.12.012>
- Storm Prediction Center, 2019: Derecho composite parameter (DCP). Website. Accessed 16 April 2019, http://www.spc.noaa.gov/exper/mesoanalysis/help/help_dcp.html
- Taszarek, M., Brooks, H.E., and Czernecki, B., 2017: Sounding-derived parameters associated with convective hazards in Europe. *Mon. Weather Rev.* 145, 1511–1528.
<https://doi.org/10.1175/MWR-D-16-0384.1>
- Taszarek, M., Pilgaj, N., Orlikowski, J., Surowiecki, A., Walczakiewicz, Sz., Pilorz, W., Piasecki, K., Pajurek, L., and Pórolniczak, M., 2019: Derecho evolving from a mesocyclone - a study of 11 August 2017 severe weather outbreak in Poland: event analysis and high-resolution simulation, *Mon. Weather Rev.* 147, 2283–2306. <https://doi.org/10.1175/MWR-D-18-0330.1>
- Thompson, R.L., Edwards, R., Hart, J.A., Elmore, K.L., and Markowski, P., 2003: Close Proximity Soundings within Supercell Environments Obtained from the Rapid Update Cycle, *Wea. Forecasting* 18, 1243–1261.
[https://doi.org/10.1175/1520-0434\(2003\)018<1243:CPSWSE>2.0.CO;2](https://doi.org/10.1175/1520-0434(2003)018<1243:CPSWSE>2.0.CO;2)
- University of Wyoming, 2019: Upperair Air Data, Soundings, Website. Accessed 16 April 2019, <http://www.weather.uwyo.edu/upperair/sounding.html>
- Weisman, M. L. and Trapp, R. J., 2003: Low-level mesovortices within squall lines and bow echoes. Part I: Overview and dependence on environmental shear. *Mon. Weather Rev.* 131, 2779–2803.
[https://doi.org/10.1175/1520-0493\(2003\)131<2779:LMWSLA>2.0.CO;2](https://doi.org/10.1175/1520-0493(2003)131<2779:LMWSLA>2.0.CO;2)
- Weisman, M.L., 1992: The role of convectively generated rear-inflow jets in the evolution of long-lived mesoconvective systems. *J. Atmos. Sci.* 49, 1826–1847.
[https://doi.org/10.1175/1520-0469\(1992\)049<1826:TROCGR>2.0.CO;2](https://doi.org/10.1175/1520-0469(1992)049<1826:TROCGR>2.0.CO;2)
- WorldClimate, 2019: WorldClimate. Website, Accessed 16 April 2019, <http://www.worldclimate.com/>
- Youtube, 2019: Nevreme u Hrtkovcima 1, 2017, Website, Accessed 16 April 2019, <https://www.youtube.com/watch?v=naJ8kaSuNu0>, Nevreme (Tornado)-Srbija 17.09.2017 (Okolina Zrenjanina-Tomasevac), Website, Accessed 16 April 2019, <https://www.youtube.com/watch?v=utP-TPNRbDQ>,

IDŐJÁRÁS

Quarterly Journal of the Hungarian Meteorological Service
Vol. 125, No. 1, January – March, 2021, pp. 39–52

Sounding-derived parameters associated with severe hail events in Romania

Vasilică Istrate^{1,2,*}, Radu Vlad Dobri^{1,2}, Florentina Bărcăcianu¹,
Răzvan Alin Ciobanu^{1,2}, and Liviu Apostol¹

¹*University Alexandru Ioan Cuza of Iași*
Blvd. Carol I, No.11, 700506, Iași Romania

²*S.C. Intervenții Active în Atmosferă S.R.L*
Răcari St. No. 5, Bucharest, Romania

**Corresponding author E-mail: istratesasile87@gmail.com*

(Manuscript received in final form April 15, 2020)

Abstract— The present paper analyzes 549 severe weather events reported to the ESWD (European Severe Weather Database) that caused large hail in the territory of Romania.

Values of atmospheric instability indices have been analyzed for these episodes using data from Bucharest and Budapest sounding stations. For a period of 140 days with episodes of large hail, 24 instability indices were analyzed to describe the atmospheric conditions of the main daily convective activity.

The mean values for most indices characterize an unstable atmospheric environment. Of the indices that measure potential instability, VT (vertical totals index) and TT (totals index) had values that described a conductive atmospheric environment for the development of hailstorms. In addition, the interquartile values of LIV (lifted index using virtual temperature) had values lower than zero. For SWEAT (severe weather threat index) and CAPEV (convective available potential energy index using virtual temperature), only the values in the 75th percentile describe a very unstable environment (according to the literature).

Strong linear correlations were registered between several pairs of indices such as CAPEV-LIV and SWEAT-SI that can be used for the operational forecast of hail.

Key-words: hailstorm, atmospheric instability indices, correlation, hail forecast

1. Introduction

Hailstorms are posing high risk to agriculture, infrastructure, and vehicles (Hohl *et al.* 2002; Sioutas *et al.*, 2009; Istrate *et al.*, 2016), causing major losses estimated in certain cases to tens of millions of Euros (Kunz and Puskeiler, 2010)

Consequently, hail climate trends have been developed, permitting the identification of hail affected areas, hail frequency, its seasonality and intensity. The spatial distribution of mean hail days per year shows the lowest values in the south-eastern and eastern parts of Romania, while the average number of hail days increases in the other parts of the country as the altitude of the terrain increases (*Clima României*, 2008). The plains of the south, east, and west, and some mountain areas are characterized by average values of 0.5–1.5 hail days, while on the mountain slopes and peaks, the average multiannual hail days range between 2 and 11. The minimum value is 0.3 in the southeast, near the Black Sea, and the maximum value is 11.8, found in the mountains, in the northwestern part of Romania (Burcea *et al.*, 2016). High frequencies (1.02–1.09 hail days) were also found in big urban areas (Apostol and Machidon, 2011). The national network of weather stations in Romania consists of approximately 160 locations. Based on data collected from these stations, an estimation has been made for the mean hail days per year, and, in our case scenario, this value is around 1.5 days (*Clima României*, 2008). For a 12-year time span, around 2500–3000 hail reports were given from weather stations. The present work, based on the ESDW network, represents an additional source of information, as the ESDW observation points locate in other places than the ones from the weather stations. The European Severe Storms Laboratory (ESSL) developed a preliminary climatology, based on large hail (> 2 cm) reports over Europe, for the period 2000–2007 (Hand and Cappelluti, 2011).

A good severe instability forecast is a strong requirement for improving nowcasting-type forecasts. The characteristics of other dangerous phenomena caused by severe atmospheric instability are presented in monographic or scientific articles by different authors. Atmospheric lightning could be considered the primary atmospheric phenomenon triggered by high atmospheric instability. Southeast Europe represents one of the regions with the highest annual spatial frequency of atmospheric lightning at continental level (Anderson and Klugmann, 2014). Some studies have found that the maximum annual CG lightning density occurs in the southwestern and central areas of Romania (Iliescu, 1989; Antonescu and Burcea, 2010).

Therefore, in Romania, the convective phenomena and hailstorms happen quite often during the warm season. Furthermore, the precipitation regime generally displays a continental pattern, especially during the warm semester of the year, with its maximum in July, with a highlighted role of convective precipitation due to periods of enhanced atmospheric instability (Apostol, 2008). National annual precipitation amounts generally remained stable (trends without

statistical significance), except for certain areas in the northwest/southeast, where statistically significant positive/negative trends were recorded (Marin et al., 2014). Consequently, extreme convective manifestations happen more and more frequently and cause considerable amount of rainfall in the warm season (Croitoru et al., 2015). The intensity and frequency of hailstorms have been studied over the last two decades with the help of weather radar. Studies in this regard focused especially on the western part of the country. For the period 2004–2009, the meteorological radar from Bobohalma recorded numerous hailstones with a diameter of over 7 cm (Maier et al., 2010). Weather-radar-based investigation of long-lived thunderstorms in Hungary in the period of 2004–2012 estimated the number of supercells in a year to be around 67 (Horváth et al., 2015). For the northwestern part of Romania, over the same period, more than 100 highly severe thunderstorms were reported (Seres and Horváth, 2015).

This evolving process could be caused by recent climate changes. Throughout the entire territory of Romania, the climatic water deficit trends are due to a partial decrease in precipitation (statistically insignificant) and an increase in general evaporation (Právělie et al., 2019). For the Extra-Carpathian area, the temperature anomaly variation is characterized by an upward trend, better observed after 1991 (Barcacianu et al., 2015).

That is why we consider that enhancing the medium-term forecasting precision of these disastrous weather phenomena would be beneficial. Multiple forecasting techniques are based on data from sounding stations that forgo the possible hailstorms. The Fawbush–Miller nomogram (Fawbush and Miller, 1953) made the first step by trying to forecast hail size by measuring temperature, dew point, and wind speed. The nomogram correlates hail size with buoyancy energy between the cloud base and the -5 C° isotherm height.

Recent studies show that in the USA, parameters that combine measures of buoyancy, vertical shear, and low-level moisture reflect the strongest ability to discriminate between supercell classes (Thompson et al., 2003).

Doswell and Schultz (2006) developed a framework for the classification of forecast variables, which indicates the limitations of such variables and their suitability for operational diagnosis and forecasting. Analyzing sounding-derived indices from Europe, the highest probability for extreme hail is maximized when the 800–500 hPa temperature lapse rate exceeds 7 K.km^{-1} , and when the 0–500 m above ground level mixed layer mixing ratio (MIXR) is around 15 gkg^{-1} (Taszarek et al., 2017). For East Europe, during the summer months, more than 50% of days are characterized by positive buoyancy force ($\text{CAPE} > 0\text{ Jkg}^{-1}$) (Siedlecky et al., 2009). For the northern area of Northern Greece Sioutas and Flocas (2003) found that severe thunderstorm development can be anticipated in a percentage ranging from 13.9% of the days (according to TT) and up to 18.8% (according to CAPE).

For the eastern area of Romania (Sfică et al., 2015), it was found that thunderstorms could be better forecasted using CAPE and LI for the mountain region, while KI and CAPE could be used mainly for thunderstorm forecast out

of the Carpathian region. For the same area, LI, SWEAT, and TT seemed to be the most powerful forecasting hail indices according to recorded values (*Istrate et al.*, 2015).

The purpose of this study is the enhancement of hail forecasting in Romania, which stands as a support for nowcasting warnings, but also for the proper conduct of operations within the National System of Hail Suppression, which is rapidly expanding (*Istrate et al.*, 2019).

2. Data and methods

The data used in this study comes from two different sources, namely ESWD and sounding stations from Bucharest and Budapest.

Severe weather reports were derived from ESWD for the period of 2006–2017. The main goal of the ESWD database (*Groenemeijer et al.*, 2004, 2005) is to collect and to provide detailed and quality controlled information on severe convective storm events in Europe using a homogeneous data format and web-based, multi-lingual user interfaces where both the collaborating European national meteorological and hydrological services and the public can contribute and retrieve observations (*Dotzek et al.*, 2009).

The European Severe Storms Laboratory (ESSL) rates the credibility of the reports on a 4-level scale: as received (QC0), plausibility check passed (QC0+), report confirmed (QC1), and event fully verified (QC2). In the present study, only the confirmed reports were used (QC1). The development of social media and the increasing number of people interested in severe weather that has taken place in recent years have significantly increased the number of reports (often accompanied by a photograph of the event). This database, which tries to collect all the hailstorms, is not complete, but it is the best existing source for the Romanian territory. The number of reports development over the ten years has been highly influenced by the progress of the ESWD network. The density of large hail reports for the Romanian territory is low (50–70 reports per 10000 km²) compared to Germany, Austria, or northern Italy, where there are over 200 reports per 10000 km² (*Groenemeijer et al.*, 2017). In the first year, 2007, a very poor number of events were reported for the territory of Romania. During 2008–2010, between 40 and 50 reports were recorded per year (*Istrate et al.*, 2017). From April 1 to September 30, 2006–2017, there were 549 QC01 credibility rated events reported for the ESWD. Many of these were reported from the neighboring local areas affected by the same hailstorm (*Fig 1*). In addition, we can notice some areas without any reports as the southeastern area or the mountains. In this case, the lack of data can be linked to the sparse population of these territories or the few people interested in meteorological phenomena.

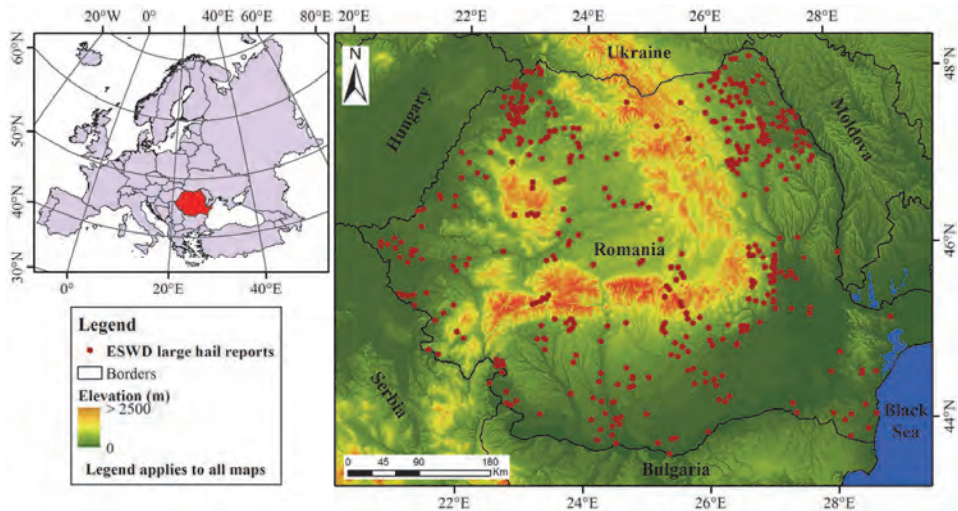


Fig. 1. ESWD large hail reports from April 1 to September 30, 2006–2017, used in this study for analysis.

The rawinsonde measurements were derived from the sounding database of the University of Wyoming. For the period between 2006 and 2017, all the available measurements for 12 UTC were downloaded for the stations from the studied area. Only the data coming from Bucharest and Budapest were used because these two were and still are the most relevant radiosonde stations for the studied territory, from which we were able to access 12 UTC data. In a 24-hour cycle, the maximum of convection phenomena takes place in the afternoon and in the evening. For this reason, the day sounding (12 UTC) better presents the conditions favorable for the development of severe hailstorms. The Carpathian Mountain chain, which causes diurnal air temperature differences that are greater in the east (Apostol and Sfiică, 2013), mainly influence the local conditions and extreme rainfall values (Croitoru et al., 2015). For the Extra-Carpathian area, we used data observed at the Bucharest, the Intra-Carpathian, and the Budapest weather stations.

We used isotherm heights such as 0 °C (H0), -10 °C (H-10), and -20 °C (H-20). These can be considered key isotherms used for a medium-term hail forecasting or to detect convective storm cells with hail probability (Abshaev et al., 2010; Potapov and Garaba, 2016). The altitude of these isotherms was determined by calculating a local, thermal gradient. Furthermore, we established the vertical thermal gradient by using the following formula: $\gamma = \frac{\Delta T}{\Delta z}$, where $\Delta T = T_1 - T_2$ and $z = z_1 - z_2$ stand for

temperature and height increases. Other used variables are the altitude differences between the $-10\text{ }^{\circ}\text{C}$ and $0\text{ }^{\circ}\text{C}$ (ΔH1), $-20\text{ }^{\circ}\text{C}$ and $-10\text{ }^{\circ}\text{C}$ (ΔH2) and the $-20\text{ }^{\circ}\text{C}$ and $0\text{ }^{\circ}\text{C}$ (ΔH3) isotherms.

Thunderstorms are more likely to form when the boundary layer's mixing ratios are higher than 8 gkg^{-1} . Deep convection is also more likely to occur when the vertical temperature lapse rates (between the 800 and 500 hPa air pressure layers) exceed $6\text{ }^{\circ}\text{C.km}^{-1}$ (Kolendowicz *et al.*, 2017). The values of the thermal gradients for the analyzed scenarios exceeded $0.6\text{ }^{\circ}\text{C}/100\text{ m}$, reaching $0.9\text{ }^{\circ}\text{C}/100\text{ m}$ in some cases, recording a temperature lapse rate of at least $6\text{ }^{\circ}\text{C km}^{-1}$ between the 800 and 500 hPa air pressure layers.

24 indices were analyzed, derived from the sounding data over a period of 140 days in which large hail was reported. Besides the main height of isotherm indices, meteorological variables from the Showalter sounding-derived indices of atmospheric instability were used (Showalter, 1953; Hart and Korotky, 1991), such as total totals (TT), vertical totals (VT), cross totals (CT) (Miller, 1975), K index (KI) (George, 1960), lifted index (LI) (Galway, 1956; Johns and Doswell III, 1992), CAPE and CAPEV (Glickman, 2000), and other sounding-derived parameters (Table 1).

We statistically analyzed these indices to find possible correlations between them. Using the XLSTAT software, we discretized the variables, analyzed some variables using the box plot diagrams and the correlation matrix.

3. Results and discussion

3.1. Characterization of sounding-derived indices

The H0, H-10 and H-20 monthly mean values are showing an increasing trend from May to August (Fig. 1). This case scenario is typical in the climate zone in which Romania is situated. The western oceanic influences dispense thermic inertia, which is a common thing happening in the high lands, with peak values in August (Clima României, 2008). For April, when only two events were recorded, the high values can be considered as exceptions.

For values between 3000 and 4000 m for the $0\text{ }^{\circ}\text{C}$ isotherm, 5000 and 6000 m for the $-10\text{ }^{\circ}\text{C}$ isotherm, and 6500–7500 m for the $-20\text{ }^{\circ}\text{C}$ isotherm, most storms were accompanied by hail.

Table 1. The 24 sounding-derived indices investigated in this study. Units are shown in the second column in parentheses

Acronym	Index name	References	Minimum	Maximum	Mean	Std. deviation
H0	Height of the 0°C isotherm (m)	-	1642	5524	3445	679.7
H-10	Height of the -10°C isotherm (m)	-	2941	7383	5051	675.4
H-20	Height of the -20°C isotherm (m)	-	4311	8518	6538	678.5
ΔH1	Altitudinal difference between the -10°C and 0°C isotherms (m)	-	806	2523	1605	234.2
ΔH2	Altitudinal difference between the -20°C and -10°C isotherms (m)	-	1010	2955	1487	194.9
ΔH3	Altitudinal difference between the -20°C and 0°C isotherms (m)	-	2478	4981	3093	283.4
SI	Showalter index	<i>Showalter (1947)</i>	-5.15	10.15	0.98	2.57
LIV	Lifted index using virtual temperature	<i>Galway (1956)</i>	-9.41	12.11	-1.36	3.1
SWEAT	SWEAT index	<i>Miller (1972)</i>	24.68	364.56	158.5	69.06
KI	K index	<i>George (1960)</i>	-11.7	37.4	26.98	7.54
CTI	Cross totals index	<i>Miller (1975)</i>	7.1	29.9	21.3	3.4
VT	Vertical totals index	<i>Miller (1975)</i>	17.7	47.8	27.87	2.94
TT	Total totals index	<i>Miller (1975)</i>	34.3	731.45	53.79	57.41
CAPEV	CAPE computed by using the virtual temperature (J/kg)	<i>Glickman (2000)</i>	0	3052.4	542.49	607.14
CIN	Convective inhibition (J/kg)	<i>Colby (1984)</i>	-412.08	0	-66.19	82
EL	Equilibrium level (hPa)	<i>Glickman (2000)</i>	0	748.42	357.25	151.01
LFC	Level of free convection (m)	-	454.81	947.99	756.03	82.62
BRNV	Bulk Richardson number using CAPV	<i>Weisman and Klemp (1982)</i>	0	3320.43	104.94	412.78
LCLT	Temperature (°C) at the lifted condensation level	-	-3.15	18.52	8.31	22.63
LCLP	Pressure [hPa] of the lifted condensation level	-	287.18	956.14	839.33	70.773
MLPT	Mean mixed layer potential temperature	-	8.46	855.25	301.65	47.051
MLMR	Mean mixed layer mixing ratio(g/kg)	-	4.01	300.32	11.67	24.48
1000-500 hPa Thick	1000 hPa to 500 hPa thickness (meters)	-	11.99	5809	5588.641	478.63
TPW	Precipitable water (mm) for the entire sounding.	-	13.4	5651	67.47	471.91

In the situation of having a strong updraft, the ice pellets can grow to impressive sizes if their course runs more into the cold area of the cloud. Therefore, in more than 70% of the reports, the $\Delta H3$ value was between 3000 and 4000 meters (*Fig. 2*).

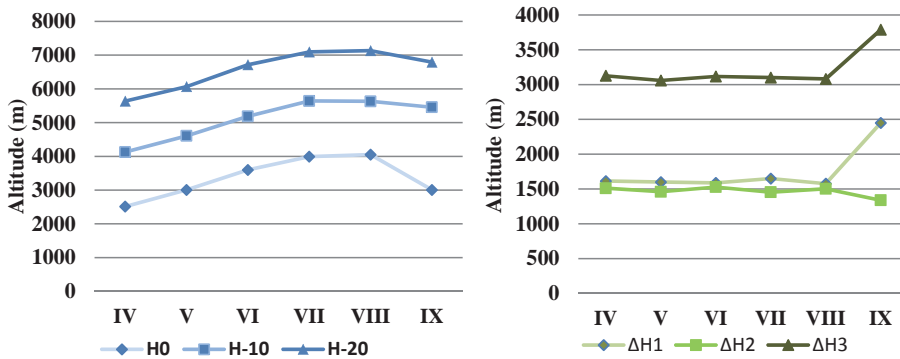


Fig. 2. The evolution of the monthly mean indices, H-10, H-20, $\Delta H1$, $\Delta H2$, $\Delta H3$ for 140 days with large hail reported.

Looking at $\Delta H1$, and $\Delta H2$, one can observe the backwards correlation between them. In the months in which the $\Delta H1$ value increases, $\Delta H2$ decreases, and vice versa. The figures of these two indices also indicate how the vertical temperature gradients evolve in the days in which hail occurs. In the first part, with negative temperatures between H0 and H-10, the gradients are larger compared to the area between H-10 and H-20 in all of the warm season months.

The SI, KI, LIV, CTI, VT, and TT sounding-derived indices group, that measures the potential instability of the atmosphere, only includes indices calculated by using information from two levels. Out of the two-level instability, indices VT and TT have mean values, which describe an atmosphere that would develop extreme convections. The interquartile values of LIV are negative, and SI shows values which stand for extreme instability in the atmosphere (*Fig. 3*).

Another group of indices is the one that measures the potential instability above the level of free convective. The box-plots for two of these kind of indices – sweat index and CAPV – only show the highest values as being close to the ones that would describe an extremely unstable atmosphere. However, in all of the days, when their values were analyzed, hailstorms were reported. The explanation for this would be the climate conditions and the relief in Romania that are different from those in the US, where these indices were built in the first place. Also, the box-plot for the CAPE index values that came out in this study is nearly identical to most of the ones in Europe in days with large hail (*Taszarek et al., 2017*).

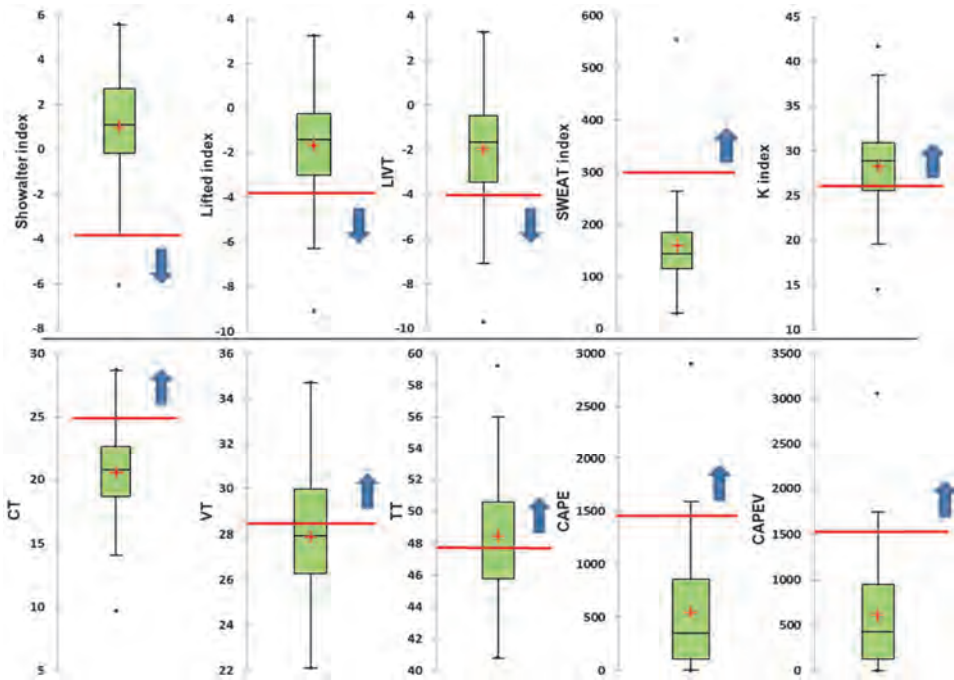


Fig. 3. Box-and-whisker plot of 10 selected indices. The median is represented as a horizontal line inside the box, edges of the box represent the 25th and 75th percentiles, while whiskers represent the 10th and 90th percentiles. The red line represents the limit from which the parameter value describes a very unstable environment (according to the literature), and the blue arrow indicates the direction in which the evolution of its value would lead to extreme convective manifestations.

In the northwestern part of Spain, the mean values of CAPE index with hail observations are 360 Jkg^{-1} , while thunderstorm occurrence shows a mean CAPE index of about 260 Jkg^{-1} (López *et al.*, 2001). Over northern Italy, tornado events are observed when KI index exceeds 30. CAPE values are $700\text{--}2,500 \text{ Jkg}^{-1}$ and SWEAT index is $250\text{--}300$ (Costa *et al.*, 2001). Over Cyprus, 10% of the strongest thunderstorms are observed when KI index exceeds 30. Over Greece (Dalezios and Papamanolis, 1991), there is a high probability of hail occurrence when KI index is above 25 and TTI index exceeds 44. In Switzerland, weak, isolated thunderstorms give average CAPE values of 210 Jkg^{-1} at 00 UTC radio soundings and 400 Jkg^{-1} at 12 UTC radio soundings, over the Czech Republic, during severe weather, 80 percent of CAPE is around 322 Jkg^{-1} (Pešice *et al.*, 2003). This means that for both this index and other indices, another scale of values should be fixed, adjusted to the topographic and climatic conditions, which could show different convective instability rates. Therefore, for most of the days when hail was reported, CAPEV index values were between 100 and 800 Jkg^{-1} , SWEAT between 120 and 200 , Showalter index between -0.5 and 2 , and LIV between 0 and -3 .

3.2. Correlations among indices

To establish which indices are the most suited to be used for hail forecasting, we chose a bivariate primary analysis of all these 24 indices. In order to be relevant in forecasting, these sounding-derived indices should be able to describe the pre-convective atmospheric details with decent precision. For 52 indices, *Manzato* (2012) made a bivariate analysis between each index, and the hit hail pads in 6 h were done as a preliminary attempt to evaluate the utility of these indices for forecasting hail. It is found that some measures of instability (like updraft, hail diameter, and LI) seem to have more skill than the other indices when classifying the hail-event occurrence. When estimating the number of hit hail pads, the best correlation is obtained by the indices belonging to the "lifted index family". The correlation matrix of these 24 variables indicates a Pearson coefficient value of over 0.7 only to several pairs of indices (*Fig. 4*).

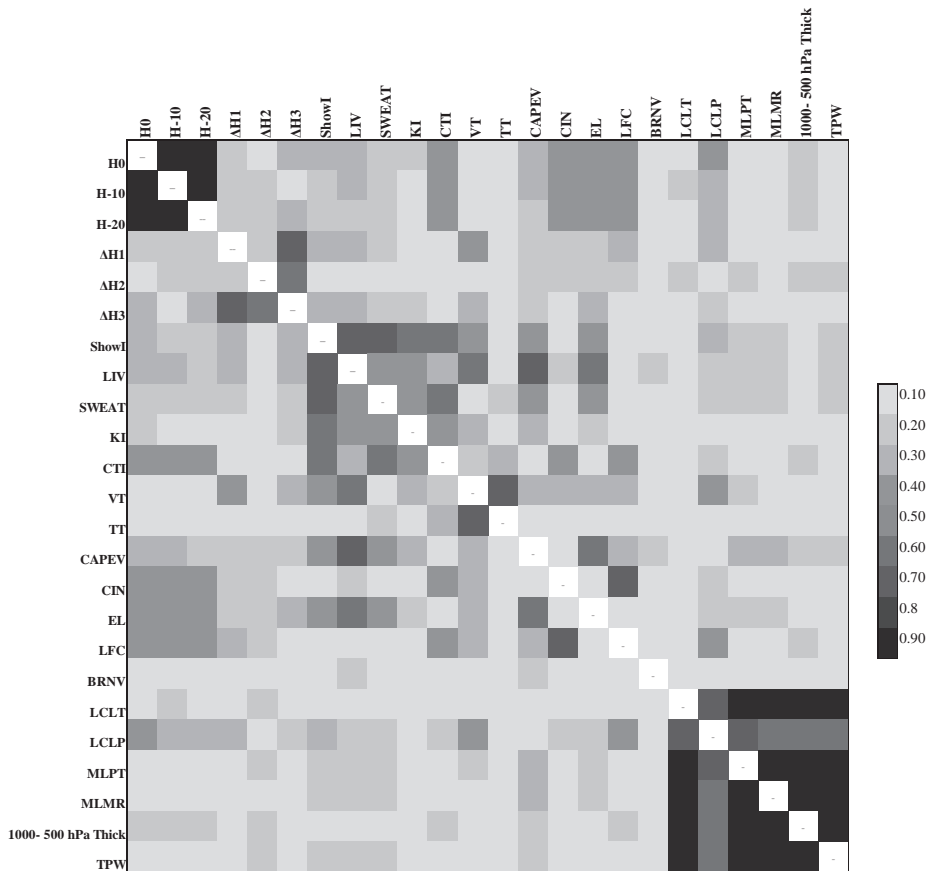


Fig. 4. The absolute value of the correlation matrix among the 24 sounding-derived indices listed in *Table 1*. The absolute values of the Pearson's $|R|$ are shown in grayscale: high $|R|$ is dark and $|R| = 0$ is white.

In most of the cases, the highest coefficient values reveal autocorrelations between indices that use the same parameters. These autocorrelations are not suggestive, and they cannot add any contribution for hail forecasting. One of the autocorrelations that can help to forecast hail is the one between SI and SWEAT indices. SI indicates the increase of convective potential when a cold air mass of less than 850 mb approaches. SWEAT index takes into account many essential parameters, including low-level moisture, instability, and vertical wind shear. Therefore, under the circumstance of a cold front, the accretion of ice pellets is faster when the updraft contains a large amount of water. This large amount of water caused by the tremendous relative humidity values from the lower troposphere. Another relevant and robust correlation is the one between CAPV and LIV indices. The negative value of LIV indicates that the planetary boundary level is unstable, compared to the middle troposphere, and the CAPV's high values reflect a significant amount of latent heat released following the condensation of water vapor. Thus, almost every day of the 140 days in which hail occurred, the atmosphere was characterized by pronounced instability, fluctuating energy, positive buoyancy, and a large amount of humidity.

Strong correlations were also found in the indices group that describe the convective air from a temperature point of view (*Table 2*). One can observe the correlation between H0 and H-10, respectively H-20 or between H-10 and H-20. Strong bonds can also be seen between ΔH_2 and ΔH_3 . These correlations can be explained by the existence of positive vertical gradients and, consequently, the absence of temperature inversion between H0 and H-20. Also, the in-tandem increase of ΔH_2 and ΔH_3 describes a larger area of growing ice particles. Therefore, under the circumstance of the convective energy described by other indices, the growing size trend has led to impressive ice stone diameters which did not have enough time to melt in the troposphere's layer with positive temperatures when falling onto the ground.

Table 2. Groups of sounding-derived indices that have a linear correlation coefficient $|R| \geq 0.7$

Indices	Couples	R
SI	SI-SWEAT index	-0.75
CAPV	LIV – CAPV	-0.80
LIV	LIV – EL	0.80
H0	H0 – H-10	0.86
H-10	H0 – H-20	0.88
H-20	H-10 – H-20	0.93
ΔH_2	$\Delta H_2 – \Delta H_3$	0.73

4. Conclusion

This paper has analyzed a number of sounding-derived parameters associated with ESWD hail reports in Romania. Out of the 549 ESWD database reports between 2007 and 2017, with QC1 credibility rate, many of these were recorded from the same hailstorm that affected the neighboring local areas. We found 140 days in which hail was reported for which we characterized the atmospheric conditions of the main daily convective activity using 24 sounding-derived indices coming from Bucharest and Budapest stations.

Out of the two-level instability indices, VT and TT had the mean values, which describe an atmosphere that would develop extreme convections. The interquartile values, between 75th and 25th percentiles for CAPEV, were between 100 and 800 Jkg^{-1} , 120 and 200 for SWEAT, -0.5 and 2 for ShowI and for LIV, between 0 and -3. In 50% of the days when hail occurred, the atmosphere characterized by pronounced instability, flotation energy, positive buoyancy, and large amounts of humidity.

The primary analysis of the 24 indices used in this study revealed several strong linear correlations. The strongest correlations were found between the following indices: LIV – CAPV, SI – SWEAT, LIV – EL, H0 – H-10, H0 – H-20, and H-10 – H-20. The main drawback of this study is that hail reports occurred far from the sounding sites. In the future, we intend to use convection-related parameters and synoptic-scale fronts from ERA5 reanalysis to improve these results.

The present study was done as a preliminary attempt to evaluate the utility of these indices for forecasting hail in Romania.

Acknowledgements: The authors would like to thank the European Severe Storms Laboratory (ESSL) team for providing data on large hail reports on the territory of Romania between 2007 and 2017, from the European Severe Weather Database (ESWD).

References

- Abshaev M.T., A.M., Abshaev Malkarova A.M., and Zharashuev M.V., 2010: Automated Radar Identification, Measurement of Parameters, and Classification of Convective Cells for Hail Protection and Storm Warning. *Russian Meteorology and Hydrology* 35, 182–189. <https://doi.org/10.3103/S1068373910030040>
- Administrația Națională de Meteorologie, 2008: Clima României. Editura Academiei, Bucharest, 365 (in Romanian)
- Anderson G., Klugmann D. 2014: A European lightning density analysis using 5 years of ATDnet data. *Nat Hazards Earth Syst Sci* 14, 815–829. <https://doi.org/10.5194/nhess-14-815-2014>
- Antonescu B., Burcea S., 2010: A cloud-to-ground lightning climatology for Romania. *Mon Weather Rev* 138, 579–591. <https://doi.org/10.1175/2009MWR2975.1>
- Apostol L., 2008: The Mediterranean cyclones—the role in ensuring water resources and their potential of climatic risk, east of Romania. *Present Environment and Sustainable Development* 2, 143–163.
- Apostol, L., Machidon O. M., 2011, Considerations on the hail regime in Moldavia between the Siret and Prut rivers. *Air and Water - Components of the Environment Conference*, 3, 45–52.
- Apostol L., Sfică L., 2013: Thermal Differentiations Induced by the Carpathian Mountains on the Romanian Territory. *Carp J Earth Environ Sci* 8, 215–221.

- Bărcăcianu F., Sîrghiea L., Iordache I., Apostol L., and Sfică L., 2015, Recent changes in air temperature in extra-Carpathian Moldavia. SGEM2015 Conference Proceedings 15 1001-1008. <https://doi.org/10.5593/SGEM2015/B41/S19.129>
- Burcea S., Cica R., and Bojariu R., 2016: Hail Climatology and Trends in Romania: 1961-2014. *Month. Weather Rev.* 144, 4289–99. <https://doi.org/10.1175/MWR-D-19-0204.1>
- Croitoru A.E., Piticar A., and Doina C., 2015: Changes in Precipitation Extremes in Romania. *Quarter. Int.* 415, 325–35. <https://doi.org/10.1016/j.quaint.2015.07.028>
- Costa S., Mezzasalma P., Levizzani V., Alberoni P.P., and Nanni S., 2001: Deep convection over Northern Italy: synoptic and thermodynamic analysis. *Atmos. Res.* 56, 73–88. [https://doi.org/10.1016/S0169-8095\(00\)00091-0](https://doi.org/10.1016/S0169-8095(00)00091-0)
- Dalezios N.R. and Papamanolis N.K., 1991: Objective assessment of instability indices for operational hail forecasting in Greece. *Meteorol. Atmos. Phys.* 45, 87-100
- Doswell, C.A. III and Schultz D.M., 2006: On the use of indices and parameters in forecasting severe storms. *Electr. J. Severe Storms Meteor.* 1, 1–22.
- Dotzek, N., Groenemeijer, P., Feuerstein B., and Holzer A.M., 2009: Overview of ESSL's severe convective storms research using the European Severe Weather Database ESWD. *Atmos. Res.* 93, 575–586. <https://doi.org/10.1016/j.atmosres.2008.10.020>
- Fawbush, E.J. and Miller, R.C., 1953: A method for forecasting hailstone size at the earth's surface. *Bull. Amer. Meteorol. Soc.* 34, 235–244. <https://www.jstor.org/stable/26242128>
- Galway, J.G., 1956: The Lifted Index as a Predictor of Latent Instability. *Bulletin of the American Meteorological Society* 37, 528-529. <https://doi.org/10.1175/1520-0477-37.10.528>
- George, J.J., 1960, Weather Forecasting for Aeronautics. *Academic Press*, San Diego
- Glickman, T., Ed. 2000: Glossary of Meteorology. 2nd ed. *Amer. Meteor. Soc.*, 855
- Groenemeijer, P., Dotzek, N., Stel, F., Brooks, H., Doswell, C., Elsom, D., Giajotti, D., Gilbert, A., Holzer, A., Meaden, T., Salek, M., Teittinen, J., and Behrendt, J., 2004: ESWD—A standardized, flexible data format for severe weather reports., 3rd European Conf. on Severe Storms, León, 9–12. November. www.essl.org/projects/ESWD/ Accessed 15 June 2018
- Groenemeijer P., Dotzek N., Stel, F., and Giajotti, D., 2005: First results of the European Severe Weather Database ESWD. Preprints, 5th Ann. Meeting of the European Meteor. Soc., Utrecht, 12.–16. September. www.essl.org/projects/ESWD/ Accessed 15 June 2018
- Groenemeijer, P., Púčik, T., Holzer, A.M., Antonescu, B., Riemann-Campe, K., Schultz, D.M., Kühne, T., Feuerstein, B., Brooks, H.E., Doswell, C.A., Koppert, H., and Sausen, R., 2017: Severe Convective Storms in Europe: Ten Years of Research and Education at the European Severe Storms Laboratory. *Bull. Amer. Meteor. Soc.* 98, 2641–2651. <https://doi.org/10.1175/BAMS-D-16-0067.1>
- Hand, W.H., and G. Cappelluti, 2011: A global hail 470 climatology using the UK Met Office 471 convection diagnosis procedure (CDP) and model analyses. *Met. Apps.*, 18, 446–458. <https://doi.org/10.1002/met.236>
- Hart, J.A. and Korotky, W.D., 1991: The SHARP workstation _v 1.50. A Skew T/Hodograph Analysis and Research Program for the IBM and Compatible PC: User's Manual. NOAA/NWS Forecast Office, Charleston.
- Hohl, R., H. H. Schiesser, and D. Aller, 2002: Hailfall: the relationship between radar-derived hail kinetic energy and hail damage to buildings. *Atmos. Res.*, 63, 177–207. [https://doi.org/10.1016/S0169-8095\(02\)00059-5](https://doi.org/10.1016/S0169-8095(02)00059-5)
- Horváth, A., Seres, A. T., and Németh, P., 2015: Radar-based investigation of long-lived thunderstorms in the Carpathian Basin. *Időjárás* 119, 39-51.
- Iliescu, M.C., 1989: Atmospheric Electrical Activity over Romania. Editura Academiei Republicii Socialiste Romania, Bucharest. (in Romanian)
- Istrate, V., Apostol, L., Sfică, L., Iordache, I., and Bărcăcianu, F., 2015: The status of atmospheric instability indices associated with hail events throughout Moldova. Conference Air And Water components of the Environment 7, 323–331. https://doi.org/10.17378/AWC2015_43
- Istrate, V., Axinte, A.D., Apostol, L., Florea, D., and Machidon, O.M., 2016: The Efficacy of Hail Suppression in Iași County (Romania) Case Study 09 July 2015. SGEM2016 Conference Proceedings 16 631–38. <https://doi.org/10.5593/SGEM2016/B42/S19.081>
- Istrate, V., Dobri, R.V., Bărcăcianu, F., Ciobanu, R.A., and Apostol, L., 2017: A ten years hail climatology based on ESWD hail reports in Romania, 2007-2016. *Geographia Technica* 12, 110-118. doi:10.21163/GT_2017.122.10

- Istrate, V., Ursu, A., Radu, D. V., Aurel, A. D., and Dorinel, S., 2019: Hail suppression system in Romania and its relation with land cover, SGEM 2019 Conference Proceedings, 19, 871-878. <https://doi.org/10.5593/sgem2019/2.2/S11.107>
- Johns, R.H. and Doswell, III C.A., 1992: Severe local storms forecasting. *Weather Forecast.* 7, 588–612. [https://doi.org/10.1175/1520-0434\(1992\)007<0588:SLSF>2.0.CO;2](https://doi.org/10.1175/1520-0434(1992)007<0588:SLSF>2.0.CO;2)
- Kolendowicz, L., Taszarek, M., Czernecki, B., 2017: Atmospheric circulation and sounding-derived parameters associated with thunderstorm occurrence in Central Europe. *Atmospheric Research* 191, 101-114. <https://doi.org/10.1016/j.atmosres.2017.03.009>
- Kunz, M. and Puskeiler M., 2010: High-resolution assessment of the hail hazard over complex terrain from radar and insurance data. *Meteorol. Z.*, 19, 427–439. <https://doi.org/10.1127/0941-2948/2010/0452>
- López, L., Marcos, J.L., Sánchez, J.L., Castro, A., and Fraile, R., 2001: CAPE values and hailstorms on north western Spain. *Atmos. Res.* 56, 147–160. [https://doi.org/10.1016/S0169-8095\(00\)00095-8](https://doi.org/10.1016/S0169-8095(00)00095-8)
- Maier, N., Lacatus, D., and Rus, T., 2010: Hail in the area covered distribution of WSR-98D radar from Bobohalma. *Air and Water - Components of the Environment* 2, 404–411.
- Manzato, A., 2012: Hail in Northeast Italy: Climatology and Bivariate Analysis with the Sounding-Derived Indices. *J. Appl. Meteorol. Climatol.* 51, 449-467 <https://doi.org/10.1175/JAMC-D-10-05012.1>
- Marin, L., Birsan, M.V., Bojariu, R., Dumitrescu, A., Micu, D.M., Manea, A., 2014: An overview of annual climatic changes in Romania: trends in air temperature, precipitation, sunshine hours, cloud cover, relative humidity and wind speed during the 1961–2013 period. *Carpath J Earth Environ Sci* 9, 253–258.
- Miller, R.C., 1975: Notes on Analysis and Severe-Storm Forecasting Procedures of the Air Force Global Weather Central. Technical Report no 200. <https://apps.dtic.mil/dtic/tr/fulltext/u2/744042.pdf>.
- National Meteorological Administration, 2008: Climate of Romania The publishing house of the Romanian Academy, Bucharest. (In Romanian)
- Potapov, E.I. and Garaba, I.A., 2016: Technological Features of Hail Suppression Activities in the Republic of Moldova. *Russian Meteorology and Hydrology* 41(4):268–275. <https://doi.org/10.3103/S1068373916040063>
- Pešice, P., Sulan, J., and Řezáčová, D., 2003: Convection precursors in the Czech territory. *Atmospheric Research*, 67-68, 523-532. [https://doi.org/10.1016/S0169-8095\(03\)00070-X](https://doi.org/10.1016/S0169-8095(03)00070-X)
- Právělie, R., Pitićar, A., Roșca, B., Sfićă, L., Bandoc, G., Tiscovschi, A., Patriche, C., 2019: Spatio-temporal changes of the climatic water balance in Romania as a response to precipitation and reference evapotranspiration trends during 1961–201. *Catena* 172, 295-312. <https://doi.org/10.1016/j.catena.2018.08.028>
- Seres, A.T. and Horváth, A., 2015: Thunderstorm climatology in Hungary using Doppler radar data, *Időjárás* 119, 185-196.
- Showalter, A.K., 1953: A stability index for thunderstorm forecasting. *Bull Am Meteorol Soc* 34, 250–252. <https://doi.org/10.1175/1520-0477-34.6.250>
- Siedlecki, M., 2009: Selected instability indices in Europe. *Theor Appl Climatol* 96:85–94. <https://doi.org/10.1007/s00704-008-0034-4>
- Sioutas, M.V. and Flocas H.A., 2003: Hailstorms in northern Greece: synoptic and thermodynamic environment. *Theor. Appl. Climatol.* 75, 189–202. <https://doi.org/10.1007/s00704-003-0734-8>
- Sioutas, M.V., Meaden G.T., and Webb J.D., 2009: Hail frequency, distribution and intensity in northern Greece. *Atmos. Res.* 93, 526–533. <https://doi.org/10.1016/j.atmosres.2008.09.023>
- Sfićă, L., Apostol, L., Istrate, V., Lesenciuc, D., Necula, M.F., 2015: Instability indices as predictors of atmospheric lightning - Moldova region study case. SGEM 2015 Conference Proceedings 15, 387 – 394. <https://doi.org/10.5593/SGEM2015/B31/S12.050>
- Thompson, R.L., Edward, R., Hart, J.A., Elmore, K.L., and Markowski, P., 2003: Close proximity soundings within supercell environments obtained from the Rapid Update Cycle. *Wea. Forecasting* 18, 1243–1261. [https://doi.org/10.1175/1520-0434\(2003\)018<1243:CPSWSE>2.0.CO;2](https://doi.org/10.1175/1520-0434(2003)018<1243:CPSWSE>2.0.CO;2)
- Taszarek, M., Brooks, H.E., and Czernecki, B., 2017: Sounding-Derived Parameters Associated with Convective Hazards in Europe. *Mon. Weather Rev.* 145, 1511–1528. <https://doi.org/10.1175/MWR-D-16-0384.1>

IDŐJÁRÁS

Quarterly Journal of the Hungarian Meteorological Service
Vol. 125, No. 1, January – March, 2021, pp. 53–82

A statistical analysis of the relationship between domestic hot water consumption and mean outdoor temperature in Budapest

András Horkai *

Óbuda University
Ybl Miklós Faculty of Architecture and Civil Engineering
H-1146 Budapest, Thököly út 74.

**Corresponding author E-mail: horkai.andras@hotmail.com*

(Manuscript received in final form April 22, 2020)

Abstract— This study analyzes how outdoor temperature influences domestic hot water consumption in multiapartment large-panel system buildings in Budapest, Hungary. The analysis is based on data from the validated invoicing system of the district heating provider, and from two weather stations of the Hungarian Meteorological Service. The official monthly hot water consumption data of 72 buildings for 7 consecutive years and the corresponding monthly mean temperatures were used in this study. Linear regression analysis and time series decomposition were carried out. The results prove that the outdoor temperature and the domestic hot water consumption are definitely related. The model based on regression analysis could account for 74% of values. The time series decomposition model is able to estimate hot water consumption per apartment per day for a future month with 94% probability. The study relies on data obtained from a projection of two regional climate models each, namely ALADIN-Climate and RegCM. Based on these data, the model forecasts how the effects of climate change will probably influence domestic hot water consumption in the near future. These results shed light on the factors influencing hot water consumption, and may help authorities and decision makers to form sustainability policies and to plan sustainable resource management.

Key-words: Budapest, climate, domestic hot water, household, mean outdoor temperature, statistical data analysis, water consumption

1. Introduction

The complex energy system and energy consumption of buildings consists of several subsystems and their consumption, which is necessary for the intended use of the building. In Hungary, the Decree of the Minister without Portfolio on the determination of the energy characteristics of buildings takes into account the consumption, efficiency, losses, and self-consumption of all building engineering systems necessary for the intended use of the building when determining the aggregate energy characteristics (which is the sum of the primary energy consumption of building engineering and lighting systems per unit of heated floor area). These systems include: heating, domestic hot water supply, air technology, cooling, and lighting (7/2006. (V. 24.), Decree, 2006; Baumann et al., 2009).

Domestic energy consumption makes up 28% of overall energy use of the EU (based on data from 2017), while for Hungary this figure is 36% (Eurostat; Magyar Energetikai és Közmű-szabályozási Hivatal). Looking at the average consumption structure of Hungarian households, two independent studies have reached similar results. 75% of the full energy expenditure is spent on heating and air-conditioning, 10% is spent on hot water production, while 10% is spent on the energy used by electrical appliances (e.g., consumer electronics, household appliances) (Energia Klub, 2004; Energiaoldal, 2012). In the USA, the proportion of hot water costs amounts to the 20% of full energy expenses (NAHB Research Center, 2002). In 2015 Hakala concluded that the second largest item in domestic energy balance is hot water production in Finland. Consequently, the production of domestic hot water (DHW) accounts for a significant proportion of the energy balance of residential buildings (Hakala, 2015). It must be noted, however, that the proportion of DHW consumption in the energy balance depends on several parameters, and consumer profiles are very complex and change over time (Ahmed et al., 2016).

Approximately 13% of the Hungarian housing stock is built with large-panel system (LPS) technology, and one-eighth of the population live in such type of flats (Központi Statisztikai Hivatal, 2014). Central heating and domestic hot water supply are provided by district heating in these houses. This study analyzes the domestic hot water consumption data of a housing estate built with large-panel system in Budapest, Hungary and the outdoor temperature in the course of several years. It aims to reveal how outdoor temperature change influences domestic hot water consumption in multiapartment buildings. More precisely, the study aims to map how DHW consumption and outdoor temperature are related, by breaking down the data into different spatial (full housing estate, certain building types) and temporal (year, season) figures. The results are used to predict future tendencies of DHW consumption.

2. Background

2.1. Factors influencing energy and water consumption

Models of energy consumption influencing factors aim to determine how these factors can be categorized. *Kowsari and Zerriffi (2011)* established two major factor categories: (i) endogenous factors depend on the household examined; while (ii) exogenous factors depend on outdoor circumstances. The major categories are further divided into subcategories.

Based on the above holistic model, *Putzer and Pavluska (2013)* introduced the model illustrated in *Fig. 1* to describe energy consumption (energy profile) for Hungary. All factors were included into the model that have shown a significant correlation with domestic energy consumption in the literature.

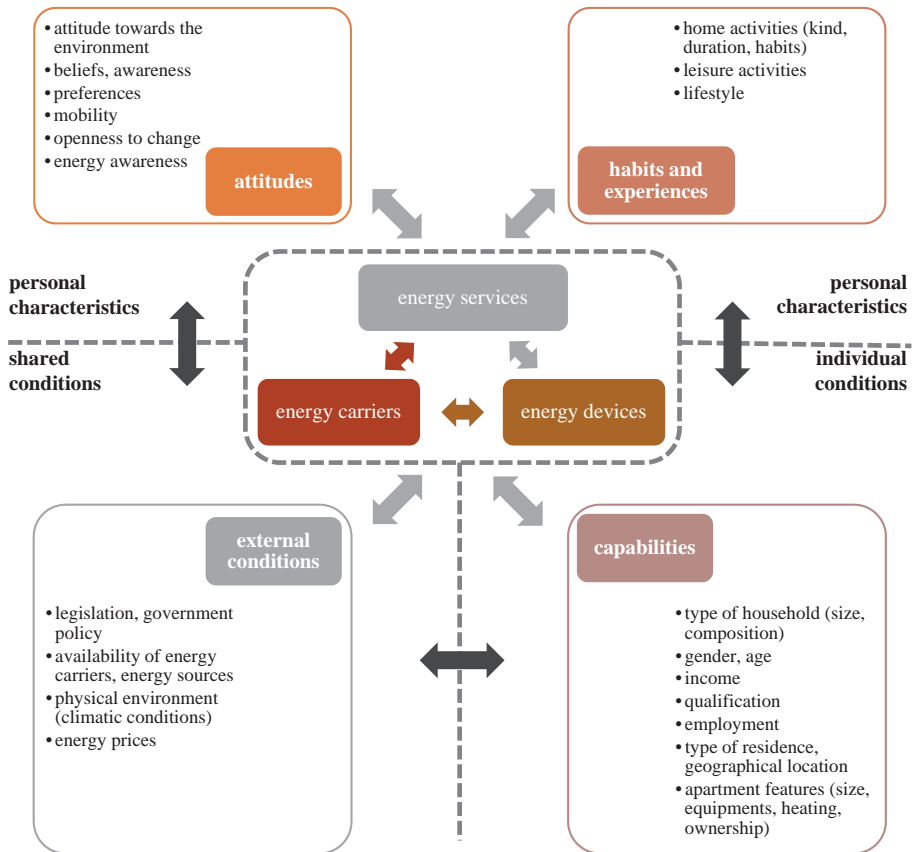


Fig. 1. Energy consumption model of Hungarian households – major influencing factors. Figure by the author based on *Horkai and Kiss (2019)*.

The model shows factors that affect energy use in general. Given that domestic hot water consumption is part of the total energy consumption, a significant proportion of the factors presented influence the energy use: physical environment and climatic factors – examined in the present article – have appeared as influencing factors in several other studies (*Egyedi*, 1963; *Hobbi and Siddiqui*, 2009; *March and Saurí*, 2010; *Menyhárt*, 1977; *Otaki*, 2003; *Pérez-Lombard et al.*, 2008). Contrarily to these, in their study on climatic and geographical factors, *Romano et al.* (2016) found that only the height above sea level had a significant effect on water consumption, temperature did not.

As for climatic factors, several studies point out that seasonality (i.e., tendencies shown by data in yearly, monthly, weekly, and daily breakdowns play a crucial role in DHW consumption (*Abrams and Shedd*, 1996; *Becker and Stogsdill*, 1990b; *Csoknyai and Csoknyai*, 2014; *Egyedi*, 1963; *George et al.*, 2015; *Gerin et al.*, 2014; *Horkai*, 2019; *Menyhárt*, 1977; *Meyer*, 2000; *Perlman and Mills*, 1985). Details of the research can be found in Section 5.2.2.

2.2. Climatic conditions of Hungary

Hungary is situated in the northern continental climate zone, characterized by four seasons and westerlies. The weather is rather changeable owing to the fact that the country is affected by oceanic, continental, and Mediterranean effects as well (*Kocsis*, 2018).

The most important factors influencing the temperature are as follows: (i) latitude; (ii) altitude; (iii) distance from the seas. The yearly mean temperature in the majority of the country is between 10 °C and 11 °C. Based on data between 1981 and 2010, the national average is 10.4 °C. Mean temperatures above 11 °C appear in the southern-southeastern parts of the country, on slopes with southern or southwestern exposure, and in Budapest owing to the urban heat island effect. It must be noted, however, that an extensive appearance of such high mean temperatures (above 11 °C) is only characteristic of the past 30 years (*Kocsis*, 2018).

According to the Köppen–Geiger climate classification system, the majority of Hungary belongs to the Dfb category (i.e., cold (continental), no dry season, warm summer), while the surveyed area is partly Dfb and Dfa (i.e., cold (continental), no dry season, hot summer) (*Beck et al.*, 2018), see *Fig. 2*.

According to the local climate zones (LCZ) in Budapest defined by *Gál et al.* (2015), the Füredi housing estate falls into the category LCZ 5 – open mid-rise. *Dian et al.* (2020) compared these local climate zones with surface temperature satellite data. Based on their studies, it was found that in this category, SUHI (surface temperature-based urban heat island) is above 1 °C throughout the year, with up to 4–5 °C during the day in summer compared to non-urban areas outside Budapest. Thus, the Füredi housing estate belongs to the category of LCZ with the second highest SUHI in the capital.

3. Data

3.1. Description of the surveyed area

The primary factor for selecting an area for analysis was to have available data about domestic hot water consumption from an authorized source. The metering of heating and domestic hot water consumption in buildings with district heating is general practice in Hungary, which allows for the detailed analysis of consumption data. For other types of buildings, such surveys would be impossible to carry out in the lack of appropriate data. The overwhelming majority of buildings provided with district heating are multiapartment LPS buildings in housing estates (Horváth *et al.*, 2016).

More than a third of Hungarian LPS buildings are in Budapest (Birghoffer and Hikisch, 1994; Dési, 1996), therefore, the plot to be examined was selected in this city. The Fűredi housing estate (Fűredi út, district XIV) is the fifth largest housing estate of LPS buildings in the city. It was built in three phases between 1967 and 1978, using LPS technology (Berza, 1993).

The housing estate is made up of 83 buildings, out of which 72 were taken into this survey. As for the remaining 11 buildings, for some houses the data series provided by the public utility company were incomplete or missing, while others were excluded from this study owing to their crucially different energetic structure (e.g., solar collectors).

3.2. Data on domestic hot water consumption

Hong *et al.* (2017) warns that it is advisable to use data from an integrated source (e.g., energy consumption data from the public utility company) for the analysis of consumers and consumer habits. It is equally important to note that if data is collected directly from consumers, the inconsistency between real and reported habits might be a limitation of data collection (Young *et al.*, 2013). Based on these policies, this study does not use data obtained directly from consumers. It relies on quantitative data provided by the public utility company and found in the official census, and only this dataset is used for a statistical analysis of the relationships between different variables.

For the present study, the district heating provider (FŐTÁV Budapesti Távhőszolgáltató Zrt. – Budapest District Heating Works Private Company Limited by Shares) provided the consumption data broken down to the primary heat substations of each building, both for heating and domestic hot water for the time period between 2010 and 2016, in monthly breakdown. These datasets had served as the basis for accounting after automatic or manual checking, i.e., the sets can be regarded as official and validated. The basic unit of this analysis is the building. If there is more than one heat substation in a given building, the relevant datasets were collapsed.

According to information from the district heating provider, the buildings can be regarded as uniform with respect to the domestic hot water providing system, there is no significant difference between them. The present study does not take into account whether the building envelope was refurbished.

3.3. Temperature data

The mean temperatures in monthly breakdown were taken at two weather stations (Budapest-Pestszentlőrinc and Budapest-Inner City) of the Hungarian Meteorological Service (OMSZ). The averages of the two datasets were used in this study. The air distance of the two weather stations from the examined plot is approximately 8.75–9.00 km.

Fig. 2 shows the climate classification map of Hungary, Budapest, and the surveyed area (based on the Köppen–Geiger system), as well as the location of the weather stations and the Fürediv housing estate within Budapest.

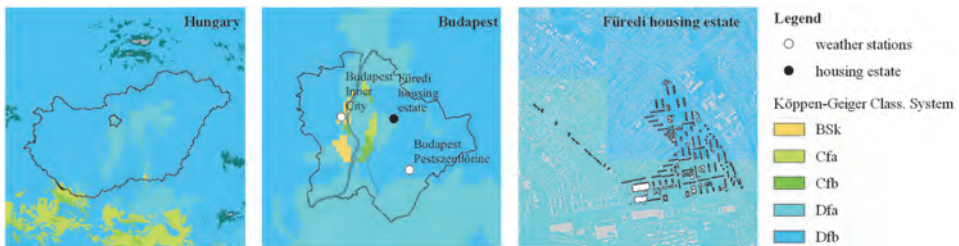


Fig. 2. Weather stations and the surveyed area on a climate classification map based on the Köppen–Geiger system (Beck *et al.*, 2018).

3.4. Basic data from climate projections

Temperature data for the estimation of future domestic hot water consumption were obtained from the National Adaptation Geo-Information System (NAGiS). This database was created from data gained from the CarpatClim-Hu database—which resulted from validated and homogenized meteorological measurement data interpolated on a regular grid, and harmonized at the borders; furthermore, from data resulting from a projection of models ALADIN-Climate (Csima and Horányi, 2008) and RegCM (Sitz *et al.*, 2017), respectively. Climate model projections were created with Representative Concentration Pathway (RCP) scenarios. These scenarios take into consideration the international mitigation initiatives, which are characterized by the possible range of radiative forcing values in the year 2100. In this study, we used the pessimistic RCP8.5 scenario for ALADIN-Climate, while for RegCM the optimistic RCP4.5 scenario was used to create the model simulations (i.e., supposing 8.5 and 4.5 W/m² radiative forcing

for 2100, respectively). Their data correspond to the periods 1971–2000, 2021–2050, and 2069–2098. Naturally, model simulations are loaded with insecurity resulting from the natural changeability of climate, the fact that physical processes can be described with a limited precision, and the unpredictability of social and economic processes that exercise an effect on the system (*Kajner et al., 2017; Nemzeti Alkalmazkodási Térinformatikai Rendszer (NATÉR) - ENG: National Adaptation Geo-information System (NAGiS)*).

Based on the results of the two models, the raising of the mean temperature in Hungary will continue, concerning both monthly and yearly averages. Between 2021 and 2050, the predicted growth is 1–2 °C for the end of the period, while for the end of the 2071–2100 period, it is 3–5 °C. It is not straightforward which seasons will change the most. For the middle of the century, the ALADIN-Climate model predicts the greatest changes for the summers, while the RegCM model claims the spring mean temperatures are to raise considerably (*Kajner et al., 2017*).

Table 1 shows the expected change in the yearly mean temperatures for the periods 2021–2050 and 2071–2100, based on the projections of climate models ALADIN-Climate and RegCM, compared to the period between 1961 and 1990. The values shown here are the differences between mean temperatures in the two periods.

Table 1. Predicted changes in yearly mean temperature (°C) in Hungary based on projections of ALADIN-Climate and RegCM climate models compared to period 1961–90 (*Nemzeti Alkalmazkodási Térinformatikai Rendszer (NATÉR) - ENG: National Adaptation Geo-information System (NAGiS)*)

model	ALADIN-Climate (RCP8.5)		RegCM (RCP 4.5)	
	2021–2050	2071–2100	2021–2050	2071–2100
year	1.5–2.0	3.0–3.5	1.0–1.5	3.0–3.5
winter	1.0–1.5	2.0–2.5	1.0–1.5	3.0–3.5
spring	1.5–2.0	3.0–3.5	1.5–2.0	2.5–3.0
summer	2.0–2.5	4.0–4.5	0.5–1.0	3.5–4.0
autumn	1.5–2.0	3.0–3.5	0.5–1.0	3.0–3.5

4. Methods




4.1. Levels of analysis

Owing to the availability and detailedness of the data, this analysis examines domestic hot water consumption broken down to different spatial (whole housing estate, certain building types) and temporal (year, season, month) levels. It does not differentiate between buildings before or after energetic refurbishment; the

domestic hot water systems of these buildings are treated uniformly based on the resolution of the district heating provider.

Altogether 72 buildings (11,211 apartments) were surveyed. Building types in which the total number of apartments reaches 10% of the total number of flats in the housing estate: Types K1, K2, and Kx4 (see *Table 2* for the parameters of these building types) were chosen for the building type level analysis.

Table 2. Parameters of the surveyed building types (Horkai et al., 2018)

	K1	K2	Kx4
type			
number of apartments per building	132	264	172
weighted average size of apartments [m ²]	48.90	45.60	58.88
weighted average number of rooms per apartment	2.33	2.00	2.51
heated volume [m ³]	16,900	31,400	26,000

In sum, the survey examines the whole housing estate, certain building types, and the cumulative parameters of all other building types. *Fig. 3* illustrates this hierarchy.

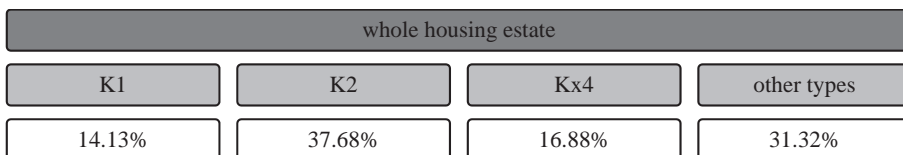


Fig. 3. Hierarchy and distribution of apartments in building types in the housing estate.

4.2. The parameters examined

The data on DHW consumption were given in m³/building/month by the district heating provider. Similarly to other studies (*Energy Monitoring Company*, 2008), in order to eliminate the differences in building types (i.e., a different number of apartments) and the length of the months, the data series was normalized and the unit of consumption was changed to l/apartment/day (henceforth l/apt/day). Concerning the number of hot water taps, each flat in the housing estate (irrespective of size) is equipped with a wash basin and a bathtub in the bathroom, and a sink in the kitchen.

No data is available on the number of inhabitants of individual flats or houses, only detailed demographic data available on ~35% of the housing estate (3960 dwellings) can be used to deduce the average density of housing, which is 1.53 people per apartment. It must be noted that this number is well below (almost 38 percentage points lower, than) the national average, which is 2.48 person/apartment (*Központi Statisztikai Hivatal*, 2014).

On the one hand, the low density of the dwellings can be explained by the location. In fact, nearly 40% of residential dwellings in the capital are occupied by people living alone (compared to 30% of the national average). Furthermore, in Hungary, as we go down the hierarchy of settlements, apartments become more densely populated: Budapest has the lowest density ratio with 2.13 people/apartment. This number is 2.35 in county capitals and county towns, 2.57 in other cities, and 2.72 in municipalities (*Központi Statisztikai Hivatal*, 2014).

The low density of apartments, on the other hand, can be explained by the age structure. The number of residents over 60 years of age in Füredi housing estate is higher than the national average, and nearly 30% of the over-65s live in a single household in Hungary (*Balázs et al.*, 2017).

4.3. Statistical methods

The available data was analyzed with the help of MS Excel. The normality of the data set was examined using the Kolmogorov-Smirnov test.

The correlations between DHW consumption and weather data were explored with the help of regression analysis with two variables: in our model the independent variable was the monthly mean temperature, while the dependent variable was the domestic hot water consumption.

Time series were analyzed with decomposition methods, aiming to find the following components of time series.

- Trend (T₁): long-term direction of the basic time series, i.e., what tendency can be quantified in the time series taken as a function of time.
- Seasonality (S_j): regularly recurring short-term (within a year) deviations from the trend (i.e., regular fluctuations).

- Random component (E_t): part not explained by either the trend or seasonality, random effect.

The first step of the time series decomposition was to model the trend with a linear regression function, where the explanatory variable was the passage of time (from January 2010 to December 2016, broken down to months). In the next step, the estimated values were subtracted from the actual measured data, which gave the sum of seasonality and random components. In step 3, averages were calculated and corrected to arrive at the pure seasonal values. The aim of correction was to make the mean of seasonal effects zero, in order that it should not contain tendencies. Pure seasonal values show the deviations from the trend of the given month.

5. Results and discussion

5.1. Statistical parameters of the basic dataset

The statistical parameters of the basic datasets corresponding to 84 months are given in *Table 3*.

Table 3. Statistical parameters of the basic datasets

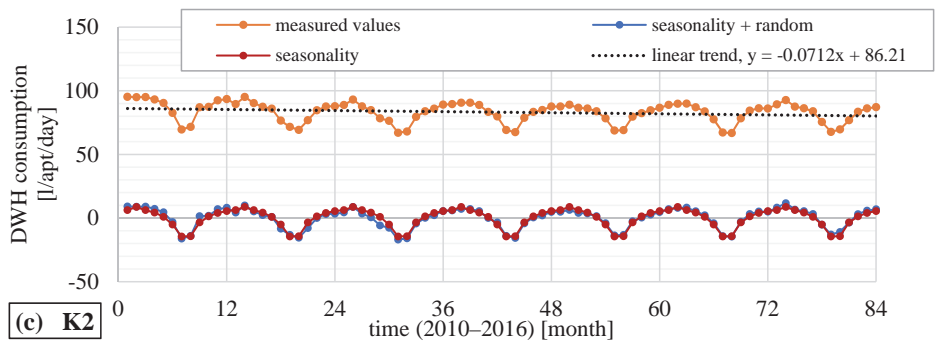
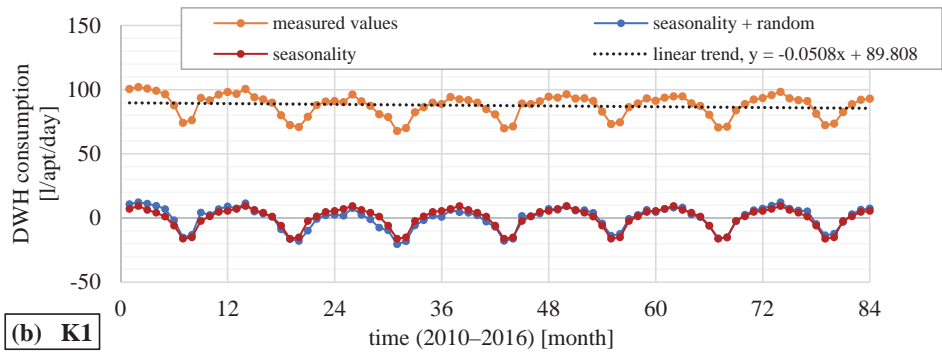
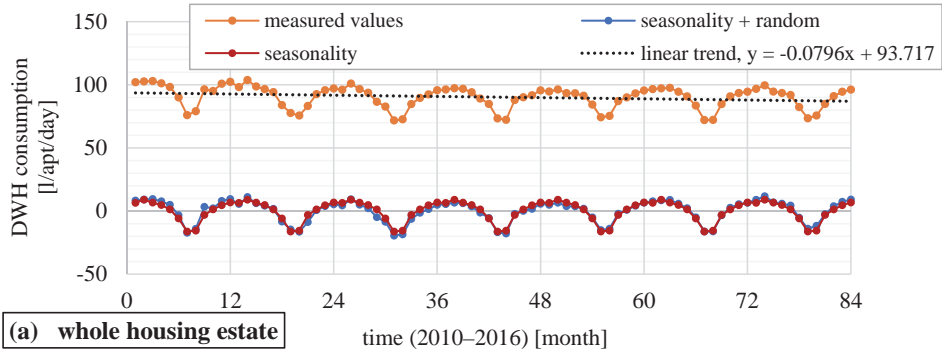
	outdoor	DHW consumption [l/apt/day]				other types
	temperature [°C]	whole housing estate	K1	K2	Kx4	
N	84	84	84	84	84	84
Sum	1059.60	7588.01	7362.50	6987.46	7749.91	8325.03
Mean	12.61	90.33	87.65	83.18	92.26	99.11
Median	13.00	93.33	90.08	85.95	95.05	101.00
Min	-1.20	71.76	67.77	66.76	73.23	77.57
Max	25.10	103.72	102.02	95.27	103.17	115.78
Deviation	7.97	8.76	8.71	7.96	8.67	10.12
Kurtosis	-1.29	-0.41	-0.43	-0.49	-0.26	-0.38
Skewness	-0.08	-0.77	-0.72	-0.71	-0.96	-0.64

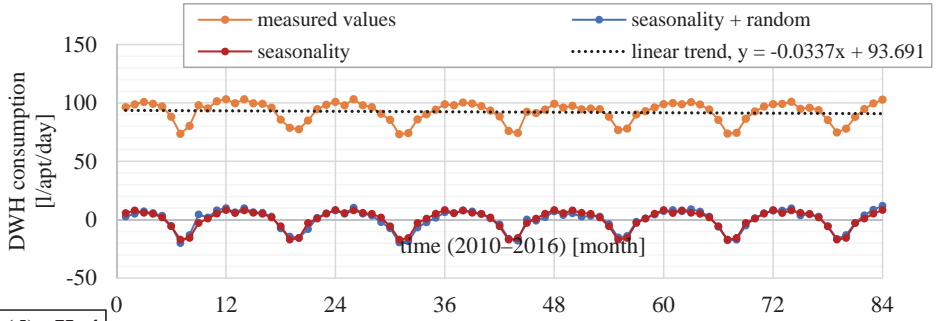
The Kolmogorov-Smirnov normality test of the data proved that the distribution of sample elements does not significantly deviate from the normal distribution.

5.2. Analysis of hot water consumption

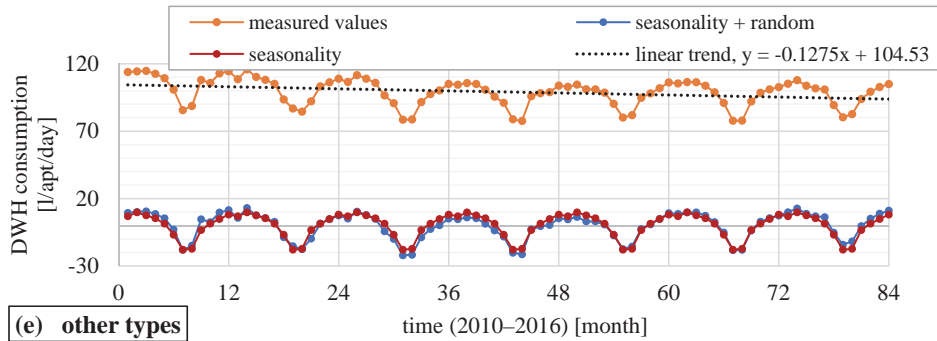
5.2.1. Decomposition models

Figs. 4.(a–e) depict the decomposition models of the domestic hot water consumption of each unit of analysis.





(d) Kx4



(e) other types

Fig. 4 (a-e). Decomposition models of the domestic hot water consumption of each unit of analysis.

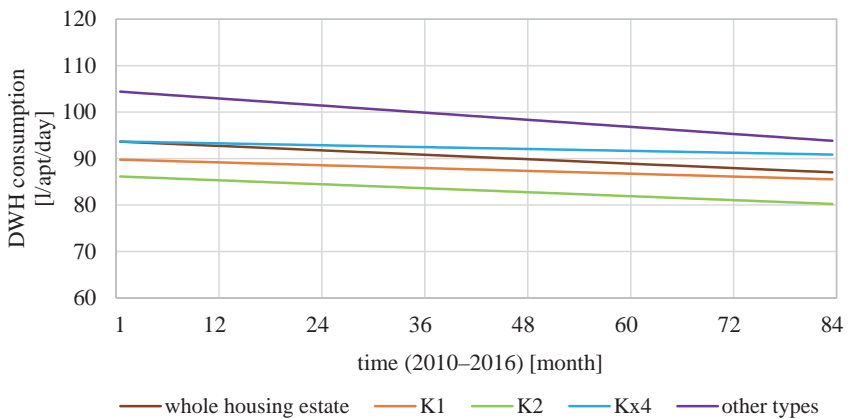


Fig. 5. Trends in hot water consumption in the surveyed period.

The basic trends for 7 years of each survey unit are illustrated in the above figures: in the long run, DHW consumption decreased. The smallest basic domestic hot water consumption (l/apt/day) was recorded in Type K2 buildings, while the biggest basic consumption was recorded in Type Kx4. This difference in basic consumption may stem from several factors, such as the different size of apartments (which affects the number of inhabitants), distribution losses, the age of plumbing, the different behavior of consumers.

Concerning the slope of the trendlines, the consumption of Kx4 buildings decreased the least, while the decrease was the biggest for other and K2 buildings.

As Fig. 6 illustrates, a very similar seasonality effect is witnessed at all units of survey, as seasonality influences them in the same way. An inverse relationship is present between the outdoor temperature and DHW consumption, the corresponding curves change in the same fashion.

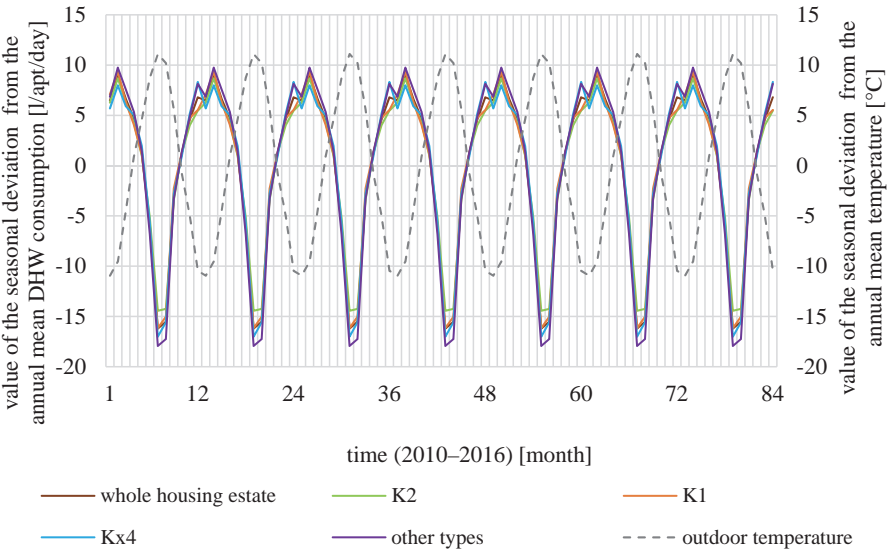


Fig. 6. Seasonality of outdoor temperature and DHW consumption

5.2.2. Consumption broken down to seasons

The average DHW consumption of units in the whole survey period (2010–2016) and also broken down to months are given in *Table 4*.

Table 4. Average and seasonal DHW consumption (average of years 2010–2016)

l/apt/day	whole housing estate	K1	K2	Kx4	other types
winter	97.87	95.05	90.10	99.64	107.54
spring	94.74	91.59	87.20	96.63	104.21
summer	77.77	75.23	71.89	79.51	85.05
autumn	90.96	88.72	83.55	93.26	99.63
average of the period	90.33	87.65	83.18	92.26	99.11
% (expressed as an average of years 2010–2016)	whole housing estate	K1	K2	Kx4	other types
winter	108.34	108.44	108.31	108.00	108.51
spring	104.88	104.50	104.82	104.74	105.14
summer	86.09	85.83	86.42	86.18	85.82
autumn	100.69	101.23	100.44	101.08	100.53
average of the period	100.00	100.00	100.00	100.00	100.00

Fig. 7 shows the average and seasonal DHW consumption of each unit of analysis.

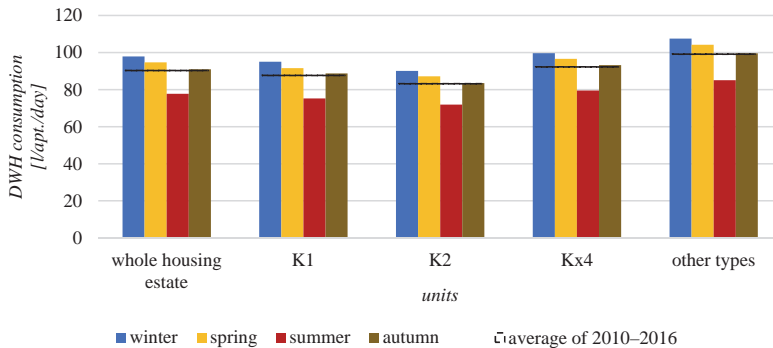


Fig. 7. Average and seasonal DHW consumption (average of years 2010–2016)

The data proves that domestic hot water consumption changes considerably within a year: the highest consumption was recorded in winter, which is 8 percentage points higher than the average, while summer consumption is 14 percentage points lower than the yearly average of the surveyed period. Consequently, the difference between winter and summer consumption is 22 percentage points. Autumn consumption roughly equals the yearly average.

Several Hungarian and international studies confirm that seasonality effect DHW consumption. *Egyedi* (1963) found a 16–22% difference between winter and summer consumption. *Menyhárt* also states that weather is the primary factor in influencing water consumption and that consumption is periodic within the year, month, week and day (*Menyhárt*, 1977).

Perlman and *Mills* found that winter DHW consumption might exceed summer consumption by 45% (*Perlman* and *Mills*, 1985). According to *Becker* and *Stogsdill* seasonality is the main influencing factor for DHW consumption: winter consumption is higher than summer consumption (*Becker* and *Stogsdill*, 1990a, 1990b). The same authors found the average winter consumption to be 13% higher than the average summer consumption (*Becker* and *Stogsdill*, 1990a). *Meyer* examined water consumption in South Africa, where the difference between summer and winter consumption might reach 37% (*Meyer*, 2000). It must be noted that owing to the geographical situation of the country, in South Africa summer consumption is higher than winter consumption. *Gerin et. al.* (2014) surveyed the DHW consumption of Belgian apartments, and found that winter consumption was 12% higher and summer consumption was 13% lower than the average consumption.

In their study on heat and DHW consumption in LPS buildings in Hungary, *Csoknyai* and *Csoknyai* (2014) found that the difference between summer minimum and winter maximum consumption might be very high (between -10 and +25%). *George et. al.* (2015) report that winter consumption is almost 10% higher than the summer consumption, exceeding the annual average by 3%, while the summer consumption is 6% below the average. They claim that the increase in consumption in cold seasons may be a direct consequence of lower outdoor temperatures and the lower temperature of the water in the system. In a study on a plot with LPS buildings, *Horkai* (2019) found that the difference between winter and summer hot water consumption was 22.45%.

5.2.3. Monthly domestic hot water consumption

Monthly consumption averages in the surveyed period (see *Fig. 8*) show that although outdoor temperature rises at the beginning of the year, DHW consumption also grows and reaches its maximum in February. In spring, DHW consumption decreases, plummeting in May. Minimal consumption occurs in July, and consumption steeply increases in August. In autumn, the consumption increases as the temperature decreases.

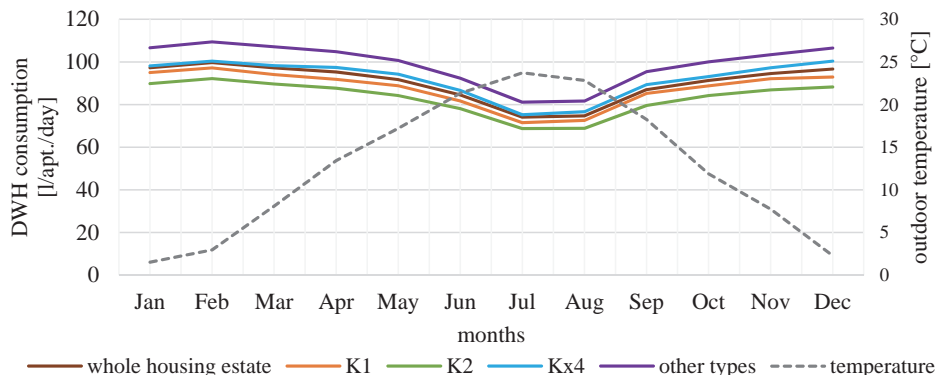


Fig. 8. Yearly pattern of DHW consumption (mean of years 2010–2016).

Ahmed and his colleagues (2015) analyzed Finnish households. The highest DHW consumption was recorded from November to February, while the lowest consumption was from May to July, the two extremes occurring in November and July (Ahmed *et al.*, 2015).

The minimum of DHW consumption in summer may be accounted for by the fact that people tend to go on holiday at this time of the year, and thus the lowest number of people stay at home. Csoknyai and Csoknyai (2014) in their survey of Hungarian LPS buildings found the lowest consumptions in July and August. The reasons for it included holidays and lower needs of consumers (lowest temperature of hot water and shorter bathing time).

A survey conducted on request of the Magyar Turizmus Zrt. in 2003 underpins our findings. They proved that 61% of trips abroad and 53% of domestic trips are realized in summer, with an average length of 3.1 nights. Concerning major trips, the temporal distribution of major travels was as follows: 37% of travellers went for a major trip in July, 29% in August, and 10% in June. 79% of major domestic trips and 67% of major trips abroad were realized in summer, with an average length of 8.63 nights (M.A.S.T. Piac- és Közvéleménykutató Társaság, 2004).

5.3. The model describing the correlation of outdoor temperature and domestic hot water consumption

The correlation between DHW consumption and weather data was analyzed with regression analysis with two variables. The independent variable was the monthly average temperature, while the dependent variable was DHW consumption.

Table 5 sums up the parameters of the theoretical statistical models described below. All models are significant. Furthermore, the change of outdoor temperature accounts for ~70–74% of the changes in DHW consumption.

Table 5. Regression statistics for the analysis of correlations between outdoor temperature and DHW consumption for the units of analysis – linear regression

	whole housing estate	K1	K2	Kx4	other types
R	0.8611	0.8441	0.8628	0.8595	0.8378
R²	0.7415	0.7125	0.7444	0.7387	0.7019
Adjusted R²	0.7384	0.7090	0.7413	0.7355	0.6983
Std. error of the estimate	4.4784	4.6962	4.0490	4.4578	5.5613
N	84	84	84	84	84
F	235.2337	203.1888	238.7789	231.8514	193.0716
Significance	< 0.001	< 0.001	< 0.001	< 0.001	< 0.001

As a result of regression analysis, based on the table showing coefficients, it can be determined that a 1 °C rise in outdoor temperature results in an approximately 1 liter (0.86–1.06 l) decrease in domestic hot water consumption per apartment per day. The values of the curves intersecting the axis show that at 0 °C, the average DHW consumption per flat is between 94.06 and 112.53 l (see Table 6).

Table 6. Summary of coefficients for the analysis of correlations between outdoor temperature and DHW consumption for the units of analysis – linear regression

		Coefficients	Std. error	t	p	95.0% confidence interval for coefficients	
						Lower bound	Upper bound
whole housing estate	Constant	102.2682	0.9188	111.3009	< 0.001	100.4403	104.0960
	outdoor temperature	-0.9461	0.0617	-15.3373	< 0.001	-1.0688	-0.8234
K1	Constant	99.2802	0.9635	103.0379	< 0.001	97.3634	101.1970
	outdoor temperature	-0.9221	0.0647	-14.2544	< 0.001	-1.0508	-0.7934
K2	Constant	94.0553	0.8307	113.2191	< 0.001	92.4027	95.7079
	outdoor temperature	-0.8618	0.0558	-15.4525	< 0.001	-0.9728	-0.7509
Kx4	Constant	104.0547	0.9146	113.7703	< 0.001	102.2353	105.8741
	outdoor temperature	-0.9350	0.0614	-15.2267	< 0.001	-1.0571	-0.8128
other types	Constant	112.5341	1.1410	98.6265	< 0.001	110.2643	114.8040
	outdoor temperature	-1.0644	0.0766	-13.8950	< 0.001	-1.2168	-0.9120

Linear regression functions are shown in *Table 7*.

Table 7. Summary of regression functions for the analysis of correlations between outdoor temperature and DHW consumption for the units of analysis – linear regression

spatial level	Regression equation
whole housing estate	$y = -0.9461 \times t + 102.2682$
K1	$y = -0.9221 \times t + 99.2802$
K2	$y = -0.8618 \times t + 94.0553$
Kx4	$y = -0.9350 \times t + 104.0547$
other types	$y = -1.0644 \times t + 112.5341$

where:

- y – estimated DHW consumption of the j th month [l/apt/day]
- t – mean temperature of the j th month [°C]

Fig. 9 shows the values estimated by the linear model and the corresponding measured values, together with the errors for the whole of the housing estate.

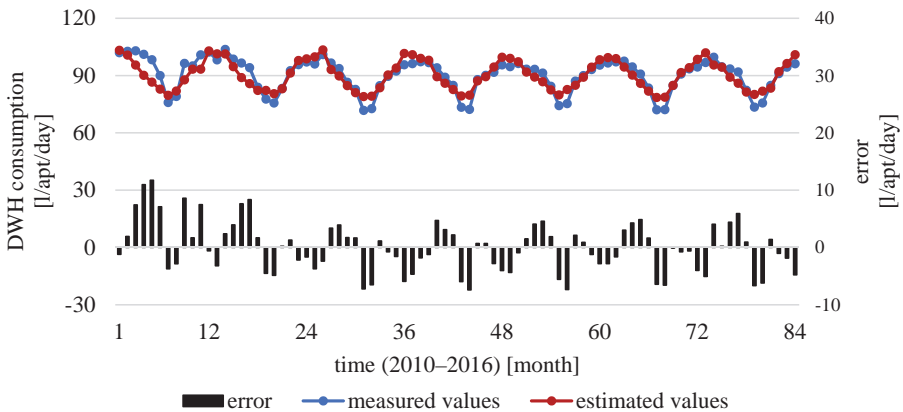


Fig. 9. Values estimated by the linear model of the outdoor temperature and the corresponding measured values, together with the errors.

Besides the fitting of a linear function, polynomial fitting was also applied in order to test the efficiency of linear fitting. *Table 8* shows the quadratic polynomial regression functions and the corresponding R^2 values. *Table 9* shows the cubic polynomial regression functions and the corresponding R^2 values.

Table 8. Summary of regression functions for the analysis of correlations between outdoor temperature and DHW consumption for the units of analysis – quadratic polynomial regression

unit	Regression function	R^2	F	Sig.
whole housing estate	$y = -0.055 \times t^2 + 0.4082 \times t + 97.383$	0.8532	236.3675	< 0.001
K1	$y = -0.0564 \times t^2 + 0.4662 \times t + 94.273$	0.8312	199.4102	< 0.001
K2	$y = -0.0475 \times t^2 + 0.3086 \times t + 89.834$	0.8453	221.2752	< 0.001
Kx4	$y = -0.0608 \times t^2 + 0.5617 \times t + 98.656$	0.8779	291.1011	< 0.001
other types	$y = -0.0603 \times t^2 + 0.4216 \times t + 106.19$	0.8142	164.1521	< 0.001

where:

- y – estimated DHW consumption of the j th month [l/apt/day]
- t – mean temperature of the j th month [°C]

Table 9. Summary of regression functions for the analysis of correlations between outdoor temperature and DHW consumption for the units of analysis – cubic polynomial regression

unit	Regression function	R^2	F	Sig.
whole housing estate	$y = -0.0043 \times t^3 + 0.1035 \times t^2 - 1.0516 \times t + 99.5123$	0.8843	203.8365	< 0.001
K1	$y = -0.0041 \times t^3 + 0.0917 \times t^2 - 0.8981 \times t + 96.2624$	0.8587	162.0385	< 0.001
K2	$y = -0.0037 \times t^3 + 0.0864 \times t^2 - 0.9252 \times t + 91.6332$	0.8722	181.9718	< 0.001
Kx4	$y = -0.0039 \times t^3 + 0.0828 \times t^2 - 0.7606 \times t + 100.5849$	0.9039	250.866	< 0.001
other types	$y = -0.0055 \times t^3 + 0.1404 \times t^2 - 1.4296 \times t + 109.8797$	0.8504	139.4099	< 0.001

where:

- y – estimated DHW consumption of the j th month [l/apt/day]
- t – mean temperature of the j th month [°C]

Fig. 10 shows the values estimated by the quadratic polynomial model and the corresponding measured values, together with the errors for the whole of the housing estate.

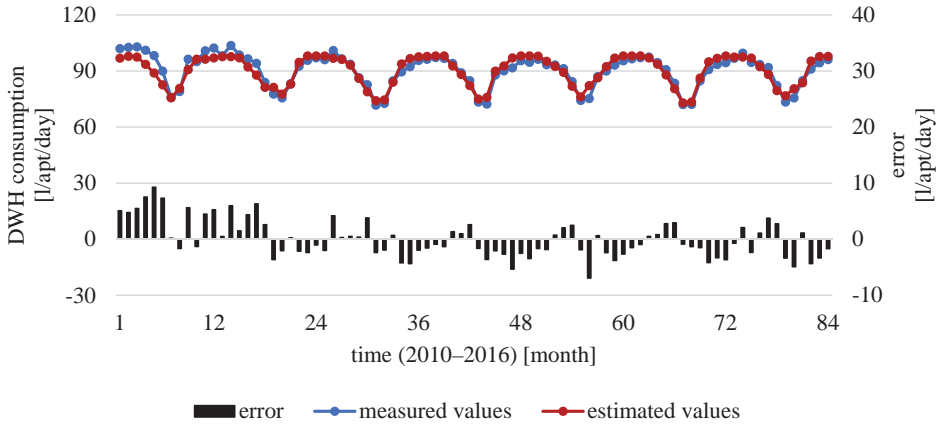


Fig. 10. Values estimated by the quadratic polynomial model of the outdoor temperature and the corresponding measured values, together with the errors

Fig. 11 shows the values estimated by the cubic polynomial model and the corresponding measured values, together with the errors for the whole of the housing estate.

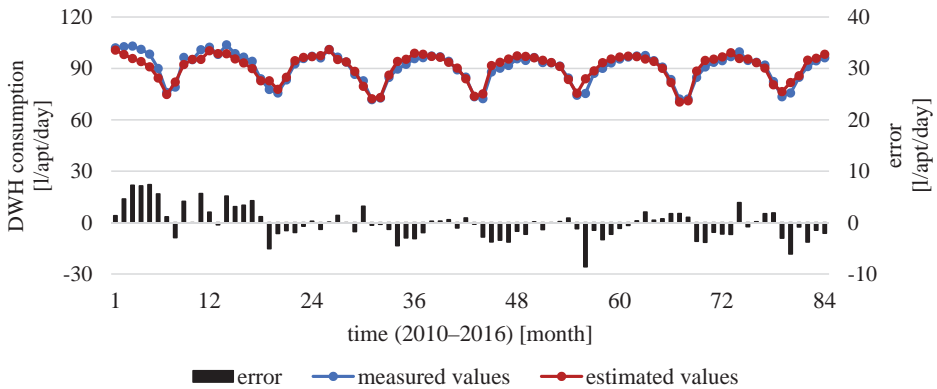


Fig. 11. Values estimated by the cubic polynomial model of the outdoor temperature and the corresponding measured values, together with the errors.

Fig. 12 illustrates the linear, quadratic, and cubic polynomial functions fitted to the data series of the whole housing estate.

The explanatory force of quadratic and cubic regression functions exceeded by approximately 10–12 percentage points the 75% value of the fitted linear curve. This value is higher, i.e., means better fittings, but this does not make the linear model useless, as the difference is not very big.

It must be noted that in the case of estimation, the results are better with polynomial models. However, this is only true if the temperature, i.e., the explanatory variable, is interpreted within the interval experienced up to now (i.e., between -1.2 and 25.1 °C), as the behavior of both of the polynomial regression functions is questionable outside this domain. The linear regression functions for each analyzed unit are shown in Fig. 13.

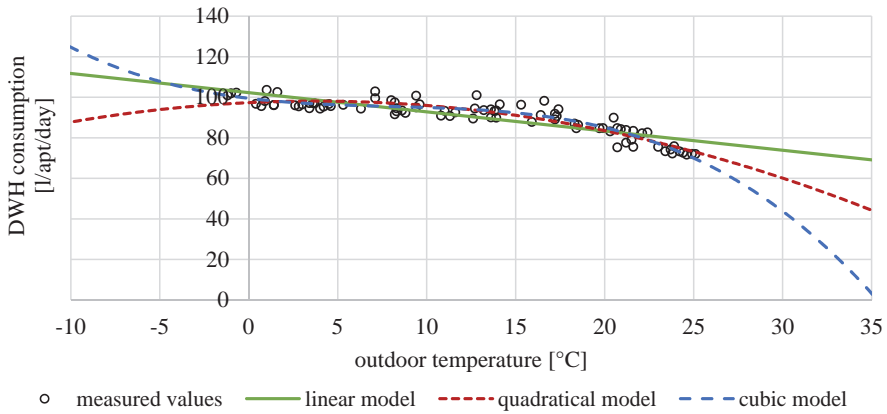


Fig. 12. Regression functions fitted to the data series of the whole housing estate.

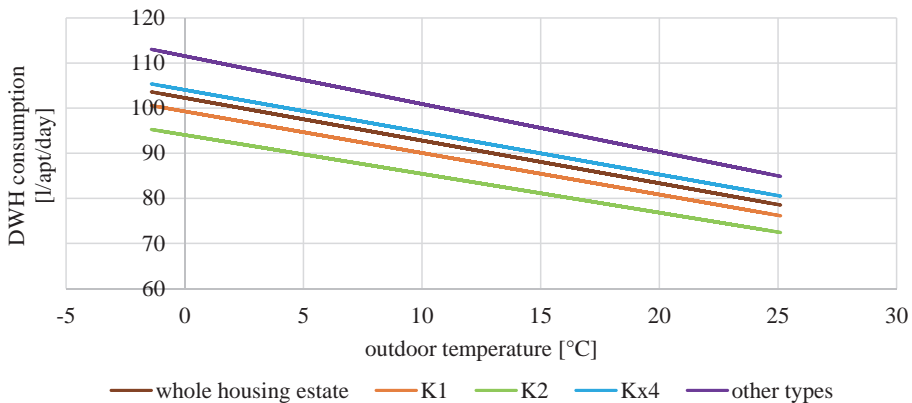


Fig. 13. Linear regression functions for each unit of analysis.

In sum, for each unit of analysis, 1 °C increase in outdoor temperature results in approximately 1 l decrease in DHW consumption per apartment per day. The units of analysis react in a similar way to the change in temperature. The corresponding curves are almost parallel, but actually converge towards each other. This is because buildings with a higher consumption will react to temperature change to a higher degree than buildings with a lower consumption. The most favorable type of building concerning DHW consumption per apartment is Type K2.

By using the established linear or polynomial regression functions, it is possible to estimate the DHW consumption of the apartments or buildings on an outdoor temperature basis, which is most useful for district heat providers.

5.4. Prognosis based on climate projections

Based on the linear model described above in Section 5.3 and the climate projections in Section 3.4, future DHW consumption and its possible changes can be estimated in the light of temperature changes. After determining the mean seasonal temperatures based on data from the 2010–2016 period, these temperatures were increased by the expected rise in temperature. The linear model was then applied to these data to determine the expected amount of DHW consumption. The actual data of the 2010–2016 period, and the expected temperatures calculated by two climate models are given in *Table 10* below, while the corresponding domestic hot water consumption data are enlisted in *Table 11*.

Table 10. Predicted mean temperatures (°C) for Hungary based on projections by ALADIN-Climate and RegCM climate models

model	current	ALADIN–Climate (RCP8.5)		RegCM (RCP 4.5)	
	temperature [°C]	2021–2050	2071–2100	2021–2050	2071–2100
period	average of 2010–2016 years				
year	12.61	14.11–14.61	15.61–16.11	13.61–14.11	15.61–16.11
winter	2.27	3.27–3.77	4.27–4.77	3.27–3.77	5.27–5.77
spring	12.92	14.42–14.92	15.92–16.42	14.42–14.92	15.42–15.92
summer	22.64	24.64–25.14	26.64–27.14	23.14–23.64	26.14–26.64
autumn	12.63	14.13–14.63	15.63–16.13	13.13–13.63	15.63–16.13

Table 11. Predicted DHW consumption for the whole housing estate (l/apt/day) based on projections by ALADIN-Climate and RegCM climate models

model	current consumption [l/apt/day] average of 2010–2016 years	ALADIN–Climate (RCP8.5)		RegCM (RCP 4.5)	
		2021–2050	2071–2100	2021–2050	2071–2100
year	90.34	88.44–88.92	87.02–87.50	88.92–89.39	87.02–87.50
winter	100.13	98.71–99.18	97.76–98.23	98.71–99.18	96.81–97.29
spring	90.04	88.15–88.62	86.73–87.20	88.15–88.62	87.20–87.68
summer	80.85	78.49–78.96	76.59–77.07	79.91–80.38	77.07–77.54
autumn	90.32	88.43–88.90	87.01–87.48	89.38–89.85	87.01–87.48

As climate projections predict the rising of the mean temperature in all seasons, this should result in a decreasing DHW consumption.

5.5. Time series decomposition model to describe the correlation of time and domestic hot water consumption

For the estimation based on the decomposition method presented in Section 4.3, using the trend parameter as the independent variable, the estimated trend values can be produced. If the seasonal deviation of the given month (seasonal deviations are determined by the month, and are uniform across the years) is added to the corresponding trend value, the DHW consumption of the given month is produced (l/apt/day). As the expected value of the random component is zero, it was not employed in the estimation model.

Fig. 14 below shows the seasonal coefficients, i.e., the absolute degree of monthly difference from the annual average of DHW consumption.

The values of the time series decomposition models are given in *Table 12* below. All models proved to be significant.

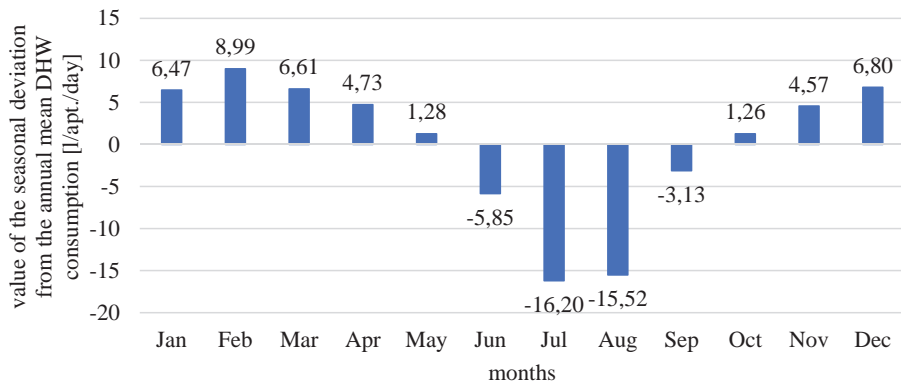


Fig. 14. Seasonal monthly coefficients of DHW consumption – whole housing estate.

Table 12. Statistical values for the analysis of the correlation between time and DHW consumption – time series decomposition model

	whole housing estate	K1	K2	Kx4	other types
R	0.9677	0.9418	0.9745	0.9694	0.9418
R²	0.9365	0.8870	0.9496	0.9397	0.8871
Adjusted R²	0.9258	0.8679	0.9411	0.9296	0.8680
Std. error of the estimate	2.3849	3.1817	2.1249	2.3237	3.1813
N	84	84	84	84	84
F	87.3006	46.4596	111.51	92.2791	46.4725
Significance	< 0.001	< 0.001	< 0.001	< 0.001	< 0.001

Owing to the high R^2 values, the estimations given by the model can be considered good for a one-year-long time span (compared to the baseline period 2010–2016); for the following 2 years it can be regarded reliable; while on the long run (in 5 years or later) the results must be considered with reservations.

The regression coefficients of each unit of analysis are given in Table 13.

Table 13. Summary of coefficients for the analysis of the correlation between time and DHW consumption – time series decomposition model

unit		Coefficients	Std. error	<i>t</i>	<i>p</i>	95.0% Confidence interval for coefficients	
						Lower bound	Upper bound
whole housing estate	Constant	93.7172	1.8912	49.5550	< 0.001	89.9551	97.4794
	ID of the month	-0.0796	0.0387	-2.0599	< 0.001	-0.1565	-0.0027
K1	Constant	89.8079	1.9087	47.0515	< 0.001	86.0109	93.6050
	ID of the month	-0.0508	0.0390	-1.3024	< 0.001	-0.1284	0.0268
K2	Constant	86.2103	1.7208	50.0991	< 0.001	82.7871	89.6335
	ID of the month	-0.0712	0.0352	-2.0247	< 0.001	-0.1412	-0.0012
Kx4	Constant	93.6914	1.9116	49.0124	< 0.001	89.8886	97.4941
	ID of the month	-0.0337	0.0391	-0.8616	< 0.001	-0.1114	0.0441
other types	Constant	104.5262	2.1342	48.9757	< 0.001	100.2805	108.7719
	ID of the month	-0.1275	0.0436	-2.9231	< 0.001	-0.2143	-0.0407

The general equation of the time series decomposition model is

$$Y_{i,j} = T_{i,j} + S_j + E_{i,j}, \quad (1)$$

where

$Y_{i,j}$ is the estimated DHW consumption of the j th month of the i th year (l/apr/day),

$T_{i,j}$ is the estimated trend value of DHW consumption of the j th month of the i th year,

S_j is the seasonal component of the j th month,

$E_{i,j}$ is the error component j th month of the i th year (expected value: 0).

For example, the values in Equation (1) are as follows for the whole housing estate for January 2017 (month 85, counting from January 2010):

$$Y_{i,j} = 93.7172 - 0.0796 * 85 + 6.47 = 93.4180. \quad (2)$$

Fig. 15 illustrates the DHW consumption values measured in the survey period (2010–2016) and the estimated values for years 2017–2019 for the whole housing estate.

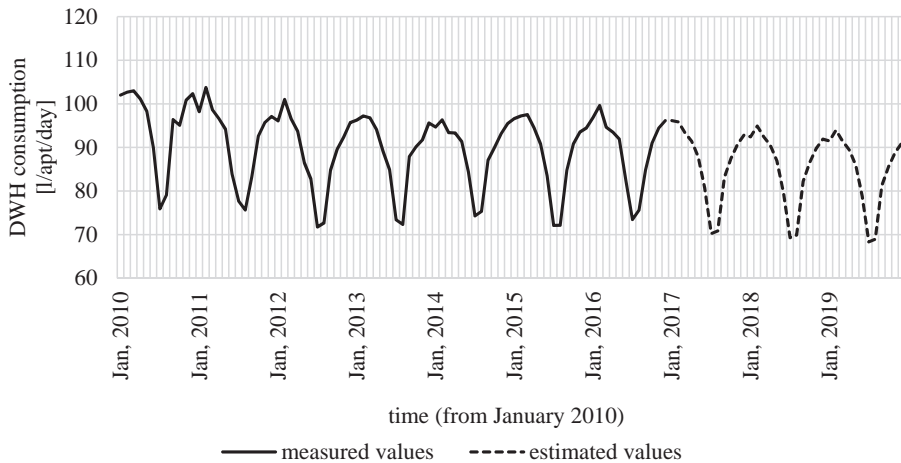


Fig. 15. Measured and estimated DHW consumption values by the time series decomposition model – whole housing estate.

Using the model based on the time series analysis created, it is possible to estimate the DHW consumption per apartment per day for any future month, which could be a basic operational planning data for district heating providers. The model takes into account both the expected outdoor temperature for the month and the typical domestic hot water consumption values for that month (absolute deviations from the annual mean consumption). By extending the available time series (e.g., by including data after 2016), the accuracy of the model can be verified and refined as needed.

6. Conclusion and directions for future research

This study surveyed how changes in outdoor temperature influence domestic hot water consumption in a housing estate of LPS buildings in Budapest, Hungary with the help of statistical analyses of DHW consumption data and changes in mean temperatures. The urban heat island effect is very significant in the investigated Fűredi housing estate, therefore, it is especially important to analyze the energy consumption of people living in this type of building.

The results have proved that changes in the outdoor temperature significantly influence the DHW consumption. The model created by regression analysis estimates DHW consumption based on outdoor temperature data, and accounts for 74% of the measured values. It has been found that a 1 °C rise in the mean outdoor temperature results in an approximately 1 l/apt/day decrease in DHW consumption. Furthermore, if the outdoor mean temperature is 0 °C, DHW consumption is between 94–112 l/apt/day. These values can be regarded as a rule of thumb for estimating DHW consumption.

Given that the explanatory force of the linear model is 74%, it can be seen, that other factors than outdoor temperature influence the seasonality and consumption values seen in DHW usage. By including additional independent variables – e.g., from the holistic model of factors influencing energy consumption –, the explanatory force of the model can be increased. This study is an outdoor temperature-based estimation for DHW consumption. A different method, which has no impact on the outdoor temperature-based estimation could be a home-stay-based estimation, in which it could be analyzed, how the number and proportion of working days and holidays affect the DHW consumption in each year.

Based on the analysis of DHW consumption broken down to seasons and months, the seasonal coefficient for each month was determined. Using the time series decomposition model, the expected daily DHW consumption of a flat of a given future month in the near future can be estimated with 94% reliability.

The same data series may be analyzed in the future by a stochastic time series analysis, or a polynomial trend might be fitted to the data instead of a linear one in the time series decomposition model. The present study did not take into account whether the building envelop had been energetically refurbished. This factor may also be researched.

Acknowledgments: The author thanks FŐTÁV Budapest Távhőszolgáltató Zrt. (Budapest District Heating Works Private Company Limited by Shares) for making the data available for research. Special thanks to Zsolt Ónodi and Csenge Dian for their useful comments on the draft of this article.

Comments: The map shown in Fig. 2 was edited using official basic data. Permit for using the data: FF/947/1/2017 by the Földművelődésügyi Minisztérium (Ministry of Agriculture). Source of further data: OpenStreetMap. The present study used the datasets of the Hungarian Meteorological Service (OMSZ). Registration number: GFO-456-2/2018, code: H/27.

Conflicts of Interest: The authors declare no conflict of interest.

References

- 7/2006. (V. 24.) TNM rendelet az épületek energetikai jellemzőinek meghatározásáról - ENG: 7/2006. (V. 24.) Decree of the Minister without Portfolio on the determination of the energy characteristics of buildings. (2006).
- Abrams, D.W., and Shedd, A.C., 1996: Effect of seasonal changes in use patterns and cold inlet water temperature on water-heating loads. United States: American Society of Heating, Refrigerating and Air-Conditioning Engineers, Inc., Atlanta, GA (United States).

- Ahmed, K., Pylsy, P., and Kurnitski, J., 2015: Monthly domestic hot water profiles for energy calculation in Finnish apartment buildings. *Energ. Build.* 97, 77–85.
<https://doi.org/10.1016/j.enbuild.2015.03.051>
- Ahmed, K., Pylsy, P., and Kurnitski, J., 2016: Hourly consumption profiles of domestic hot water for different occupant groups in dwellings. *Solar Energy* 137, 516–530.
<https://doi.org/10.1016/j.solener.2016.08.033>
- Balázs, P., Bácskay, A., Boros, J., Kemény, R., Székely, G., and Vargha, L., 2017: Ezüstkor: korosodás és társadalom. KSH, Budapest. (in Hungarian)
- Baumann, M., Csoknyai, T., Kalmár, F., Magyar, Z., Majoros, A., Osztrólczy, M., . . . Zöld, A. 2009: *Épületenergetika* (Ed. Baumann M.): Pécsi Tudományegyetem Pollack Mihály Műszaki Kar. (In Hungarian)
- Beck, H., Zimmermann, N., McVicar, T., Vergopolan, N., Berg, A., and Wood, E., 2018: Present and future Köppen-Geiger climate classification maps at 1-km resolution. *Scientific Data* 5, 180214.
<https://doi.org/10.1038/sdata.2018.214>
- Becker, B.R. and Stogsdill, K.E. (1990a). Development of a hot water use data base. Paper presented at the Annual meeting of the American Society of Heating, Refrigerating and Air-Conditioning Engineers (ASHRAE), St. Louis, Missouri, United States, 9-13 Jun 1990.
- Becker, B.R. and Stogsdill, K.E., 1990b: A Domestic Hot Water Use Database: Identifying the factors that influence domestic hot water use can help develop more efficient systems. *ASHRAE Transactions* 32(9), 21–25.
- Berza, L. 1993: *Budapest Lexikon*. Budapest: Akadémiai Kiadó. (In Hungarian)
- Birghoffer, P. and Hikisch, L. 1994: A panelos lakóépületek felújítása. Budapest: Műszaki Könyvkiadó. (In Hungarian)
- Csima, G. and Horányi, A., 2008: Validation of the ALADIN-Climate regional climate model at the Hungarian Meteorological Service. *Időjárás* 112, 155–177.
- Csoknyai, I. and Csoknyai, T., 2014: A HMV hő- és vízfogyasztás vizsgálata panelépületeknél. *Magyar Épületgépészet* 2014/6, 19–21. (In Hungarian)
- Dési, A. 1996: Panelkalauz. Budapest: Építésügyi Tájékoztatói Központ Kft. (In Hungarian)
- Dian, C., Pongrácz, R., Dezső, Z., and Bartholy, J., 2020: Annual and monthly analysis of surface urban heat island intensity with respect to the local climate zones in Budapest. *Urban Climate* 31, 100573. <https://doi.org/10.1016/j.uclim.2019.100573>
- Egyedi, L. 1963: *Épületgépészeti kézikönyv I*. Budapest: Műszaki Könyvkiadó. (In Hungarian)
- Energia Klub., 2004: Hol szökik az energia? Mit tehetünk a háztartási energiafelhasználás csökkentésért? (In Hungarian)
Retrieved from: <https://www.energiaklub.hu/dl/kiadvanyok/holszokikazenergia.pdf>
- Energiaoldal, 2012: Akár a jövedelem felét is elviszi a lakásrezsi Magyarországon. (In Hungarian)
Retrieved from <https://energiaoldal.hu/akar-a-jovedelem-felet-is-elviszi-a-lakasrezsi-magyarorszagon/>
- Energy Monitoring Company, 2008: Measurement of Domestic Hot Water Consumption in Dwellings. Retrieved from https://assets.publishing.service.gov.uk/government/uploads/system/uploads/attachment_data/file/48188/3147-measure-domestic-hot-water-consump.pdf
- Eurostat. Final energy consumption by sector. Retrieved from:
<https://ec.europa.eu/eurostat/databrowser/view/ten00124/default/table?lang=en>
- Gál, T., Bechtel, B., and Unger, J., 2015: Comparison of two different Local Climate Zone mapping methods. Paper presented at the ICUC9 - 9th International Conference on Urban Climate jointly with 12th Symposium on the Urban Environment, Toulouse, France, (20–24 July 2015).
- George, D., Pearre, N., and Swan, L., 2015: High resolution measured domestic hot water consumption of Canadian homes. *Energ. Build.* 109, 304–315.
<https://doi.org/10.1016/j.enbuild.2015.09.067>
- Gerin, O., Bleys, B., and De Cuyper, K., 2014: Seasonal variation of hot and cold water consumption in apartment buildings. Paper presented at the CIBW062 Symposium 2014, São Paulo, Brasil. (8-10 September 2014).
- Hakala, J., 2015: Energy consumption in households 2014. Retrieved from Helsinki:
https://www.stat.fi/til/asen/2014/asen_2014_2015-11-20_en.pdf
- Hobbi, A. and Siddiqui, K., 2009: Optimal design of a forced circulation solar water heating system for a residential unit in cold climate using TRNSYS. *Solar Energy* 83, 700-714.

- <https://doi.org/10.1016/j.solener.2008.10.018>
- Hong, T., Yan, D., D'Oca, S., and Chen, C.-f., 2017: Ten questions concerning occupant behavior in buildings: The big picture. *Build. Environ.* 114, 518–530.
<https://doi.org/10.1016/j.buildenv.2016.12.006>
- Horkai, A., 2019: Lakossági hideg- és melegvíz fejadagok tervezési értékeinek vizsgálata a múltban és a jelenben. *Magyar Épületgépészet 2019/7–8*, 17–21. (In Hungarian)
- Horkai, A., Khaut, N., and Nagy, Z., 2019: A Zuglói lakótelep felújítási energiapotenciál becslése. *Magyar Épületgépészet 2019/3*, 9-13. (In Hungarian)
- Horkai, A., and Kiss, G., 2019: Használatimegvíz-felhasználást befolyásoló egyéni keretfeltételek statisztikai elemzése. *Magyar Energetika 2019/5*, 6–14. (In Hungarian)
- Horváth, M., Csoknyai, T., and Szánthó, Z., 2016: Panelépületek használati melegvíz hőfelhasználásának számítása. *Magyar Épületgépészet 2016/7–8*, 8-11. (In Hungarian)
- Kajner, P., Czira, T., Selmeczi, P., and Sütő, A., 2017: National adaptation geo-information system in climate adaptation planning. *Idojaras 121*, 345–370.
- Kocsis, K. 2018: *Magyarország természeti atlasza 2. kötet. Természeti környezet*. Budapest: Magyar Tudományos Akadémia, Csillagászati és Földtudományi Kutatóközpont, Földrajztudományi Intézet. (In Hungarian)
- Kowsari, R. and Zerriffi, H., 2011: Three dimensional energy profile: A conceptual framework for assessing household energy use. *Energy Policy* 39, 7505–7517.
<https://doi.org/10.1016/j.enpol.2011.06.030>
- Központi Statisztikai Hivatal. 2014: *12. Lakásvizonyok*. Budapest: Központi Statisztikai Hivatal. (In Hungarian)
- M.Á.S.T. Piac- és Közvéleménykutató Társaság. (2004). *Összefoglaló*. Retrieved from <https://adoc.pub/sszefoglalo-keszitette-a-magyar-turizmus-rt-kutatasi-igazgat.html> (In Hungarian)
- Magyar Energetikai és Közmű-szabályozási Hivatal. Az egyes ágazatok részesedése a végső energiacélú felhasználásból. (In Hungarian) Retrieved from <http://mekh.hu/az-egy-es-agazatok-reszesedese-a-vegso-energiacelu-felhasznalaslbol?f=0>
- March, H. and Saurí, D., 2010: The Suburbanization of Water Scarcity in the Barcelona Metropolitan Region: Sociodemographic and Urban Changes Influencing Domestic Water Consumption. *The Professional Geographer* 62, 32–45. <https://doi.org/10.1080/00330120903375860>
- Menyhárt, J. 1977: *Az épületgépészet kézikönyve*. Budapest: Műszaki Könyvkiadó. (In Hungarian)
- Meyer, J., 2000: A review of domestic hot water consumption in South Africa. *Res. Develop. J.* 16, 55–61.
- NAHB Research Center, 2002: Domestic Hot Water System Modeling for the Design of Energy Efficient Systems. Retrieved from:
<https://www.homeinnovation.com/~media/Files/Reports/domestichotwater.pdf>
- Nemzeti Alkalmazkodási Térinformatikai Rendszer (NATÉR) - ENG: National Adaptation Geo-information System (NAGiS). Retrieved from <https://map.mbfisz.gov.hu/nater/>
- Otaki, Y. 2003) Residential water demand analysis by household activities. Paper presented at the 2nd International Conference on Efficient Use and Management of Water for Urban Supply, Tenerife, Canary Islands, Spain, (2–4 April 2003).
- Pérez-Lombard, L., Ortiz, J., and Pout, C., 2008: A review on buildings energy consumption information. *Energy and Buildings* 40(3), 394-398.
doi:<https://doi.org/10.1016/j.enbuild.2007.03.007>
- Perlman, M. and Mills, B.E., 1985: Development of residential hot water use patterns. *ASHRAE Transactions* 91, 657–679.
- Putzer, P., and Pavluska, V., 2013: Szakirodalmi összefoglaló az energia- és alternatív energiafogyasztás Magyarországon témakörében. (In Hungarian) Retrieved from:
https://ktk.pte.hu/sites/ktk.pte.hu/files/images/szervezet/intezetek/mti/putzer_pavluska_szakirodalmi_osszefoglalo_az_energia_es_alternativ_energiafogyasztas_magyarorszagon_temakoreben_2013.pdf
- Romano, G., Salvati, N., and Guerrini, A., 2016: An empirical analysis of the determinants of water demand in Italy. *J. Cleaner Product.* 130, 74–81.
<https://doi.org/10.1016/j.jclepro.2015.09.141>

- Sitz, L., Di Sante, F., Farneti, R., Fuentes Franco, R., Coppola, E., Mariotti, L., . . . Giorgi, F., 2017: Description and evaluation of the Earth System Regional Climate Model (RegCM-ES). *J. Adv. Modeling Earth Syst.* 9, 1863–1886. doi:<https://doi.org/10.1002/2017MS000933>
- Young, C., Davis, M., McNeill, I., Malhotra, B., Russell, S., Unsworth, K., and Clegg, C., 2013: Changing Behaviour: Successful Environmental Programmes in the Workplace. *Business Strat. the Environ.* 24. <https://doi.org/10.1002/bse.1836>

IDŐJÁRÁS

Quarterly Journal of the Hungarian Meteorological Service
Vol. 125, No. 1, January – March, 2021, pp. 83–104

Spatial and temporal variability of precipitation extreme indices in arid and semi-arid regions of Iran for the last half-century

Sadegh Karimi¹, Hamid Nazaripour^{2,*}, and Mohsen Hamidianpour²

¹ *Department of Geography*

Shahid Bahonar University of Kerman, Kerman, Iran.

² *Department of Physical Geography*

University of Sistan and Baluchestan, Zahedan, Iran.

**Corresponding author E-mail: h.nazaripour@gep.usb.ac.ir;*

(Manuscript received in final form April 15, 2020)

Abstract— Precipitation variability analysis, on different spatial and temporal scales, has been of great concern during the past century because of the attention given to global climate change by the scientific community. According to some recent studies, the Iranian territory has been experienced a precipitation variability, especially in the last 50 years, and the arid and semi-arid areas seem to be more affected. The present study aims to analyze precipitation extreme indices over a wide time interval and a wide area, detecting potential trends and assessing their significance. The investigation is based on a wide range of daily and multi-day precipitation statistics encompassing basic characteristics and heavy precipitation. Two different methods of trend analysis and statistical testing are applied, depending on the nature of the statistics. Linear regression is used for statistics with a continuous value range, and logistic regression is used for statistics with a discrete value range. The trends are calculated on annual and seasonal bases for the years 1951–2007. Statistical analysis of the database highlight that a clear trend signal is found with a high number of sites with a statistically significant trend. In winter, significant increases are found for all statistics related to precipitation strength and occurrence. In spring, statistically, significant increases are found only for the statistics related to heavy precipitation, whereas precipitation frequency and occurrence statistics show little systematic change. The trend signal is strongest in highlands and mountainous terrains. In autumn and summer, the heavy and basic precipitation statistics did not show statistically significant trends.

Key-words: trend analysis, regression, precipitation variability, precipitation extremes, APHRODITE

1. Introduction

Extreme weather events (droughts, heavy rainfall, floods, and heatwaves) are a matter of great topical importance and interest in a variety of environmental and social situations. One of the anticipated effects of climate change is the possible increase in both the frequency and intensity of extreme weather events. Heavy precipitation events are among the most disruptive of atmospheric phenomena. Changes in extreme precipitation events have significant impacts and pose serious challenges to societies, especially in arid and semi-arid environments. Such extremes are likely to have profound impacts on human societies (e.g., *Zhang et al.*, 2005) and can lead to loss of lives and property. Climate extremes, as defined by the World Meteorological Organization (WMO), are rare meteorological and climatological phenomena that surpass a defined threshold (*Das et al.*, 2003).

Understanding the mechanisms associated with extreme events at the regional scale could provide useful insights for resource planners, system managers, and policymakers to help to mitigate financial losses; therefore, comprehensive regional studies are crucial to assess the mechanisms and impacts of extreme events in a global context (*Soltani et al.*, 2016).

There are numerous regional studies of recent trends and variability in the precipitation nature over Iran (*Alijani et al.*, 2008; *Amiri and Eslamian*, 2010; *Ghahraman and Taghvaeian*, 2010; *Raziei et al.*, 2008; *Abbaspour et al.*, 2009; *Abolverdi et al.*, 2014, 2016; *Modarres and Sarhadi*, 2009; *Hasaniha and Meghdadi*, 2010; *Tabari and Talaee*, 2011a, 2011b; *Tabari et al.*, 2012; *Tabari and Aghajanloo*, 2013; *Terink et al.*, 2013; *Nazaripour and Daneshvar*, 2014; *Zhang et al.*, 2011; *Dhorde et al.*, 2014; *Darand et al.*, 2015).

However, there has been little work on precipitation related extremes in Iran. Prior research has shown changes in the frequency and intensity of precipitation extremes over the past century in Iran (*Alijani*, 2007; *Sabzevari et al.*, 2015; *Rahimzadeh et al.*, 2009; *Sohrabi et al.*, 2013; *Tabatabai and Hosseini*, 2003; *Taghavi*, 2010; *Marofi et al.*, 2011; *Dinpashoh et al.*, 2004; *Zhang et al.*, 2011; *Peterson*, 2005; *Molanejad et al.*, 2014; *Tabari et al.*, 2014). The international reports emphasized the lack of information on trends and changeability in daily climate and climate extremes (*Nicholls et al.*, 1996). Most of the studies in Iran were conducted based on monthly and yearly dataset.

Floods are the most significant natural consequences of extreme precipitations in arid and semi-arid regions. More than 80 percent of Iran's territory is located in the arid and semi-arid zone of the world. During the past 60 years (1951–2010), more than 4670 flood events have been recorded in Iran, 42 percent of them occurred in the last decade (*Molanejad and Ranjbar*, 2014). During recent decades, the arid and semi-arid regions of Iran have experienced several events of extreme precipitation conditions that have led to severe damages and fatalities.

According to a global assessment report in disaster risk reduction (UN, 2009), in the period of 1986–2007, among the flood-affected Iranian provinces, Kerman was in the second rank in terms of death per 10,000 inhabitants. Moreover, the highest number of buildings damaged or destroyed was observed in Kerman. Also, according to the Iran Water Resources Management Company report (IWRMC, 2006), in the period of 1972–1996, in terms of flood occurrence, the study area was the third most affected area with 72 events. One of the most important events in the study area was the 1993 flood event. In this flood, 211 people have been killed. These events in recent decades have raised concern that the frequency of precipitation extremes has gradually changed over the 20th century, possibly in response to global climate change.

Although the science community unanimously agrees that any changes in frequency and intensity of extreme climate events would affect significantly the natural system and human society, little information on trends and variability in daily climate and climate extremes is available (Nicholls *et al.*, 1996). Therefore, a study on extreme climate events at the watershed scale is necessary to provide useful insights for resource planners, system managers, and policymakers concerning the climate variability and the responsible operations and resource management.

This paper builds on the earlier findings for Iran by examining trends in indices for extremes of daily precipitation. Investigations of extreme events have not yet materialized for arid and semi-arid lands of Iran. In this study, we investigate long-term variations and trends of precipitation extremes during the last half-century in arid and semi-arid regions of Iran. For this purpose, daily precipitation data are analyzed from a dense network, all of which have been continuously operated since 1951. The trend analysis is based on a wide range of diagnostics, covering basic precipitation statistics and heavy precipitation events. In this study, we undertake a trend analysis for a range of diagnostics with different data characteristics. To account for the different nature of the diagnostics, we apply two different statistical methods for trend estimation and statistical testing: linear regression and a non-parametric trend test for diagnostics with continuous data (e.g., precipitation amounts) and logistic regression for discrete data (e.g., the number of events above a threshold).

2. Data and methodology

The data used in this study consisted of daily precipitation in one of the arid and semi-arid regions of Iran (see *Fig. 1*). This data are derived from the APHRODITE database, which has been launched in 2006 by the research foundation of Japan Meteorological Agency with the membership of several other countries. This database has been formed based on precipitation gauging stations of such sources as local meteorological and hydrological organizations, regional

researchers, the Global Historical Climatology Network (GHCN), the Carbon Dioxide Information Analysis Center (CDIAC), the National Center for Atmospheric Research (NCAR-DS), the National Climate Data Center (NCDC), and the Global Telecommunication System (GTS) (Yatagai et al., 2012; Hamada et al., 2011). The APHRODITE database daily gridded precipitation data for the Middle East region have been prepared with 0.5×0.5 and 0.25×0.25 resolution for the time interval 1951 to 2007.

In this study, the version V1101 of APHRODITE database in the Middle East on the daily gridded precipitation data has been utilized for one of the arid and semi-arid regions of Iran with 0.25×0.25 degree of geographical longitude/latitude resolution. In this research, extraction of daily precipitation data for the study area has been conducted by using the INPOLYGON function in MATLAB 2015b software. Thus, a sub-database has been formed with a $P_{20819 \times 268}$ structure. Study area and spatial coverage of daily precipitation network are shown in Fig. 1.

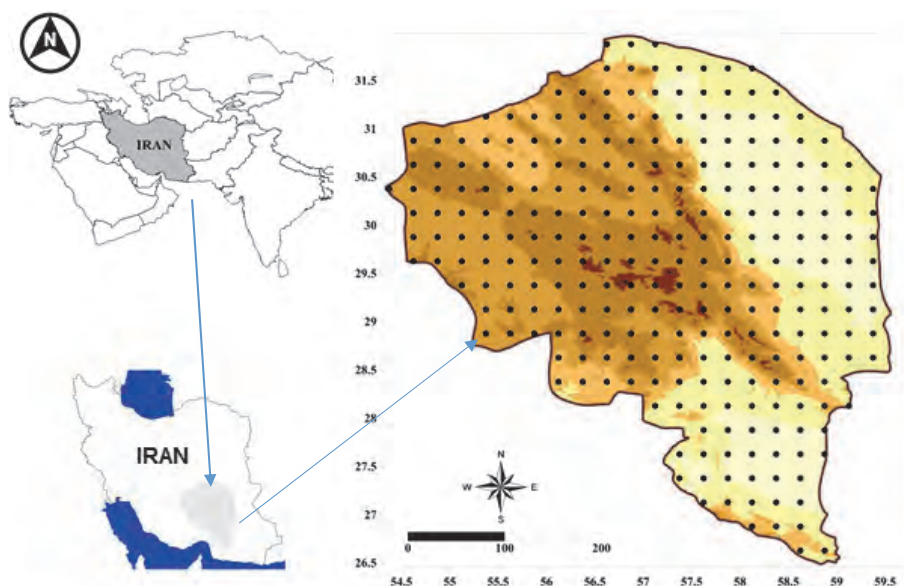


Fig. 1. Study area and database station location (0.25×0.25).

To cover long-term trends from a range of characteristics in precipitation extremes, we considered several diagnostics evaluated from time series of daily precipitation totals. Many of these diagnostics were found to be useful as a reference for comparing trend results between different regions (Nicholls and

Murray, 1999). The diagnostics will be called indices in the remainder of the paper. The set of indices is listed in *Table 1*. They are grouped into two different categories: basic and heavy precipitation indices. Category ‘basic’ is not necessarily indicative of extremes, but the wet-day frequency, mean precipitation, and wet-day intensity are useful statistics for interpretation. A threshold of 1 mm is chosen for wet days. Category ‘heavy precipitation’ encompasses several indices defined in terms of threshold exceedances. These indices are the following ones: heavy precipitation threshold (pqN), heavy precipitation days (pnlN), heavy precipitation proportion (pflN), greatest N-day precipitation (pxNd), heavy precipitation frequency (pnNmm), precipitation day frequency (wd), mean precipitation (pav) and precipitation intensity (pint), respectively based in *Table 1*. All indices are calculated individually based on STARDEX (Climate Research Unit, 2005) for the whole network, resulted in annual and seasonal time series for 1951–2007.

Table 1. List of extreme precipitation indices used in this study. The indices are grouped into two categories (from top to bottom). The last column indicates the method used to estimate the trend: linear regression (linear), logistic regression using event counts (logit.counts), and logistic regression using event probabilities (logit.probs) [8].

No.	Name (ID)	Description	Trend	Unit
1	pqN	NNth percentile of wet-day amounts (NN=90, 95)	Linear	mm/day
2	pnlN	Number of events > long-term NNth percentile (NN = 85,90)	Logit.counts	day
3	pflN	The fraction of total precipitation above long-term 90th percentile	Linear	%
4	pxNd	Maximum N-day total precipitation (N = 3,4,5)	Linear	mm
5	pnNmm	Number of events ≥ 5 mm	Logit.counts	days
6	wd	Frequency of wet days (precipitation ≥ 1 mm)	Logit.probs	days
7	pav	Precipitation average	Linear	mm/day
8	pint	Simple daily intensity (rain per rain day)	Linear	rain/wet-day

Two different methods were used to calculate trend magnitudes and to test for statistical significance, depending on the value range of the index. For indices with a continuous value range (e.g., mean precipitation and precipitation

intensity), trends were calculated with conventional linear regression. These indices are indicated by ‘linear’ in *Table 1*. The trend magnitude is then expressed as a percentage change over the 57 years relative to the 57 years mean value of the index.

Linear regression is one of the simplest methods to calculate the trend of data in time series. The equation of the linear regression line is given by $Y = a + bX$, where X is the independent variable and Y is the dependent variable. The slope line is b , and a is the intercept (value of Y when $X = 0$). The slope of regression describes whether the trend is positive or negative. In this study, Y is the precipitation and X is the year. Linear regression requires the assumption of normal distribution. In this study, the null hypothesis is that the slope of the line is zero or there is no trend in the data. The significance of the slope is shown by the probability value (P -value) of it. Microsoft Excel was used to calculate the lines and statistical values of linear regression analysis. The P -value from the analysis is the test for the significant level $\alpha = 0.05$. In the ‘linear’ case, statistical significance is assessed following the nonparametric Kendall’s tau test (*Kendall, 1970*). This is a robust, rank-based test, which, unlike the conventional Student’s t -test, does not depend on the assumption of Gaussian distributed residuals.

Kendall’s tau differs from the Spearman rank-order correlation in that it only uses the relative ordering of ranks when comparing points. It is calculated over all possible pairs of data points using the following formula:

$$\tau = \frac{\text{concordant} - \text{discordant}}{\sqrt{\text{concordant} + \text{discordant} + \text{same}X} \sqrt{\text{concordant} + \text{discordant} + \text{same}Y}}, \quad (1)$$

where *concordant* is the number of pairs where the relative ordering of X and Y are the same, *discordant* where they are the opposite, *same X* where the x values are the same, and *same Y* where the Y values are the same. τ is approximately normally distributed with zero mean and variance:

$$\text{Var}(\tau) = \frac{4N+10}{9N(N-1)}. \quad (2)$$

One advantage of Kendall’s tau over the Spearman coefficient is the problem of assigning ranks when data are tied. Kendall’s tau is only concerned whether a rank is higher or lower than the other, and, therefore, it can be calculated by comparing the data themselves rather than their rank. When data are limited to only a few discrete values, Kendall’s tau is a more suitable statistic.

For indices with a discrete value range, e.g., for counts of threshold exceedances and frequencies, we used logistic regression for trend calculation. Logistic regression is a special case of the generalization of regression techniques (see *McCullagh and Nelder, 1989*). It is appropriate for dealing with number

counts and probabilities, for which the assumptions of linear regression with uniform variance and Gaussian residuals are not satisfied. The logistic regression approach of this paper is similar to the application in *Frei and Schär (2001)*. In particular, we used the logit function as a link function and the maximum likelihood method for parameter estimation. Moreover, in the assessment of statistical significance, we corrected for overdispersion in the data series, which is an implicit account of the serial correlation in the annual series. Our calculations are based on the software MATLAB, where slightly different formal approaches are needed for counts compared with probabilities (see also *Venables and Ripley, 1997*). Indices for which trends are calculated and tested by logistic regression are labeled as *logit.counts* and *logit.probs* in *Table 1*.

Frei and Schär (2001) suggest the use of binomial distribution to model the count n of events at a particular time (e.g., the number of heavy daily precipitation in a particular summer). The probability for n events in m -independent trials (days) is given by

$$B(n; \pi, m) = \binom{m}{n} \pi^n (1 - \pi)^{m-n} \quad (3)$$

with

$$\binom{m}{n} = \frac{m!}{n!(m-n)!}, \quad (4)$$

where π is the probability of the event occurrence. The expected value $\langle n \rangle$ and variance $\text{var}(n)$ of the distribution are

$$\langle n \rangle = m\pi, \quad \text{var}(n) = m \cdot \pi \cdot (1 - \pi). \quad (5)$$

The logistic regression model expresses a transformed form of the expected value of counts (or equivalently the event probability π) as a linear of a covariate x :

$$\eta(\pi) = \alpha + \beta \cdot t, \quad (6)$$

where t is the time, α and β are the regression intercept and coefficient, respectively, to be estimated from the data. η is a prescribed link function that transfers the value range of $\pi \in [0,1]$ on to the real axis, to ensure compatibility with the linear model on the right hand side of Eq. (6). In principle, various link functions can be appropriate. Here we chose the canonical link of the logistic regression model:

$$\eta(x) = \text{logit}(x) \equiv \log\left(\frac{x}{1-x}\right). \quad (7)$$

As a result, the connection between the expected value of events and the covariate takes the form:

$$\pi(t; \alpha, \beta) = \exp(\alpha + \beta \cdot t) / [1 + \exp(\alpha + \beta \cdot t)]. \quad (8)$$

The magnitude of the trend, as given by model parameter β , is conveniently expressed as the odds ratio Θ , defined as

$$\Theta \equiv \frac{\pi(t_2)}{1-\pi(t_2)} / \frac{\pi(t_1)}{1-\pi(t_1)} = \exp[\beta \cdot (t_2 - t_1)]. \quad (9)$$

The odds ratio represents the relative change in the ratio of the events against nonevents during the period (t_1, t_2) , and it is an exponential function of the period length. In the case of rare events ($\pi \ll 1$), Eq.(5) approximates an exponential trend and the odds ratio represents the fractional change of the rare event probability from the beginning to the end of the period [$\Theta \approx \pi(t_2) / \pi(t_1)$].

The parameters α and β of logistic regression model are estimated using an S-plus implementation of the maximum likelihood method (Zarenistanak *et al.*, 2014). The statistical significance of the estimated trend parameter can be inferred from the p -value testing against the null hypothesis ($\beta = 0$). (The p -value represents the probability of accepting the null hypothesis). In our applications, p -values were obtained by using the deviance difference between the trend model and the null hypothesis as the test statistic (McCullagh and Nelder, 1989). Test results will be given for a two-tailed test with a significance level of 5%.

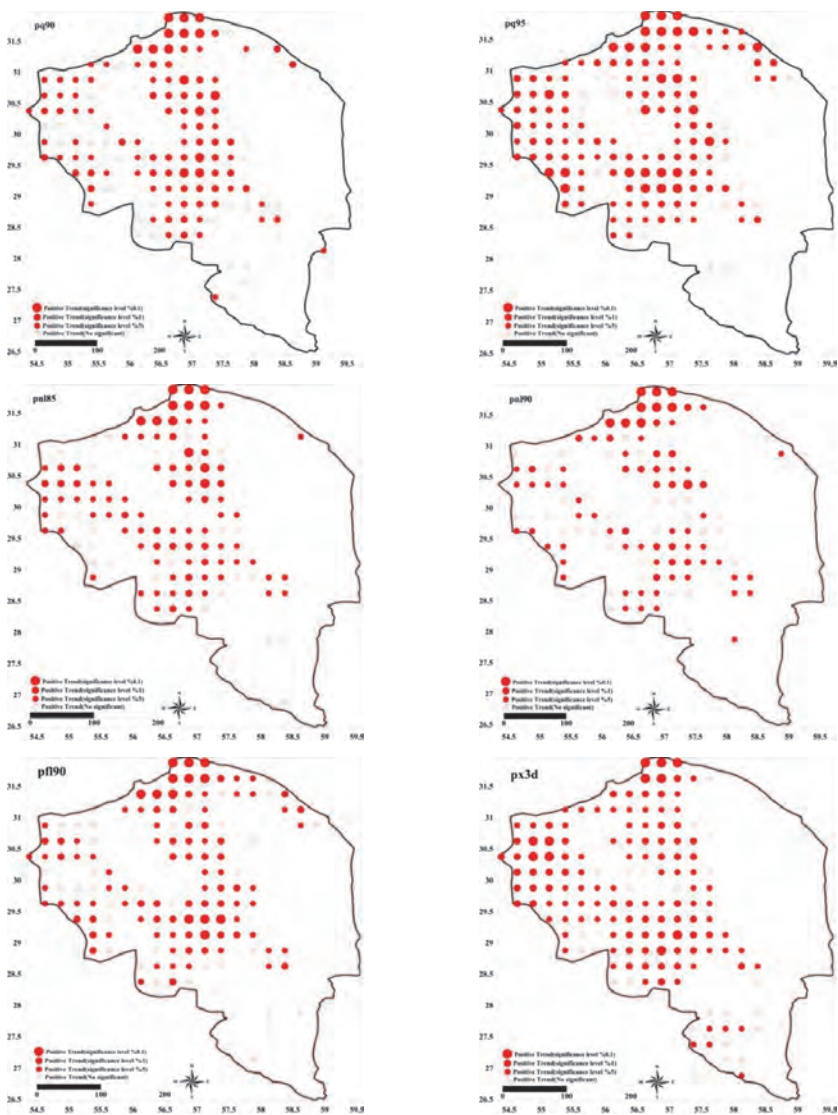
For convenience in displaying the results, the trend magnitudes derived by logistic regression are converted into relative changes over the 57 years as for linear regression. Yet it should be noted that trend magnitudes between the two regression methods are not strictly comparable. For example, the change in the probability of a threshold exceedance differs from the respective change in the threshold (e.g., Katz and Brown, 1970; Fowler and Hennessy, 1995).

3. Results and discussion

First, precipitation indices (Table 1) were calculated for spatial precipitation networks (Fig. 1) in annual and seasonal scales, the trend of which was later analyzed based on the trend estimation method (the last column in Table 1). Finally, a more precise analysis of their spatial and temporal variability during the last half-century was performed.

3.1. Annual Trend

Fig. 2 shows the spatial distribution of the results related to the annual trend for heavy precipitation group indices in the studied area. These results are presented for the first 5 indices in Table 1 as follows: (1) pq90 and pq95, (2) pn185 and pn190, (3) pf190, (4) px3d, px4d, and px5d, and (5) pn5mm. Also, the spatial distribution of the significance levels of this trend for these indices along with the base precipitation group indices are presented in Fig. 5.



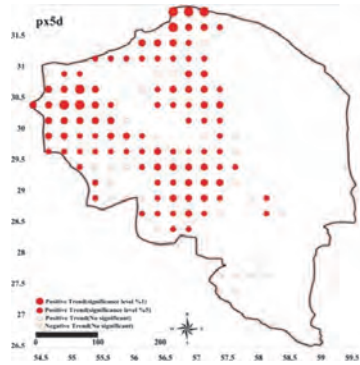
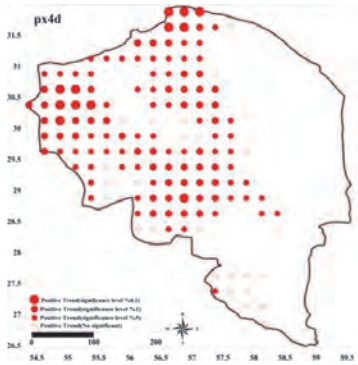
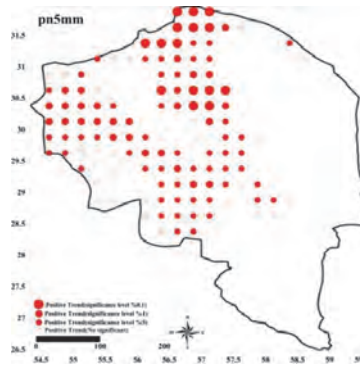


Fig. 2. Annual trends of the heavy precipitation indices. (*pq95* and *pq90*: heavy precipitation threshold; *pnl85* and *pnl90*: heavy precipitation day; *pf190*: heavy precipitation proportion; *px3d*, *px4d* and *px5d*: greatest *N*-day precipitation; *pn5mm*: heavy precipitation frequency)



In the annual scale (Fig. 2), trend analysis reveals a similar trend for all of the heavy precipitation indices. All of these indices show an evident bump for the positive-trend estimates (circles as opposed to triangles), which is significant in a large number of the network pixels (filled symbols). The greatest incremental trend is observed in the heavy precipitation frequency and threshold indices at a very high significance level (0.01%). At the high significance level (1%), indices of heavy precipitation days, heavy precipitation threshold, and maximum *n*-day precipitation had a large range. At the average significance level (5%), all the heavy precipitation indices had a large range. Thus, the incremental trend range was maximum at a 5% significance level compared with other levels. The geographical scope of the areas with the incremental trend in heavy precipitation indices matched the spatial distribution of the uneven areas (Fig. 4). Therefore, considering the characteristics of mountainous areas such as high slope and low permeability, the probability of increasing floods and their future effects is increased.

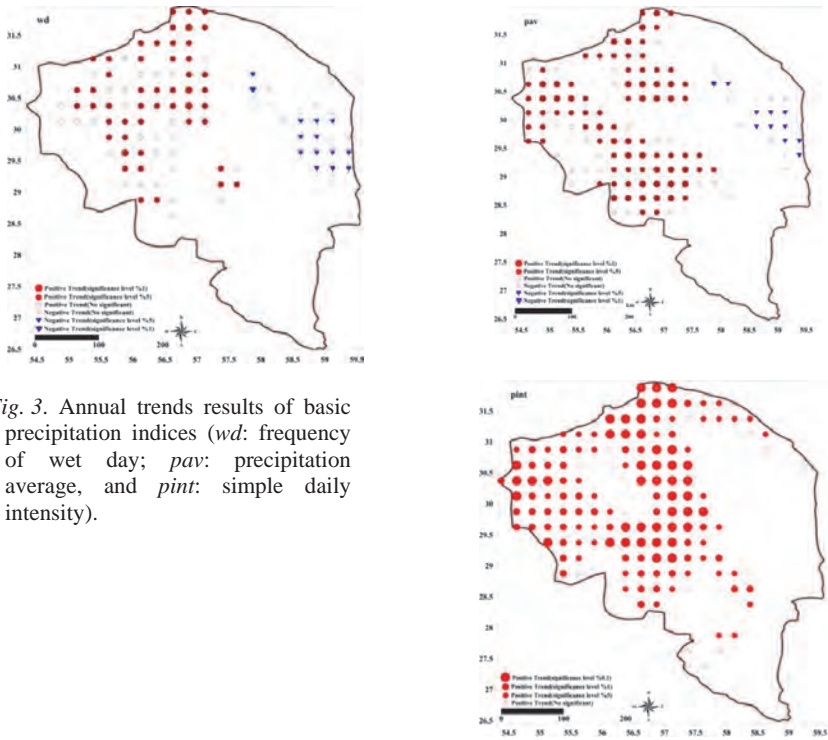


Fig. 3. Annual trends results of basic precipitation indices (*wd*: frequency of wet day; *pav*: precipitation average, and *pint*: simple daily intensity).

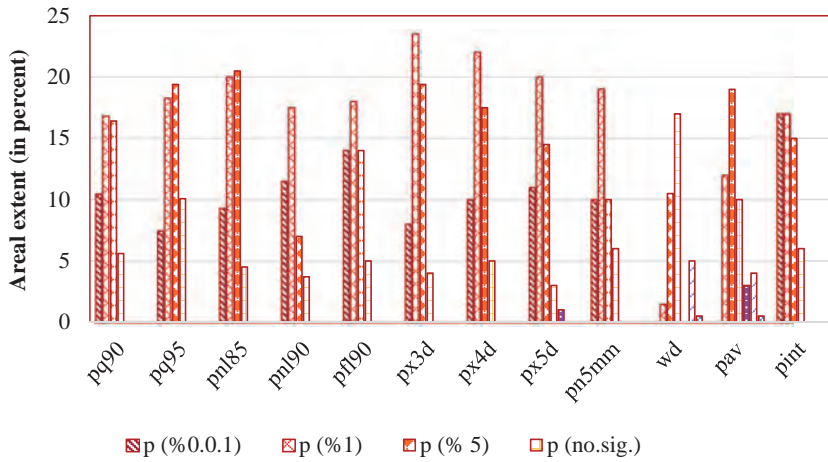


Fig. 4. The areal extent of statistical significance levels in the annual trend of heavy and basic precipitation indices (p and n are respectively positive and negative trend symbols).

3.2. Seasonal trend

Fig. 5 demonstrates the spatial distribution of seasonal precipitation for a long period in the studied area. The precipitation regime was of winter and spring nature in the studied area. In other words, winter and spring had maximum share in supplying the annual precipitation. Thus, probable changes in the indices of heavy and base precipitation groups were investigated for these two seasons (Nazaripour and Daneshvar, 2017).

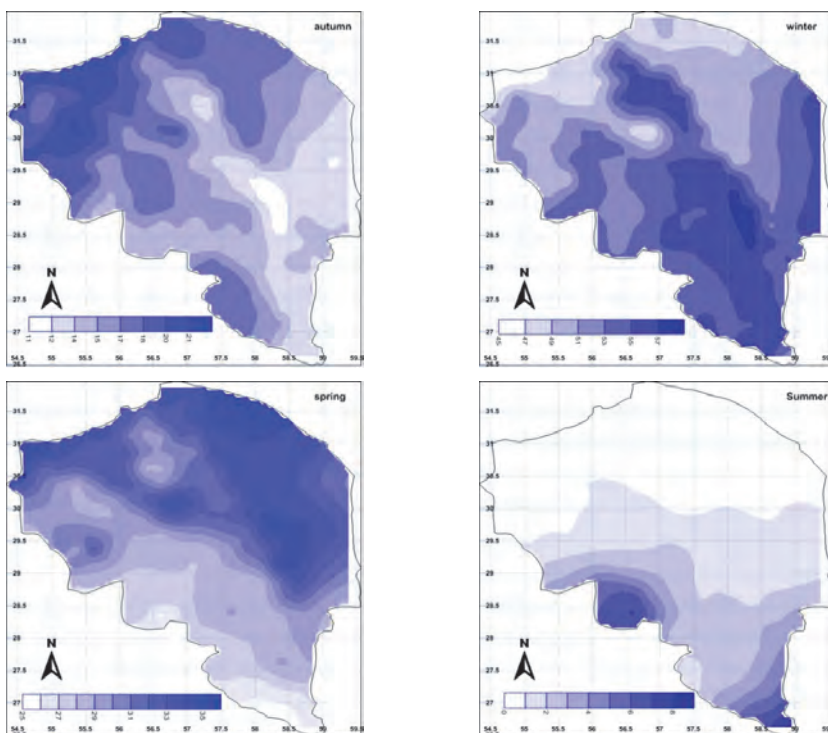
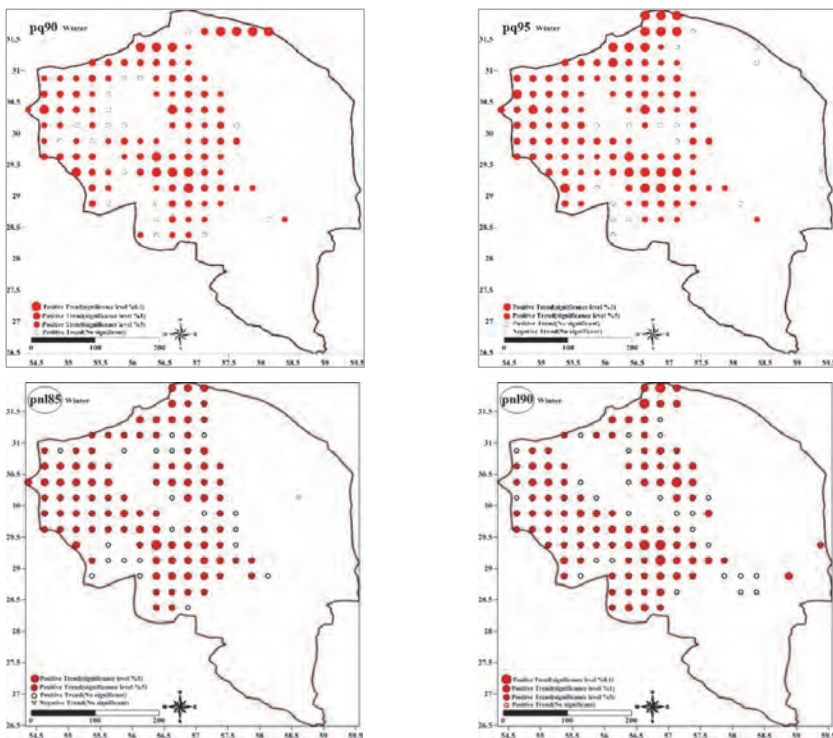


Fig. 5. Spatial distribution of seasonal precipitation in the study area, that was obtained by surface interpolation (kriging method) of the long-term mean of seasonal precipitation.

Fig. 6 shows the results of the trend for the heavy precipitation indices in winter for the studied area. The trend analysis found a similar trend for all of the heavy precipitation indices in winter. Results of the statistical and spatial trend analysis represented a clear positive trend with statistical significance in a large

part of the studied area. The geographical scope of the regions with a trend in winter was in full agreement with the annual scale. In other words, the variability of heavy precipitation indices was associated with winter as the region with maximum precipitation. The geographical scope of the areas with the incremental trend in heavy precipitation indices matched the spatial distribution of uneven areas. The largest scope of very high statistical significance (0.01%) in heavy precipitation indices associated with winter was observed in the greatest n-day precipitation indices and heavy precipitation ratio. At a high significance level (1%), the scope of each heavy precipitation indices was high. At the medium significant level (5%), heavy precipitation threshold indices, heavy precipitation days, and the greatest n-day precipitation had a large scope. The spatial range of the statistical insignificance level was minimum compared with the other levels (Fig. 8). More precise analysis of the spatial distribution of significance levels related to the incremental trend in the heavy precipitation indices showed that the incremental trend of these indices was very significant in winter.



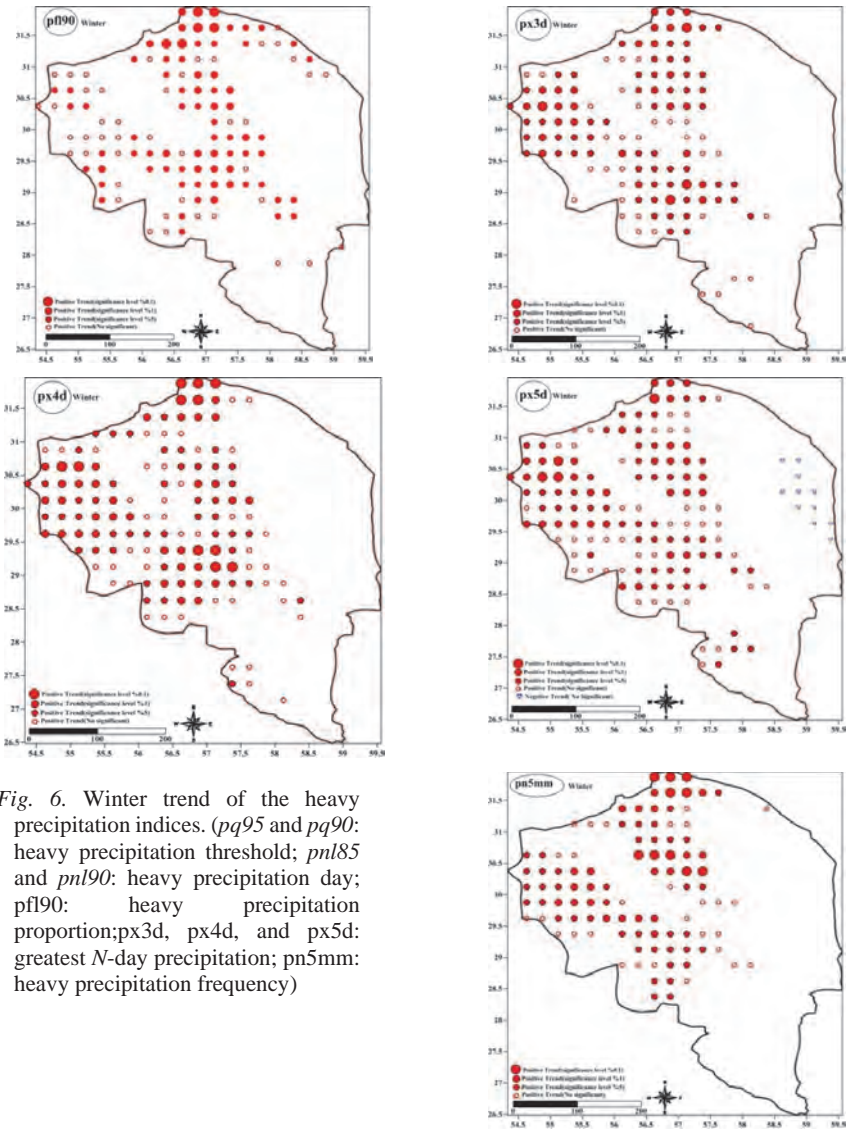


Fig. 6. Winter trend of the heavy precipitation indices. (pq95 and pq90: heavy precipitation threshold; p0185 and p0190: heavy precipitation day; p0190: heavy precipitation proportion; px3d, px4d, and px5d: greatest N-day precipitation; pn5mm: heavy precipitation frequency)

Fig. 7 shows the trend of the base precipitation group indices for winter. Similar to the annual scale, the precipitation intensity index showed a clear bump in the incremental trend. The maximum spatial scope for the precipitation intensity index was at average, high, and very high significance levels,

respectively. Conversely, the two other indices of the base precipitation group did not show the same trend. A significant incremental trend in the relatively large spatial scope was observed in rainy days and average precipitation indices, which was limited to the eastern part of the studied area. On the other hand, a decremental trend was observed at the average significance level in these indices. The spatial range of this decremental trend was limited to two areas. One was the eastern half situated on the edge of Dasht-e Lut desert and the other was located on the southern corner in Jazmurian wetland, both of which had very low precipitation.

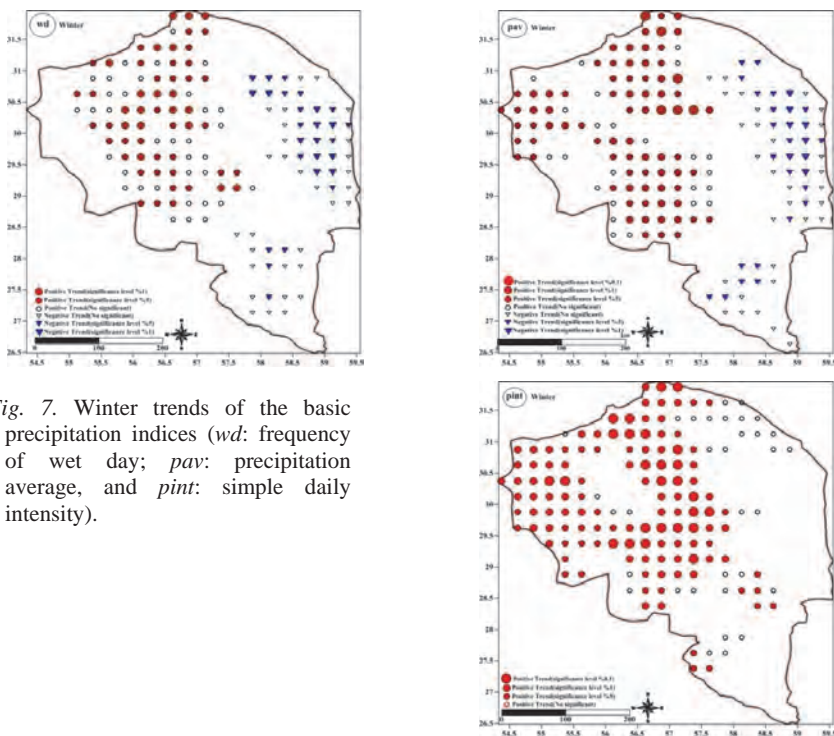


Fig. 7. Winter trends of the basic precipitation indices (*wd*: frequency of wet day; *pav*: precipitation average, and *pint*: simple daily intensity).

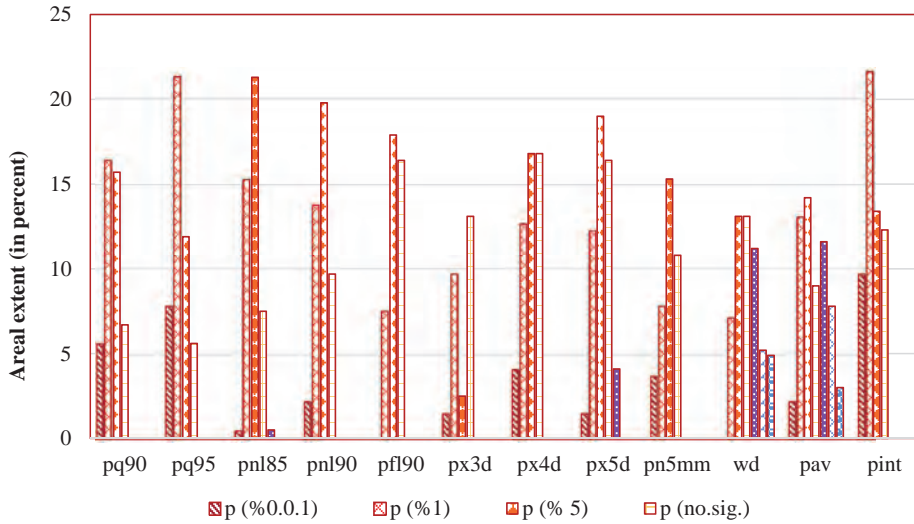


Fig. 8. The areal extent of statistical significance levels in the winter trend of heavy and basic precipitation indices (p and n are respectively positive and negative trend symbols).

Fig. 9. shows the trend of the heavy precipitation group indices in spring. Unlike the annual scale and winter, the only indices that had a trend were heavy precipitation threshold, heavy precipitation days, and heavy precipitation ratio, the trends of which were not the same. Results of statistical and trend analyses indicated an incremental trend in the northern half and a decremental one in the southern half of the studied area. The spatial range of the incremental trend was more than that of the decremental one. Nevertheless, the trends were not highly significant (Fig. 11). Temporal and spatial variability in spring compared with winter could justify the lack of spatial uniformity in the trend. In contrast to winter, the maximum precipitation of spring was limited to the northern half of the studied area. Thus, the incremental trend of heavy precipitation indices in spring matched the maximum spatial distribution of precipitation in this season.

Fig. 10 represents the trend of base precipitation indices for spring. The average precipitation index showed a clear trend in the northern half of the studied area, the highest scope of which was located in the eastern part of the area and the edge of Dasht-e Lut. Rainy day index had an incremental trend as well, but it was less statistically and spatially significant. Also, precipitation intensity index was less statistically and spatially significant in the studied area.

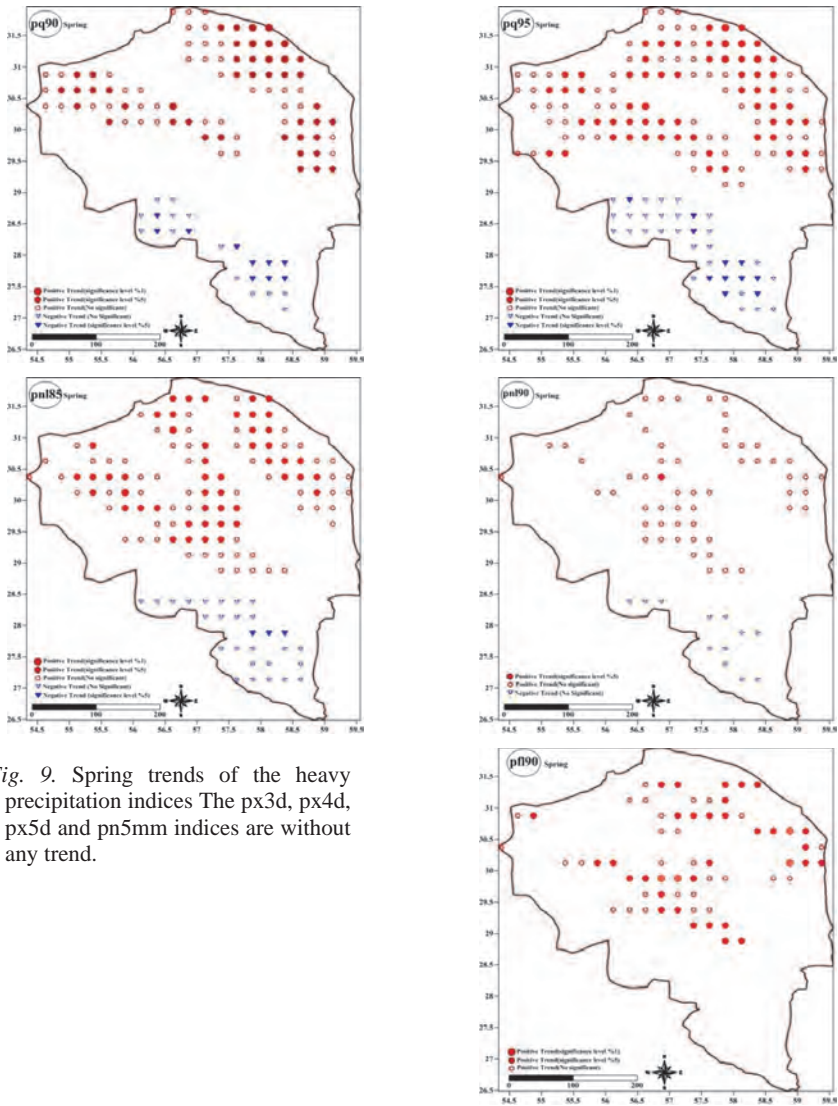


Fig. 9. Spring trends of the heavy precipitation indices The px3d, px4d, px5d and pn5mm indices are without any trend.

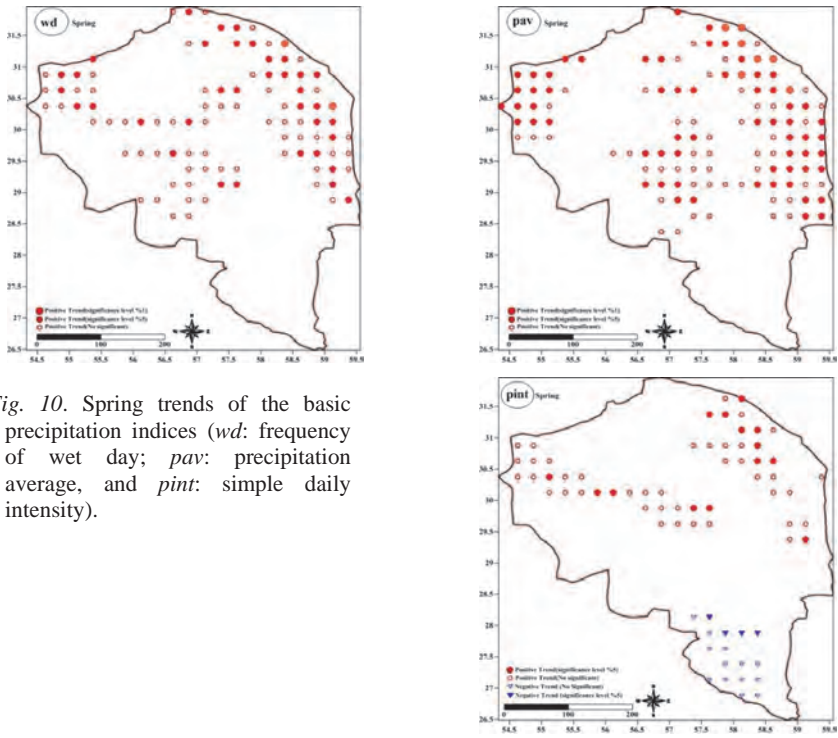


Fig. 10. Spring trends of the basic precipitation indices (*wd*: frequency of wet day; *pav*: precipitation average, and *pint*: simple daily intensity).

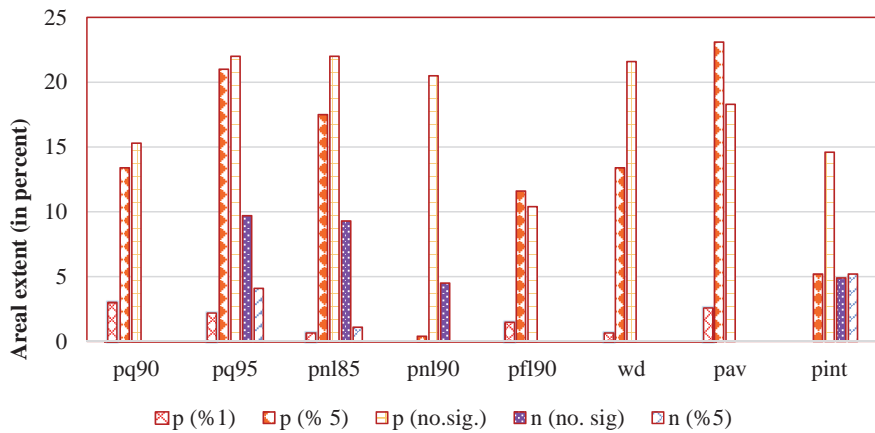


Fig. 11. As Fig. 8, but for spring. The areal extent of statistical significance levels in the spring trend of heavy and basic precipitation indices (p and n are respectively positive and negative trend symbols).

4. Conclusions

In this study, we have analyzed daily precipitation data from the dense network in one of the arid and semi-arid regions of Iran for trends in daily precipitation statistics over the last half-century. The statistics encompass basic characteristics and measures of heavy precipitation. Two different methods of trend analysis and statistical assessment were applied, depending on the data nature of the indices. Our analysis has identified spatially coherent and statistically significant trends for most statistics related to the heavy precipitation category.

In the annual scale, a statistically significant and spatially coherent incremental trend was observed for all the indices of heavy precipitation groups as well as the precipitation intensity index. The strong statistical significance of the incremental trend was more prominent in the indices related to the highlands and the studied mountainous area. These indices in the lowlands including the marginal land of the Dasht-e Lut desert in the east and the south-east desert of Jazmurian wetland in the studied area lacked any trend. The incremental trend of the heavy precipitation indices was considered a climatic warning in the high and mountainous lands, which are flood-prone. There was also an incremental trend, both statistically and spatially, in heavy precipitation indices of winter and spring, which was the same as the annual scale. However, there were differences in the statistical and spatial characteristics between the two seasons. In winter, an almost identical change was found in each heavy precipitation group indices as well as in the precipitation intensity index of the base precipitation group. However, in spring, the situation was more complicated. Here, there was variability in some indices of the heavy precipitation category including heavy precipitation threshold, heavy precipitation days, and heavy precipitation ratio. The variability of spring indices was not statistically and spatially significant. In other words, a large volume of the annual variation of heavy variability indices could be explained by the winter season. In autumn and summer, the heavy precipitation indices did not show statistically significant trends, and there was no evidence for long-term trends in the statistics related to the basic precipitation category.

References

- Abbaspour, K.C., Faramarzi, M., Ghasemi, S.S., and Yang, H., 2009: Assessing the impact of climate change on water resources in Iran. *Water Resour. Res.* 45, W10434. <https://doi.org/10.1029/2008WR007615>
- Abolverdi, J., Ferdosifar, G., Khalili, D., and Kamgar-Haghighi, A.A., 2016: Spatial and temporal changes of precipitation concentration in Fars province, southwestern Iran. *Meteorol. Atmosph. Phys* 128, 181–196. <https://doi.org/10.1007/s00703-015-0414-0>
- Abolverdi, J., Ferdosifar, G., Khalili, D., Kamgar-Haghighi, A.A., and Haghighi, M.A., 2014: Recent trends in regional air temperature and precipitation and links to global climate change in the Maharlo watershed, Southwestern Iran. *Meteorol. Atmosph. Phys* 126, 177–192. <https://doi.org/10.1007/s00703-014-0341-5>

- Alijani B., 2007: Time series analysis of daily rainfall variability and extreme events. 10th International Meeting on Statistical Climatology, Beijing, China.
- Alijani, B., O'Brien, J., and Yarnal, B., 2008: Spatial analysis of precipitation intensity and concentration in Iran. *Theor. Appl. Climatol.* 94, 107–124.
<https://doi.org/10.1007/s00704-007-0344-y>
- Amiri, M.J. and Eslamian, S.S., 2010: Investigation of climate change in Iran. *J Environ Sci Technol*, 3, 208–216. <https://doi.org/10.3923/jest.2010.208.216>
- Climatic Research Unit, 2005: STARDEX: Statistical and Regional dynamical Downscaling of Extremes for European regions [Internet]. Climatic Research Unit; [cited 2011 Sep 9]. Available from: <http://www.cru.uea.ac.uk/projects/star-dex/>
- Darand, M., Nazari-pour, H., and Daneshvar, M.M., 2015: Spatial and temporal trend analysis of temperature extremes based on Iranian climatic database (1962–2004). *Arabian J. Geosci.* 8, 8469–8480. <https://doi.org/10.1007/s12517-015-1840-5>
- Das, H.P., Adamenko, T.I., Anaman, K.A., Gommès, R.G., and Johnson, G., 2003: Agrometeorology related to extreme events. World Meteorological Organization, Technical Note No 201.
- Dhorde, A.G., Zarenistanak, M., Kripalani, R.H., and Preethi, B., 2014: Precipitation analysis over southwest Iran: trends and projections. *Meteorol. Atmosph. Phys.* 124, 205–216.
<https://doi.org/10.1007/s00703-014-0313-9>
- Dinpashoh, Y., Fakheri-Fard, A., Moghaddam, M., Jahanbakhsh, S., and Mirnia, M., 2004: Selection of variables for the purpose of regionalization of Iran's precipitation climate using multivariate methods. *J. Hydrol.* 297, 109–123. <https://doi.org/10.1016/j.jhydrol.2004.04.009>
- Fowler, A.M. and Hennessy, K.J., 1995: Potential impacts of global warming on the frequency and magnitude of heavy precipitation. *Nat. Hazards* 11, 282–303.
<https://doi.org/10.1007/BF00613411>
- Frei, C. and Schär, C., 2001: Detection probability of trends in rare events: theory and application of heavy precipitation in the Alpine region. *J. Climate* 14, 1568–1584.
[https://doi.org/10.1175/1520-0442\(2001\)014<1568:DPOTIR>2.0.CO;2](https://doi.org/10.1175/1520-0442(2001)014<1568:DPOTIR>2.0.CO;2)
- Ghahraman, B. and Taghvaeian, S., 2010: Investigation of annual rainfall trends in Iran. *J. Agric. Scie. Technol.* 10, 93–97.
- Hamada, A., Arakawa, O., and Yatagai, A., 2011: An automated quality control method for daily rain-gauge data. *Glob. Environ. Res.* 15, 183–192.
- Hasaniha, H.A. and Meghdadi, M., (2010): The Analysis of Spring Precipitation in Semi-Arid Regions: Case Study in Iran. *J. Water Res. Protect.* 2, 69.
<https://doi.org/10.4236/iwarp.2010.21008>
- IWRMC, 2006: Draft of Flood damage assessment, Bulletin A. 296, Ministry of Energy. (In Persian)
- Katz, R.W. and Brown, B.G., 1992: Extreme events in a changing climate: variability is more important than averages. *Climatic Change* 21, 289–302.
<https://doi.org/10.1007/BF00139728>
- Kendall, M.G., 1970: Rank Correlation Methods, 4th edn. London: Griffin.
- Marofi, S., Sohrabi, M.M., Mohammadi, K., Sabziparvar, A.A., and Abyaneh, H.Z., 2011: Investigation of meteorological extreme events over coastal regions of Iran. *Theor. Appl. Climatol.* 103, 401–412. <https://doi.org/10.1007/s00704-010-0298-3>
- McCullagh, P. and Nelder, J.A., 1989: Generalized Linear Models. Monographs on Statistics and Applied Probability, 37, 2nd edn. Chapman and Hall: London.
- Modarres, R. and Sarhadi, A., 2009: Rainfall trends analysis of Iran in the last half of the twentieth century. *J. Geophys. Res.: Atmosph.* (1984–2012), 114(D3).
<https://doi.org/10.1029/2008JD010707>
- Molanejad, M. and Ranjbar, A., 2014: Climatic Extreme Events over Iran: Observation and Future Projection, 3 rd Meeting of COMSATS' International Thematic Research Group on 'Climate Change and Environmental Protection, Islamabad, Pakistan.
- Molanejad, M., Soltani, M., and Ranjbar, A., 2014: Changes in precipitation extremes in climate variability over northwest Iran. *Int. J. Agric. Policy. Res.* 2, 334–345.
- Nazari-pour, H., and Daneshvar, M.M., 2014. Spatial contribution of one-day precipitations variability to rainy days and rainfall amounts in Iran. *Int. J. Environ. Sci. Technol.* 11, 1751–1758.
<https://doi.org/10.1007/s13762-014-0616-x>

- Nazaripour, H., & Daneshvar, M. R. M. 2017. Rain gauge network evaluation and optimal design using spatial correlation approach in arid and semi-arid regions of Iran. *Theoretical and Applied Climatology*, 129(3), 1255-1261.
- Nicholls, N. and Murray, W., 1999: Workshop on indices and indicators for climatic extremes: Asheville, NC, USA, 3–6 June 1997 Breakout Group B: precipitation. *Climatic change* 42: 23–29. https://doi.org/10.1007/978-94-015-9265-9_4
- Nicholls, M., Gruza, G.W., Jouzel, J., Karl, T.R., Ogallo, L.A., and Parker, D.E., 1996: Chapter 3, observed climate variability and change., In: *Climate change 1995: the science of climate change. Contribution to Working Group I to IPCC SAR.* (eds.: J.T. Houghton et al.) Cambridge Univ. Press, 137–192.
- Peterson, T.C., 2005: The workshop on enhancing south and central Asian climate monitoring and indices, Pune, India, February 14–19, 2005. *CLIVAR Exch.* 10(6).
- Rahimzadeh, F., Asgari, A., and Fattahi, E., 2009: Variability of extreme temperature and precipitation in Iran during recent decades. *Int. J. Climatol.* 29, 329–343. <https://doi.org/10.1002/joc.1739>
- Raziei, T., Bordi, I., and Pereira, L.S., 2008: A precipitation-based regionalization for eastern Iran and regional drought variability. *Hydrol. Earth Syst. Sci.* 12, 1309–1321. <https://doi.org/10.5194/hess-12-1309-2008>
- Sabzevari, A.A., Zarenistanak, M., Tabari, H., and Moghimi, S., 2015: Evaluation of precipitation and river discharge variations over southwestern Iran during recent decades. *J. Earth Syst. Sci.* 124, 335–352. <https://doi.org/10.1007/s12040-015-0549-x>
- Sohrabi, M.M., Ryu, J.H., and Alijani, B., 2013: Spatial and temporal analysis of climatic extremes over the mountainous regions of Iran. *Int Climate Change* 4(4), 19–36. <https://doi.org/10.18848/1835-7156/CGP/v04i04/37183>
- Soltani, M., Laux, P., Kunstmann, H., Stan, K., Sohrabi, M.M., Molanejad, M., Sabziparvarm A.A., Ranjbar SaadatAbadi, A., Ranjbar, F., Rosta, I., Zavar-Reza, P., Khoshakhlagh, F., Soltanzadeh, I., Babu, C.A., Azizi, G.H., and Martin, M.V., 2016: Assessment of climate variations in temperature and precipitation extreme events over Iran. *Theor. Appl. Climatol.*, 126, 775–795. <https://doi.org/10.1007/s00704-015-1609-5>
- Tabari, H. and Talaee, P.H., 2011a: Analysis of trends in temperature data in arid and semi-arid regions of Iran. *Glob. Planetary Change*, 79, 1–10. <https://doi.org/10.1016/j.gloplacha.2011.07.008>
- Tabari, H. and Talaee, P.H., 2011b: Temporal variability of precipitation over Iran: 1966–2005. *J. Hydrol.* 396, 313–320. <https://doi.org/10.1016/j.jhydrol.2010.11.034>
- Tabari, H., Abghari, H., Tabari, H., and Talaee, P.H., Hosseinzadeh Talaee, P., 2012: Temporal trends and spatial characteristics of drought and rainfall in arid and semiarid regions of Iran. *Hydrol. Process.* 26, 3351–3361. <https://doi.org/10.1002/hyp.8460>
- Tabari, H. and Aghajanloo, M.B., 2013: Temporal pattern of aridity index in Iran with considering precipitation and evapotranspiration trends. *Int. J. Climatol.* 33, 396–409. <https://doi.org/10.1002/joc.3432>
- Tabari, H., AghaKouchak, A., and Willems, P., 2014: A perturbation approach for assessing trends in precipitation extremes across Iran. *J. Hydrol.* 519, 1420–1427.
- Tabatabai, A. and Hosseini, M., 2003: Investigation of climate change in Semnan city by using monthly precipitation and averaged monthly temperature (in Persian). Bureau of Meteorology of Semnan province, Third Regional and National Conference of Climate Change in Isfahan, 91–98.
- Taghavi, F., 2010: Linkage between climate change and extreme events in Iran. *J. Earth Space Physics* 36(2), 33–43.
- Terink, W., Immerzeel, W. W., and Droogers, P., 2013: Climate change projections of precipitation and reference evapotranspiration for the Middle East and Northern Africa until 2050. *Int. J. Climatol.* 33, 3055–3072. <https://doi.org/10.1002/joc.3650>
- UN, 2009: Global Assessment Report on Disaster Risk Reduction. United Nations, Geneva, Switzerland. <http://www.preventionweb.net/english/hyogo/gar/report/>.
- Venables, W.N. and Ripley, B.D., 1997: Introduction. In: *Modern Applied Statistics with S-PLUS.* Springer New York. 1–18. https://doi.org/10.1007/978-1-4757-2719-7_1

- Yatagai, A., Kamiguchi, K., Arakawa, O., Hamada, A., Yasutomi, N., and Kitoh, A., 2012: APHRODITE: Constructing a long-term daily gridded precipitation dataset for Asia based on a dense network of rain gauges. *Bull. Amer. Meteorol. Soc.* 93, 1401–1415. <https://doi.org/10.1175/BAMS-D-11-00122.1>
- Zarenistanak, M., Dhorde, A.G., and Kripalani, R.H., 2014: Trend analysis and change point detection of annual and seasonal precipitation and temperature series over southwest Iran. *J. Earth Syst. Sci.* 123, 281–295. <https://doi.org/10.1007/s12040-013-0395-7>
- Zhang, X., Aguilar, E., Sensoy, S., Melkonyan, H., Tagiyeva, U., Ahmed, N., Kotaladze, N., Rahimzadeh, F., Taghipour, A., Hantosh, T.H., Albert, P., Semawi, M., Karam Ali, M., Halal Said Al-Shabibi, M., Al-Oulan, Z., Zatari, T., Al Dean Khelet, I., Hammoud, S., Sagir, R., Demircan, M., Eken, M., Adiguzel, M., Alexander, L., Peterson, T.C., and Wallis, T., 2005: Trends in Middle East climate extremes indices during 1930-2003. *J. Geophys. Res.* 110 (D22), 104. <http://dx.doi.org/10.1029/2005JD006181>
- Zhang, X., L. Alexander, G. C. Hegerl, P. Jones, A. K. Tank, T. C. Peterson, B. Trewin, and F. W. Zwiers, 2011: Indices for monitoring changes in extremes based on daily temperature and precipitation data, *Wiley Interdiscip. Rev. Clim. Change*, 2, 851–870. <https://doi.org/10.1002/wcc.147>

IDŐJÁRÁS

Quarterly Journal of the Hungarian Meteorological Service
Vol. 125, No. 1, January – March, 2021, pp. 105–122

Soil-specific drought sensitivity of Hungarian terroirs based on yield reactions of arable crops

Mihály Kocsis^{1*}, Attila Dunai², János Mészáros³, Zoltán Magyar¹
and András Makó^{1,4}

¹*Department of Environmental Sustainability*
Hungarian University of Agriculture and Life Sciences, Institute for Environmental Sciences
Georgikon Campus
Deák Ferenc utca 16., H-8360, Keszthely, Hungary

²*Department of Agronomy*
Hungarian University of Agriculture and Life Sciences, Institute of Agronomy
Georgikon Campus
Festetics út 7., H-8360, Keszthely, Hungary

³*Department of Soil Mapping and Environmental Informatics*
Institute for Soil Sciences and Agricultural Chemistry
Centre for Agricultural Research
Herman Ottó út 15., H-1022, Budapest, Hungary

⁴*Department of Soil Physics and Water Management*
Institute for Soil Sciences and Agricultural Chemistry
Centre for Agricultural Research
Herman Ottó út 15., H-1022, Budapest, Hungary

*Corresponding author E-mail: kocsis.mihaly@uni-mate.hu

(Manuscript received in final form April 20, 2020)

Abstract—The hypothetical climate change and the stress influences caused by the increasingly frequent found meteorological extremities affect the fertility of soils in even more degree. During our soil-climate sensitivity researches, the expression of the drought sensitivity as a stress influence, evolved as a result of lack of precipitation in soil fertility was studied. During our work, effects of increasing droughts of last decades were investigated through the yield results of the three most important crops, winter wheat (*Triticum aestivum* L.), corn (*Zea mays* L.), and sunflower (*Helianthus annuus* L.), based on the area rate in the Hungarian sowing structure, in relation to the natural geographical microregions and fertility of sites. For the examinations, yield data of the National Pedological and Crop Production Database (NPCPD) were used. The database contains complex plot-level crop production and soil information for 5 years (1985–1989). The examination results prove the considerable drought sensitivity of that lands, where soil types with high sand or clay content can be found. The mainly exposed microregions for the effects of drought are, e.g., the Dorozsma-Majsa Sand Ridge, Kerka Riverscape, Dévaványa Plain etc., while less sensitive sites are e.g. the Enying Ridge, Tolnai-Sárköz, Nógrád Basin etc.

Key-words: physical geography microregion, soil-specific drought sensitivity, soil variation, yield, NPCPD ver3.0 database

1. Introduction

The increasing climatic anomalies (extreme precipitation distributions, decreases in annual or seasonal precipitation, and increases in average temperature) resulted in the increase of fluctuation of yields (Pepó, 2005). The extreme meteorological situations (Patrick, 2002; Szász, 2005) can be considered as natural stress effects affected on soils. Birkás *et al.* (2007) considered the stress evolved in soils due to the climate change and the effect-specific replies given to this as the „climate sensitivity” of soils. According to Nagy (2005), the evaporation in the plant-soil water management system under semiarid climate circumstances is continuous throughout the growing season, but as a result of climate variability, the distribution of precipitation is not uniform in space and time. The biomass production of soil is highly depended on the water providing ability and water supply, so the water storage characteristics of soils play more and more significant role (Rajkai, 2004).

Máté *et al.* (2009) studied the shifting and changing of Hungarian soil zones occurred as a result of climate change with the help of 120-year-long (1881–2000) data queues of 16 meteorological stations disassembled to 30-year intervals. According to the results, the Atlantic and Mediterranean climatic effects were increased periodically but verifiably both by chernozem and brown forest soils, at the same time, the continental effect was dramatically decreased, especially by chernozem soils. The study concludes that climate, as an important soil-forming factor, is slowly changing the soil types and also the individual soil characteristics.

Csorba *et al.* (2012) developed 18 mesoregions with the merging of the Hungarian physical geography mesoregions, then investigated the potential future effects of climate change on different meteorological and environmental indicators (drought, inundation, inland water, water erosion, wind erosion, etc.) (Pálfai and Herceg, 2011; Van Leeuwen *et al.*, 2008; Rakonczai, 2011). According to the results it can be concluded, that the expectable change will certainly affects humid habitats (e.g., marsh forests, moss and peat bogs, saline lakes, wet meadows, floodplain forests). In crop production, the drought stress evolved as a result of more and more frequently occurred water deficit and heat-waves resulted in significant yield losses (Ladányi *et al.*, 2014).

The evolution of climatic relations was well supported by the results of Rácz (1999). According to his county-scale research, the amount of winter- (from the first half of the 1900s), spring- and autumn- (from the 1950s), and summer- (from the 1980s) precipitation was progressively decreased. From 1983, the seriously drought-damaging areas have been expanding from east and southeast directions towards north and west (Bocz, 1995). In the 1981–2000 period, the amount of drought seasons were doubled (increased by 52.6%) on the account of the average seasons (26.3%) (Pepó, 2007).

One of the most well-known consequences of extreme warm and low rainfall is the development of drought, which is a complex phenomenon and has many definitions. Meteorological drought is defined as periods of abnormally low rainfall (Molnár and Gácsér, 2014). Lack of rainfall, mainly during the vegetation period, affects natural vegetation (forests, meadows) and crop yields. Gyuricza (2007) distinguishes three different forms of drought (atmospheric, physiological and soil droughts). The soil drought, as the most harmful form of droughts evolves when the moisture content of soils was limited to the unavailable water content only. In this case, there are not enough water in the soil for plants. The „soil drought sensitivity” is when certain functions of soils (e.g., water storage and water supplying ability) cannot provide their work as a result of drought periods or considerable lack of precipitation. In crop production it is resulted yield fluctuation (t/ha) (decreasing or, under extreme circumstances, total yield deficit) in different extent in different crops, which expresses in the decreasing of soil productivity.

For the quantification of soil-climatic interactions, the possibilities are limited. With indirect methods, it is possible to conclude to the soil component of the crop fluctuation caused by the climate using multiannual meteorological and yield data registered by different soil parameters. But, in fact, the crop fluctuation caused by the climate has other components also (e.g., phytopathological, physiological); and between the years, there are not only meteorological differences (e.g., differences between the varieties of plants, agricultural game damage, tillage failures, etc.) (Jolánkai, 2005; Pepó, 2005). Kismányoky (2005) estimated a 0.7/0.3 average soil/climate effect ratio determining the amount of yield.

Késmárki *et al.* (2005) studied the impacts of climate change on the yields of winter wheat, corn and alfalfa in the case of carbonated Danube Fluvisols, near Mosonmagyaróvár, Hungary. According to results, the length of vegetation period has a positive effect on the yield in case of different corn varieties, independently of the seasonal effects, and the soil drought-decreasing role of the subsoil water content. Varga-Haszonits and Varga (2005) investigated the relationship of the climate and yield of corn in Western Hungary. However, the analysis based on the data queues of meteorological stations and the data of Hungarian Central Statistical Office were not suitable to the accurate assessment of the climate impacts in case of different soil varieties, but they can be used as useful information on the climate sensitivity of the western-Hungarian forest soils. The authors concluded that in the examined area – which is the most humid area in Hungary –, primarily the moisture supply plays a significant role in formation of yield. A weak relationship was found between the length of the vegetation period and yield, which is – according to the authors – referring to the secondary role of the thermic factors in the formation of yield. The moisture

conditions were described with a „precipitation-evaporation index” and the yield-decreasing impact of the excessive high and low water supply were presented by an optimum curve.

Harnos N. (2003) and *Harnos Zs.* (2005) investigated the effects of global climate change on the production of winter wheat using simulation models validated by almost 30 years meteorological and yield data of Győr-Moson-Sopron and Hajdú-Bihar counties. According to the results, it can be stated, that even 20% of yield decreasing can occur in the case of the investigated climate change scenarios. *Jolánkai et al.* (2003) investigated climatic and yield data of long-term winter wheat experiments (1996–2002) set on Chernozem soils. They did not find a significant relationship between the annual rate of precipitation and the yield of winter wheat, however, the rate of precipitation in the vegetation period and the average yield showed a close correlation. The extent and fluctuation of yields strongly depended on the applied agrotechnical treatments and the rate of (nitrogen) fertilization.

Pepó (2005) analyzed the seasonal effects on yields in long-time crop production experiments (1985–2003) set on Chernozem and Meadow soils. He established that the impact of climate factors (especially the lack of precipitation) appeared in an interactive and cumulative way in the case of winter wheat (e.g. the unfavorable effects of weather were buffered by the optimal fertilization, or the unfavorable forecrop effect was intensified in drought years). The author reported that the water supply of the crop is a key factor relating to the amount of yield in case of corn, and the favorable fertilization and forecrop effects were ascertainable only by the appropriate water supply. *Kismányoky* (2005) used and analyzed the yield results of decades-long field experiments set on Ramann-type brown forest soil (Keszthely) in terms of climate change. He found that the amount of yield did not decrease significantly in arid years in comparison with average years in case of winter wheat. However, in years, which were wetter than average, the amount of yield was significantly lower, probably due to phytopathological reasons. In case of corn, the yield differences between arid and humid years were substantially higher (the yield of corn in favorable humid years was almost double than the yield in arid years besides the same agrotechnical method). The differences between the two crops were explained by the length of vegetation periods and the precipitation distribution.

Ruzsányi (1996) summarized the crop production effects of drought based on literature data and introduced the drought susceptibility of the 9 Hungarian meteorological districts and the drought sensitivity of the major field crops (corn, winter wheat, sugar beet, sunflower). During the statistical analyzes, average yields concerned to regions and based on statistical data originated from districts, counties, or farms were compared to the amount of precipitation, with

the simplification of 4 season types (average, droughty, arid, humid). The different drought sensitivity of the crops and regions were explained, among others, with water management (hydrophysical) properties of characteristic soil types of the regions.

During our research, the effects of natural plant water supplying depended on precipitation and evaporation circumstances on yield results were investigated in the frame of site-scale and physical geography microregion (Dövényi *et al.*, 2010) levels of soil climate sensitivity on the plot-level data of the vectoral National Pedological and Crop Production Database (NPCPD) (Kocsis *et al.*, 2014). The season effect was investigated by crops using the Pálfaí Drought Index (PaDI) of meteorological grids ordered to NPCPD plots (Szalai *et al.*, 2014).

2. Materials and methods

The NPCPD contains pedological information about different crop production sites of Hungary (arable land, meadows, pastures, vineyards, gardens, orchards, and forests). The database includes data from about four million hectares of land and their complex crop production of seven years (1984-1990) (Tóth, 2001). In addition, it provides time series data about the fertilizer and manure use per field as well as the crop yields of 196 cultivated plant types and their forecrops (Kocsis *et al.*, 2014).

Statistical analysis of the relationship between the soil-crop-seasonal effects were carried out on the basis of the filtered data of the NPCPD (NPCPD ver3.0), so inaccurate records resulting from erraneous data recording were excluded. Moreover, the data queues containing incompatible basic analysis data within each soil subtypes were also excluded. The crop yields were also filtered. Next, the winter wheat, corn, and sunflower yields were normalized to a scale ranging from 1 to 100 (Eq. 1):

$$Crop_{100} = 1 + \left(\frac{Crop - Crop_{min}}{Crop_{max} - Crop_{min}} \right) \times 99 \quad (1)$$

where $Crop_{100}$ is the yield of a certain crop normalized to a 1–100 scale; $Crop$ is the yield of a certain crop ($t\ ha^{-1}$); $Crop_{min}$ is the minimum yield of a certain crop ($t\ ha^{-1}$); $Crop_{max}$ is the maximum yield of a certain crop ($t\ ha^{-1}$). The minimum and maximum yield was explained in national level, regarding 5 years (1985–89) of the NPCPD ver3.0.

The normalized yield maps for the three crops were made by seasons with ordinary kriging. In order to carry out annual climate effect analysis, the annual Pálfaí Drought Index (PaDI) was assigned to the crop yields (Eq. 2). The PaDI is

calculated with the monthly mean temperature and monthly precipitation data (Bihari *et al.*, 2012) only using the following formula:

$$PaDI_0 = \frac{[\sum_{i=apr}^{aug} T_i] / 5 \times 100}{c + \sum_{i=oct}^{sept} (P_i \times w_i)} \quad (2)$$

where $PaDI_0$ is the base value of the Pálfaí Drought Index ($^{\circ}C \ 100 \ mm^{-1}$); T_i – is the monthly mean temperature from April to August ($^{\circ}C$); P_i is the monthly precipitation from October to September (mm); w_i is a weighing factor; c is a constant value (10 mm). The data related to droughtness are in CARPATCLIM database, where the values of Hungary, apart from the western border, are situated in a meteorological graticule containing 1,045 grid with a spatial resolution of 10×10 km (Szalai *et al.*, 2014). The CARPATCLIM database is a long-term (1951–2010) series of climate data for the Carpathian region, derived from meteorological station measurement data using homogenization and interpolation processes. The dataset contains a number of measured weather parameters, such as meteorological variables, and climate and drought indices (Lakatos *et al.*, 2013). 200×200 m resolution raster maps were generated displaying the extent of drought in the country on the basis of the meteorological grid values per years. Then, the agricultural years of the NPCPD (1985–1989) were characterized by drought category variables assigned to the PaDI values of the drought maps (without drought= <4 ; light drought= $4-6$; moderate drought= $6-8$; medium drought= $8-10$; severe drought= $10-15$; very high drought= $15-30$; extreme heavy drought= >30), on the basis of Bihari *et al.* (2012). Drought-free areas were marked per year and drought-free crop yields were collected. In areas where none of the years under study was drought-free (e.g., the Danube-Tisza Sand Ridge), we considered the yield of the mildest drought year to be drought-free. By combining the drought-free crop yields per plant, we prepared a 5-year drought-free yield map for winter wheat, corn, and sunflower (normalized for a 1–100 scale). These maps can be considered as optimized crop maps, with crop results independent of drought effects.

When generating the soil drought sensitivity index, the difference between the "normal" (actual, not independent of drought) crop yields and the previously determined drought-free crop yields was calculated, then the result was divided with the Pálfaí drought index value (Table 1).

Table 1. Measured and drought-free yields and their differences by the investigated crops, in the years of NPCPD database

Years	Normalized 1–100 scale	Winter wheat				Corn				Sunflower			
		PADI categories											
		1.	2.	3.	4.	1.	2.	3.	4.	1.	2.	3.	4.
1985	Measured yields	48.6	59.4	0.0	0.0	57.2	57.2	2.1	0.0	46.4	52.8	0.0	0.0
	Drought-free yields	50.7	58.3	0.0	0.0	57.2	57.6	46.3	0.0	47.5	54.0	0.0	0.0
	Difference	2.1	1.1	0.0	0.0	0.0	0.4	44.2	0.0	1.0	1.2	0.0	0.0
	Number of cases	23647	24051	0	0	21530	22938	1	0	5166	6122	0	0
1986	Measured yields	42.6	50.2	47.9	0.0	57.8	53.7	36.9	0.0	52.1	57.8	61.8	0.0
	Drought-free yields	47.7	56.7	63.5	0.0	56.6	57.7	48.0	0.0	48.0	51.6	58.3	0.0
	Difference	5.1	6.6	15.6	0.0	1.2	4.0	11.0	0.0	4.1	6.2	3.5	0.0
	Number of cases	10935	25589	1083	0	14731	35427	1519	0	2894	9621	515	0
1987	Measured yields	50.2	47.3	49.4	0.0	59.3	47.6	33.8	0.0	47.6	61.0	56.9	0.0
	Drought-free yields	54.3	55.6	53.8	0.0	57.8	57.1	53.7	0.0	51.3	50.7	46.0	0.0
	Difference	4.1	8.3	4.4	0.0	1.5	9.5	19.8	0.0	3.7	10.4	11.0	0.0
	Number of cases	12029	13177	641	0	22703	25164	738	0	5227	6124	493	0
1988	Measured yields	55.6	65.9	70.4	13.2	53.9	47.3	34.8	36.1	47.7	49.9	47.0	46.5
	Drought-free yields	44.4	54.0	65.4	32.0	49.3	58.3	55.5	52.0	40.0	50.7	56.7	58.3
	Difference	11.1	11.8	5.0	18.9	4.6	11.0	20.6	15.8	7.7	0.8	9.7	11.8
	Number of cases	3331	12096	1460	9	1581	32633	6098	16	463	9149	1881	67
1989	Measured yields	60.2	59.3	59.4	0.0	55.7	49.4	54.0	0.0	49.7	49.8	0.0	0.0
	Drought-free yields	54.0	54.2	60.3	0.0	57.9	57.8	43.7	0.0	50.2	54.6	0.0	0.0
	Difference	6.1	5.1	0.9	0.0	2.3	8.3	10.3	0.0	0.5	4.9	0.0	0.0
	Number of cases	8143	4095	122	0	29272	5814	6	0	6906	2220	0	0

Pálfai Drought Index (PaDI) categories: 1. without drought category; 2. light drought category; 3. moderate drought category; 4. medium drought category.

The decision tree technique CHAID (Chi-square automatic interaction detection) was used to classify the results (Tóth *et al.*, 2012) by taking into account the most important soil parameters originated from the NPCPD database (sub-type, soil texture, pH_{KCl}, humus and lime content) from the point of view soil fertility. The NPCPD contains information regarding agricultural fields for 38 soil main types of the total 40, besides, 84 sub-types (Jassó, 1989) of the total 86 mentioned in the Hungarian Genetical Soil Classification System. Based on

the taxonomic units and measured soil parameters, the database contains totally 8,530 soil varieties on the 76,849 agricultural plots and sub-plots. In case of the used soil-based investigations, the soil texture based on plasticity limit (liquid limit) was determined according to the Arany method (a Hungarian method to estimate soil texture), humus content was determined according to the Tyurin-method, pH_{KCl} was calculated potentiometrically, while CaCO_3 content was determined with the Scheibler-calcimeter (Buzás *et al.*, 1988, 1993). The soil investigation data used for estimation was decoded to the soil mapping category system included in the National Large-scale Soil Mapping Guide (Jassó *et al.*, 1989). In this code system, map categories and measuring ranges (e.g. loamy texture, low humus content etc.) are allocated to the soil examination results instead of exact values (Farkas *et al.*, 2009; Makó *et al.*, 2010). Equal-ranking category variables ranging from 1 to 10 were formed from the mean values of the groups estimated with the help of the CHAID method (SPSS/Transform/Visual binning) (Fig. 1).

Due to the lack of meteorological and drought index (PaDI) data, soil drought sensitivity index was not computed for the soils located to the west of 17°E – the western frontier of Hungary. The drought sensitivity categories for this area were determined by estimation, and in order to do so, the known soil-type parameters and crop yields from other parts of the country were used. Next, a one-factor analysis of variance (one-way ANOVA) was carried out to see if the previously formed categories differ significantly from each other.

The determined drought sensitivity values were extended to the 230 physical geography microregions with zone statistic. The mapping of the average drought sensitivity values were not performed where the sowing area of corn, winter wheat and sunflower based on the NPCPD in average of the 5 investigated years was under 500 hectares, separately. The numbers following the microregion names represent the microregion codes, which indicate the position of the microregions in the maps presented, based on the nomenclature of Inventory of Microregions in Hungary (Dövényi *et al.*, 2010).

For the vectoral map operations, other GIS applications and geostatistical analyses (i.e. ESRI ArcGIS 10.0 GIS software) were used. For further statistical tests, the IBM SPSS Statistics 18.0 software was used.

3. Results

According to the results, the year 1988 was the driest based on the PaDI index from the years of NPCPD database (Table 2). Depending on the crop, moderate drought was observed in the 8.3–17.2% of sowed area in that year. Medium drought was also observed, but the extent of these fields (0.5%) was not significant. Winter wheat was hit in the highest, while sunflower in the lowest extent by water scarcity in 1988.

Table 2. Distribution of Palfai Drought Index by the investigated crops to the years of the NPCPD database.

Plants	Years	PaDI categories (Total area, %)							Field units
		Without drought (<4)	Light drought (4-6)	Moderate drought (6-8)	Medium drought (8-10)	Severe drought (10-15)	Very high drought (15-30)	Extreme heavy drought (>30)	
Winter wheat	1985	45.94	54.06	0.00	0.00	0.00	0.00	0.00	12 963
	1986	28.83	68.06	3.11	0.00	0.00	0.00	0.00	11 115
	1987	44.70	52.99	2.31	0.00	0.00	0.00	0.00	8 801
	1988	22.39	69.28	8.30	0.04	0.00	0.00	0.00	6 706
	1989	59.60	38.99	1.41	0.00	0.00	0.00	0.00	5 276
Corn	1985	48.21	51.79	0.00	0.00	0.00	0.00	0.00	8 093
	1986	29.68	67.15	3.17	0.00	0.00	0.00	0.00	9 501
	1987	49.87	48.66	1.47	0.00	0.00	0.00	0.00	8 916
	1988	5.94	78.08	15.95	0.04	0.00	0.00	0.00	7 467
	1989	82.27	17.64	0.09	0.00	0.00	0.00	0.00	6 421
Sunflower	1985	42.73	57.27	0.00	0.00	0.00	0.00	0.00	2 976
	1986	21.61	73.97	4.42	0.00	0.00	0.00	0.00	3 465
	1987	44.49	51.66	3.84	0.00	0.00	0.00	0.00	3 042
	1988	2.82	79.60	17.15	0.43	0.00	0.00	0.00	2 853
	1989	75.41	24.59	0.00	0.00	0.00	0.00	0.00	2 246

For the adequate water supply of crop production, the most optimal conditions were in 1989, because more than a half (59.6–75.4%) of the fields were drought-free. It can also be stated by the distribution of PaDI-values by different categories, that in 1985 there were not areas affected by moderate drought, so this generated favorable conditions for crop production. In 1986 and 1987, the amount of areas affected by moderate drought by crops were between 2.3 and 4.4%. Considering the investigated 5 years (1985–1989) and the crops together, it can be observed that the amount of slightly drought fields were high; in 1988, which was the driest year, it was 69.3% in case of winter wheat, 78.1% in case of corn, and 79.6% in case of sunflower. The amount of slightly drought fields was between 17.6% and 39% in the least dry year of 1989.

During the formation of drought sensitivity indices, 133 groups (nodi) were separable by the CHAID method. Since the Levene's test of homogeneity showed that the standard deviations are different, the Tamhane's T2 probe was applied by one-way ANOVA. Based on the results of the test, the groups of each

category could not be separated from each other explicitly, so certain groups were merged. At the end, Hungarian soils were characterized in 7 different drought-sensitive groups (categories). The determined groups were represented plant specifically in drought sensitivity maps, where the category 1 means the highest, the category 4 means medium while the category 7 means the lowest sensitivity or the non-sensitive soils (*Fig. 1*).

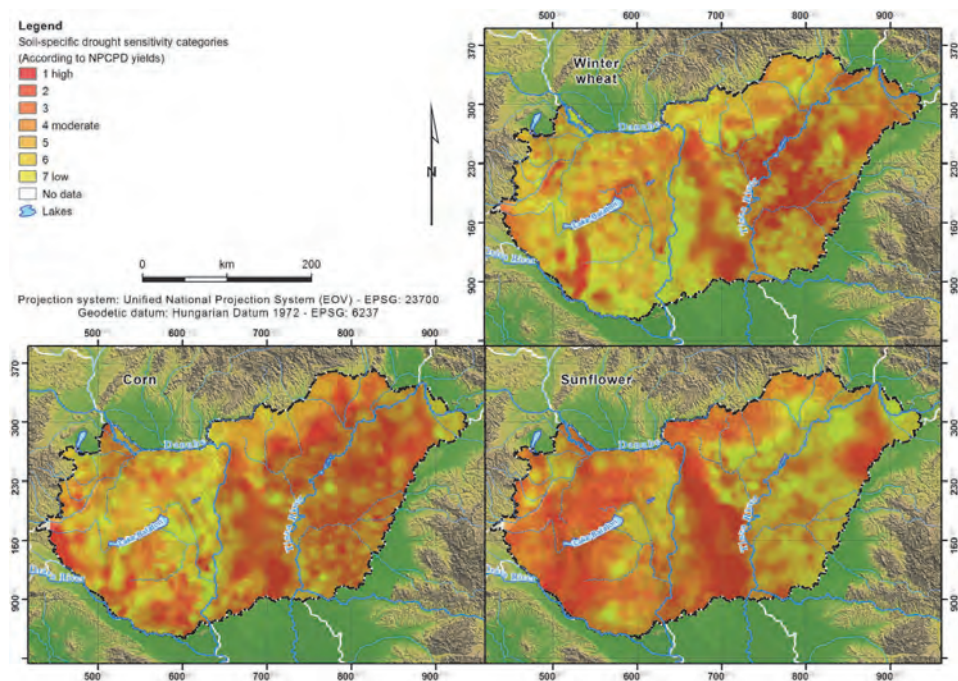


Fig. 1. Soil-specific drought sensitivity maps to the three crops produced in the largest area rate in Hungary.

For winter wheat, among the 230 micro regions, areas with predominantly clayey or sandy soils are the most prone to drought. The extreme drought sensitivity of clay and heavy clay textured soils can be explained with the high amount of plant unavailable water (below the permanent wilting point). Eastern Inside Somogy (4.2.12), Heves Plain (1.9.22) and Bihar Plain (1.12.21) proved to be medium drought sensitive areas. By winter wheat, Tolna Sárköz (1.1.24), Cserhátalja (6.3.24), Mohács Island (1.1.25) and Nyárád-Harkány Plain (1.5.13) microregions are the least drought sensitive areas (*Fig. 2*).

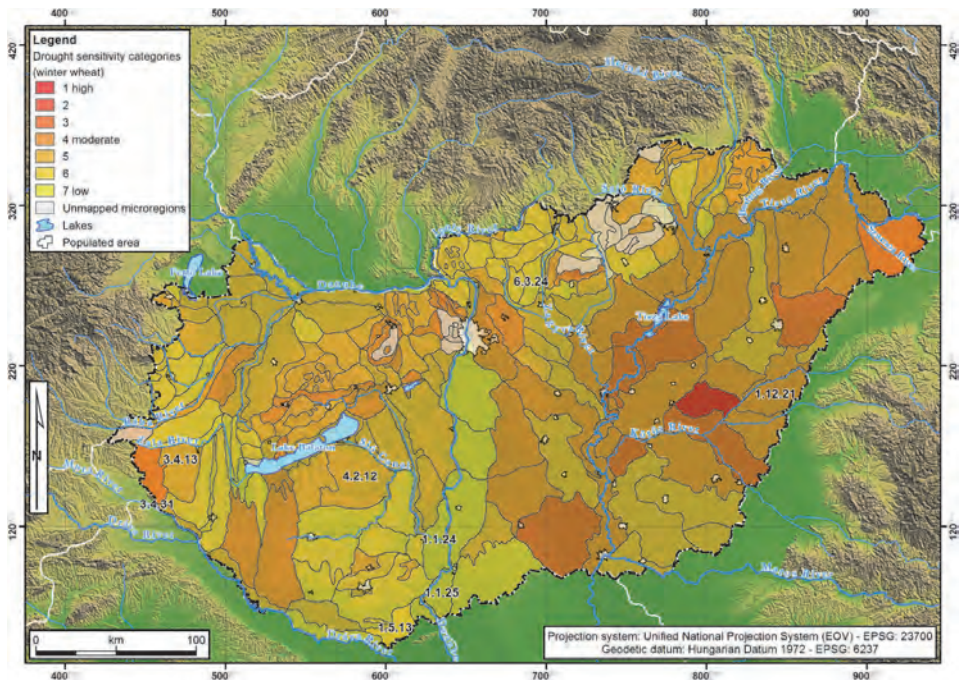


Fig. 2. Soil-specific drought sensitivity of the microregions of Hungary, according to the yield rates of winter wheat.

In case of corn, based on the average drought sensitivities, it can be concluded that the Kerka Riverscape (3.4.12), Western Mátraalja (6.4.22), Dorozsma-Majsa Sand Ridge (1.2.15) and Western or Loess Nyírség (1.10.21) are the most sensitive areas in term of drought sensitivity (Fig. 3). At less extent than the previous areas, but the Miskolc Bükkalja (6.5.23), Harangod (1.9.33), Dévaványa Plain (1.12.11), Bugac Sand Ridge (1.2.14), Érmellék Loess Ridge (1.12.14), Western Cserhát (6.8.54), Kiskunság Sand Ridge (1.2.13), Eastern Mátraalja (6.4.21), Southeastern Nyírség (1.10.13) microregions are also sensitive at high extent.

In case of corn, there are medium drought sensitive soils in the middle mountains and their basins, as well as in Bereg Plain (1.6.11), Szatmár Plain (1.6.12), Sárrét (1.4.23) and Baranya Mountridge (4.4.12) microregions. The non-drought sensitive areas can be found in the Southern Mezőföld (1.4.25), Tolna Sárköz (1.1.24), Enying Ridge (1.4.31), Káloz-Igar Loees Ridge (1.4.32), and Litke-Etes Hills (6.3.42) microregions (Fig. 3).

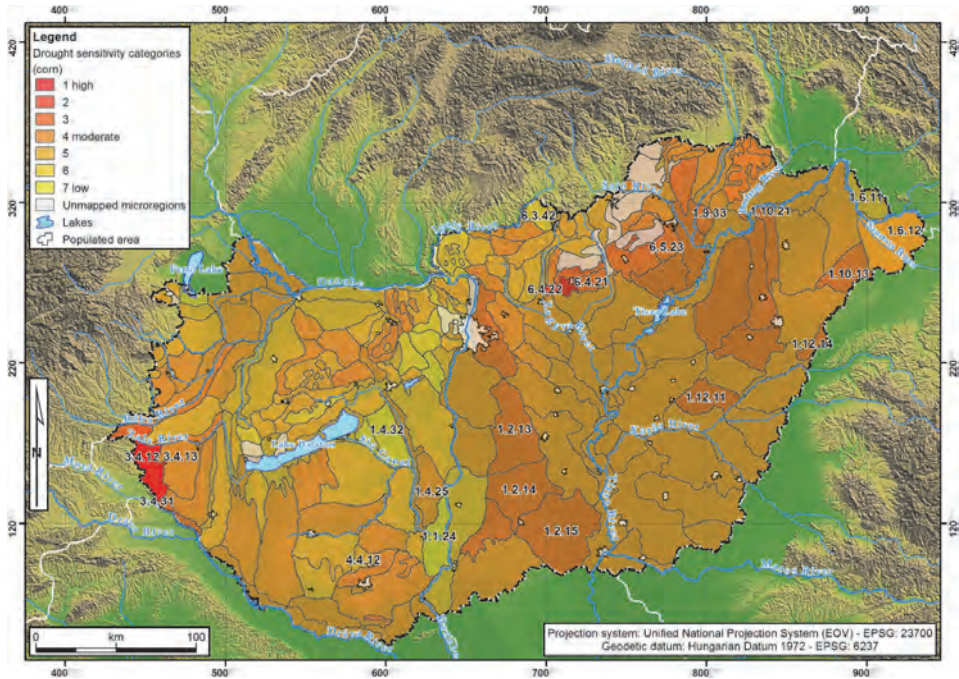


Fig. 3. Soil-specific drought sensitivity of the microregions of Hungary, according to the yield rates of corn.

In case of sunflower, significantly the sand fields are sensitive at the highest extent to the droughty meteorological periods. This sensitivity can be traced back to the disadvantageous characteristics of the soils formed there (good water conductivity, bad water holding characteristics). The great Hungarian sand areas, e.g. Marcali Ridge (4.3.11), Kemenesalja (2.2.12), Ikva Plain (3.2.11), Szigetköz (2.1.11) etc. have less sensitivity (Fig. 4). The results confirmed the conclusion of *Frank* (1999) for the terrain, whereas the cooler mountains and close basins are not suitable for sunflower production.

Related to the plant specificity, it can be stated that while in case of winter wheat the area of Mohács Island (1.1.25) was not drought-sensitive, simultaneously in case of sunflower, high drought sensitivity was observed. In case of sunflower there are medium drought sensitive areas, e.g. the Enying Ridge (1.4.31), Csanád Ridge (1.13.11), Sió Valley (1.4.33), Békési Ridge (1.13.12) and Jászság (1.7.15) microregions. According to the examinations, in case of sunflower the areas of Bereg Plain (1.6.11), Szatmár Plain (1.6.12), Harangod (1.9.33), Western or Loess Nyírség (1.10.21) microregions were not (or at very small extent) drought sensitive (Fig. 4).

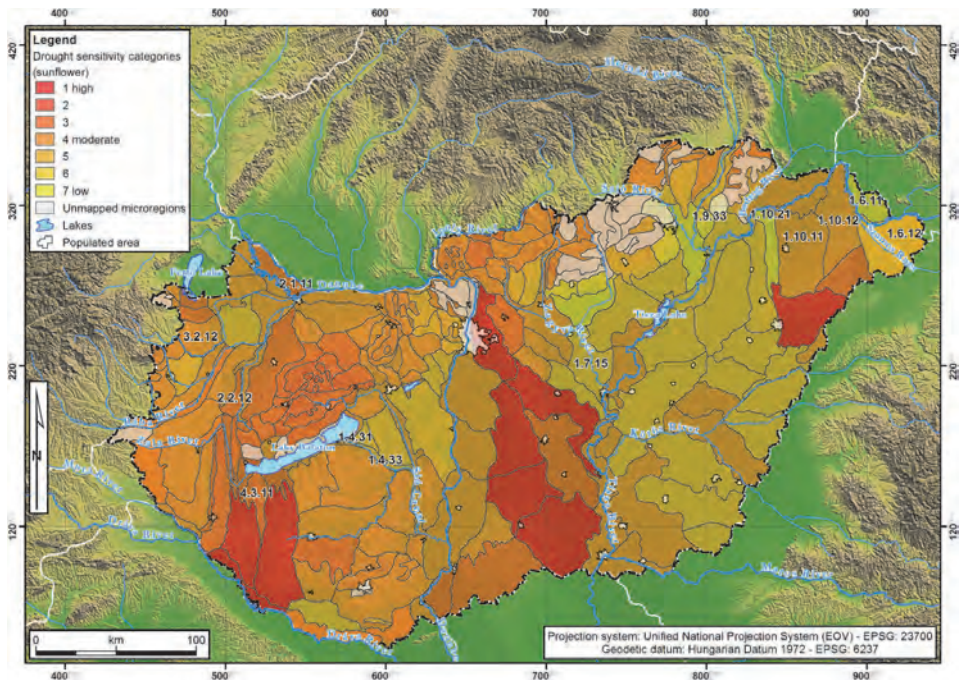


Fig. 4. Soil-specific drought sensitivity of the microregions of Hungary, according to the yield rates of sunflower.

For all three plants, it can be generally stated that among different soil types, Brown forest soils, Chernozem soils, Marsh soils, Alluvial and Slope deposit soils are the least sensitive for drought (Fig. 5). The highest drought sensitivity can be observed in soil types with high sand content and in saline soils which have extreme water properties. Sandy soils belonging to the Skeleton soils have very low humus content (e.g. Inside Somogy, Duna-Tisza Interfluve Sand Ridge, Nyírség), their fertility is also low. Increasing drought sensitivity of soils with high humus content can be explained with the combined effect of other soil properties (texture, pH, humus- and lime content etc.). As a result of high clay and unavailable water content, drought sensitivity of soils with high humus content can be higher. It is presumably formed as a result of the combination effect of the soil variety attributes. However, clay expresses the opposite effect, because it can protect the organic material from the rapid decomposition with surface bonding. In case of the given soil types, the relationship between humus- and clay content and effects evolving together was determined by the amounts and qualitative composition of these two materials. Due to the „double role” of clay, it is hard to determine how and to what extent

can a certain soil attribute takes part in the combined effects forming together the response of soils to the stress effects caused by drought. Meadow soil types are medium sensitive for natural water supply.

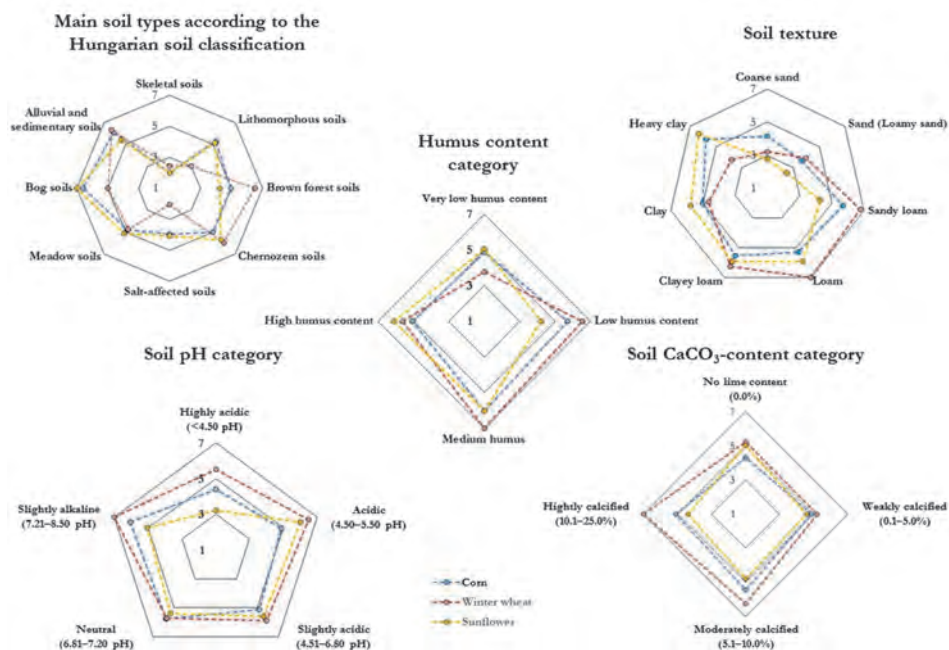


Fig. 5. Distribution of the drought sensitivity categories based on the examined soil parameters in case of the three most important crops. Cross-lines show the drought sensitivity categories: 1–extremely high drought sensitivity, 3–moderate drought sensitivity, 5–favorable drought sensitivity, 7–very low drought sensitivity.

The maps constructed to winter wheat and corn (Figs. 2 and 3) well demonstrate the statements of some authors (Pepó, 2007; Jolánkai and Birkás, 2009) that in the past decades the drought observed in Hajdúság, Nagyunság and Körös-Maros Interfluve became more and more severe because of the more and more serious (in average 200–300 mm) lack of precipitation. As a result, high yield deficit can be observed. Not only the increasing of drought periods and their seriousness can be problematic, but the increasing of the mean

temperature can also cause the increase of drought. According to our estimations and based on the data of the investigated period (1985–1989), the latter can be observed in the southwestern part of Hungary, in the area of the Kerka Riverscape (3.4.12), the left riverside of the Mura (3.4.31) and in the Central Zala Hills (3.4.13) (where the most rainy places are situated in Hungary), where in average 800 mm precipitation is available (*Varga-Haszonits and Varga, 2005*).

In the regions, where the Mediterranean climate effects are intensified, according to the 30 years (1980–2010) data queue of the Hungarian Meteorological Service (*Bartholy et al., 2011*), the mean summer temperatures has been increased with 2°C in average. The latter was verified by the climate sensitivity researches of *Máté et al. (2009)*, whereas the Hungarian soil zones are shifting, and in certain areas, the Mediterranean climate effects become dominant on the account of continental effects. The drought sensitivity of low fertile, strongly acidic brown forest soils (with clay illuviation, pseudogley) situated in the southwestern part of Hungary can increase by the fact that these soil types were formed on fluvial alluvial gravel-sandy parent material and they are loamy textured, which types have bad water storage capacity. The yield fluctuations and depressions evolved to the joint effect of stress caused by the drought (longer and higher extent water deficit periods, increasing mean temperature) and the very extreme precipitation distribution may get worse in the next decades.

High drought sensitivity is clearly detectable in the microregions where strongly acidic soils can be found. Medium-acidic and pH-neutral soils can tolerate the stress effects caused by lack of water at medium extent (*Fig. 5*). The examination results of lime content are also confirmed this (*Késmárki et al., 2005*): generally the pH-neutral soils and soils with medium lime content have the best drought-resistance ability. The appropriate carbonate content with neutral pH resulted in structure stabilization. The high amount of Ca-bridges evolved from carbonate can allow the formation of appropriate amount of organomineral complexes in soil, which can be favorable in terms of formation of ideal agronomical soil structure. Tendencies of forming crusts can decrease, and as a result of this, possibility of cultivation can be better, and the precipitation can pass into the surface and can settle there. These can favorably influence the water management of soils, high-quality organic matter can form, the nutrient turnover becomes optimal, and the efficiency of nutrient supply can increase. These positive effects can decrease or even neutralize the harmful effects of drought.

Assorting the microregions by the soil's texture, it can be observed that the sandy soils are the most drought sensitive, while the loam and clay loam soils are the least sensitive soils, which harmonizes with the scientific results of

Gyulai and Nagy (1995). The drought sensitivity is slightly increased in case of clay soils. Research results of *Csorba et al. (2012)* are proved the drought sensitivity of clay soils, whereas the drying caused by climate change can remarkably affect the wet and clayey sites situated in the Hungarian Great Plain.

4. Conclusions

Results of the investigation confirm that the drought sensitivity of the soils is different by plants, which can explain the different water demands and vegetation periods of corn, winter wheat and sunflower.

It is determinable that winter wheat is a shallow-rooted (20–30 cm) plant, so it can utilize only that water stock which is stored in the upper soil layer. Theoretically, it is sensitive to periods having insufficient amount of precipitation, but as a plant sowing in October, it can manage with the autumn-winter precipitation as well. Corn and sunflower are more sensitive to the spring arid periods than the cultures which are sown in autumn. The roots of corn and sunflower can reach to 2–3 meters deep in the soil, so across the capillary pores, they can easily obtain the moisture situated in the deeper soil layers.

During our fertility investigation, we subjectively selected some important soil properties only. The investigated soil parameters determine the drought sensitivity of soils through unascertained mode of action together with the other, uninvestigated attributes. The results are suited for demonstration of the main tendencies only.

As for future research direction, making more precise drought sensitivity indicators are planned on the basis of the strong relationship between the precipitation of the vegetation period and crop yields as determined by *Jolánkai et al. (2003)* and on the basis of meteorological datasets for the vegetation period. We would like to investigate the relation between the soil drought sensitivity indicators and the applied agrotechnical methods and the nutrient management – how the drought sensitivity depends on the applied agrotechnical methods, the effect of forecrop and the application of fertilizers.

The large scale (national) soil fertility research creates the possibility of preparing 1:10,000 scale climate sensitivity maps of crop production sites, which could contribute to the soil- and plant-specific crop production, that can adapt to climate change.

Acknowledgments: This research was supported by the European Union and the State of Hungary, co-financed by the European Social Fund in the framework of TÁMOP-4.2.4.A/ 2-11/1-2012-0001 „National Excellence Program” and TÁMOP-4.2.2.A-11/1/KONV-2012-0064 project. The publication is supported by the EFOP-3.6.3-VEKOP-16-2017-00008 project. We acknowledge the financial support of Széchenyi 2020 under the EFOP-3.6.1-16-2016-00015.

References

- Bartholy J., Bihari Z., Horányi A., Krüzselyi I., Lakatos M., Pieczka I., Pongrácz R., Szabó P., Szépszó G., and Toma Cs., 2011: Hazai éghajlati tendenciák. In: (Eds: Bartholy J., Bozó L. and Haszpra L.) Klímaváltozás – 2011. Klímaszcenáriók a Kárpát-medence térségére. Magyar Tudományos Akadémia – Eötvös Loránd Tudományegyetem Meteorológiai Tanszék, Budapest, 145–169. (in Hungarian)
- Bihari Z., Gauzer B., Gnandt B., Gregorič, G., Herceg Á., Kovács T., Kozák P., Lakatos M., Mattányi Zs., Nagy A., Németh Á., Pálfi I., Szalai S., Szentimrey T., and Vincze E., 2012: Délkelet-Európai Aszálykezelési Központ – DMCSEE projekt. Összefoglaló a projekt eredményeiről. Országos Meteorológia Szolgálat, Budapest. (in Hungarian)
https://www.met.hu/doc/DMCSEE/DMCSEE_zaro_kiadvany.pdf
- Birkás M., Jolánkai M., Stingli A., and Bottlik L., 2007: Az alkalmazkodó művelés jelentősége a talaj- és klímavédelemben. „AGRO-21” Füzetek 51, 34–47. (in Hungarian)
- Bocz E., 1995: A fenntartható fejlődés időszerű kérdései. In: A fenntartható fejlődés időszerű kérdései a mezőgazdaságban. XXXVII. Georgikon Napok, Pannon Agrártudományi Egyetem, Georgikon Mezőgazdaságtudományi Kar, Keszthely, 1–20. (in Hungarian)
- Buzás I., Bálint I., Füleky Gy., Györi D., Hargitai L., Kardos J., Lukács A., Molnár E., Murányi A., Osztóics A.-né, Pártay G., Rédly L.-né & Szebeni Sz.-né, 1988: Talaj- és agrokémiai vizsgálati módszertan. 2. Mezőgazdasági Kiadó, Budapest. (in Hungarian)
- Buzás I., Daróczy S., Dódy I., Kálmán A., Kocsis I., Pártay G., Rajkai K., Rózsavölgyi J., Stefanovits P., Szili Kovács T., Szűcs L., and Várallyay Gy., 1993: Talaj- és agrokémiai vizsgálati módszertan. 1. INDA 4231 Kiadó, Budapest. (in Hungarian)
- Csorba P., Blanka V., Vass R., Nagy R., Mezősi G., and Burghard, M., 2012: Hazai tájak működésének veszélyeztetettsége új klímaváltozási előrejelzés alapján. *Földrajzi Közlemények* 136, 237–253. (in Hungarian)
- Dövényi Z., Becse A., Mezősi G., Ádám L., Juhász Á., Marosi S., Somogyi S., Szilárd J., Ambrózy P., Konkolyiné Bihari Z., Király G., Molnár Zs., Bölöni J., Csiky J., Vojtkó A., Rajkai K., Tóth G., Tiner T., Michalkó G., and Keresztesi Z., 2010: Magyarország kistájainak katasztere. Második, átdolgozott és bővített kiadás. MTA Földrajztudományi Kutatóintézet, Budapest. (in Hungarian)
- Farkas Cs., Hernádi H., Makó A., Marth P., and Tóth B., 2009: A Magyarországi Részletes Talajfizikai és Hidrológiai Adatbázis (MARTHA) bemutatása. Mezőgazdasági Szakigazgatási Hivatal Központ, Növény- és Talajvédelmi Igazgatósága, Budapest. (in Hungarian)
- Frank J., 1999: A napraforgó biológiája, termesztése. Mezőgazda Kiadó, Budapest. (in Hungarian)
- Gyulai B. and Nagy J., 1995: A napraforgó termesztés legfontosabb agrokémiai szempontjai. *Agrofórum* 6 (4), 40–41. (in Hungarian)
- Gyuricza Cs., 2004: A víztakarékos talajművelés lehetőségei. *Agro Napló* 8 (5), 16–18. (in Hungarian)
- Harnos N., 2003: A klímaváltozás hatásának szimulációs vizsgálata őszi búza produkciójára. „AGRO-21” Füzetek 31, 56–73. (in Hungarian)
- Harnos Zs., 2005: A klímaváltozás és lehetséges hatásai a világ mezőgazdaságára. *Magyar Tudomány* 7, 826–832. (in Hungarian)
- Jassó F., Horváth B., Izsó I., Király L., Parászka L., and Szabóné Kele G., 1989: '88 útmutató a nagyméretarányú országos talajterképezés végrehajtásához. Agroiinform Kiadó, Budapest. (in Hungarian)
- Jolánkai M., 2005: A klímaváltozás hatása a növénytermesztésre. „AGRO-21” Füzetek 41, 45–58. (in Hungarian)
- Jolánkai M. and Birkás M., 2009: Climate change and water availability in the agro-ecosystems of Hungary. *Columbia University Seminars* 38–39, 171–180.
- Jolánkai M., Szentpétery Zs., and Szöllösi G., 2003: Az évszázad hatása az őszi búza termésére és minőségére. „AGRO-21” Füzetek 31, 74–82. (in Hungarian)
- Késmárki I., Kajdi F., and Petróczki F., 2005: A globális klímaváltozás várható hatásai és válaszai a Kisalföld szántóföldi növénytermelésében. „AGRO-21” Füzetek 43, 24–38. (in Hungarian)
- Kismányoky T., 2005: A globális klímaváltozás hatásai és válaszai Közép- és Dél-Dunántúl szántóföldi növénytermelésében. „AGRO-21” Füzetek 41, 81–94. (in Hungarian)

- Kocsis M., Tóth G., Berényi Üveges J. and Makó A., 2014: Az Agrokémiai Irányítási és Információs Rendszer (AIR) adatbázis talajtani adatainak bemutatása és térbeli reprezentativitás-vizsgálata. *Agrokémia és Talajtan* 63 (2), 223–248. (in Hungarian)
- Ladányi Zs., Blanka V., Rakonczai J., and Mezősi G., 2014: Az aszály és biomassza-produkció anomália közötti kapcsolat vizsgálata. In. (Eds: Kórodi T., Sansumné Molnár J., Siskáné Szilasi B. and Dobos E.) VII. Magyar Földrajzi Konferencia Kiadvány. Miskolci Egyetem, Földrajz – Geoinformatikai Intézet, Miskolc, 389–394. (in Hungarian)
- Lakatos M., Szentimrey T., Bihari Z., and Szalai S., 2013: Creation of a homogenized climate database for the Carpathian region by applying the MASH procedure and the preliminary analysis of the data. *Időjárás* 117, 143–158.
- Makó A., Tóth B., Hernádi H., Farkas Cs., and Marth P., 2010: Introduction of the Hungarian Detailed Soil Hydrophysical Database (MARTHA) and its use to test external pedotransfer functions. *Agrokémia és Talajtan* 59, 29–38.
- Máté F., Makó A., Sisák I., and Szász G., 2009: A magyarországi talajzónák és a klímaváltozás. „KLÍMA-21” *Füzetek* 56, 36–42. (in Hungarian)
- Molnár Á. and Gácsér V., 2014: Szélsőséges éghajlat – szeszélyes időjárás. *Iskolakultúra* 11–12, 4–12. (in Hungarian)
- Molnár K., 1996: Hazai csapadékváltozások. *Természettudományi Közlöny, Különszám* 127 (1), 66–68. (in Hungarian)
- Nagy J., 2005: A mezőgazdasági földhasználat, a szántóföldi növénytermelés és vízgazdálkodás. „AGRO-21” *Füzetek* 41, 38–46. (in Hungarian)
- Patrick J.M., 2002: Global Warming. Cato Institute, Washington, USA.
- Pálfai I. and Herceg Á., 2011: Droughtness of Hungary and Balkan Peninsula. *Riscuri și Catastrofe* 9 (2), 145–154.
- Pepó P., 2005: A globális klímaváltozás hatásai és válaszai a Tiszántúl szántóföldi növénytermelésében. „AGRO-21” *Füzetek* 41, 59–65. (in Hungarian)
- Pepó P., 2007: A Klímaátalakulás kedvezőtlen hatásai és az alkalmazkodás természetstechnológiai elemei a szántóföldi növénytermesztésben. *Agrofórum XVIII. (11)*, 17–26. (in Hungarian)
- Rajkai K., 2005: A víz mennyisége, eloszlása és áramlása a talajban. MTA Talajtani és Agrokémiai Kutatóintézet, Budapest. (in Hungarian)
- Rakonczai J., 2011: Effects and consequences of global climate change in the Carpathian Basin. In. (Eds: Blanco J. and Kheradmand H.) *Climate Change. Geophysical Foundations and Ecological Effects*, Intech Open Access Publisher, 297–322. (in United Kingdom)
- Rácz L., 1999: Climate History of Hungary Since 16th Century: Past, Present and Future. Discussion paper. – Center for Regional Studies of the Hungarian Academy of Sciences, Pécs, Hungary.
- Ruzsányi L., 1996: Aszály hatása és enyhítésének lehetőségei a növénytermesztésben. In. (Eds.: Cselőtei L. and Harnos Zs.) *Éghajlat, időjárás, aszály*. Akaprint, Budapest, 5–66. (in Hungarian)
- Szalai S., Spinoni J., Galos B., Bessenyei M., Molar P., and Szentimrey T., 2014: Use of regional database for climate change and drought. 5th IDRC Davos 2014, Global Risk Forum (GRF). 24–28 August 2014, Davos, Switzerland.
- Szász G., 2005a: Az éghajlat változékonysága és a szántóföldi növények termésingadozása. „AGRO-21” *Füzetek* 38, 59–77. (in Hungarian)
- Tóth B., Makó A., Guadagnini A., and Tóth G., 2012: Water retention of salt affected soils: quantitative estimation using soil survey information. *Arid Land Res. Manage.* 26, 103–121.
- Tóth G., 2001: Soil productivity assessment method for integrated land evaluation of Hungarian croplands. *Acta Agronomica Hungarica* 49 (2), 151–160.
- Van Leeuwen B., Tobák Z. and Szatmári J., 2008: Development of an integrated ANN, GIS framework for inland excess water monitoring. *J. Environ. Geograph.* 1 (3–4), 1–6. (in Hungarian)
- Varga-Haszonits Z. and Varga Z., 2005: Nyugat-Magyarország éghajlati viszonyai és a kukorica. „AGRO-21” *Füzetek* 43, 71–79.

IDŐJÁRÁS

*Quarterly Journal of the Hungarian Meteorological Service
Vol. 125, No. 1, January – March, 2021, pp. 123–135*

eostatistical comparison of UERRA MESCAN-SURFEX daily temperatures against independent data sets

Hristo Chervenkov* and Kiril Slavov

*National Institute of Meteorology and Hydrology – Bulgarian Academy of Sciences
66, Tsarigradsko Shose blvd Sofia 1784, Bulgaria*

**Corresponding author E-mail: hristo.tchervenkov@meteo.bg*

(Manuscript received in final form April 23, 2020)

Abstract— Regional reanalyses are attractive new sources of meteorological data for the growing society of the end users, due to their physical consistency, dynamical coherency, and multivariate products at higher than the global reanalyses spatio-temporal resolution. The assessment and quantification of uncertainties of the products of the regional reanalyses and their added value are crucial for the interpretation. Hence these products could be also incorporated in the regional climatology, consistent comparisons of their long-term timeseries against independent and representative data sets have to be performed. The present study could be considered as step ahead in this direction - the MESCAN-SURFEX, which is the product with the most detailed spatial structure among all others in the UERRA (Uncertainties of Ensembles in Regional Reanalysis) project, is compared against two gridded observational data sets in South-east Europe: the well-known regional CARPATCLIM and the product of the Bulgarian National Institute of Meteorology and Hydrology ProData. The comparison aims to assess the skill of MESCAN-SURFEX to reproduce the climatological field of the mean temperature. Additionally, the daily extreme temperatures are estimated using the MESCAN-SURFEX output on sub daily basis and the results are compared against their CARPATCLIM- and ProData-counterparts. The computation of the mean and extreme temperatures with the MESCAN/SURFEX data are performed for the whole time span of this product and the comparison against the references for the whole time span of each of them on daily basis. The main conclusion of the study, which agrees with the outcomes of more detailed recent evaluations, is that MESCAN-SURFEX reproduces realistically the regional temperature field over Southeast Europe. According to the mean temperature, the differences remains under certain limits (RMSE generally below 2 °C) without, at least not apparent, systematic and spatial pattern. The estimation of the extreme temperatures produces results with biases comparable to the biases of the mean temperature, which makes the proposed method applicable for certain cases.

Key-words: UERRA, MESCAN-SURFEX, CARPATCLIM, ProData, uncertainties estimation, mean and extreme temperatures

1. Introduction

Daily minimum, mean, and maximum temperatures, noted subsequently hereafter for the sake of brevity t_n , t_d , and t_x , as well as the daily precipitation sum, are essential climate variables (ECVs) particularly involved in determining climate change impacts on society and ecosystems (*Birsan et al.*, 2014). They are also widely used, both in regional and global scales, as input parameters for computation of climate indices as the ETCCDI (Climate Extreme Indices) dataset (*Chervenkov and Slavov*, 2019; *Cheval et al.*, 2014; *Lakatos et al.*, 2013b; *Sillmann and Röckner*, 2008). The growing demand of the user community for high resolution meteorological data, both in space and time, could be addressed by various downscaling methods, with variable success depending on meteorological parameter, method applied, and spatial scale (*Kaiser-Weiss, et al.*, 2019). Atmospheric reanalysis (RA) provides a physically consistent and dynamically coherent description of the state of the atmosphere. The main merit of RA are that they provide a multivariate, spatially complete, and coherent record of the atmospheric state – far more complete than any observational dataset is able to achieve (*Ridal et al.*, 2018). This is the basic reason for the remarkable success of the widely used global RA, serving tens of thousands of users in need of climatological information (*Kaiser-Weiss, et al.*, 2019). Recently, due to the progress of the scientific knowledge and computation power, regional reanalyses (RRA) which can ingest additional observations and achieve higher resolution by means of regional numerical weather prediction (NWP) models, become possible. Hence wind speed and solar irradiation are strongly fluctuating parameters requiring the evaluation of their fields at highly-resolved spatial (a few kilometers) and temporal (hours) scales, the RRA products could address also the needs of the growing user community in the energy sector (*Niermann et al.*, 2017).

The objective of the project-driven collaborative initiative UERRA (Uncertainties in Ensembles of RRA; www.uerra.eu) is to produce ensembles of European RRA of ECVs for several decades and estimate the associated uncertainties in the data sets (*Ridal et al.*, 2018; *Unden*, 2018). It also includes recovery of historical (last century) data and creation of user friendly data services. Within UERRA, three different NWP models have been employed to generate European regional reanalyses and subsequent surface reanalysis products. All models share the same boundary conditions (provided by RA ERA-Interim and ERA40) and domain (CORDEX-EUR11, European domain of the Coordinated Regional Climate Downscaling Experiment, <http://www.euro-cordex.net>; *Kaiser-Weiss, et al.*, 2019; *Niermann et al.*, 2017).

The assessment and quantification of uncertainties of the RRA products and their added value is crucial for the interpretation. The proper use in applications and downstream services depends on the knowledge of the quality of the RRA and the representation of uncertainties. The information content of

the RRA UERRA and their uncertainties are statistically assessed by comparison against observation-based independent data sets, with several different methods, at user-relevant scales (*Niermann et al.*, 2017). One of these methods ('Method C') consist of comparison against gridded station observations. Advantage of the method, as stated in *Niermann et al.* (2017) is that the aggregation of data over selected regions in the European domain and over time provides one simple measure which can be used as an easy-to-interpret metric for the overall quality of the RRA product. For the pan-European approach, gridded observational data E-OBS (*Cornes et al.*, 2018) based on a dense network of stations covering Europe is used to assess reanalysis results. Beside the fact that the spatial aggregation from the finer (UERRA) to coarser (E-OBS) grid obscures possible local problems, E-OBS itself is prone to quality and reliability issues over regions with sparse station coverage as Southeast (SE) Europe (*Cornes et al.*, 2018) This problem is addressed in *Niermann et al.* (2017) performing additional comparisons against regional gridded observational datasets (APGD, NGCD, ROCADA). Hence these sources, being products of National Meteorological Services (NMS) and/or regional initiatives, they generally incorporate many more station series compared to E-OBS. Therefore, it would be expected to produce gridded datasets that are closer to the 'true' climate field (*Cornes*, 2016). Only one of the aforementioned products, however, the Romanian ROCADA (*Birsan and Dumitrescu*, 2014), is situated in SE Europe. Although ROCADA contains many variables, only evaluations for drought-related quantities and not for the temperature are presented in the UERRA-related documentation.

The present work, which is not comprehensive evaluation study, is dedicated to the comparison of the long-term temperature field, reproduced with UERRA MESCAN-SURFEX with the regional gridded dataset CARPATCLIM and the gridded dataset of the Bulgarian NMS ProData. It is worth emphasizing, however, that generally, all observations come with uncertainties, which will impact more or less the output from any such comparison (*Kaiser-Weiss et al.*, 2019). The domains of CARPATCLIM and ProData are in SE Europe, the full time spans with daily temporal resolution of both datasets are considered. The work also try to answer the question: How realistic are the daily minimum and maximum temperature obtained from the MESCAN-SURFEX output in 6-hour temporal resolution?

The article is structured as follows. The considered datasets are described in Section 2 — MESCAN-SURFEX in Subsection 2.1 and CARPATCLIM and ProData in Subsection 2.2. The applied numerical techniques for estimation of t_n , t_d , and t_x , which are rather simple indeed, are explained in Section 3. The core of the article is in Section 4, where the performed comparisons and the obtained results are presented. The concise concluding remarks are in Section 5.

2. *MESCAN-SURFEX and reference datasets*

2.1. *Short Description of MESCAN-SURFEX*

The MESCAN-SURFEX system analysis uses the 2D-analysis system MESCAN (Soci *et al.*, 2016) and the land surface platform SURFEX (Bazile *et al.*, 2017) to generate a coherent surface and soil analysis. The UERRA-NWP HARMONIE-ALADIN at 11 km grid spacing is used as a starting point to further downscaling. For the forcing for the SURFEX surface and soil model, downscaling was only done through interpolation by Météo-France. These downscaled fields are refined with additional data in a surface analysis with observations that are not used in the 3D reanalysis, resulting in the MESCAN-SURFEX at 5.5 km grid spacing (Bazile *et al.*, 2017). It is run offline, i.e., without feedback to the atmospheric analysis. Beside the other parameters, MESCAN-SURFEX produces temperature at 2 m above the surface in 6-hour temporal resolution, i.e., at 00, 06, 12, and 18 UTC for the period 1961–2018.

2.2. *Reference datasets - CARPATCLIM and ProData*

We use two independent data sets as reference in this study; both of them are based on surface measurements and are in form of gridded digital maps. Climate of the Carpathian Region (CARPATCLIM; <http://www.carpatclim-eu.org>) is a collaborative international project over the area, developed with the joint effort of NMSs from all the Carpathian countries. Main aim of the project was to enhance the climatic information in the region by providing comprehensive, temporally and spatially homogeneous data sets of the main meteorological variables, and the corresponding metadata (Cheval *et al.*, 2014; Lakatos *et al.*, 2013a). Besides the common software, the harmonization of the results across country borders was promoted also by near border data exchange. The database of CARPATCLIM is produced at daily temporal resolution, covers the period 1961–2010 for the Carpathian Region (44°N–50°N and 17°E–27°E) with 0.1° grid spacing. It provides relevant outcomes, suitable for various applications in the regional climatology (Birsan *et al.*, 2014; Lakatos *et al.*, 2013b). Comprehensive studies as Spinoni *et al.* (2015) prove the suitability of CARPATCLIM for elaboration of objective climatologies and estimation of the trends of key variables. It is worth emphasizing, that CARPATCLIM is used also as reference in the UERRA project (Cornes, 2016), although not for evaluation of MESCAN-SURFEX.

ProData is a product of the Bulgarian NMS and runs operationally since the second half of 2013. ProData assimilates ground-based in situ measurements from more than 140 automatic weather and hydrological stations, satellite-derived products, and auxiliary data and produces estimates of 10 near-surface meteorological parameters. The ProData domain covers Bulgaria entirely with

horizontal resolution of 0.045° , which is very close to the native resolution of MESCAN-SURFEX. The main purpose of the system is to serve as a reliable source of consistent meteorological information with high spatial and temporal (1 hour) resolution with minimal latency from the input data acquisition time (Chervenkov *et al.*, 2017). The everyday practical experience as well as validation against independent data (synoptic measurements and satellite-derived products, see Chervenkov and Slavov (2021) for details) reveals the high performance skill of the system. Beyond its operative applications, the system is used recently in climatological studies (Chervenkov and Slavov, 2020; Ivanov and Chervenkov, 2019) as source of valuable information.

The main characteristics of the considered datasets are listed in *Table 1*, and the orography of the model domain as well as the spatial extent of CARPATCLIM and ProData is shown in *Fig. 1*.

Table 1. Overview of the main characteristics of the considered datasets

	spatial/temporal coverage	spatial/temporal resolution
MESCAN-SURFEX	CORDEX-EUR11/1961–2018	5.5 km×5.5 km/6-hourly
CARPATCLIM	Carpathian Basin/1961–2010	$0.1^\circ \times 0.1^\circ$ /daily
ProData	Bulgaria/2014–2018	$0.045^\circ \times 0.045^\circ$ /1-hourly

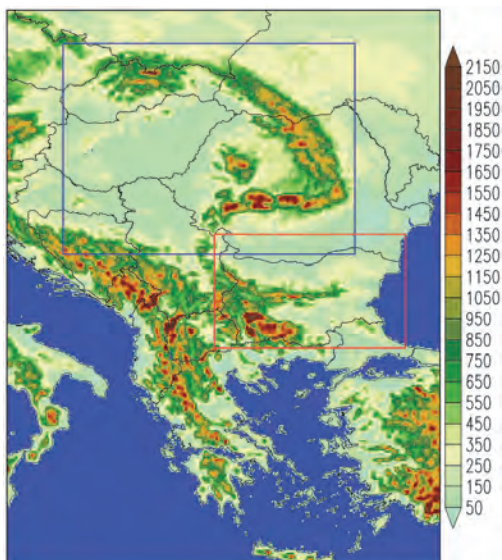


Fig. 1. Orography of the model domain in 0.05° resolution. The borders of CARPATCLIM and ProData are shown in blue and red, respectively.

3. Estimation of the temperatures

The complex nature of missing daily t_n , t_d , and t_x is a problem in many climatological applications. There are different ways to calculate daily mean temperature from data collected at different times of the day. In many countries, including the US, the approach is to average the minimum and maximum temperatures observed. In other countries, a linear combination of measurements taken at different times of the day is used, sometimes including the minimum and maximum as well. For example, the Nordic countries each have a different linear combination of data, depending on the frequency of recorded observations (*Ma and Guttorp, 2013*), while Germany employs yet another linear combination of data (see *Dall'Amico and Hornsteiner (2006)* and citations therein). The World Meteorological Organization defines the mean daily temperature as the 'mean of the temperature observed at 24 equidistant times in the course of a continuous interval of 24 hours, or a combination of temperatures observed at less numerous times, so arranged as to depart as little as possible from the mean defined above' (*Dall'Amico and Hornsteiner, 2006*). In the present work, the mean daily temperature is computed as average from five values: the MESCAN-SURFEX-output at 06, 12, 18 UTC and both values which bound the current day – at 00 UTC of the same day and 00 UTC of the next one. This method is most natural, physically consistent, and, not at last, close to definition above in the considered case. The methods used for estimates of daily temperature minima and maxima vary also greatly in complexity and sophistication. Traditionally, tabulated values have been published for a given region or country. At the other end of the scale, some groups have analyzed detailed daily time series of temperatures to prepare synthetic data (*Huld et al., 2006*). Researchers have relied on a variety of techniques to estimate missing data depending on the region, time of year, spatial distribution of neighboring stations (*Allen and DeGaetano, 2001*), or more recently, remote sensing products. Other methods rely on temporal interpolation by means of polynomial fitting or implementation of piecewise cosine functions (*Huld et al., 2006*). Such methods attempt to reproduce the diurnal temperature cycle using additionally data for the sunrise/sunset times. Hence our task is limited to the estimation of the extreme temperatures only, the most simple solution, based on the polynomial fitting, is to find a local polynomial of 2nd order around the time horizon with the minimum/maximum (hereafter minimum for the sake of brevity) temperatures:

$$T(t) = At^2 + Bt + C, \quad (1)$$

where T is the temperature, t is the time, and A , B , and C are the coefficients of the polynomial, which passes through the point of the minimum temperature and the two neighboring points. This popular and simple procedure, which is ought

to find the minimum in a single iteration, is technically called parabolic interpolation (*Press et al.*, 1986; *Stoer and Bulirsch*, 2002). If we apply the quadratic Lagrange interpolating polynomials, then:

$$T(t) = T_1 \frac{(t-t_2)(t-t_3)}{(t_1-t_2)(t_1-t_3)} + T_2 \frac{(t-t_1)(t-t_3)}{(t_2-t_1)(t_2-t_3)} + T_3 \frac{(t-t_1)(t-t_2)}{(t_3-t_1)(t_3-t_2)}, \quad (2)$$

where $T_1 = T(t=t_1)$, $T_2 = T(t=t_2)$, and $T_3 = T(t=t_3)$. The time of minimum temperature t_{\min} can be found by simple differentiation of the polynomial in Eq. (2):

$$t_{\min} = \frac{1}{2}(t_1 + t_2) + \frac{1}{2} \frac{(T_1 - T_2)(T_2 - T_3)(T_3 - T_1)}{(t_2 - t_3)T_1 + (t_3 - t_1)T_2 + (t_1 - t_2)T_3} \quad (3)$$

Finally, we get the minimum temperature T_{\min} , substituting Eq.(3) in Eq.(2): $T_{\min} = T(t=t_{\min})$.

This is the generic case for sufficiently smooth functions, in particular the near-surface temperature in relatively calm weather conditions. The method is also applicable if the minimum temperature is in internal point (i.e., not at 00 UTC of the current or 00 UTC of the next day), and its accuracy depends on the distance between the interpolation knots. From meteorological point of view, however, its main weakness is obvious: every (sudden enough) change of the diurnal thermal cycle, caused by events with characteristic time scale smaller than the distance between the knots (in our case: 6h), leads to deviation which the method can not encounter. Typical examples are the various convection-related events, which are frequent for the considered domain. Thus, the method could be treated only as pragmatic workaround in cases of absence of data for the extreme temperatures, like the present situation with MESCAN-SURFEX. According to our main idea, if the biases of the extreme temperatures are comparable with the bias of the mean temperature, which is computed much more consistently, the method, at least in certain extent, could be accepted as justified. Thus, we will try to estimate empirically the validity of this approach for long-term data series, comparing its outcomes with reference data, in order to assess its suitability for climatological applications.

4. Comparison and discussion

The UERRA reanalysis datasets are freely available. The analyses are downloadable from the Copernicus Climate Data Store (CDS; <https://cds.climate.copernicus.eu>) and, applying the functionality of the python package cdsapi, we get directly the necessary data.

Due to pragmatic reasons, we selected a sub-domain over Southeast Europe, shown in *Fig. 1*, constraining the computations over the land only. The MESCAN-SURFEX dataset has a native resolution 5500×5500 m (see *Table 1* again) and Lambert Conic Conformal projection, and it is distributed in GRIB2 format, which can be handled with specific tools, at best the *ecCodes* library of the European Centre for Medium Range Weather Forecasts (ECMWF). In order to prepare testbed for further computations, we regridded the temperature data to the regular $0.05^\circ \times 0.05^\circ$ grid with 301×321 gridcells using a first-order conservative remapping procedure. The computation of the daily mean, as well as the extreme temperatures, is performed according to the methodology described in Section 2 for the full available time span of the MESCAN-SURFEX data set 1961–2018. For the present analysis, we mapped the MESCAN-SURFEX intercept over CARPATCLIM and ProData in the native grid of both products. All GRIB and netCDF file manipulations are performed with the powerful and convenient collection of the Climate Data Operators (<https://code.zmaw.de/projects/cdo>), compiled with *ecCodes*.

Comparison of the cumulative and density probability functions of the reference and the model is frequently used within climate modeling (*Harding et al.*, 2015). The quantile-quantile (Q-Q) plot, which is a plot of the quantiles of the first data set against the quantiles of the second one, is a commonly used technique for checking whether two data sets are distributed differently (*Gadzhev et al.*, 2020). The method could be generalized for two dimensional samples, limiting the comparison for some key quantiles, for example, the 10th, 25th (lower quartile), 50th (median), 75th (upper quartile), and 90th percentiles, traditionally noted as X10, X25, X50, X75, and X90, respectively. Similar approach, based on 95% quantiles and interquantiles (between the 10% and the 90% quantiles) is applied in the comprehensive UERRA-evaluation study (*Niermann et al.*, 2017) for comparison against gridded station observations. The quantiles of the minimum, mean, and maximum temperatures from MESCAN-SURFEX for the time span of CARPATCLIM (1961–2010) and ProData (2014–2018) are superimposed to their corresponding counterparts from CARPATCLIM and ProData, as shown in *Figs. 2* and *3*.

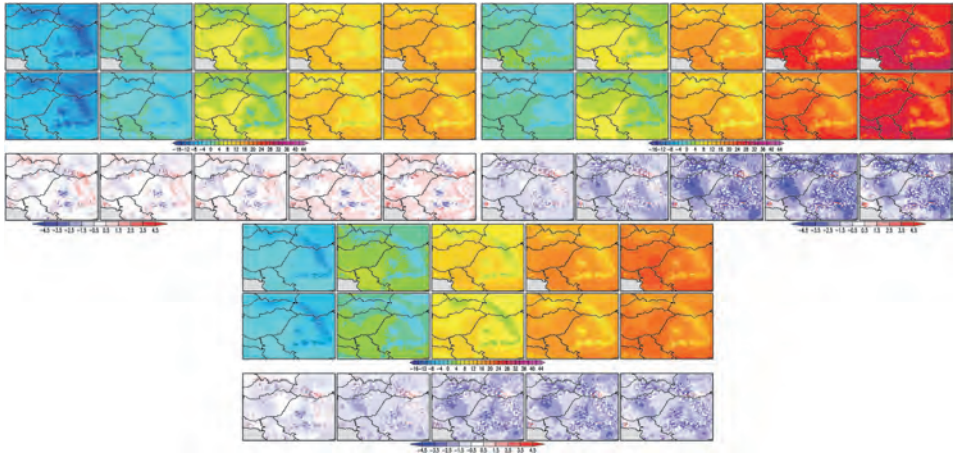


Fig. 2. Upper left corner: tnX10, tnX25, tnX50, tnX75, and tnX90 from CARPATCLIM (first row, reference) and MESCAN-SURFEX (second row), as well as the bias between them (third row); upper right corner: same as in the upper left corner, but for tx; bottom middle: same as in the upper left corner, but for td. The units are $^{\circ}\text{C}$.

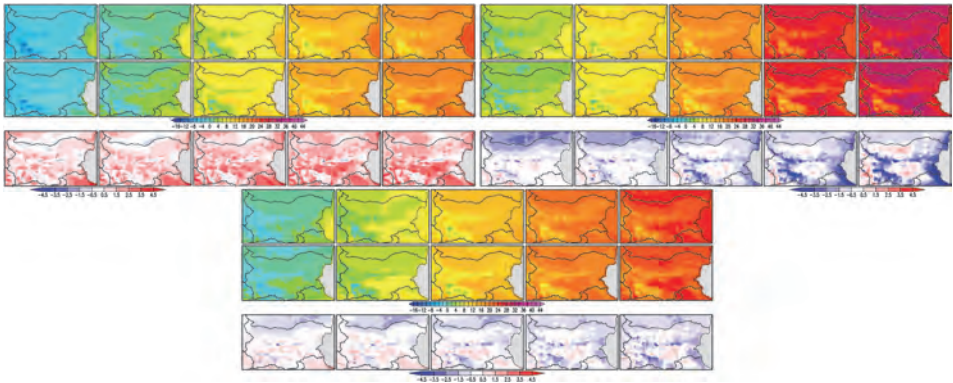


Fig. 3. Same as Fig. 2, but for ProData used as reference.

Fig. 2 shows that the minimum temperature is relatively well reproduced: the spatially prevailing bias is between -0.5°C and 0.5°C . The maximum temperature is, however, negatively biased with values about roughly -3°C – -2°C . Mean temperatures are also underestimated with average biases of about -1.5°C . There is neither apparent geographical structure of the bias, nor clear dependence of the magnitude of the deviation from the value of the percentile. Thus, the bias for the upper tail of the distribution of the maximum temperature (txX90) is not generally bigger than the median txX50. The spatially dominating bias of the minimum temperature in Fig. 3 is positive, but, surprisingly, the extreme low values, i.e., tnX10, are with the smallest bias of

about 0.5 °C–1.5 °C. The spatial distributions of the tx-percentiles in *Fig. 3* are the single ones with clear altitudinal dependence — hence the bias over the flat regions is near to zero, its value over the mountains is negative, with increasing tendency from the lower to the higher percentiles. Over the Rila Mountain, in the southwestern corner of the domain, the model underestimates the reference with more than 4 °C. It is worth emphasizing that this issue could be explained with the poor station coverage there, which affects the ProData product. Same could be the reason for the strong disagreement over the southeastern corner of the domain; hence ProData utilizes only Bulgarian (and not Turkish) observations. The bias of the mean temperature is without clear spatial structure; its values are generally between -1.5 °C and 1.5 °C.

Popular statistical scores as the root mean square error (RMSE) and mean bias (MB) are frequently used in the climatology as estimators of the model score (*Chervenkov and Slavov, 2019*) and uncertainty measures in the UERRA project (*Cornes, 2016; Kaiser-Weiss et al., 2019; Niermann et al., 2019*). The spatial distributions of the MB and RMSE of the comparison of tn, td, and tx between UERRA and reference datasets are shown in *Fig. 4*. *Fig. 4* reveals that the mean and maximum MESCAN-SURFEX-temperatures are, compared with CARPATCLIM, negatively biased with average values of roughly -1.5 °C. The spatially dominating MB of td is near zero. The biggest bias is (according its absolute value and among all performed comparisons) the positive bias of the comparison MESCAN-SURFEX-tn – ProData-tn, shown in the fifth column of *Fig. 4*. Its values are, over limited area indeed, up to 3.5 °C. The peak values of the MB for td and tx are negative and clearly situated over the mountain heights.

The RMSE of both panels in *Fig. 4* are generally in the interval 0.5–2.5 °C with slightly smaller values for td in the evaluation against ProData. A vertical gradient, not well expressed indeed, could be distinguished, mainly over the main Carpathian ridge for tn and the Balkan and Rila Mountain in Bulgaria.

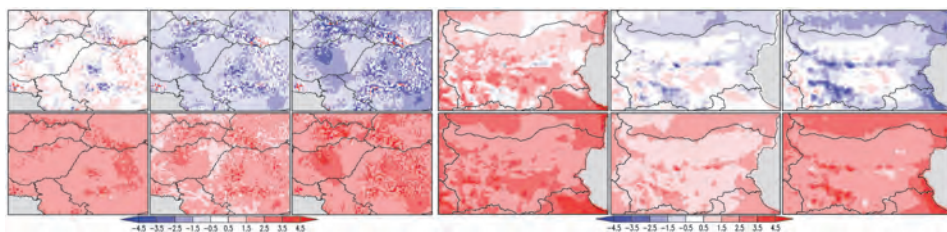


Fig. 4. MB (first row) and RMSE (second row) of the performed comparisons between MESCAN-SURFEX and CARPATCLIM (left panel) and ProData (right panel). tn, td, and tx are in the first, second, and third column of each panel, respectively. The units are °C.

The comparison results of any RRA-validation study depend on the location and the time scale and spatial scale considered, and thus, any generalization could be accepted with caution (*Kaiser-Weiss et al., 2019*). The applied method, namely comparison against gridded observational datasets, has also limitations, rooted mainly in the specific weaknesses of the reference data (*Niermann et al., 2017*). As it was demonstrated, however, confidence in both products can be gained when they agree in their general spatial patterns, or in their magnitude, or when their differences can be explained (e.g., when differences get larger for areas of poor data coverage used for the gridded fields).

5. Conclusion

The RRA within UERRA and more especially MESCAN-SURFEX, which has the highest horizontal spacing, constitute an attractive new source of highly-resolved spatial and temporal meteorological data. In many cases, for example for the vertical wind profiles, this source has practically no alternative. The performed comparisons of the mean temperature with the regional data set CARPATCLIM and the national ProData are novel. They reveals that the differences remains under certain limits without, at least not apparent, systematic and spatial pattern. Our opinion is that a part of these biases could be attributed to the principally different nature of the considered data sets, which are practically unavoidable. Obviously, the RRA product MESCAN-SURFEX is able to capture the regional temperature distribution in SE Europe. This conclusion agrees generally with the outcomes of the comprehensive evaluation studies (*Cornes, 2016; Niermann et al., 2017*) adding new results for the region of SE Europe.

The applied method for estimation of the minimum and maximum temperatures, rather simple and schematic, as emphasized in Section 3, is intended as pragmatic workaround in case of absence of data for these parameters. Nevertheless, the obtained results show biases generally comparable to the biases of the mean temperature. Such approach seems justified for specific applications when the highest available resolution is crucial (and the use of *tn* and *tx* from coarser resolution RRA, as for example HARMONIE, is not an option) and/or in case of 'moderate extremes', causing potential pitfalls for threshold applications such as climate indices (*Kaiser-Weiss et al., 2019*).

Conceptually, the UERRA project is the necessary prerequisite before the start of exploitation of unified pan-European RRA, similarly to the global RA. Subsequently, the positive consequences to the end user community will be manifold.

With the global RA running at higher resolution (i.e., ERA-5 with grid resolution of about 30 km), the RRA will benefit from higher quality boundary conditions, and at the same time, the question of added value and estimation of the uncertainties will arise anew (*Kaiser-Weiss et al., 2019*).

The output parameters computed in this study, more specifically the mean daily temperature, could be used as a surrogate for computation for some climate indicators, as for example, agrometeorological indices (*Chervenkov and Slavov 2019; Harding et al., 2015*). The data sets with the daily mean, as well as the extreme temperatures, are in standard form (GrADS binary/descriptor files and netCDF files) could be supplied from the corresponding author upon request.

Acknowledgments: This work is based on the UERRA EU FP7 Collaborative Project, Grant agreement 607193. Hence this study is entirely based on free available data and software, the authors would like to express their deep gratitude to the organizations and institutions (UERRA project, CARPATCLIM, MPI-M, UNI-DATA, Copernicus Data Store), which provides free of charge software and data. Without their innovative data services and tools this work would be not possible. Personal thanks to I. Tsonevsky from ECMWF for the cooperation. Not at least we thank to the anonymous reviewers for their comments and suggestions which led to an overall improvement of the original manuscript.

References

- Allen, R.J. and DeGaetano, A.T., 2001: Estimating Missing Daily Temperature Extremes Using an Optimized Regression Approach. *Int. J. Climatol.* 21, 1305–1319.
<https://doi.org/10.1002/joc.679>
- Bazile, E., Abida, R., Verelle, A., Le Moigne, P., and Szczypta, C., 2017: MESCAN-SURFEX surface analysis, deliverable D2.8 of the UERRA project.
<http://www.uerra.eu/publications/deliverable-reports.html>
- Birsan, M.-V. and Dumitrescu, A., 2014: ROCADA: Romanian daily gridded climatic dataset (1961–2013) V1.0. Administratia Nationala de Meteorologie, Bucuresti, Romania.
<https://doi.org/10.1594/PANGAEA.833627>
- Birsan, M.-V., Dumitrescu, A., Micu, D. M., and Cheval, S., 2014: Changes in annual temperature extremes in the Carpathians since AD 1961. *Nat. Hazards*, 74, 1899–1910.
<https://doi.org/10.1007/s11069-014-1290-5>
- Chervenkov, H. and Slavov, K., 2019: STARDEX and ETCCDI Climate Indices Based on E-OBS and CARPATCLIM. Part Two: ClimData in Use, in G. Nikolov *et al.* (Eds.): NMA 2018, LNCS 11189, 368–374. <https://doi.org/10.1007/978-3-030-10692-8>
- Chervenkov, H. and Slavov, K., 2021: Modelled versus Satellite Retrieved Estimation of the Direct Normal Irradiance and the Sunshine Duration over Bulgaria, *Advanced Computing in Industrial Mathematics, Studies in Computational Intelligence*, vol. 961, I. Georgiev, K. Georgiev (eds), Springer (in press)
- Chervenkov, H. and Slavov, K., 2021: Solar Radiation Modelling for Bulgaria Based on Assimilated Surface Data, *Advanced Computing in Industrial Mathematics, Studies in Computational Intelligence*, vol. XXX, I. Georgiev, K. Georgiev (eds), Springer (in press)
- Chervenkov, H., Spiridonov, V., Artinyan, E., Neytchev, P., Slavov, K., and Stoyanova, M., 2017: The Operative System ProData — Part One: Current Stage and Recent Improvements. *Bul. J. Meteor Hydro* 22, 73–86.
- Cheval, S., Birsan, M.-V., and Dumitrescu, A., 2014: Climate variability in the Carpathian Mountains Region over 1961–2010. *Glob. Planet. Change* 118, 85–96.
<https://doi.org/10.1016/j.gloplacha.2014.04.005>
- Cornes, R., 2016: Assessment of the potential for enhancing the gridding resolution in parts of Europe, together with more comprehensive comparisons with NMHS derived gridded products, deliverable D1.11 of the UERRA project. <http://www.uerra.eu/publications/deliverable-reports.html>

- Cornes, R., van der Schrier, G., van den Besselaar, E.J.M. and Jones, P.D., 2018: An Ensemble Version of the E-OBS Temperature and Precipitation Datasets. *J. Geophys. Res. Atmos.*, 123. <https://doi.org/10.1029/2017JD028200>
- Dall'Amico, M. and Hornsteiner, M., 2006: Simple Method for Estimating Daily and Monthly Mean Temperatures from Daily Minima and Maxima. *Int. J. Climatol.* 26, 1929–1936 <https://doi.org/10.1002/joc.1363>
- Gadzhev G., Ivanov V., Valcheva R., Ganey K., and Chervenkov H. (2021) HPC Simulations of the Present and Projected Future Climate of the Balkan Region. In: Dimov I., Fidanova S. (eds) Advances in High Performance Computing. HPC 2019. Studies in Computational Intelligence, vol 902, 234–248 Springer, Cham. https://doi.org/10.1007/978-3-030-55347-0_20
- Harding, A. E., Rivington, M., Mineter, M. J., and Tett, S. F. B., 2015: Agrometeorological indices and climate model uncertainty over the UK. *Climat. Change* 128, 113–126. <https://doi.org/10.1007/s10584-014-1296-8>
- Huld, T. A., Šúri, M., Dunlop, E., and Fabio, M., 2006: Estimating average daytime and daily temperature profiles within Europe. *Environ. Modell. Software* 21, 1650–1661. <https://doi.org/10.1016/j.envsoft.2005.07.010>
- Ivanov, V. and Chervenkov, H., 2021: Modelling Human Biometeorological Conditions Using Meteorological Data from Reanalysis and Objective Analysis —Preliminary Results, *Advanced Computing in Industrial Mathematics, Studies in Computational Intelligence*, vol. 961, I. Georgiev, K. Georgiev (eds), Springer (in press)
- Kaiser-Weiss, A. K., Borsche, M., Niermann, D., Kaspar, F., Lussana, C., Isotta, F. A., van den Beselaar, E., van der Schrier, G., and Undén, P. Added value of regional reanalyses for climatological applications 2019: *Environ. Res. Commun.* 1, 071004 <https://doi.org/10.1088/2515-7620/ab2ec3>
- Lakatos, M., Bihari, Z., Szentimrey, T., Szalai, S. and the CARPATCLIM project Team, 2013a: Climate of the Carpathian Region - summary of the CarpatClim project. 3th EMS Annual Meeting & 11th European Conference on Applications of Meteorology (ECAM) — 09–13 September 2013, Reading, United Kingdom. <http://presentations.copernicus.org/EMS2013-501presentation.pdf>
- Lakatos, M., Szentimrey, T., Bihari, Z., and Szalai, S. 2013b: Investigation of climate extremes in the Carpathian region on harmonized data. *Int. Scient. Conf. on Environmental Changes and Adaptation Strategies*, Sep., 2013.
- Ma, Y. and Guttorp, P., 2013: Estimating daily mean temperature from synoptic climate observations. *Int. J. Climatol.* 33, 1264–1269. <https://doi.org/10.1002/joc.3510>
- Niermann D., Borsche M., Kaiser-Weiss A. K., and Kaspar, F., 2019: Evaluating renewable energy relevant parameters of COSMO-REA6 by comparing against station observations, satellites and other reanalyses. *Met. Zeit.*, Vol. 28, No. 4, 347–360 <https://doi.org/0.1127/metz/2019/0945>
- Niermann, D., Borsche, M., van den Besselaar, E., Lussana, C., Isotta, F., Frei, C., Kaiser-Weiss, C., Cantarello, L., Tveito, O. E. van der Schrier, G., Cornes, R., de Vreede E., and Davie, J., 2017: Scientific report on assessment of regional analysis against independent data sets. deliverable D3.6 of the UERRA project, <http://www.uerra.eu/publications/deliverable-reports.html>
- Press, W. H., Flannery, B. P., Teukolsky, S. A., and Vetterling, W. T., 1986: *Numerical Recipes: the Art of Scientific Computing*. Cambridge University Press, Cambridge, UK. [https://doi.org/10.1016/S0003-2670\(00\)82860-3](https://doi.org/10.1016/S0003-2670(00)82860-3)
- Ridal, M., Schimanke, S., and Hopsch, S., 2018: Documentation of the RRA system: UERRA. deliverable D322 Lot1.1.1.2 in the scope of the Copernicus service C3S 322 Lot1, available via Copernicus.
- Sillmann, J. and Röckner, E., 2008: Indices for extreme events in projections of anthropogenic climate change *Climatic Change* 86, <https://doi.org/83.10.1007/s10584-007-9308-6>
- Spinoni, J., Szalai, S., Szentimrey, T., Lakatos, M., Bihari, Z., Nagy, A., Németh, A., Kovács, T., Mihic, D., Dacic, M., Petrovic, P., Kržič, A., Hiebl, J., Auer, I., Milkovic, J., Štěpánek, P., Zahradníček, P., Kilar, P., Limanowka, D., Pyrc, R., Cheval, S., Birsan, M.-V., Dumitrescu, A., Deak, G., Matei, M., Antolovic, I., Nejedlík, P., Štastný, P., Kajaba, P., Bochníček, O., Galo, D., Mikulová, K., Nabyvanets, Y., Skrynyk, O., Krakovska, S., Gnatiuk, N., Tolasz, R., Antofie, T.,

- and Vogt, J. 2015: Climate of the Carpathian Region in the period 1961–2010: climatologies and trends of 10 variables. *Int. J. Climatol.* 35,1322–1341. <https://doi.org/10.1002/joc.4059>
- Soci, C., Bazile, E., Besson, F., and Landelius, T., 2016: High-resolution precipitation re-analysis system for climatological purposes. *Tellus A*: 68, <https://doi.org/10.3402/tellusa.v68.29879>
- Stoer, J. and Bulirsch, R., 2002: Introduction to Numerical Analysis, Texts in Applied Mathematics, 3rd ed., Vol. 12, Springer, New York. <https://doi.org/10.1007/978-0-387-21738-3>
- Unden, P., 2018: UERRA: Final Report, Project No.: 607193, Period number: 3rd Ref: 607193 UERRA Final Report-13 20180319 112103 CET.pdf

IDŐJÁRÁS

Quarterly Journal of the Hungarian Meteorological Service
Vol. 125, No. 1, January – March, 2021, pp. 137–149

Evapotranspiration and yield components of soybean

Angela Anda*, László Menyhárt, and Brigitta Simon

Hungarian University of Agriculture and Life Sciences, Gödöllő
Georgikon Campus of Keszthely
Festetics György út 7, 8360 Keszthely, Hungary

**Corresponding author E-mail: anda.angela@uni-mate.hu*

(Manuscript received in final form April 3, 2020)

Abstract— Observation was conducted to determine the impact of water deprivation under flowering on the yield components of soybean at Keszthely, in the growing seasons between 2017 and 2018. The soybean represents an artificial ecosystem in this study. Three water levels designated as full watering in traditionally operated evapotranspirometer (ET), water withdrawal under crop flowering in modified evapotranspirometer (RO), and rainfed (P) crops were used. In RO treatments, the crops received half of the water based on the amount of unlimited water supply. Irrespective of variety, the highest water uses were obtained in ET, while the lowest ones were observed in RO over both growing seasons. Surprisingly, in spite of different variety standards provided by the crop breeders, and irrespective to water supply, no significant impact in actual evapotranspiration rate, ET_a , between the two varieties was observed. Significant impact in soybean water losses between the treatments was observed in RO as compared to the evapotranspiration of crops with unlimited watering.

There was no significant difference in yield components between soybean varieties of rainfed treatments. As compared to variety Sigalia (Sig), variety Sinara (Sin) produced better yield in unlimited water level over 2017 weather conditions, and its seed had greater oil and lower protein content in RO treatment in 2018 conditions.

Key-words: soybean, evapotranspiration, seed yield, yield components

1. Introduction

Evapotranspiration rate (ET_a), the largest energy consumer of crop canopies' water budget, is also the link between mass and energy exchanges. Solar radiation interacts with ET_a in a complex manner that makes this investigation very complex. Anapalli *et al.* (2018) called the attention for the missing research work integrating crop water demands (ET_a) with available water supplies (rainfall and irrigation) in water management decision making. Therefore, new information related to plant ET_a , including soybean, is required to determine robust solutions for irrigation scheduling even in Hungary.

Irrigated soybean's ET_a sum of 650 mm by Candogan *et al.* (2013) in Turkey was close to the water loss result in the treatment with unlimited watering. However, ET_a totals of rainfed soybean amounting 300 mm in China (Wei *et al.*, 2015), agreed with those results of water withdrawn one in this observation.

Soybean (*Glycine max* (L.) Merr.) is not the most important arable crop in Hungary occupying of about 50–60 thousand ha harvest area, that account for less than 1% of the total crop growing area. Nevertheless, the percentage of soybean growing area, among other arable crops, is permanently increasing. Nowadays, the majority of soybean is seeded under rainfed conditions. Due to the local impacts of global warming, the uneven seasonal distribution of precipitation in Hungary, the increasing importance of irrigation can be predicted in the near future. The high protein and oil content of the seeds make this crop irreplaceable source of feed for livestock, nutrients for human, and biofuel resources as well (Aydinsakir, 2018). The number of soybean seed users is increasing worldwide.

The most sensitive stage of soyabean to water deficit is the flowering. Kross *et al.* (2015) reported that soybean was more susceptible to extreme weather conditions between reproductive stages R4 and R6 (flowering and pod formation), when water deficiencies resulted in significant seed loss. Reduction in soybean yield varied widely from 24% (Momen *et al.*, 1979) to 45% (Candogan *et al.*, 2013) due to the lack of water during flowering. Limiting water is the main factor that contributes to the potential yield decline under field conditions. Although the quadratic relationship obtained through comparison between seed yield and ET_a totals reported by Candogan *et al.* (2013) should also be accounted.

The aim of the study was to investigate the effect of soybean's water deprivation on the seed yield and its components. Soybean's growth indicators applied in the analysis were the total aboveground biomass (*TDM*), shoot dry matter (*DM*), seed yield, 1000-seed weight, protein and oil contents. Out of these six variables, the protein and oil contents are qualitative traits, while all the remaining four ones are quantitative traits. These properties are affected by water stress, and they are indicative of final soybean production including seed yield. This analysis served as an example for crop-water relation in a such artificial (field grown) ecosystem as the soybean is.

2. Materials and methods

The study of actual evapotranspiration, ET_a , and yield components in soybean (*Glycine max*, (L.) were carried out at the Agrometeorological Research Station, ARS, Keszthely, during the growing seasons between 2017 and 2018. Two soybean varieties Sinara (Sin) and Sigalia (Sig), widely cultivated in Hungary, have different water demands; Sin is a water stress-tolerant variety, while Sig is bred for “normal” weather conditions.

Three water levels are included in the study:

- unlimited watering in evapotranspirometer’s growing chambers (ET),
- water deprivation in half; water supply of modified evapotranspirometers were restricted to every second day during flowering (RO), and
- rainfed crops (P).

In case of RO, the rainfall was excluded by means of mobile rainout shelters (2.5 m long, 4.5 m wide, 2–2.5 m height). The technical solution of the shelters and the operation of the evapotranspirometer in RO were documented in *Anda et al.* (2019).

Due to the fixed nature of the evapotranspirometer, six growing chambers of Sin and six growing chambers of Sig were arranged in two complete blocks with three replications on the northern side of the ARS. Rainfed plots, P, were placed behind the block of the evapotranspirometers (50 m wide and 60 m long for each soybean variety).

To measure the daily evapotranspiration of soybean, a Thornthwaite-Mather type compensation evapotranspirometer was used. Presentation in water losses of different treatments was based on phenological phases. Daily water uses were also summed up for the whole vegetation period.

At the ARS of Keszthely (latitude: 46°44'N, longitude: 17°14'E, elevation: 124 m above sea level), a QLC-50 climate station (Vaisala, Helsinki, Finland) with a pyranometer (Kipp & Zonen Corp., Delft, the Netherlands) are operational. Combined air temperature (T_a) and humidity sensors are placed at a standard height of 2 m above the surface level. Signals from meteorological sensors are collected every 2 seconds, and 10-min averages are logged.

The crops were sown at the end of April in 2017, and at the beginning of May in 2018 applying conventional tillage (the plant density was 40 plant m⁻²; the harvest population was approximately 25,000–30,000 plants ha⁻¹). Phenological phases were recorded using the scale of *Fehr and Caviness* (1977). Parallel with evapotranspirometer’s growing chambers, randomly selected five subplot’s (2 m×2 m) aboveground biomass (*TDM*) was harvested in each variety at the beginning of each September. *TDM* was oven-dried at 65 °C for constant weight. Seed of soybean was separated from other yield components through threshing the pods by hand. Their weights were adjusted to 13% moisture. 1000-grain

weight was also weighed. Inframatic 9200 NIR Grain Analyzer (PerkinElmer, US) was used to determine the protein and oil content of seeds on dry-matter basis.

Used statistics

Principal component analysis (PCA) was used to visualize the data observed in the 6-dimensional space of the yield variables (TDM, shoot dry matter (DM), seed yield, 1000-grain weight, protein and oil contents). The PCA analysis is performed on a data table representing observations described by several dependent variables, which are, in general, intercorrelated. Its goal is to extract the important information from the data table and to express this information as a set of new orthogonal variables called principal components, PCs (Hervé and Williams, 2010). In this study, PCA was used to discover new variables that best describe the measured soybean yield components.

The first two principal components were varimax-rotated to study the structure of the variables. The aim of the varimax-rotation was to find uncorrelated factors so that each yield variable is strongly correlated with one of the factors and weakly correlated with the other. The analysis and plotting were performed in R 3.6.0 (R Core Team, 2019), using the psych (Revelle, 2018) and ggplot2 (Wickham, 2016) packages.

3. Results and discussion

3.1. Weather conditions during soybean growth (May-August 2017 and 2018)

The two growing seasons' T_a values were 1.3 °C and 2.4 °C ($p < 0.001$) higher in 2017 and 2018, respectively, than the climate norm of 1971–2000. Although the difference in seasonal mean T_a between the two studied seasons did not vary ($p = 0.637$), the extremes (T_{max} : maximum and T_{min} : minimum temperatures) showed statistically proved deviation (Fig. 1). In the case of the soybean of tropical origin, the upper T_a limit of proper crop development is 30 °C. The number of days with T_{max} above 30 °C was 38 and 28 during 2017 and 2018, respectively. For the same time period, the variation in mean T_{max} did not differ significantly (2017: 27.4 °C; 2018: 27 °C; $p = 0.440$). Contrary to the increased number of hot days during 2017, the mean T_{min} of this growing season was 1.3 °C lower than that of the average T_{min} over 2018 ($p < 0.001$). High T_a variability was characteristic for the vegetation period of 2017 that might influence the soybean development and yield formation as well.

Limiting to the growing season only, the precipitation in 2017 was characteristic of a dry growing season (44.9% less rainfall than the climate norm; $p = 0.006$), while 2018 received 6.4% higher ($p = 0.046$) rainfall amount in comparison to the climate norm. Rainfall events had an even distribution in both vegetation periods (Fig. 1).

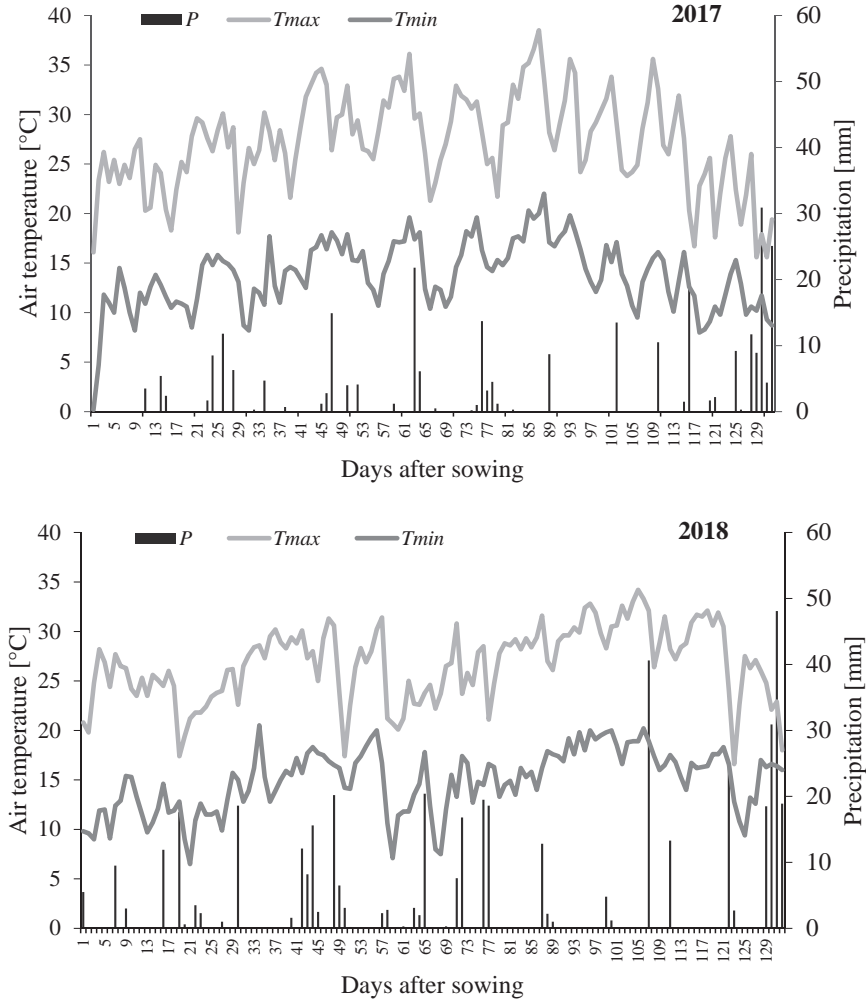


Fig. 1. Daily air temperature extremes (T_{max} and T_{min}) and daily precipitation sums from the beginning of May to the end of August in 2017 and 2018.

3.2. ET_a of soybean in the growing seasons of 2017 and 2018

The soybean began to emerge at the end of April in 2017 and at the beginning of May in 2018. At mid-summers, the soybean reached its maximum leaf area index of around 5.0 and 3.5 in ET and RO treatments, respectively, irrespective of

growing season and/or variety (data not shown). Visible signs of senescence were shown at the end of each August. Later on, due to accelerated senescence, there were no green leaves remaining by the first decade of September. Independently on growing seasons and studied water/variety treatments, the lengths of vegetation cycles hardly varied (115–120 days). The soybean grown in growing chambers of evapotranspirometer (ET) had a few days longer growing seasons than that of the rainfed and RO crops (data is not shown).

Daily mean ET_a was analyzed on the basis of soybean's reproductive phenological stages (Fig. 2) after the *Fehr and Caviness (1977)* scale. The following stages were used: VE – emergence; V3 – third node; V5 – fifth node; R1 – beginning bloom; R2 – full bloom; R3 – beginning pod; R4 – full pod; R5 – beginning seed; R6 – full seed; R7 – beginning maturity; R8 – full maturity. At unlimited watering, a similar seasonal ET_a pattern was observed, irrespective to studied season; low daily mean ET_a of about 1.8 mm were measured in VE, while peak daily ET_a of 9.8 mm in R4 (Sig in 2017) and 7.0 mm in R5 (Sin in 2018) were detected. Independently on variety/season, a somewhat higher daily mean ET_a of 3–4 mm in R8 were observed in comparison to the average ET_a of VE. The ET_a in different phenological phases of the two studied varieties hardly varied. Unexpectedly, during mid-summers, the ET_a of unlimited watering in the warmer 2018 were lower than the ET_a during the cooler 2017. The soybean is known to be extremely sensitive to air humidity as a tropical origin crop; the crops prefer humid (wet) weather conditions. Probably the increased number of days with higher RH during the wetter 2018 explains the lower ET_a related to higher water losses over 2017 (Fig. 3). Probably the driving force of ET_a , the varied air humidity, might impact the ET_a events to a greater extent than the T_a throughout the studied growing seasons.

Water restriction modified both the shape of the ET_a course (smoothed out curves) and the mean ET_a in both seasons. Declines in seasonal mean ET_a rates of water withdrawn crops ranged from 65.8% (Sig 2018; $p < 0.001$) to 77.8% (Sin 2018; $p < 0.001$) during the study period. It is important to mention that the water deprivation was limited to flowering only.

Despite different variety standards provided by the crop breeders and irrespective of water supply, no significant impact in ET_a between the two varieties was observed ($p = 0.244–0.697$).

Seasonal ET_a totals varied from 276.1 (Sig RO) to 669.2 mm (Sin ET) in 2017 and 316.8 (Sin RO) to 720.6 mm (Sin ET) in 2018 among the treatments. The only significant difference of 51.4 mm ($p < 0.017$) in Sin ET_a sums between 2017 and 2018 was registered at unlimited watering. ET_a totals of crops with unlimited water supply in this study were close to the ET_a sum of 650 mm by *Candogan and Yazgan (2016)* measured in irrigated soybean grown in Turkey (40°N, 28°E). The same authors reported that the water withdrawn soybean's ET_a total was at about the half of the fully irrigated ones.

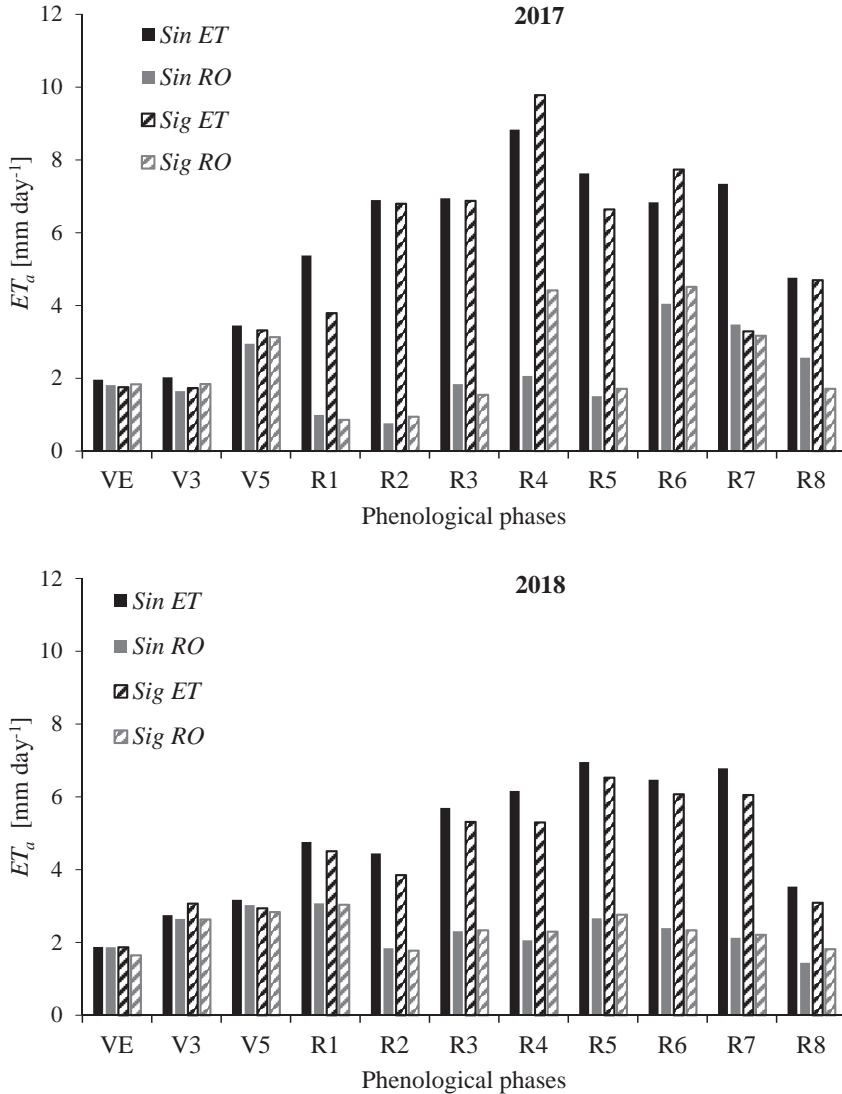


Fig. 2. Daily mean evapotranspiration of phenological stages from soybean in the growing seasons of 2017 and 2018. Abbreviations: ET – evapotranspirometer with unlimited water supply; RO – 50% water deprivation in evapotranspirometer; Sin – Sinara; Sig – Sigalia.

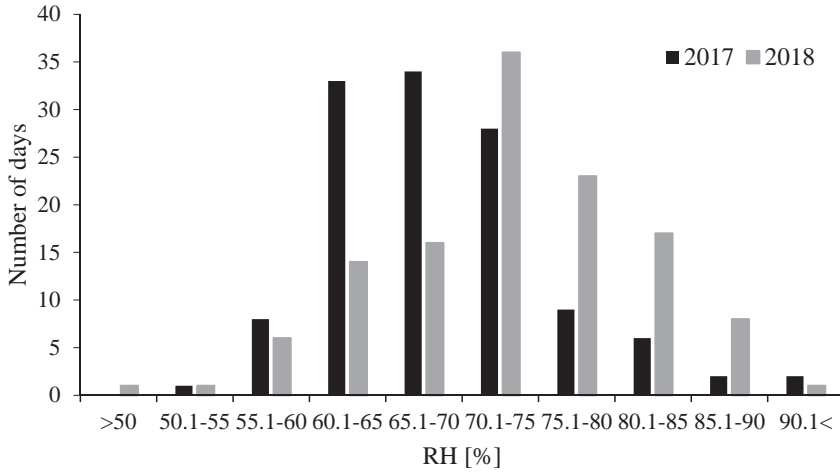


Fig. 3. Distribution of the number of days with different daily mean relative humidity values (%) during the growing seasons of 2017 and 2018 at Keszthely.

3.3. Yield component analysis by PCA

The most important yield component, the seed yield, as an example is emphasized in Fig. 4.

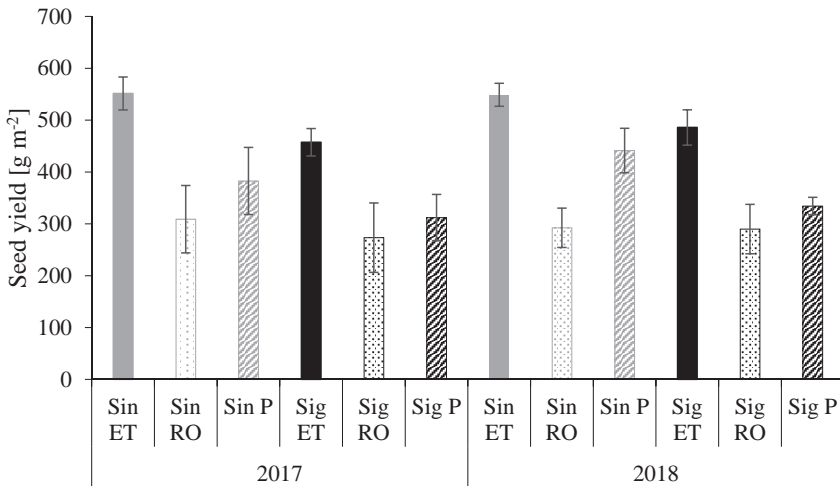


Fig. 4. Seed yield of soybean varieties Sin and Sig in three different water levels (ET: unlimited water; RO: water withdrawn crops; P: rainfed soybean) in 2017 and 2018.

The seed yield advantage of ET was clearly visible in both varieties. Similarly, the detrimental impact of water deprivation also left no doubt in the case of RO treatments.

The yield-related variables were analyzed with principal component analysis (PCA). This analysis has of primary importance as it accounts the impacts of different yield components together. Two PCs were distinguished; PC1 and PC2 accounted for 63% and 20% of the total variance, respectively. Projecting the data onto the plane defined by the first two PCs, the observations from different years were well separated (*Fig. 5*). The loading vectors of the yield-related variables are presented along with the PCA scores in a biplot (*Fig. 6*).

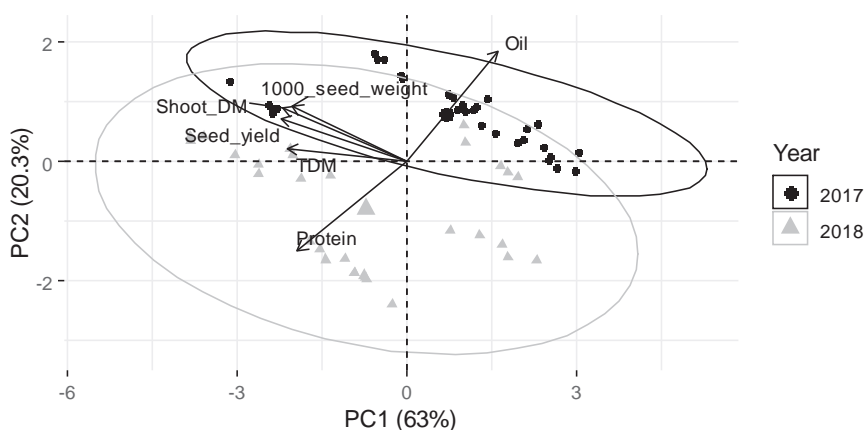


Fig. 5. Observations from the two years projected onto the plane of the first two principal components as well as the loading vectors of the observed variables. PCA was performed with the following six variables: TDM, shoot dry matter, seed yield, 1000-seed weight, protein and oil contents.

It could be seen that PC1 had positive loadings on oil content and negative loadings on all other variables. Observations from different years were presented separately in *Fig. 6*.

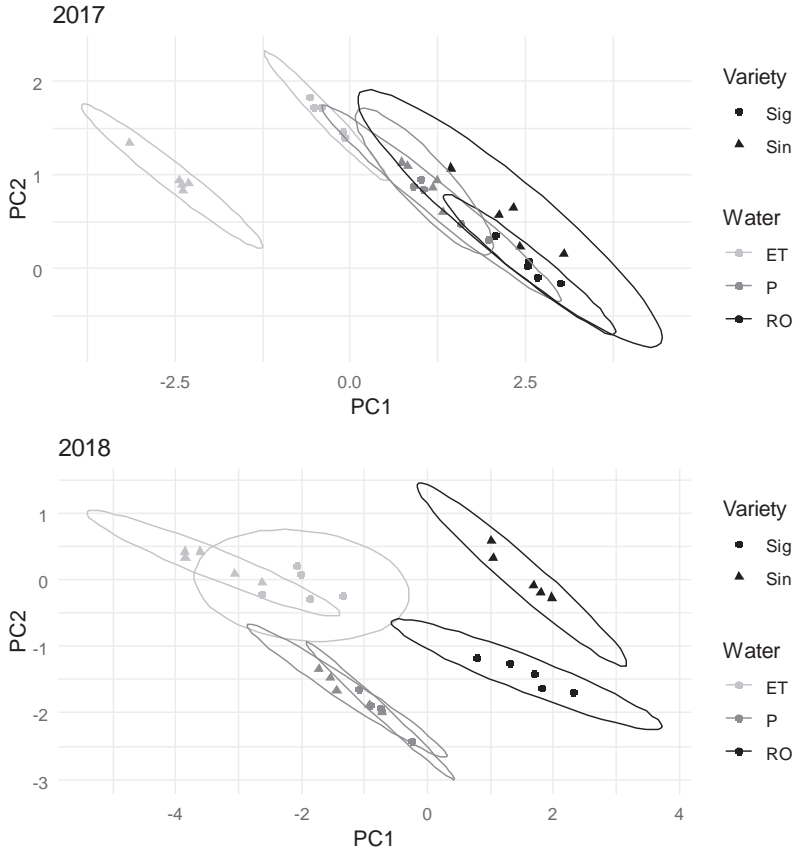


Fig. 6. Observations by variety and treatment projected onto the plane of the first two principal components (upper 2017 and lower 2018). PCs were extracted from the variables: TDM, shoot dry matter, seed yield, 1000-seed weight, protein and oil contents.

Groups from left to right represent treatment-variety combinations with higher oil, lower protein content, and lower yield amount. In 2017, the majority of the treatment-variety combinations overlapped, only the Sin ET was separated along the first principal component. Separation of Sin ET was due to the low oil content and high other values. RO treatments had been shifted to the right due to lower yield amount. Separation of the RO treatments was even more pronounced in 2018, confirming the effect of water withdrawal on the crop yield components. In that year, P and ET treatments were also be well separated by PC2. PC2 was positively correlated with yield quantity related variables and negatively

correlated with protein content. The shift of ET treatments was due to lower protein content and higher yield quantity. Observations from different varieties overlapped in the case of treatment P in both years (*Fig. 6*). In case of the treatment ET, the varieties overlapped in 2018 but were separated in 2017. It was reversed in case of treatment RO, they overlapped in 2017 and were separated in 2018 (*Fig. 6*).

The first two PCs were varimax-rotated to get factors having a high and a low loading on each yield variable. The varimax-rotated PCs and the loading vectors of the yield variables presented a clear structure (see also *Fig. 5*): the separation of the two different seed yield attributes (qualitative ones: oil and protein contents; quantitative ones: 1000-grain weight, TDM, shoot DM, seed yield).

The rotated PCs are called factors. The variance explained by the factors remained 83.3% after the rotation. The first factor explained 50.3% of the total variance. It had high loadings on the seed yield, 1000-grain weight, shoot *DM*, and *TDM* variables. The second factor explained 33% of the total variance, and it had high loadings on the oil and protein contents (*Table 1*).

Table 1. Factor loadings after varimax rotation. The loadings with an absolute value above 0.4 are in bold. The h^2 values are communalities. Loadings are the correlations between the observed variables and the factors. Communality is the proportion of the variance in an observed variable explained by the two factors.

	Factor1	Factor2	h²
Seed yield [kg m ⁻²]	0.885	0.239	0.840
1000-grain weight [g]	0.863	0.131	0.762
Shoot DM [kg m ⁻²]	0.909	0.173	0.856
TDM [kg m ⁻²]	0.739	0.379	0.690
Oil [%]	-0.133	-0.955	0.930
Protein [%]	0.313	0.906	0.919
Proportion of explained variance	0.503	0.33	

The sum of squares of the loadings are called communalities or common variance, they represent the proportion of variance of each variable explained by the factors. Each communality was above 69% (62.9%). The oil and the protein percentages had the highest communalities over 91% (92%). The first factor could be interpreted as the quantity of the seed yield, the second as the quality of the seed. *TDM* was the only variable having relatively high loadings on both factors.

This suggested that *TDM* is connected to both the nutritional content and the amount of the seed. The oil and the protein percentages were strongly negatively correlated as reported by *Marega Fihlo et al.* (2001) and *Latifi* (1989) previously.

4. Conclusions

Water deprivation in soybean changed the shape of ET_a curves and the amount of ET_a totals in both growing seasons. Irrespective of season and/or variety, declines in seasonal mean ET_a rates of RO crops were at about 70% as compared to ET_a measured at unlimited watering.

Surprisingly, significant difference in seed yield between the two varieties with different water needs was only observed at unlimited watering level. Variety Sin showed 18.6% and 12.2% higher seed yield in 2017 and 2018, respectively, as compared to Sig. The negative impact of water deprivation during flowering was almost the same in both soybean varieties.

The almost unmanageable elaborating interactions between the yield components of soybean were analyzed using the PCA. The effects of three water supplies were summarized in the experimental plots presenting the observations projected onto the plane of the first two PCs. Plants in the RO treatment were clearly separated from those in the other treatments towards a greater seed oil content and lower yield mass. There was no significant difference between the varieties in rainfed treatment, P. As compared to variety Sig, variety Sin produced better yield in unlimited water level in 2017, weather conditions and its seed had greater oil and lower protein content in RO treatment in 2018 conditions. After varimax rotation, the loading vectors of the yield variables presented a clear structure. The first factor could be interpreted as the quantity of the soybean yield, while the second as the quality of the seed.

Acknowledgements: The research leading to these results has received funding from the Hungarian Government and the European Regional Development Fund of the European Union in the frames of the Széchenyi 2020 Programme, under project number GINOP-2.3.2-15-2016-00029. The publication was also supported by the EFOP-3.6.3-VEKOP-16-2017-00008 project. The project is co-financed by the European Union and the European Social Fund. Special thanks to Karintia Ltd. for supporting us with good-quality corn-free soybean seed.

References

- Anapalli, S.S., Fisher, D.K., Reddy, K.N., and Wagle, P., 2018: Quantifying soybean evapotranspiration using eddy covariance approach. *Agric. Water Manage.* 209, 228–239. <https://doi.org/10.1016/j.agwat.2018.07.023>
- Anda, A., Simon, B., Soós, G., Teixeira da Silva J.A., and Kucserka, T., 2019: Crop-water relation and production of two soybean varieties under different water supplies. *Theor. Appl. Climatol.* 137, 1515–1528. <https://doi.org/10.1007/s00704-018-2660-9>

- Aydinsakir, K. 2018: Yield and Quality Characteristics of Drip-Irrigated Soybean under Different Irrigation Levels. *Agron. J.* 110, 1473–1481. <https://doi.org/10.2134/agronj2017.12.0748>
- Candogan, B.N. and Yazgan, S., 2016. Yield and quality response of soybean to full and deficit irrigation at different growth stages under sub-humid climatic conditions. *J. Agric. Sci.* 22, 129–144. https://doi.org/10.1501/Tarimbil_0000001375
- Candogan, B.N., Sincik, M., Buyukcangaz, H., Demirtas, C., Goksoy, A.T. and Yazgan, S., 2013: Quality and crop water stress index relationships for deficit-irrigated soybean [*Glycine max* (L.) Merr.] in sub-humid climatic conditions. *Agric. Water Manage.* 118, 113–121. <https://doi.org/10.1016/j.agwat.2012.11.021>
- Fehr, W.R. and Caviness, C.E., 1977: Stages of soybean development. Spec. Rep. 80, Iowa State University, Ames, Iowa.
- Hervé, A. and Williams, L.J., 2010: Principal Component Analysis. John Wiley and Sons, Inc. *WIREs Comp Stat* 2, 433–59. <https://doi.org/10.1002/wics.101>
- Kross, A., Lapen, D.R., McNairn, H., Sunohara, M., Champagne, C., and Wilkes, G., 2015: Satellite and in situ derived corn and soybean biomass and leaf area index: Response to controlled tile drainage under varying weather conditions. *Agr. Water Manage.* 160, 118–13. <https://doi.org/10.1016/j.agwat.2015.06.007>
- Latifi, N., 1989: Yield and morphological response of soybean to time of irrigation and sowing date. *Diss. Abstract Int.* 40, 5088–5098.
- Marega Filho, M., Destro, D., Miranda, L.A., Spinosa, W.A., Carrão-Panizzi, M.C., and Montalván, R., 2001: Relationships among oil content, protein content and seed size in soybeans. *Brazilian Arch. Biol. Technol.* 44, 23–32. <https://doi.org/10.1590/S1516-89132001000100004>
- Momen, N.N., Carlson, R.E., Shaw, R.H., and Arjmand O., 1979: Moisture-stress effects on the yield components of two soybean cultivars. *Agron. J.* 71, 86–90. <https://doi.org/10.2134/agronj1979.00021962007100010022x>
- R Core Team, 2019. R: A language and environment for statistical computing. R Foundation for Statistical Computing, Vienna, Austria. URL: <https://www.R-project.org/>.
- Revelle, W., 2018. psych: Procedures for Personality and Psychological Research, Northwestern University, Evanston, Illinois, USA. <https://CRAN.R-project.org/package=psych> Version = 1.8.12
- Wei, Z., Paredes, P., Liu, Y., Chi, W.W., and Pereira, L.S., 2015. Modelling transpiration, soil evaporation and yield prediction of soybean in North China Plain. *Agric. Water Manage.* 147, 43–53. <https://doi.org/10.1016/j.agwat.2014.05.004>
- Wickham, H., 2016: *Elegant Graphics for Data Analysis*. Springer-Verlag New York.

IDŐJÁRÁS

Quarterly Journal of the Hungarian Meteorological Service
Vol. 125, No. 1, January – March, 2021, pp. 151–166

Synoptic aspects associated with pervasive dust storms in the southwestern regions of Iran

Mahdi Sedaghat ^{1,*}, Hasan Hajimohammadi ², and Vahid Shafaie ³

¹*Department of Geography
Payame Noor University(PNU), Tehran, Iran*

²*Tarbiat Modares University, Tehran, Iran*

³*University of Tehran, Tehran, Iran*

**Corresponding author E-mail: sedaghat.me@pnu.ac.ir*

(Manuscript received in final form March 24, 2020)

Abstract— Dust storm is a natural hazardous phenomenon that affects arid and semi-arid regions of the world the same as Iran. The present research aims to investigate the formation of synoptic patterns of pervasive dust storms (PDSs) in the southwestern regions of Iran. For this purpose, daily data of visibility less than 1000m in 16 synoptic stations (Ilam and Khuzestan provinces) were reviewed during 2004–2017, and 59 PDSs with more than 2 days of duration (overlapped: 70% of the region) were extracted. In practice, mid-level atmospheric data (500, 700, 850 hPa, and sea level pressure (SLP)) with 2.5*2.5 degree resolution (domain: 0-80°E and 10-70°N) were obtained from NCEP/NCAR reanalysis dataset, and the matrix 825*59 of 500 hPa data was performed. Principal component analysis (PCA) with S-mod, were used for extracting synoptic patterns that make PDSs. PCA showed that the first four components ensured more than 86.45% of the data variance. PDSs classification based on output components showed that the patterns had seasonal structures. Synoptically, the north wind blowing in the first pattern is the most dominant structure in the formation of PDSs in the Middle East. The second and third patterns showed postfrontal structures. The fourth pattern with prefrontal structure was the reason for PDSs in the cold seasons of the year. From the four final patterns, the first three patterns showed the dominance of the Persian trough in the SLP maps. Mean values map analysis of the aerosol optical depth suggests that each of the most consistent synoptic patterns stimulates special dust centers.

Key-words: pervasive dust storms, synoptic climatology, PCA, persian trough, Iran

1. Introduction

Dust emissions play an important role in the weather, bio-cycle, and other systems of the Earth (Choobari *et al.*, 2014; Mahowald *et al.*, 2014), which could disturb the general health and economic activities (Raviand D'Odorico, 2005) and lead to soil erosion (Warren, 2014) by damaging the vegetation (Tegen *et al.*, 2004). The climate of storm dust has been well documented by various researchers through synoptic analysis of the past 50 years in Asia (Sun *et al.*, 2001; Zhou, 2001; Chun *et al.*, 2001; Qian *et al.*, 2002; Natsagdorj *et al.*, 2003, Kurosaki and Mikami, 2003; Shao and Wang, 2003). Different atmospheric phenomena lead to the occurrence of dust events at synoptic, regional, and local scales. Dust emission is intensified by some of the synoptic meteorological patterns such as the identified frontal and synoptic systems (Trigo *et al.*, 1999, 2002). The statistical results of 28 spring dust events that occurred during 2015–2018 showed that all of these dust storms were triggered by mogul cyclones or Asian highs (Li *et al.*, 2019). In western Asia, most of these phenomena are observed in one of the three subgroups, including north wind, frontal systems, and convective systems (WMO, 2013).

In a study conducted by Khoshkish *et al.* (2011), the atmosphere middle-level depression, low-pressure systems in the Persian Gulf region, and the stream resulted from temperature difference between the east of Turkey and north west of Iraq toward the Persian Gulf were identified as the main factors in transferring dust to the west of Iran. High pressure in the middle level of the atmosphere and immigrant systems of west winds are the most critical synoptic factors affecting the dust phenomenon in the Middle East, and these depressions and immigrant cyclones penetrate to the region when the subtropical high pressure is absent or weak (Zolfaghari and Abedzadeh, 2005). In another research by Zolfaghari *et al.* (2012), the convergence of the middle-level high-pressure systems, thermal low-pressure systems, and increase of pressure gradient in the days of peak activity of dust events were identified as the reasons of reinforcing high-level wind systems and transferring and emitting huge amounts of fine dusts in vast sections of eastwest, west and northwest of Iran.

In the warm period of the year and at the end of a cold period of the year and transition months (spring and autumn), thermodynamic and dynamic processes play an essential role in the formation and transfer of dust to the west of Iran, respectively (Azizi, *et al.*, 2012). Besides, a meteorological pattern called the Persian Gulf's thermal low-pressure ridge, and penetration of European high-pressure ridge on the Red Sea, and the passage of the Mediterranean Trough's middle-level waves above the northwest of Iraq and east of Syria were emphasized by Ghahri *et al.* (2012). The synoptic analysis of 19 PDSs in Khuzestan province with a duration of two days provided four general patterns (Lashkari and Sabouri; 2013). In a study by Babaei *et al.* (2016), by isolating the frequency of dust incidents in two warm and cold

periods of the year in the western half of Iran, the dominant synoptic patterns of their occurrence were interpreted.

Several case studies on dust storms in western countries of Asia have been conducted. From among these studies, analysis of the great dust storm in Saudi Arabia in March 2009 was done by *Alharbi et al.* (2012), and it was showed that this storm happened due to the passage of a cold front by emitting an intense upstream jet current. Furthermore, analysis of the meteorological reasons of an unprecedented pervasive dust after the occurrence of a lightning storm in Qatar and around the Middle East in February 4, 2010 showed, that the cold weather above Saudi Arabia began a northwest wind which led to the dust storm in some sections of the Arabian Peninsula (*Monikumar and Revikumar*; 2012). The 850 hPa level was introduced by *Abdul-Wahab et al.* (2017) as the criterion of studying changes in the pressure's synoptic patterns to study the seasonal changes of dust in the east and west of Saudi Arabia.

Nowadays, some researchers have turned to study indices such as aerosol optical depth (AOD) to study synoptically the dust phenomena using remote sensing technology (*Qi et al.*, 2013; *Alam et al.*, 2014). In this regard, *Namdari et al.* (2016) analyzed the spatiotemporal analysis of AOD index values in western Iran. The increase of dust storms' frequency during the past years has introduced this natural hazard as the most important biological threat in the western half of Iran. Thus, identification of synoptic climatic behavior of these events makes it possible to predict the origin, performance mechanism, and evaluation of measures to reduce their possible damages. In this regard, researchers attempted to study the dominant mechanisms leading to PDS in the west of Iran using a synoptic modeling method. In this area, the wind flow tracking was emphasized by studying synoptic maps for identifying and monitoring the route of dust storms (*Vali et al.*, 2014).

2. Data and methodology

A dust storm, also called sandstorm, is a meteorological phenomenon common in arid and semi-arid regions. Dust storms arise when a gust front or other strong wind blows loose sand and dirt from a dry surface. Sand and dust storms usually occur when strong winds lift large amounts of sand and dust from bare, dry soils into the atmosphere (*Nickovic, et al.*, 2015). Visibility can be used as a dust weather indicator that recorded in regular weather observations metrically (*Wang, 2015*).

In this research, using visibility less than 1000m daily data of 16 synoptic stations located at Khuzestan and Ilam provinces during the period 2004–2017 (*Fig. 1*), PDSs with more than two days duration in more than 70% of stations in the region were extracted.

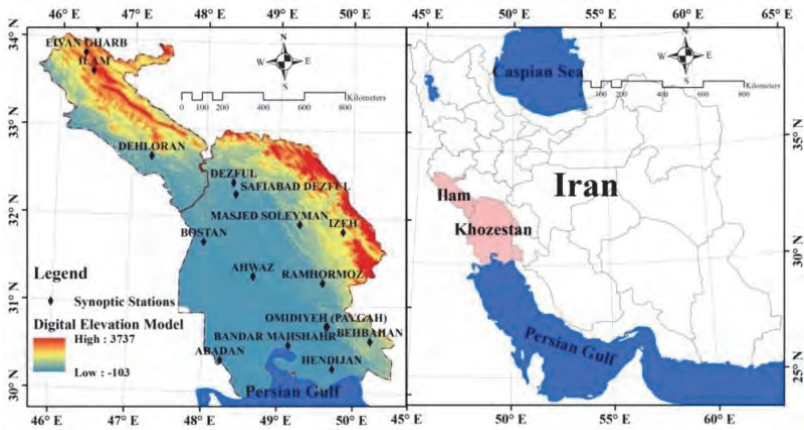


Fig. 1. The region under study and the location of synoptic stations.

Then, by establishing the mid-level atmospheric databases with $2.5^{\circ} \times 2.5^{\circ}$ degree resolution (domain: $0^{\circ}\text{--}80^{\circ}\text{E}$ and $10^{\circ}\text{--}70^{\circ}\text{N}$, Fig. 2), data were extracted from levels 500, 700, 850 hPa, and SLP of 59 selected pervasive dust events and the matrix 825×59 of 500 hPa data was performed.

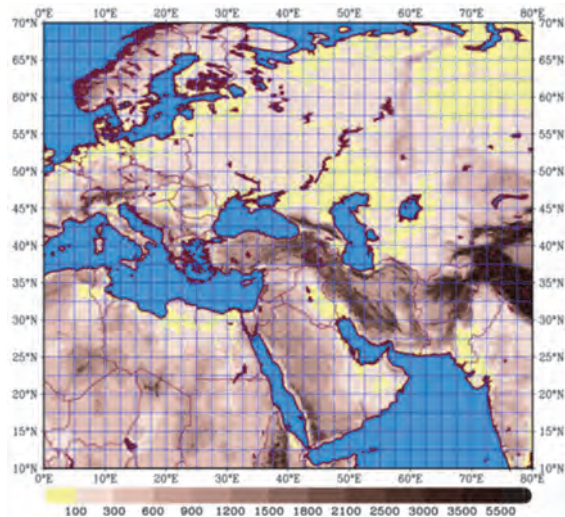


Fig. 2. The area of mid-level atmospheric data.

In the following, to find the patterns for creating dust phenomena, principal component analysis (PCA) was used. The principal component analysis (PCA) is probably the most popular multivariate statistical technique, and it is used by almost all scientific disciplines (Abdi and Williams, 2010). Its goal is to extract the important information from the data, to represent it as a set of new orthogonal variables called principal components, and to display the pattern of similarity of the observations and variables as points in maps. One of the applications of PCA in synoptic climatology is the map-pattern classification.

In this method, after the preparation of data, the investigator selects the mode decomposition, type of dispersion matrix, and type of analysis. The PCA-based map-pattern classification targets the main modes of spatial variation of just one variable; usually surface pressure or geopotential height. Therefore, the mode decomposition and the type of dispersion matrix are S-mode and correlation matrix, respectively. PCA produces component loading and component-scores matrices, with the m principal components corresponding to the N data points on the map. The investigator applies a clustering algorithm to the scores matrix to identify the most common combinations of principal-component scores. However, the PCA with S-mode enables the analysis of patterns without cluster analysis (Raziei, 2018).

Furthermore, using the global aerosol database for MODIS Global Studies Group^{*}, the aerosol optical depth index[†] was extracted for each of the patterns to show the performance of the system and the rise of dust from the level of possible centers. The aerosol optical depth can be considered as an index of dust events so that in dust storms, the index values are changed from 0.5 to 3, and when value 5 is reached, PDS is formed (Legrand *et al.*, 2001).

3. Results

The monthly and seasonal frequencies of 59 identified PDSs showed that the highest number of events was related to July with 14 days (*Fig. 3*). After that, May with 10 days got the second rank. Seasonally, spring and summer both with 20 days had the highest numbers of PDSs. Winter (especially March) and autumn were placed in the next ranks with a total of 14 and 5 events, respectively.

^{*} This base provides the aerosol optical depth based on the blue spectrum depth algorithm with spatial resolution of 10 km (Hsu *et al.*, 2004).

[†] The aerosol optical depth value dependent on wavelength is defined as the light reduction in the length unit on a specified route (Charlson and Heintzenberg, 1995).

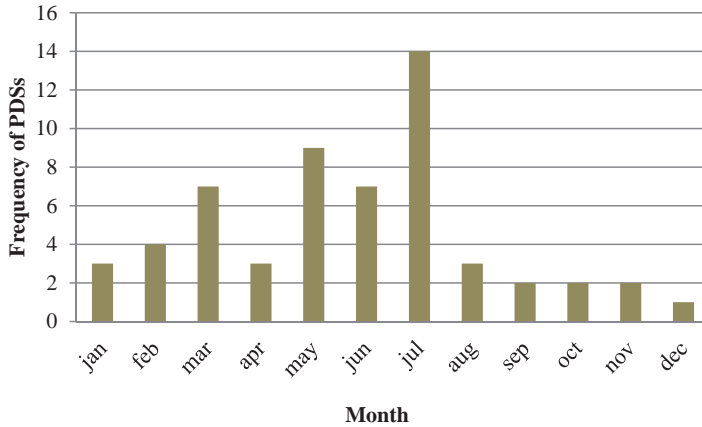


Fig. 3. The monthly frequency of PDSs in the west of Iran during 2004-2017.

After performing the PCA, the components that explained more than 5% of the variance of the data were selected as the final components (*Kaiser, 1960*). However, PCA showed that the first 4 components justify more than 86.45% of data variance (*Fig. 4*). The first component justifies more than 67.3% of this dispersion. The rest of the data dispersion is justifiable, on the other hand.

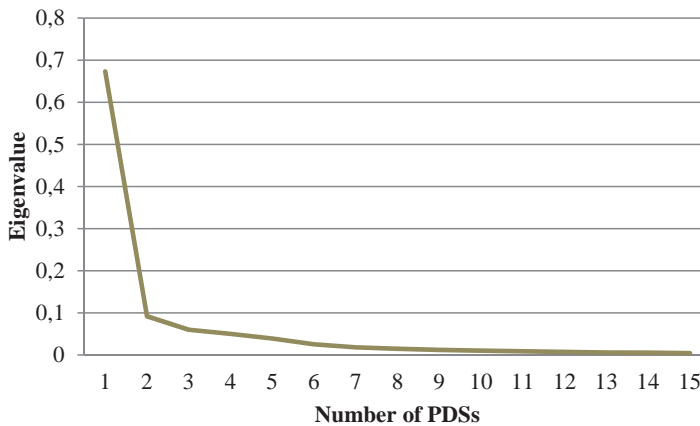


Fig. 4. Scree Plot for PCA

Adjustment of date of PDSs, which have the highest convergence with four synoptic patterns made it possible to analyze the monthly frequency of patterns leading to these events (*Fig. 5*). Results showed that Pattern2 completely was observed summer, so that 74% and 26% of cases occurred in July and two months of August and September, respectively. Pattern1 occurred in winter and somehow in spring: 27% of its cases happens in the last month of the year. 60% of cases in Pattern3 were observed in May, indicating that the desired pattern occurred in spring. Rare cases were observed in the cold period of the year, especially in autumn. Studies showed that the highest frequency of Pattern4 is related to the cold period of the year, which of course showed a 42% frequency in June.

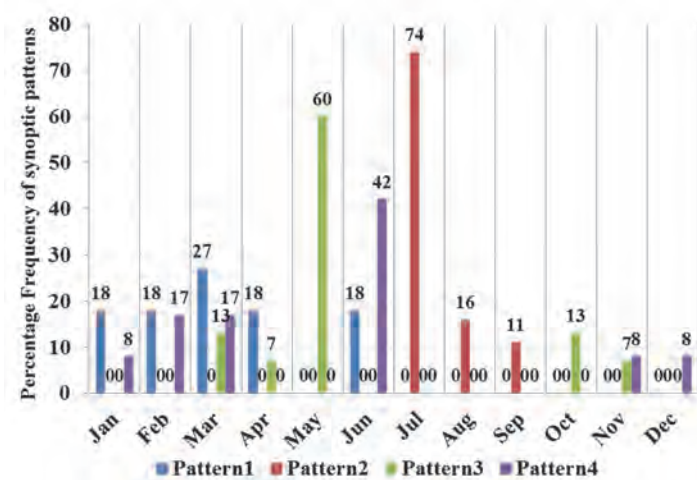


Fig. 5. Monthly frequency of synoptic patterns leading to PDSs in the southwestern regions of Iran during 2004–2017.

Then, the maps extracted from the average level of 500 hPa, stream direction and surface vorticity of 700 hPa, speed and direction of the stream at the 850 hPa level, as well as the SLP relating to all of the four final patterns, were synoptically interpreted.

3.1. Pattern1

According to a low-height field in northern Europe, the relatively low-height ridge above Turkey, and the high-height strong cell above the Arabian Peninsula, an extensive negative vorticity was formed above the Arabian Peninsula and on the southeast and northwest regions of Iran in contrast to the strong positive vorticity

above Turkey, which is obvious at levels 500 and 700 hPa (*Fig. 6a,b*). Development of the Persian trough according to the northwest-southeast trend of Zagros Mountains at the 850 hPa level and establishment of a low-pressure cell with the central curve of 1000 hPa above Oman and a high-pressure cell with the closed curve of 1010 hPa at the sea level with a pressure difference of 10 hPa led to the creation of a winter north wind in the region by the extensive northwest-southeast stream (*Figs. 6c,d*). The north wind is the most dominant structure for the creation of extensive dust in the Middle East (*Middleton, 1986*).

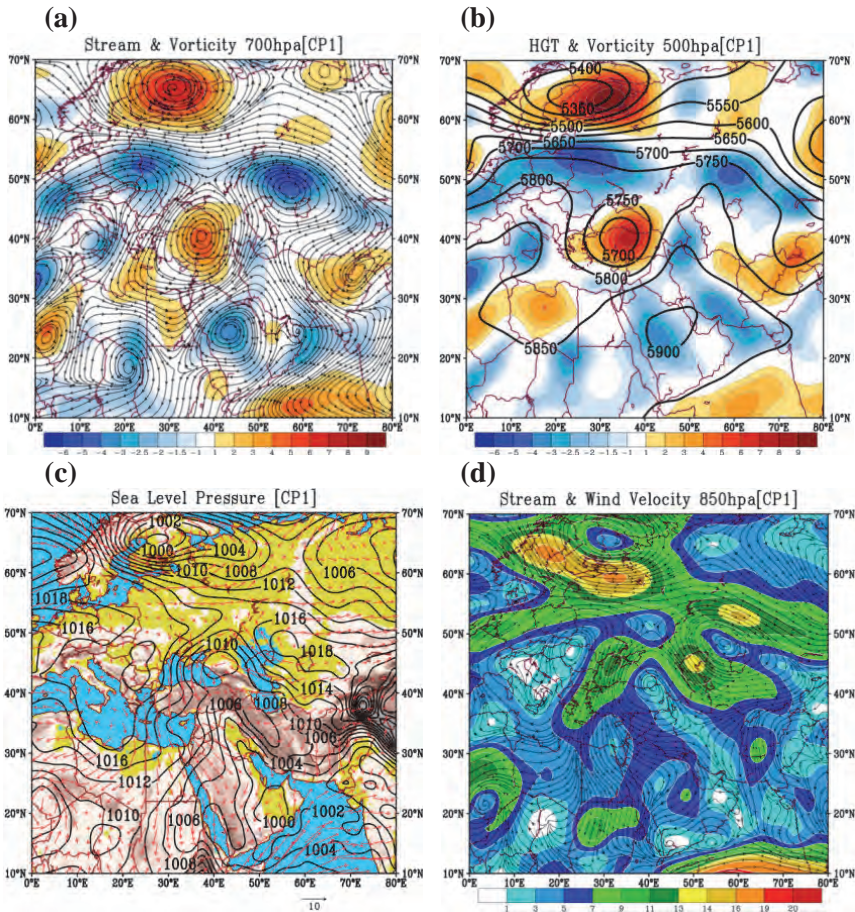


Fig. 6. Meteorological pattern: geo-potential height and vorticity of 500 hPa (a), stream direction and vorticity of 700 hPa (b), stream speed and direction of 850 hPa (c), and SLP (d) from Pattern1.

3.2. Pattern2

At the 500 hPa level of this pattern, we face a low-height system above Russia which sent a ridge toward the Mediterranean Sea and the east of Baikal Lake (Fig. 7a). This structure at the 700 hPa level led to the creation of a positive vorticity core along the Zagros Mountains at the border of Iran and the north of Iraq (Fig. 7b). The high-pressure cores located at the west of the Red Sea and the Arabian Peninsula with a strong low-pressure core above the Persian Gulf led to the creation of a western-eastern wind stream with a high speed in the central and eastern parts of Saudi Arabia up to the border of Iraq along with a summer north wind (Figs. 7c,d).

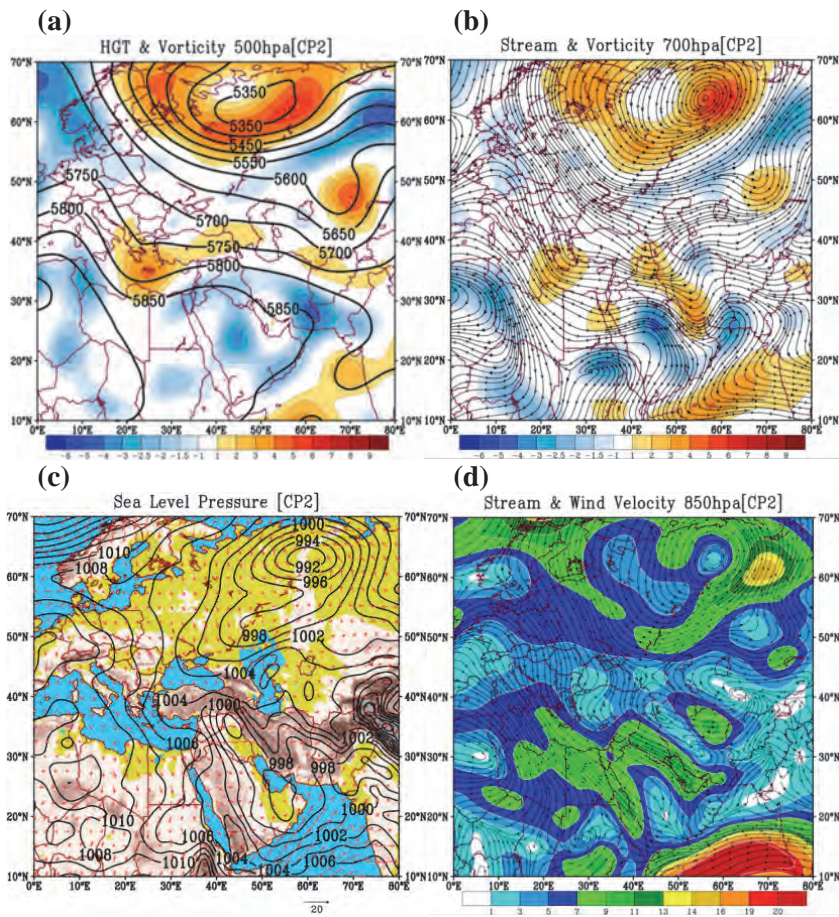


Fig. 7. Meteorological pattern: geopotential height and vorticity of 500 hPa (a), stream direction and vorticity of 700 hPa (b), stream speed and direction of 850 hPa (c), and SLP (d) from Pattern2.

3.3 Pattern3

At the 500 hPa level, the low-height system above northern Europe and the high-height system above Russia are shown which sent the low-height ridge toward the Black Sea and emitted it up to the center of the Mediterranean Sea. In lower widths and higher heights, the subtropical ridge with the curve of 5900 m was sent to northern Africa, the Arabian Peninsula, and up to the western and central parts of Iran (Figs. 8a,b). The expansion of the Persian trough in the form of the low-pressure ridge from the Indian to the Black Sea coast is seen at the levels of 850 hPa and 1000 hPa (Figs. 8c,d).

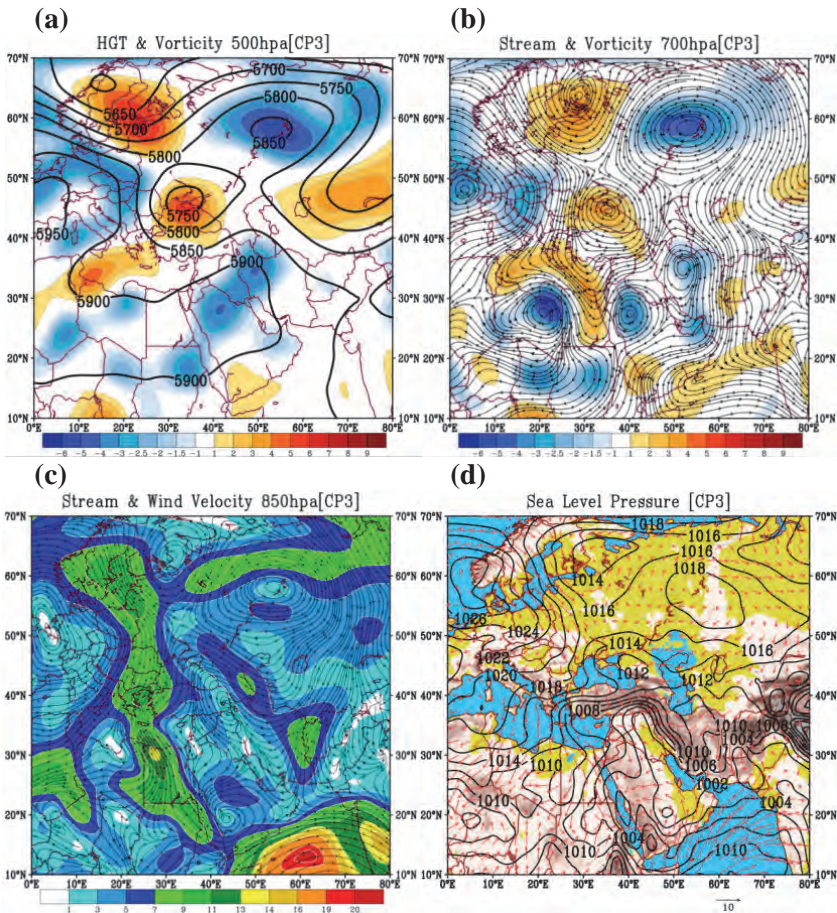


Fig. 8. Meteorological pattern: geopotential height and vorticity of 500 hPa (a), stream direction and vorticity of 700 hPa (b), stream speed and direction of 850 hPa (c), and SLP (d) from Pattern3.

3.4. Pattern4

This pattern at the 500 hPa level shows a low-pressure ridge of an immigrant system in the cold period of the year. In eastern Europe and the Arabian Peninsula, a strong high-height cell and ridge became dominant respectively, and a low-height ridge was formed between these two above the eastern part of the Mediterranean Sea. This structure has led to relatively strong vorticity above the eastern part of the Mediterranean Sea at the 500 and 700 hPa levels (Fig. 9a,b). The encounter of subtropical jet and polar jet at levels 500 and 700 hPa was evident, leading to the orbital circulation and the maximum wind speed at the 850 hPa level in the border regions of Iran, Syria, and northern parts of Saudi Arabia (Fig. 9c). The sea-level high pressure above the northern and central parts of Iran with various cores led to the stability of the dust mass (Fig. 9d).

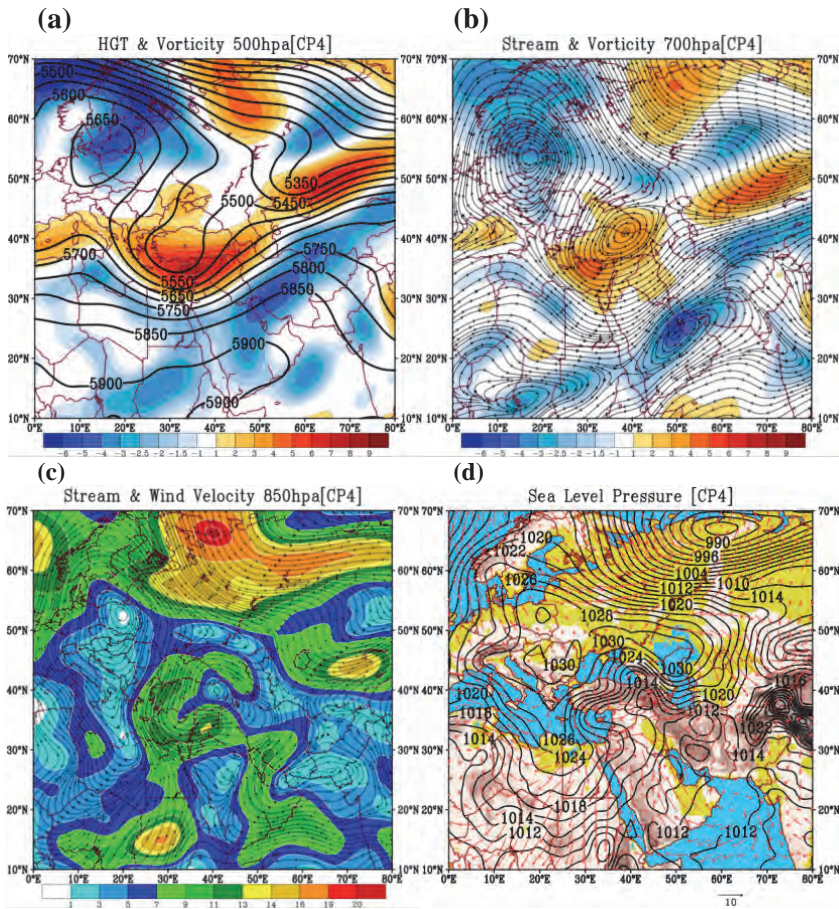


Fig. 9. Meteorological pattern: geopotential height and vorticity of 500 hPa (a), stream direction and vorticity of 700 hPa (b), stream speed and direction of 850 hPa (c), and SLP (d) from Pattern4.

Finally, mean values analysis of AOD maps estimated of the each most consistent synoptic patterns showed that in Pattern1 (Fig. 10a), the north wind stream in the northwest-southeast direction led to the rise of dust from the Mesopotamian plains all around Iran, Syria, and lagoons such as Hoor-al-Azim in Iran. Pattern2 (Fig. 10b) also stimulates dust centers in the western, central, and eastern of Saudi Arabia by intensifying the western-eastern wind stream. Despite its similarity in appearance with Pattern2, Pattern3 (Fig. 10c) affects dust centers in the border between Iraq and Syria due to its location at higher latitude. However, Pattern4 (Fig. 10d) led to the rise of dust in these regions by creating a stream with the maximum wind speed on dust centers in the border between Iraq, Syria, and the eastern parts of Saudi Arabia.

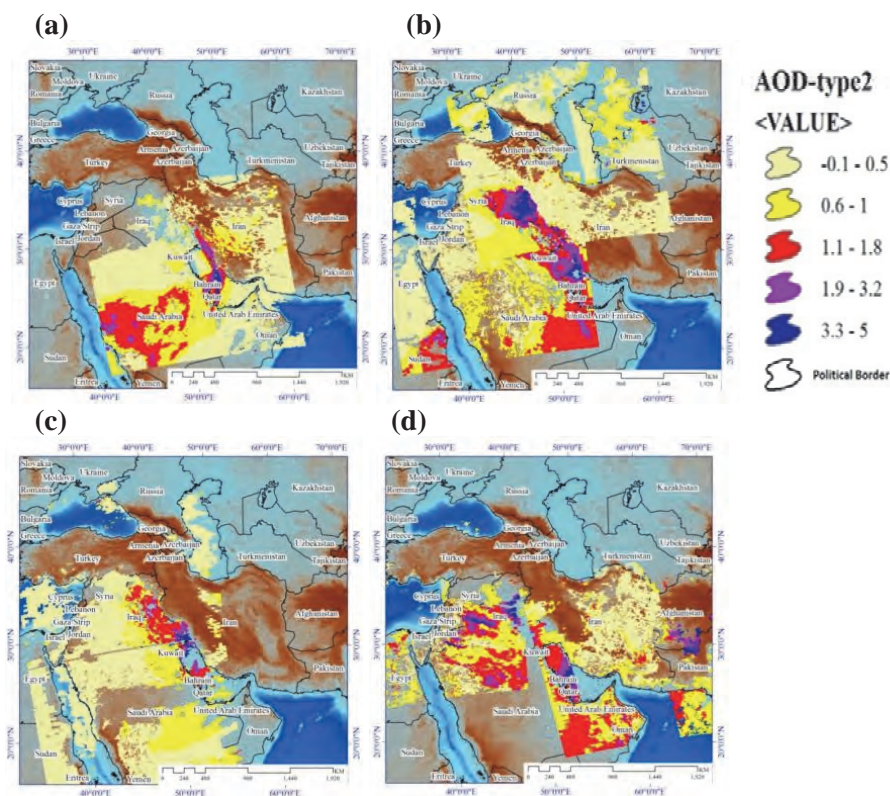


Fig. 10. The average aerosol optical depth index in patterns 1(a), 2(b), 3(c), and 4(d). The optical depth of less than 0.1 shows clear weather and the optical depth of more than 4 presents the density of aerosols.

4. Conclusion

Dust storms are natural hazards which have a significant effect on the arid and semi-arid areas of the world, including Iran (*Sedaghat et al.*, 2016). The frequency analysis of 59 pervasive dust storms (PDSs) in the west of Iran showed that the warm period of the year, especially July with 14 events had the highest frequency. The principal component analysis showed that the first 9 components justified more than 93.5% of the data variance. From among four final patterns resulted from cluster sampling, three patterns showed the dominance of the Persian trough in the SLP map. The Persian trough indicates the formation of a summer atmosphere in the region of the Mediterranean Sea (*Sedaghat and Nazaripour*; 2018).

As *Li et al.* (2019) emphasize on the Gobi Desert in China, cyclonic synoptic systems have been the main cause of dust storms in desert areas. Dust storms resulted from north winds and matched with Pattern1 in the present research by forming high pressure above the northern part of Saudi Arabia, low pressure above Afghanistan, and thermodynamic low-pressure ridge of the Persian Trough relating to the monsoon locating above the southern part of Arabian Peninsula have led to the creation and stream of north winds above the Persian Gulf. The presence of this trough at 850 hPa level was confirmed by *Lashkari and Sabouri* (2013).

Postfrontal dust storms matched with patterns 2 and 3 are formed above the Arabia Peninsula and the eastern part of Iran by establishing two low-pressure cores above the Red Sea and the Persian Gulf and consecutive high-pressure cores above the western part of Red Sea. These storms mostly happen in the transition seasons (spring and autumn) and especially in spring. Prefrontal dust storms matched with Pattern4 in this research are formed by establishing an extensive low-pressure core above the eastern part of the Mediterranean Sea, northern part of the Arabian Peninsula, and western part of Iran. The intense performance of frontal dust storms in the Sistan Basin has also been confirmed (*Kaskaoutis et al.*, 2019). The encounter of polar jet behind the front and subtropical jet ahead created an extensive convergence, leading to the intensification of rising speed and the rise of dust from surface centers (*Wilkinson*, 1991). Such a structure has been described by *Al-Jumaily and Ibrahim* (2013) in the case study of two dust storms in Iraq.

Also, as the study of the relationship between dust estimated by the aerosol optical depth and meteorological parameters in the desert areas of Iraq, Syria, and Saudi Arabia has shown the influence of synoptic systems on the emission of dust storms in the region (*Namdari et al.*; 2018). Maps preparation of aerosol optical depth average values for each of the patterns aiming at the determination of the location of rising of dust showed that each of the patterns stimulates the most consistent synoptic dust centers in the area of Iraq, Syria, and Saudi Arabia.

References

- Abdi, H. and Williams, L.J., 2010: Principal component analysis. *Comput. Stat.* 2, 433–459. <https://doi.org/10.1002/wics.101>
- Abdul-Wahab, S.M., Ahmad, O.A., Adel, M.A., and Mazen, E.A. 2017: Seasonal variability and synoptic characteristics of dust cases over southwestern Saudi Arabia, *Int. J. Climatol*, 38 105–124. DOI: 10.1002/joc.5164. <https://doi.org/10.1002/joc.5164>
- Alam, K., Trautmann, T., Blaschke, T., and Subhan, F., 2014: Changes in aerosol optical properties due to dust storms in the Middle East and Southwest Asia. *Remote Sens. Environ* 143, 216–227. <https://doi.org/10.1016/j.rse.2013.12.021>
- Alharbi, B.H., Maghrabi, A., and Tapper, N., 2012: The March 2009 dust event in Saudi Arabia: precursor and supportive environment, *Bull. Amer. Meteorol. Soc.* 94, 515–528. <https://doi.org/10.1175/BAMS-D-11-00118>
- Al-Jumaily, K. J. and Ibrahim, M.K., 2013: Analysis of synoptic situation for dust storms in Iraq. *Int. J. Energ. Environ.* 4, 851–858.
- Azizi, G., Shamsipoor, A.A., Miri, M., and Safarrad, T., 2012: The Synoptic-Statistical Analysis of Dust Phenomenon in the Western Half of Iran, *Ecology* 38(3) 123–134.
- Babaei Fini, O., Safarzadeh, T., and Karimi, M., 2016: Analysis and Identification of Synoptic Patterns of Dust Storms in the West of Iran, *Geograph. Environ. Hazards* 17, 105–119.
- Charlson, R.J. and Heintzenberg, J., 1995: Introduction in Aerosol Forcing of Climate. Report of the Dahlem Workshop on Aerosol Forcing of Climate, Berlin, April 24–29.
- Choobari.O.A., Zawar-Reza, P., and Sturman, A., 2014: The global distribution of mineral dust and its impacts on the climate system: a review, *Atmos. Res.* 138, 152–65. <https://doi.org/10.1016/j.atmosres.2013.11.007>
- Chun, Y.S., Boo, K.O., Kim, J., Park, S., and Lee, M., 2001: Synopsis, transport and physical characteristics of Asian dust in Korea, *J. Geophys. Res.* 106, 18461–18469. <https://doi.org/10.1029/2001JD900184>
- Ghahri, F., Ranjbar Saadatabadi, A., and Kairaei, P., 2012: Study of Meteorological Patterns and Extensive Summer Dust Production Sources in the South of Iran, *Marine Sci. Technol. Res.* 7, 1–20.
- Hsu, N.C., Tsay, S.I., King, M.D., and Herman, J.R., 2004: Aerosol properties over bright reflecting source regions, *IEEE Trans. Geosci. Remote Sens.* 42, 557–569. <https://doi.org/10.1109/TGRS.2004.824067>
- Kaiser, H.F., 1960: The application of electronic computers to factor analysis. *Educational Psychol. Measure.* 20, 141–151. <https://doi.org/10.1177/001316446002000116>
- Kaskaoutis, D.G., Francis, D., Rashki, A., Chaboureau, J.-P., and Dumka, U.C., 2019: Atmospheric Dynamics from Synoptic to Local Scale During an Intense Frontal Dust Storm over the Sistan Basin in Winter 2019. *Geosciences* 9, 453. <https://doi.org/10.3390/geosciences9100453>
- Khoskikh, A., Alijani, B., and Hejazizadeh, Z., 2011: The Synoptic Analysis of Dust Systems in Lorestan Province, *Appl. Res. Geograph. Sci.* 18(21), 91–110.
- Kurosaki, Y. and Mikami, M., 2003: Recent frequent dust events and their relation to the surface wind in East Asia. *Geophys. Res. Lett.* 30 (14), 1736. <https://doi.org/10.1029/2003GL017261>
- Lashkari, H. and Sabouei, M., 2013: The Synoptic Analysis of Dust Storm Patterns in Khuzestan Province, *Sepehr Geographical Inform. Quart. J.* 22, No. 87, 32–38.
- Legrand, M., Plana-Fattori, A., and N'Doumé, C., 2001: Satellite detection of dust using the IR imagery of Meteosat: Infrared difference dust index, *J. Geophys. Res.*, 106, 18251–18274. <https://doi.org/10.1029/2000JD900749>
- Li, W., Wang, W., Zhou, Y., Ma, Y., Zhang, D., and Sheng, L., 2019: Occurrence and Reverse Transport of Severe Dust Storms Associated with Synoptic Weather in East Asia. *Atmosphere*, 10(1), 4. <https://doi.org/10.3390/atmos10010004>
- Mahowald, N., Albani, S., Kok, J.F., Engelstaeder, S., Scanza, R., Ward, D.S., and Flanner, M.G., 2014: The size distribution of desert dust aerosols and its impact on the Earth system, *Aeolian Res.* 15, 53–71. <https://doi.org/10.1016/j.aeolia.2013.09.002>
- Middleton, N. J., 1986: Dust storms in the Middle East. *J. Arid Environ.* 10(2), 83–96. [https://doi.org/10.1016/S0140-1963\(18\)31249-7](https://doi.org/10.1016/S0140-1963(18)31249-7)

- Monikumar, R., and Revikumar, P.V., 2012: Occurrence of widespread dust followed by thunderstorm over Qatar on 4th February 2010 – a case study, *Pakistan J. Meteorology* 9(17), 49-56.
- Namdari, S., Karimi, N., Sorooshian, A., Mohammadi, G., and Sehatkashani, S., 2018: Impacts of climate and synoptic fluctuations on dust storm activity over the Middle East. *Atmos. Environ.* 173, 265–276. <https://doi.org/10.1016/j.atmosenv.2017.11.016>
- Namdari, S., Valizade, K.K., Rasuly, A.A., and Sarraf, B.S., 2016: Spatio-temporal analysis of MODIS AOD over the western part of Iran. *Arabian J. Geosciences* 9(3), 191. <https://doi.org/10.1007/s12517-015-2029-7>
- Natsagdorj, L., Jugder, D., and Chung, Y.S., 2003: Analysis of dust storms observed in Mongolia during 1937–1999, *Atmos. Environ.* 37, 1401–1411. [https://doi.org/10.1016/S1352-2310\(02\)01023-3](https://doi.org/10.1016/S1352-2310(02)01023-3)
- Nickovic, S., Cuevas Agulló, E., Baldasano, J. M., Terradellas, E., Nakazawa, T., and Baklanov, A., 2015: Sand and Dust Storm Warning Advisory and Assessment System (SDS-WAS) Science and Implementation Plan: 2015–2020.
- Qi, Y., Ge, J., and Huang, J., 2013: Spatial and temporal distribution of MODIS and MISR aerosol optical depth over northern China and comparison with AERONET. *Chinese Sci. Bull.* 58(20), 2497–2506. <https://doi.org/10.1007/s11434-013-5678-5>
- Qian, W., Quan, L., and Shi, S., 2002: Variations of the dust storm in China and its climatic control, *J. Climate* 15, 1216–1229. [https://doi.org/10.1175/1520-0442\(2002\)015<1216:VOTDSI>2.0.CO;2](https://doi.org/10.1175/1520-0442(2002)015<1216:VOTDSI>2.0.CO;2)
- Ravi, S. and D'Odorico, P., 2005: A field-scale analysis of the dependence of wind erosion threshold velocity on air humidity, *Geophys. Res. Lett.* 32, L21404. <https://doi.org/10.1029/2005GL023675>
- Raziei, T., 2018: A precipitation regionalization and regime for Iran based on multivariate analysis. *Theor. Appl. Climatol* 131, 1429–1448. <https://doi.org/10.1007/s00704-017-2065-1>
- Sedaghat, M. and Nazariipoor, H., 2018: A New Attitude in Determining the Summer Atmosphere of Iran, *Climatol. Res.* 9, 77–88.
- Sedaghat, M., Mehrnia, S., Barzegar, S., and Zangiabadi, M.A., 2016: The Hazardous Effects of Haloxylons around Kerman City on the Formation of Aerosol's Centers, *Nat. Hazards Manage.* 3, 199–210.
- Shao, Y., and Wang, J.J., 2003: A climatology of northeast Asian dust events. *Meteorol. Zeit.* 12 187–196. <https://doi.org/10.1127/0941-2948/2003/0012-0187>
- Sun, J., Zhang, M., and Liu, T., 2001: Spatial and temporal characteristics of dust storms in China and its surrounding regions, 1901–1999: relations to source area and climate. *J. Geophys. Res.* 106, (D10), 10325–10333. <https://doi.org/10.1029/2000JD900665>
- Tegen, I, Werner, M, Harrison, S.P., and Kohfeld, K.E., 2004: Relative importance of climate and land use in determining present and future global soil dust emission, *Geophys. Res. Lett.* 31, L05105. <https://doi.org/10.1029/2003GL019216>
- Trigo, I.F., Bigg, G.R., and Davies, T.D., 2002: Climatology of cyclogenesis mechanisms in the Mediterranean, *Month. Weather Rev.* 130, 549–569. [https://doi.org/10.1175/1520-0493\(2002\)130<0549:COCMIT>2.0.CO;2](https://doi.org/10.1175/1520-0493(2002)130<0549:COCMIT>2.0.CO;2)
- Trigo, I.F., Davies, T.D., and Bigg, G.R., 1999: Objective climatology of cyclones in the Mediterranean region, *J. Climate* 12, 1685–1696. [https://doi.org/10.1175/1520-0442\(1999\)012<1685:OCOCIT>2.0.CO;2](https://doi.org/10.1175/1520-0442(1999)012<1685:OCOCIT>2.0.CO;2)
- Vali, A.A., Khamoushi, S., Mousavi, S.H., Panahi, F., and Tamaski, E., 2014: The Climatic Analysis and Tracking of Extensive Dust Storms (EDSs) in the South and Center of Iran, *Ecology* 40, 691–972.
- Wang, J.X., 2015: Mapping the global dust storm records: Review of dust data sources in supporting modeling/climate study. *Curr. Pollut. Rep.* 1, 82–94. <https://doi.org/10.1007/s40726-015-0008-y>
- Warren, S.D., 2014: Role of biological soil crusts in desert hydrology and geomorphology: implications for military training operations, *Rev. Engineer. Geology.* 22, 177–186. [https://doi.org/10.1130/2014.4122\(16\)](https://doi.org/10.1130/2014.4122(16))
- Wilkerson, W.D., 1991: Dust and forecasting in Iraq and adjoining countries, USAF Environmental Technical Applications Center, John Wiley, New York, 72p.
- World Meteorological Organization, 2013: Establishing a WMO Sand and Dust Storm Warning Advisory and Assessment System Regional Node for West Asia: Current Capabilities and Needs. *Technical Report* 1121.
- Zhou, Z.J., 2001: Blowing sand and sand storm in China in recent 45 years. *Quat. Sci.* 21, 9–17.

- Zolfaghari, H., and Abedzadeh, H., 2005: The Synoptic Analysis of Dust Systems in the West of Iran. *Geograph. Develop.* 3(6), 173–188.
- Zolfaghari, H., Masoumpoor Samakoush, J., Shaygan Mehr, Sh., and Ahmadi, M., 2012: The Synoptic Study of Dust Storms in the western regions of Iran during 2005-2009 (Case Study: Extensive Wave in July 2009), *Geograph. Environ. Plan.* 22, 17–34.

INSTRUCTIONS TO AUTHORS OF *IDŐJÁRÁS*

The purpose of the journal is to publish papers in any field of meteorology and atmosphere related scientific areas. These may be

- research papers on new results of scientific investigations,
- critical review articles summarizing the current state of art of a certain topic,
- short contributions dealing with a particular question.

Some issues contain “News” and “Book review”, therefore, such contributions are also welcome. The papers must be in American English and should be checked by a native speaker if necessary.

Authors are requested to send their manuscripts to

Editor-in Chief of IDŐJÁRÁS
P.O. Box 38, H-1525 Budapest, Hungary
E-mail: journal.idojaras@met.hu

including all illustrations. MS Word format is preferred in electronic submission. Papers will then be reviewed normally by two independent referees, who remain unidentified for the author(s). The Editor-in-Chief will inform the author(s) whether or not the paper is acceptable for publication, and what modifications, if any, are necessary.

Please, follow the order given below when typing manuscripts.

Title page should consist of the title, the name(s) of the author(s), their affiliation(s) including full postal and e-mail address(es). In case of more than one author, the corresponding author must be identified.

Abstract: should contain the purpose, the applied data and methods as well as the basic conclusion(s) of the paper.

Key-words: must be included (from 5 to 10) to help to classify the topic.

Text: has to be typed in single spacing on an A4 size paper using 14 pt Times New Roman font if possible. Use of S.I.

units are expected, and the use of negative exponent is preferred to fractional sign. Mathematical formulae are expected to be as simple as possible and numbered in parentheses at the right margin.

All publications cited in the text should be presented in the *list of references*, arranged in alphabetical order. For an article: name(s) of author(s) in Italics, year, title of article, name of journal, volume, number (the latter two in Italics) and pages. E.g., *Nathan, K.K.*, 1986: A note on the relationship between photosynthetically active radiation and cloud amount. *Időjárás* 90, 10–13. For a book: name(s) of author(s), year, title of the book (all in Italics except the year), publisher and place of publication. E.g., *Junge, C.E.*, 1963: *Air Chemistry and Radioactivity*. Academic Press, New York and London. Reference in the text should contain the name(s) of the author(s) in Italics and year of publication. E.g., in the case of one author: *Miller* (1989); in the case of two authors: *Gamov* and *Cleveland* (1973); and if there are more than two authors: *Smith et al.* (1990). If the name of the author cannot be fitted into the text: (*Miller*, 1989); etc. When referring papers published in the same year by the same author, letters a, b, c, etc. should follow the year of publication. DOI numbers of references should be provided if applicable.

Tables should be marked by Arabic numbers and printed in separate sheets with their numbers and legends given below them. Avoid too lengthy or complicated tables, or tables duplicating results given in other form in the manuscript (e.g., graphs). *Figures* should also be marked with Arabic numbers and printed in black and white or color (under special arrangement) in separate sheets with their numbers and captions given below them. JPG, TIF, GIF, BMP or PNG formats should be used for electronic artwork submission.

More information for authors is available: journal.idojaras@met.hu

Published by the Hungarian Meteorological Service

Budapest, Hungary

ISSN 0324-6329 (Print)

ISSN 2677-187X (Online)